METAL AND SEMICONDUCTOR NANOCRYSTALS

EDITED BY: Jing Zhao, Shengli Zou, Jie He and Ou Chen
PUBLISHED IN: Frontiers in Chemistry

frontiers Research Topics

ISSN 1664-8714
ISBN 978-2-88963-362-3
DOI 10.3389/978-2-88963-362-3

About Frontiers

Frontiers is more than just an open-access publisher of scholarly articles: it is a pioneering approach to the world of academia, radically improving the way scholarly research is managed. The grand vision of Frontiers is a world where all people have an equal opportunity to seek, share and generate knowledge. Frontiers provides immediate and permanent online open access to all its publications, but this alone is not enough to realize our grand goals.

Frontiers Journal Series

The Frontiers Journal Series is a multi-tier and interdisciplinary set of open-access, online journals, promising a paradigm shift from the current review, selection and dissemination processes in academic publishing. All Frontiers journals are driven by researchers for researchers; therefore, they constitute a service to the scholarly community. At the same time, the Frontiers Journal Series operates on a revolutionary invention, the tiered publishing system, initially addressing specific communities of scholars, and gradually climbing up to broader public understanding, thus serving the interests of the lay society, too.

Dedication to Quality

Each Frontiers article is a landmark of the highest quality, thanks to genuinely collaborative interactions between authors and review editors, who include some of the world's best academicians. Research must be certified by peers before entering a stream of knowledge that may eventually reach the public - and shape society; therefore, Frontiers only applies the most rigorous and unbiased reviews.
Frontiers revolutionizes research publishing by freely delivering the most outstanding research, evaluated with no bias from both the academic and social point of view. By applying the most advanced information technologies, Frontiers is catapulting scholarly publishing into a new generation.

What are Frontiers Research Topics?

Frontiers Research Topics are very popular trademarks of the Frontiers Journals Series: they are collections of at least ten articles, all centered on a particular subject. With their unique mix of varied contributions from Original Research to Review Articles, Frontiers Research Topics unify the most influential researchers, the latest key findings and historical advances in a hot research area! Find out more on how to host your own Frontiers Research Topic or contribute to one as an author by contacting the Frontiers Editorial Office: researchtopics@frontiersin.org

METAL AND SEMICONDUCTOR NANOCRYSTALS

Topic Editors:
Jing Zhao, University of Connecticut, United States
Shengli Zou, University of Central Florida, United States
Jie He, University of Connecticut, United States
Ou Chen, Brown University, United States

Citation: Zhao, J., Zou, S., He, J., Chen, O., eds. (2020). Metal and Semiconductor Nanocrystals. Lausanne: Frontiers Media SA. doi: 10.3389/978-2-88963-362-3

Table of Contents

frontiers
in Chemistry

EDITORIAL
published: 07 May 2019
doi: 10.3389/fchem.2019.00310

Editorial: Metal and Semiconductor Nanocrystals

Jing Zhao[1]*, *Ou Chen*[2]*, *Jie He*[1]* *and Shengli Zou*[3]*

[1] *Department of Chemistry and Institute of Materials Science, University of Connecticut, Storrs, CT, United States,* [2] *Department of Chemistry, Brown University, Providence, RI, United States,* [3] *Department of Chemistry, University of Central Florida, Orlando, FL, United States*

Keywords: nanoparticles, metal, semiconductor, alloy, oxide, perovskite

OPEN ACCESS

Edited by:
Fan Zhang,
Fudan University, China

Reviewed by:
Yugang Sun,
Temple University, United States

****Correspondence:***
Jing Zhao
jing.zhao@uconn.edu
Ou Chen
ouchen@brown.edu
Jie He
jie.he@uconn.edu
Shengli Zou
shengli.zou@ucf.edu

Specialty section:
This article was submitted to
Nanoscience,
a section of the journal
Frontiers in Chemistry

Received: *22 January 2019*
Accepted: *18 April 2019*
Published: *07 May 2019*

Citation:
Zhao J, Chen O, He J and Zou S
(2019) Editorial: Metal and
Semiconductor Nanocrystals.
Front. Chem. 7:310.
doi: 10.3389/fchem.2019.00310

Editorial on the Research Topic

Metal and Semiconductor Nanocrystals

Metal and semiconductor nanocrystals have been under the spotlight for the past two decades in the rapidly developing field of nanoscience and nanotechnology. In the early days, the research of metal and semiconductor nanocrystals largely focused on Au and Cd-based materials. More recently, a broad range of compositions have been explored, including noble metal and transition metal alloys, perovskites, lead-based semiconductors, indium-based semiconductors, etc. Owing to the advancement in wet-chemical synthesis, the shape of the nanocrystals can be exquisitely controlled with high uniformity, and reproducibility. Efforts have also been devoted to developing hybrid materials that combine metal and semiconductor nanocrystals with other nano or micro materials (such as oxides and polymers) in one structure, which lead to intriguing new properties (or synergies). Currently, metal and semiconductor nanocrystals are being applied in photonics, catalysis, biological imaging, sensing and therapeutics, lighting, energy, and so on. This Research Topic collects a series of research work (both original research and review) in the field of metal and semiconductor nanocrystals. They cover a diverse range of topics, including nanomaterial synthesis, optical and electronic properties, catalytic, and biomedical applications.

Although Au nanocrystals have been extensively studied for two decades, synthesis of well-defined complex structures with high uniformity still remains challenging. Chang et al. developed a method to synthesize Au nanooctopods using a seed-mediated method. The high uniformity of the nanootopods yields a narrow plasmon band of these nanocrystals. The nanooctopods have a high photothermal conversion efficiency (>80%), making them promising photoacoustic contrast agent. In seed mediated method to grow Au nanocrystals, sometime Ag$^+$ ions were added to direct the growth. In the work reported by Athukorale et al. a mechanistic study was performed to understand the adsorption of Ag$^+$ ions on Au nanocrystals. UV-vis, zeta-potential, X-ray photospectroscopy along with surface-enhanced Raman spectroscopy were applied to study the Ag$^+$ adsorption process *in-situ* and *ex-situ*. The results indicate the bound Ag$^+$ ions remain cationic, and there were two parallel processes occurring.

Other than Au nanocrystals, three reports focus on PtNi alloy nanocrystals, and Pt, Rh, etc nanocrystals decorated on oxide nanostructures. Pt based nanocrystals are known to be good catalysts for many chemical and electrochemical reactions. Song et al. synthesized Pt-Ni alloy nanohexapods. The unique structure makes the nanohexapods good electrocatalysts for oxygen reduction reaction. Metal nanocrystals can also be decorated onto oxides to provide new functionality. In the study by Dai et al. ultrasmall Pt and Rh nanoclusters were bound to silica nanospheres. As a result, the absorption of these ultrasmall clusters were enhanced by the resonant and random scattering of light by the silica nanospheres. In another study by Demille et al. a light-mediated growth method was developed to grow a range of metal nanocrystals (Au, Ag, Cu, Pt, Pd, Tu, Ir, and Rh) from ZnO tetrapods with nanostructures. The Pd, Rh, and Ag nanocrystals decorated ZnO tetrapods show significant catalytic activity toward 4-nitrophenol reduction.

Essentially, for all nanocatalysts, one of the critical issues is their stability. Given the large surface energy of nanocatalysts, how to retain their high surface areas and defined nanostructures during the reactions has received enormous attention. The review paper by Xu et al. summarizes the recent advances in metal nanocatalysts supported on mesoporous zeolites, with an emphasis on their catalytic activity and stability for a number of organic reactions. The methodologies on the synthesis of mesoporous zeolites with pre-designed metal nanocrystals are highlighted. The coupling of metal nanocatalysts with various zeolites is discussed in the context of the catalytic synergies.

Three nice articles covering different types of semiconductor nanocrystals are collected in the topic. The work by Abeywickrama et al. describes the synthesis of colloidal cubic PbSe nanocrystals with particle size of 20–40 nm. A two-step iso-material particle growth method was proposed and nicely presented. Given their large size, the final PbSe nanocrystals possessed bulk bandgaps due to minimized quantum confinement. Interestingly, these abnormally large PbSe nanocrystals showed drastically improved film conductivity as compared to their smaller counterparts, demonstrating their potentials in optoelectronic device applications. In addition to the IV-VI semiconductor nanocrystals, Toufanian et al. reported a systematic study of III-V InP-based core/shell semiconductor nanocrystals. Two systems, i.e., InP/ZnS(e) with a type-I (or quasi-Type-II) bandgap alignment and InP/CdS(e) with a type-II bandgap structure were synthesized with fine-tuning the core size and the shell thickness. Different strategies in controlling emission energies of the particles were discovered in these two core-shell systems. This study provides valuable insights in precisely tailoring the optical properties of III-V semiconductor nanocrystals through heterostructural and/or compositional control.

Beyond conventional semiconductor nanocrystals, lead-halide perovskite quantum dots have been explosively reported and studied in recent years, and showed great potentials in a range of applications, such as solar cells, photocatalysis, light emitting devices (LEDs)/displays. In this context, however, how to synthesize high-quality perovskite quantum dots in a large scale with high production yield still remains challenging. In our collection, Zhang et al. reported a new synthesis by modifying conventional emulsion process. Gram scale production of $CH_3NH_3PbBr_3$ quantum dots with more than 70% chemical yield has been successfully achieved. Importantly, the resultant perovskite quantum dots showed great optical properties and were used as efficient blue emitters in LEDs with a maximum luminance of 32 cd/m^2.

Due to their unique properties, nanocrystals of different compositions have been applied in various disciplines. However, fundamental understanding of their unique properties still stands to be improved and more detailed experimental and theoretical works are still in high demand. For example, in synthesis, controlling the size and shape of nanocrystals with a single composition has been advanced significantly, but there are still plenty of rooms for improvement in controlling the size, shape, and compositions ratio of particles with multiple composition. While the applications of those synthesized particles including photonics, catalysis, sensing, energy harvesting and conversion, and bio-imaging, have been investigated extensively, developing simple method without intensive instrumentation to characterize the synthesized particles should also be pursued. Moreover, theoretical understanding of the growth mechanism of the nanocrystals and their size, shape, and composition dependent physical properties is far left behind. All these directions are worthy exploring in the near future.

AUTHOR CONTRIBUTIONS

All authors listed have made a substantial, direct and intellectual contribution to the work, and approved it for publication.

ACKNOWLEDGMENTS

JZ and JH acknowledge partial financial support from National Science Foundation. We would like to thank all the authors and reviewers for their dedication and time in this Frontiers Research Topic.

Conflict of Interest Statement: The authors declare that the research was conducted in the absence of any commercial or financial relationships that could be construed as a potential conflict of interest.

frontiers in Chemistry

ORIGINAL RESEARCH
published: 10 August 2018
doi: 10.3389/fchem.2018.00335

Synergistic Reducing Effect for Synthesis of Well-Defined Au Nanooctopods With Ultra-Narrow Plasmon Band Width and High Photothermal Conversion Efficiency

Yi-Xin Chang[1], *Hui-Min Gao*[2], *Ning-Ning Zhang*[1], *Xing-Fu Tao*[1], *Tianmeng Sun*[3], *Junhu Zhang*[1,4], *Zhong-Yuan Lu*[1,2], *Kun Liu*[1,4]* *and Bai Yang*[1,4]

[1] State Key Laboratory of Supramolecular Structure and Materials, College of Chemistry, Jilin University, Changchun, China, [2] Laboratory of Theoretical and Computational Chemistry, Institute of Theoretical Chemistry, Jilin University, Changchun, China, [3] The First Bethune Hospital and Institute of Immunology, Jilin University, Changchun, China, [4] State Key Laboratory of Applied Optics, Changchun Institute of Optics, Fine Mechanics and Physics, Chinese Academy of Sciences, Changchun, China

OPEN ACCESS

Edited by:
Jing Zhao,
University of Connecticut,
United States

Reviewed by:
Yugang Sun,
Temple University, United States
Xiaoji Xie,
Nanjing Tech University, China

****Correspondence:***
Kun Liu
kliu@jlu.edu.cn

Specialty section:
This article was submitted to
Nanoscience,
a section of the journal
Frontiers in Chemistry

Received: *08 June 2018*
Accepted: *19 July 2018*
Published: *10 August 2018*

Citation:
Chang Y-X, Gao H-M, Zhang N-N, Tao X-F, Sun T, Zhang J, Lu Z-Y, Liu K and Yang B (2018) Synergistic Reducing Effect for Synthesis of Well-Defined Au Nanooctopods With Ultra-Narrow Plasmon Band Width and High Photothermal Conversion Efficiency. Front. Chem. 6:335. doi: 10.3389/fchem.2018.00335

Branched Au nanoparticles have attracted intense interest owing to their remarkable properties and a wide variety of potential applications in surface-enhanced Raman spectroscopy (SERS), photothermal therapy, photoacoustic imaging, and biomedicines. The morphology and spatial arrangement of branches play the most crucial role in the determination of their properties and applications. However, it is still a synthetic challenge to control the exact arm numbers of branches with specific spatial arrangements. Here we report a facile method for the kinetically controlled growth of Au nanooctopods (NOPs) with a high yield (81%), monodispersity, and reproducibility by using the synergistic reducing effect of ascorbic acid and 1-methylpyrrolidine. The NOPs have eight arms elongated along <111> directions with uniform arm lengths. Due to their well-defined size and shape, NOPs show ultra-narrow surface plasmon band width with a full width at half maximum of only 76 nm (0.20 eV). Upon irradiation with laser, the NOPs possessed excellent photothermal conversion efficiencies up to 83.0% and photoacoustic imaging properties. This work highlights the future prospects of using NOPs with desired physicochemical properties for biomedical applications.

Keywords: nanooctopods, nanobranch, nanostar, ultra-narrow plasmon band width, photothermal conversion efficiency, photoacoustic imaging, synergistic reducing effect

INTRODUCTION

Research on Au nanoparticles has been boosted by diverse applications because of their unique size- and shape-dependent properties (Link and El-Sayed, 2000; Kelly et al., 2003; Li et al., 2014; Boles et al., 2016). The past decade has witnessed spectacular success in developing a myriad of methods for shape-controlled synthesis of anisotropic Au nanoparticles with well-defined structures, such as triangles (Malikova et al., 2002), prisms (Shankar et al., 2004), rods (Jana et al., 2001; Nikoobakht and El-Sayed, 2003), cubes (Sun and Xia, 2002; Kim et al., 2004; Zhang, J. et al., 2010), shells (Averitt et al., 1997), stars (Hao et al., 2004; Nehl et al., 2006; Kumar et al., 2007), bipyramids (Liu and Guyot-Sionnest, 2005), cages (Skrabalak et al., 2008), etc. Among them, Au nanobranches with a center core and several protruding arms with sharp tips have drawn enormous attention due to their excellent localized surface plasmon resonance (LSPR) properties (Chen et al., 2003; Guerrero-Martínez et al., 2011; Lim and Xia, 2011; Ye et al., 2015). The arm-length dependent LSPR band in the biological window (650–1,350 nm), remarkable enhanced local E-field at their sharp tips, and relative high cellular uptake and low cytotoxicity make Au nanobranches very attractive for bio-applications, such as SERS-based sensing (Khoury and Vo-Dinh, 2008; Indrasekara et al., 2014), photoacoustic imaging (Wei et al., 2009; Cheng et al., 2014), photothermal therapy (Yuan et al., 2012; Wang et al., 2013), and nanomedicines (Dam et al., 2012), etc.

Many of these applications rely on single wavelength laser to excite the plasmon resonance. To maximize the radiation efficiency and minimize the toxicity and negative side effect in bio-applications, Au nanobranches with narrow plasmon band matching with the laser wavelength is strongly desired. In addition, a narrower plasmon peak width implies a smaller plasmon damping and a larger local electric field enhancement of the nanoparticles (Sönnichsen et al., 2002). Narrow plasmon linewidth of nanoparticles is vital in many plasmonic applications (Zhu et al., 2016), such as monitoring their electron transfer to other materials (Hoggard et al., 2013), studying chemical bonding on their surface (Zijlstra et al., 2012), and developing ultrasensitive chemical and biological LSPR sensors (Mayer and Hafner, 2011). Generally, the extinction spectra of nanobranches, however, exhibit very broad UV-Vis-NIR peaks (inhomogeneous broadening effects) due to unavoidable shape differences of individual Au nanobranches, that is, the number, size, and orientation of their arms vary greatly among them. Although Au nanooctopods can be synthesized with the cubic Au seeds from previous literature protocols, the arms of the octopods were too short to exhibit highly branched architectures and sharp tips. In addition, the Au nanooctopods showed broad band due to their size and structural inhomogeneity (Smith et al., 2016). Therefore, the lack of reliable synthetic methods for highly branched Au nanoparticles with accurate control of the number of arms, spatial arrangement of arms, arm size, high yield as well as reproducibility hinders the fundamental understanding of their properties and the assessment of their potentials (Niu et al., 2015).

Herein, we report a facile kinetically controlled growth of monodisperse NOPs with a high yield and narrow LSPR band by using 1-methylpyrrolidine (1-MP) and ascorbic acid (AA) as effective co-reducing agents for $HAuCl_4$ at room temperature. With the presence of single-crystalline Au seeds, the high reduction rate of Au precursor leads to the growth of eight arms along <111> directions of the seeds. The NOPs show strong and ultra-narrow LSPR peak in the range of 660–720 nm. They exhibit remarkable photothermal conversion efficiencies up to 83.0% and a photoacoustic response upon 680 nm laser irradiation. These NOPs hold great promise of highly efficient photothermal conversion and photoacoustic dual-functional agents.

MATERIALS AND METHODS

Materials

Hexadecyltrimethylammonium bromide (CTAB), 1-methylpyrrolidine (1-MP), gold (III) chloride trihydrate ($HAuCl_4 \cdot 3H_2O$), ascorbic acid (AA), and sodium borohydride ($NaBH_4$) were purchased from Sigma-Aldrich. Monomethoxy-poly (ethylene glycol)-thiol (mPEG-SH, molecular weight = 5,000 g/mol) was purchased from JenKem Technology. All the reagents were used as received without further purification. Deionized water (18.2 MΩ·cm) was used for all solution preparations.

Synthesis of Au Seeds

The gold seed nanoparticles were prepared according to the method reported previously with a slight modification (Nikoobakht and El-Sayed, 2003). CTAB solution (3.5 mL, 0.14 M) was mixed with of $HAuCl_4$ (0.125 mL, 15 mM). A freshly prepared, ice-cold $NaBH_4$ solution (0.50 mL, 0.010 M) was injected to the mixture, resulting in the formation of a brownish yellow solution. The seed solution was vigorously stirred for 120 s and then kept at 25°C.

Synthesis of Au NOPs

The aqueous solutions of $HAuCl_4$ (15 mM, 0.38 mL), CTAB (0.40 M, 2.375 mL), and 1-MP (1.0 M, 0.90 mL) were added in a glass vial, named solution A. Deionized water (6.12 mL), AA (0.10 M, 225 μL), and seeds solution (1.8 μL) were added in another glass vial, named solution B. Solution B was quickly added to solution A, and the reaction mixture was incubated at 25°C for 5 min.

PEGylation of Au NOPs

The as-synthesized NOPs (1.0 mL) were purified by centrifugation at 9,000 rpm for 15 min. The precipitation was redispersed by 1.0 mL aqueous solution of mPEG-SH (0.10 mg/mL). The mixture was ultra-sonicated for 5 min and stirred over night at room temperature.

Materials Characterization

The size, morphology, and structure of NOPs were studied by using JEOL JEM-2100F and Hitachi H800 transmission electron microscope (TEM) with an accelerating voltage of 200 and 175 kV, respectively. The UV-Vis-NIR extinction spectra were recorded using a Lambda 950 (PerkinElmer) Spectrometer. The purification of NOPs was performed by using Eppendorf Centrifuge 5430R at 25°C. X-Ray diffraction (XRD) measurements of NOPs solutions drop-coated onto glass substrates were done on Empyrean (PANalytical B. V.) operating at a voltage of 40 kV.

Simulation of the Capping Effect of 1-MP

Density Functional Theory calculations were performed by means of the Vienna Ab Initio Simulation Package (VASP) (Hafner, 2008) using the Perdew-Burke-Ernzerhof (PBE) generalized-gradient approximation (Perdew et al., 1996). The interactions between valence electrons and ion cores were treated by Blöchl's all-electron-like projector augmented wave (PAW) method (Blöchl, 1994). The plane-wave cutoff for the wave functions was 400 eV throughout. For all calculations, we used a (4 × 4) supercell consisting of a four-layer slab with vacuum thickness of about 20 Å and molecules adsorbed on one side of the slab. The adsorbed molecule and the top three layers of Au were allowed to relax. The Brillouin zone integration was performed using a cell size dependent Monkhorst–Pack *k* point sampling (Monkhorst and Pack, 1976) and the *k*-point mesh was 3 × 3 × 1 for surface reconstruction and 7 × 7 × 1 for single-molecule adsorption. Ionic relaxation for all stable structures was carried out until all forces were smaller than 0.02 eV/Å. The adsorption energy for molecules on Au was calculated as follows:

$$\Delta E_{ads} = E_{molecule/Au} - E_{molecule} - E_{Au}$$

where $E_{\mathrm{molecule/Au}}$ is the total energy of the Au surface together with the adsorbed molecule, E_{molecule} is the total energy of the free molecule, and E_{Au} is the total energy of the bare Au surface. With this method, the negative values of adsorption energy suggest that the adsorption configuration is more stable than the corresponding bare Au surface and the free molecule.

Laser-Induced Heat Conversion of Au NOPs

A diode laser at 660 nm (LEO photonics Co. Ltd.) was employed in the experiments. PEG-modified NOPs (1.0 mL) in a quartz cuvette (1-cm path length) was irradiated by the laser with tunable power densities (0.50–2.0 W/cm^2). PEG-modified NOPs with different optical densities (ODs) (0.10–1.0) were irradiated by the laser at 1.0 W/cm^2. Deionized water was used as a negative control. The laser spot was adjusted to cover the entire surface of the sample. Real-time thermal imaging and the maximum temperature was recorded by a FLIR A310 infrared camera.

In vitro Photoacoustic Imaging of Au NOPs

PEG-modified NOPs solutions with different optical densities were introduced into agar-gel cylinders and put in deionized water at a consistent depth. Photoacoustic images were obtained at 680 nm wavelength by MSOT inVision 128 small animal scanner.

RESULTS AND DISCUSSION

The NOPs were prepared by the regrowth from well-defined single-crystalline Au seeds (see section Materials and Methods for details). In a typical synthesis, a seed solution of Au seeds and ascorbic acid (AA) were quickly added into a fresh-prepared growth solution containing $HAuCl_4$ and 1-methylpyrrolidine (1-MP) in the presence of hexadecyltrimethylammonium bromide (CTAB) at room temperature and final pH of 11.3. Both AA and 1-MP (Newman and Blanchard, 2006) were reducing agents for $HAuCl_4$, and the basic pH increased the reduction rates (vide infra). CTAB was used as a surface capping agent to provide the colloidal stability for the synthesized nanoparticles. After the mixing, the color of the solution immediately turned from colorless to peacock blue in about 5 min, indicating the formation of NOPs. Transmission electron microscopy (TEM) study (**Figure 1A**) of NOPs reveals the NOPs with a high yield (81%) of possessed eight arms with a uniform arm length and width of 19.5 ± 1.4 and 9.4 ± 1.0 nm, respectively. The NOPs also showed an extraordinary LSPR peak at 680 nm with a FWHM (Full width at half maximum) as narrow as 76 nm (0.20 eV) (Mets et al., 2012), which demonstrates high monodispersity of the NOPs (**Figure 1B**).

Figure 2A shows a high-resolution TEM image of an individual NOP, where periodic lattice fringes can be clearly resolved. The distance between adjacent lattice fringes was about 0.240 nm, corresponding to the d-spacing of Au {111} planes. The X-ray diffraction (XRD) pattern recorded on a glass substrate was displayed in **Figure 2B**. The diffraction peaks were assigned to (111), (200), (220), (311), (222) planes of face-centered cubic Au, respectively (JCPDS No. 04-0784). It is worth noting that although the ratio between the intensities of the (200) to (111) diffraction peaks was similar to the conventional values (0.50 vs. 0.52), the ratios of (220)/(111) and (220)/(200) were significantly lower than the conventional values (0.21 vs. 0.32) and (0.42 vs. 0.62), respectively. This result indicates that the NOPs were abundant in (111) and (200) facets. Close inspection and analysis of the image (**Figure 2A**) reveals that the arms grew from the eight corners of Au seeds along <111> directions to form octopod structure. To further understand the spatial arrangement of the arms, three dimensional (3D)-TEM images taken from various tilting angles were consistent with our model of NOPs at different views (**Figures 2C,D**).

The formation of anisotropic structure requires breaking the face-centered cubic symmetry of Au crystals. Therefore, the growth mechanism is important for understanding how the arms arise from Au seeds. In general, thermodynamically controlled nanocrystals with the global minimum in Gibbs free energy can be synthesized by capping agents which effectively reduce the surface free energy of the nanocrystals. To help elucidate this process, we first considered the effect of CTAB and 1-MP as capping agents. Density Functional Theory (DFT) calculations of the adsorption energy of 1-MP on different Au crystal facets indicate that 1-MP taking a flat conformation with the N atom preferentially adsorbed on the top-position of Au atoms (**Figure S1**). The sequence of 1-MP adsorption energies (ΔE_{ads}) on different crystallographic facets is in agreement with that of CTAB (Liu et al., 2011), i.e., $|\Delta E_{\mathrm{ads}}\ (111)| < |\Delta E_{\mathrm{ads}}\ (100)| < |\Delta E_{\mathrm{ads}}\ (110)|$. This result suggests that the NOPs covered by both 1-MP and CTAB would thermodynamically enclosed by higher proportion of {110} facets on the surface, which is conflicting with our analysis of XRD result (**Figure 2B**).

Our success in the synthesis of NOPs essentially relied on the kinetic control of growth process (Zhang, H. et al., 2010; Xia et al., 2013, 2015; Wang et al., 2015a). As proposed previously, for seed-mediated growth method, the ratio between the deposition rate (V_{dep}) and the diffusion rate (V_{diff}) determines the growth pathway from a single-crystal seed and thereby the morphology of the produced nanocrystals. V_{dep} is the rate for the atoms added to the active nanocrystal facets with a higher surface free energy, and V_{diff} is the rate for the adatoms migrating to the nanocrystal facets with a lower surface free energy. For a

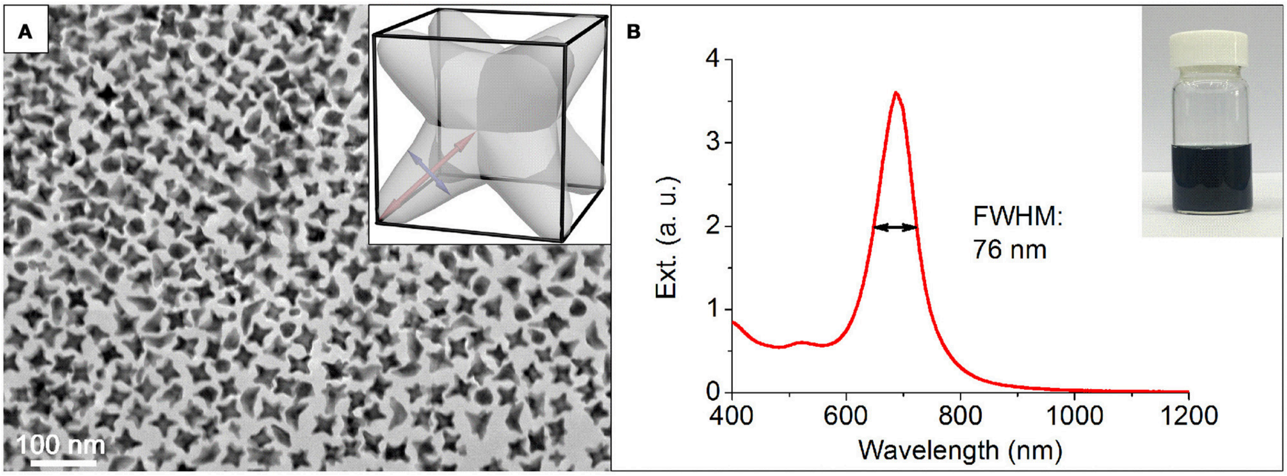

FIGURE 1 | **(A)** Representative TEM image and **(B)** extinction spectra of NOPs. Inset in **(A)**: scheme of an individual NOP. Red and blue lines represent the arm length and width, respectively. Inset in **(B)**: optical photograph of the NOP solution.

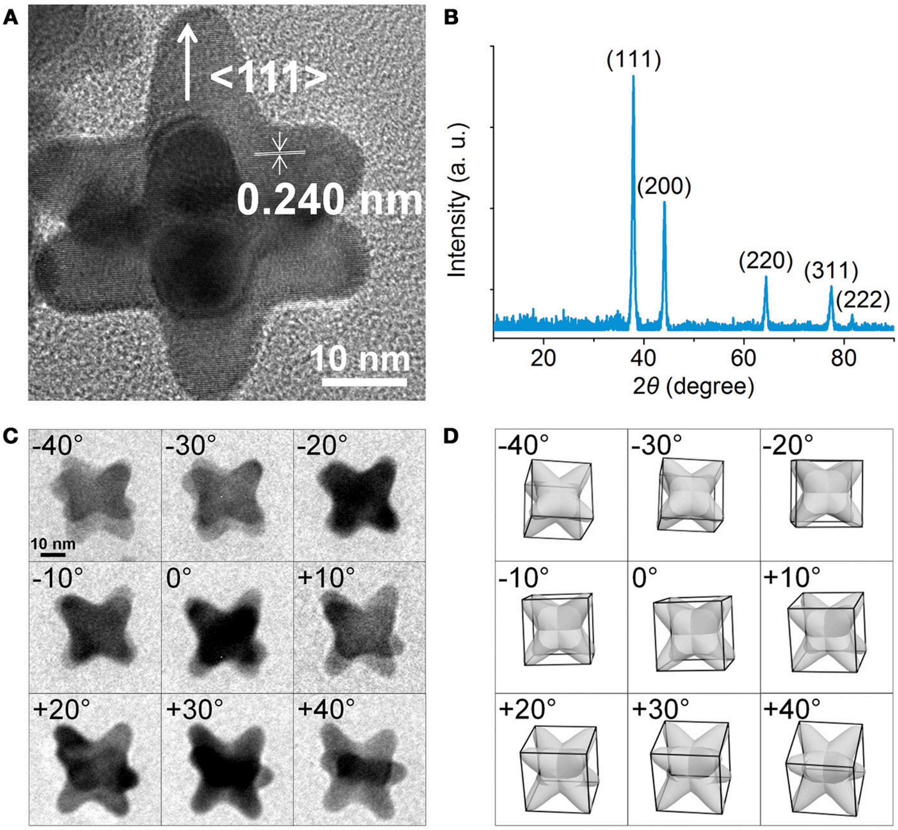

FIGURE 2 | **(A)** HRTEM image of an individual NOP. **(B)** Powder X-ray Diffraction of the NOPs. **(C)** 3D-TEM images of NOPs tilted from ca. −40° to +40°. **(D)** Corresponding 3D model images with same views from ca. −40° to +40°.

near rhombicuboctahedron-shaped single-crystal seed, due to the preferential binding of CTAB capping agent on the {100} and {110} facets, {111} corner facets are the most active sites as a result of less coverage by the capping agent (Park et al., 2013). For a slow reduction rate, $V_{\mathrm{dep}} \ll V_{\mathrm{diff}}$, most of the adatoms at the corners will migrate to edges and side facets, and the growth will prevail along the <100> and <110> directions, leading to the formation of Wulff shape (Xia et al., 2015), as favored by thermodynamics

(**Figure 3**, Path A). On the contrary, for a fast reduction rate, $V_{\mathrm{dep}} \gg V_{\mathrm{diff}}$, surface diffusion can be ignored and the growth will be switched to the <111> directions, promoting the formation of a kinetically favored octopods as the product (**Figure 3**, Path B).

Both of V_{dep} and V_{diff} are kinetic parameters and can be manipulated by varying the ratio between Au seeds and $HAuCl_4$, and the rate of reduction of $HAuCl_4$. We studied the reductive ability of AA and 1-MP in the absence of Au seeds by monitoring the peak at 395 nm which is attributed from the $[CTA]^+$ $[AuBr_4]^-$ complex (Kundu, 2013). It is well-known that AA can reduce $HAuCl_4$ to Au^+ under neutral or acidic condition, but to Au^0 under strong alkaline condition (Goia and Matijević, 1999). In the present study when only AA was added into the solution A containing $[CTA]^+$ $[AuBr_4]^-$ complex at the pH of 11.4, Au nanoparticles with a LSPR peak around 530 nm were formed in 1 min. At the meantime, the peak at 395 nm was remained (**Figure S2A**), indicating that under strong alkaline condition, AA could not quickly reduce Au^{3+} to Au^+ as it does under neutral or acid condition. The $[CTA]^+$ $[AuBr_4]^-$ complex was completely consumed after 3 h, accompanying by the formation of more Au nanoparticles with quasi-spheres (**Figure S3A**). This result suggests under strong alkaline condition, although AA can reduce Au^{3+} to form Au nanoparticles, the reduction rate of Au^{3+} to Au^0 is slow.

On the other side, when only 1-MP was used as reducing agent under the same condition, the peak of $[CTA]^+$ $[AuBr_4]^-$ complex was completely vanished in 1 min, while no Au nanoparticles were formed as indicated from the UV-Vis-NIR spectra (**Figure S2B**). The formation of Au nanoparticles was much slower compared to that of AA. This result reveals that

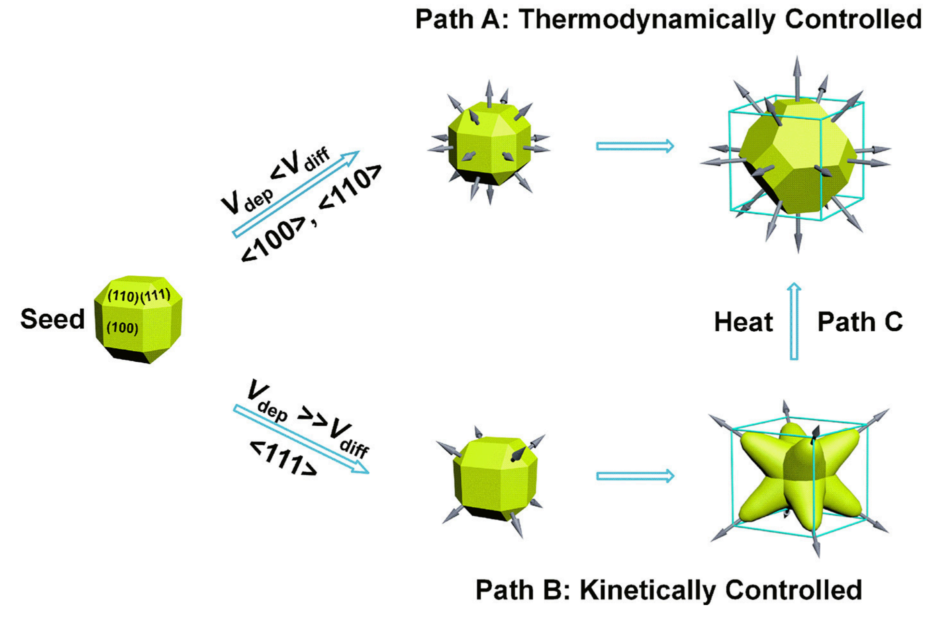

FIGURE 3 | Growth mechanism of kinetically controlled synthesis of NOPs.

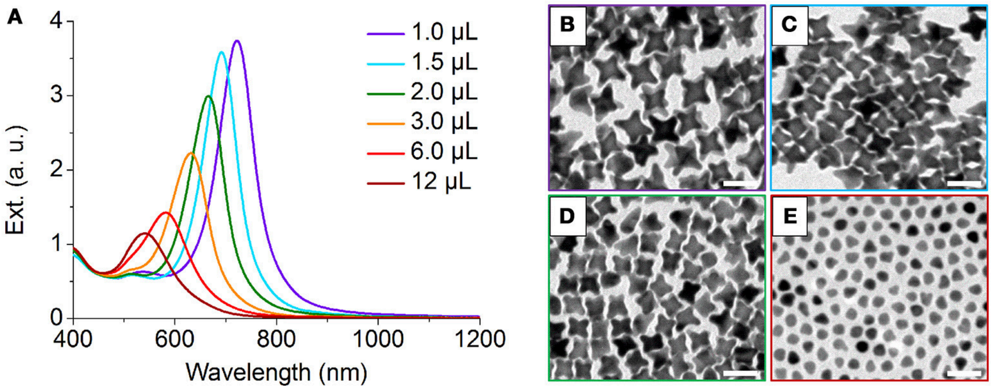

FIGURE 4 | (A) UV-Vis-NIR spectra of NOPs by increasing the volume of Au seeds solution from 1.0 to 12 μL added to the growth solution (total volume of 10 mL). **(B–E)** TEM images of NOPs with 1.0, 1.5, 2.0, and 12 μL Au seeds solution added to the growth solution, respectively. Scale bars: 50 nm.

1-MP is a reducing agent which can reduce Au^{3+} to Au^{+} with a much higher rate compared to AA under basic conditions, but its ability to further reduce Au^{+} to Au^{0} is weaker than that of AA under strong alkaline condition. From the above results we can conclude that if only AA or 1-MP is used as the solo reducing agent, the reduction rate of formation of Au^{0} is not high enough to achieve $V_{dep} \gg V_{diff}$, and only spherical or irregular shaped nanoparticles were obtained, respectively (**Figure S3**). In contrast, when both AA and 1-MP were used, 1-MP can quickly reduce Au^{3+} to Au^{+}, which can be further reduced to Au^{0} by AA to reach a high V_{dep}. Therefore, we conclude that under the strong alkaline condition, AA and 1-MP have a synergistic reducing effect for achieving the condition of $V_{dep} \gg V_{diff}$, leading to the formation of NOPs with branches along <111> directions. This result is consistent with the theoretical prediction for the scenario of $V_{dep} \gg V_{diff}$ mentioned previously (Xia et al., 2015).

We also performed control experiments to investigate the effect of seed/precursor ratio on the morphology of NOPs. By increasing the volume of Au seeds solution from 1.0 to 3.0 µL with other conditions unchanged, both of the average aspect ratios and lengths of the arms of NOPs can be continuously adjusted from 2.00 to 1.25 and 22.8 to 15.8 nm, respectively (**Figure 4**, **Table S1**), that is, the more Au seeds the smaller arms. Further increasing the amount of Au seeds to 12 µL led to only thermodynamically stable product, i.e., quasi-spheres (**Figure 4E**). This result reveals that when the number of Au atoms available for every seed is smaller, the ratio of V_{dep}/V_{diff} was reduced, leading to thermodynamic products. In addition, this result also demonstrates that one can control the aspect ratio and arm length, as well as LSPR position, by tuning the seed/$HAuCl_4$ ratio. It is worth mentioning that the arm length and aspect ratio of NOPs depend on their LSPR position, and the LSPR wavelength was linearly correlated with the aspect ratio of NOPs ($R^2 = 0.969$) (**Figure S4**).

Additionally, the reaction temperature also plays a paramount role in determining whether thermodynamic or kinetic control is dominant. High temperatures normally lead to generate thermodynamically controlled nanocrystals. After incubated at higher temperature (60°C) for 4 h, the morphology of as-synthesized NOPs was quickly transformed to Wulff shape with lower surface free energy (**Figure S5**), which is corresponding to the path C in **Figure 3**. This result confirms the NOPs are kinetically controlled product, of which the shape changes to thermodynamically stable at high temperatures.

It's worth pointing out that the NOPs are thermodynamically unstable due to a relatively high surface energy at the sharp tips, resulting in changes of their morphology to less anisotropic structures and the blue-shifting of their LSPR bands (**Figure S6**; Wang et al., 2015b). Therefore, the practical applications of the NOPs are severely limited. In search of the appropriate methods for stabilizing the NOPs, we have tried halogen ions, surfactants

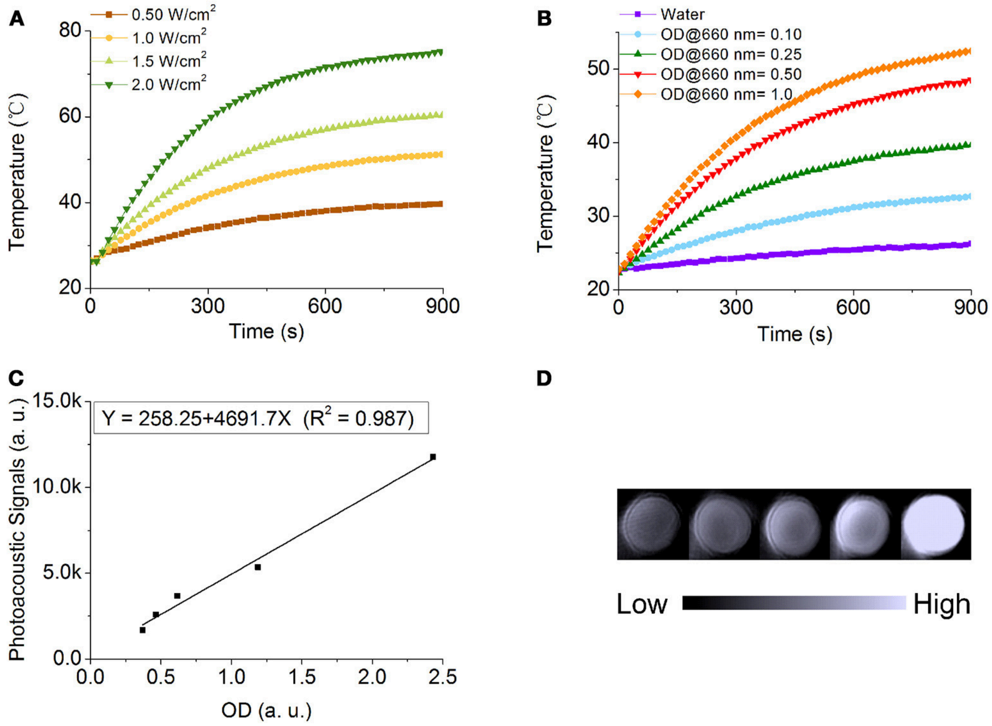

FIGURE 5 | Photothermal conversion and photoacoustic properties of NOPs. **(A)** Temperature variation of NOPs with the optical density at 660 nm (OD_{660nm}) of 1.0 irradiated at different laser power densities: 0.50 (brown), 1.0 (yellow), 1.5 (light green), and 2.0 W/cm^2 (dark green). **(B)** Temperature variation of NOPs with different OD_{660nm} values: 0.10 (blue), 0.25 (green), 0.50 (red), and 1.0 (orange) irradiated at a laser power density of 1.0 W/cm^2. **(C)** Photoacoustic signals of NOPs as a function of OD_{680nm}. **(D)** Photoacoustic images of NOPs.

(i.e., CTAB), and six thiol compounds, including cysteine, 3-mercaptopropionic acid, glutathione, 11-mercaptopropionic acid, polyetherimide, mPEG-SH. Among them, we found that mPEG-SH modified NOPs showed negligible shifting of their LSPR band in 5 days at room temperature (**Figure S7**) and good thermal-stability at high temperature (at 75°C for 30 min) (**Figure S8**).

Owing to the strong LSPR band at 680 nm of NOPs, it is worthy to evaluate their dual potential as photothermal conversion and photoacoustic contrast agents. To evaluate their photothermal conversion performance, aqueous solutions of PEG-modified NOPs with the same optical density at 660 nm (OD_{660nm}) of 1.0 were exposed to the 660 nm laser at different power densities (0.50–2.0 W/cm^2) as shown in **Figure 5A**. Additionally, PEG-modified NOPs with different optical densities (ODs) (0.10–1.0) were irradiated by the laser at 1.0 W/cm^2 (**Figure 5B**). After the laser irradiation, PEG-modified NOPs showed negligible shifting of their LSPR band and kept their morphology unchanged as well (**Figure S9**). The temperature variation was strongly depended on the laser power and concentration of NOPs (**Figures 5A,B**). **Table S2** lists the photothermal conversion values of NOPs calculated by using a modified model similar to the report by Roper et al. (Roper et al., 2007; Shao et al., 2016). NOPs showed excellent photothermal conversion efficiencies with a maximum value up to 83.0%. The ultrahigh conversion value is attributed to the narrow LSPR band of NOPs. In addition, the solution of NOPs also presented a strong photoacoustic signal at 680 nm wavelength. The photoacoustic intensity was linearly proportional to the concentration of NOPs with $R^2 = 0.987$, suggesting the NOPs as a promise photoacoustic contrast agent.

CONCLUSION

Monodisperse NOPs were synthesized through a kinetically controlled growth with a high yield and ultra-narrow LSPR band width. The synergistic reducing effects of AA and 1-MP were important for the kinetically controlled scenario of $V_{\mathrm{dep}} \gg V_{\mathrm{diff}}$, resulting the formation of the highly branched NOPs along eight <111> directions. The uniform of the number, size, and orientation of their branches makes NOPs their remarkable LSPR properties with ultra-narrow LSPR band. The NOPs offer outstanding properties in bio-applications such as photothermal therapy with high photothermal conversion efficiencies up to 83.0% and a promise photoacoustic contrast agent in photoacoustic imaging. Owing to their excellent LSPR properties, the NOPs are highly promising in diverse applications, such as sensing, nanodevices, catalysis, and bio-applications.

AUTHOR CONTRIBUTIONS

Y-XC performed the experiments and analyzed the data; H-MG and Z-YL performed the Density Functional Theory calculations; N-NZ and X-FT provided assistance in the experiments; KL, BY, JZ, and TS designed the experiments; KL and Y-XC wrote the manuscript. All authors read and approved the manuscript.

ACKNOWLEDGMENTS

KL thanks the National Natural Science Foundation of China (21474040, 21674042) and China's Thousand Talent Plan for financial support. KL and Z-YL gratefully acknowledge financial support from the National Natural Science Foundation of China (21534004). JZ, KL, and BY thank for the support of JLU Science and Technology Innovative Research Team 2017TD-06. KL and TS thank for Interdisciplinary Innovation Project of the First Hospital of Jilin University (JDYYJCHX001).

SUPPLEMENTARY MATERIAL

The Supplementary Material for this article can be found online at: https://www.frontiersin.org/articles/10.3389/fchem.2018.00335/full#supplementary-material

REFERENCES

Averitt, R. D., Sarkar, D., and Halas, N. J. (1997). Plasmon resonance shifts of Au-coated Au_2S nanoshells: insight into multicomponent nanoparticle growth. *Phys. Rev. Lett.* 78, 4217–4220. doi: 10.1103/PhysRevLett.78.4217

Blöchl, P. E. (1994). Projector augmented-wave method. *Phys. Rev. B* 50, 17953–17979. doi: 10.1103/PhysRevB.50.17953

Boles, M. A., Ling, D., Hyeon, T., and Talapin, D. V. (2016). The surface science of nanocrystals. *Nat. Mater.* 15, 141–153. doi: 10.1038/nmat4526

Chen, S., Wang, Z. L., Ballato, J., Foulger, S. H., and Carroll, D. L. (2003). Monopod, bipod, tripod, and tetrapod gold nanocrystals. *J. Am. Chem. Soc.* 125, 16186–16187. doi: 10.1021/ja038927x

Cheng, K., Kothapalli, S. R., Liu, H., Koh, A. L., Jokerst, J. V., Jiang, H., et al. (2014). Construction and validation of nano gold tripods for molecular imaging of living subjects. *J. Am. Chem. Soc.* 136, 3560–3571. doi: 10.1021/ja412001e

Dam, D. H. M., Lee, J. H., Sisco, P. N., Co, D. T., Zhang, M., Wasielewski, M. R., et al. (2012). Direct observation of nanoparticle–cancer cell nucleus interactions. *ACS Nano* 6, 3318–3326. doi: 10.1021/nn300296p

Goia, D. V., and Matijević, E. (1999). Tailoring the particle size of monodispersed colloidal gold. *Colloids Surf. A* 146, 139–152. doi: 10.1016/S0927-7757(98)00790-0

Guerrero-Martínez, A., Barbosa, S., Pastoriza-Santos, I., and Liz-Marzán, L. M. (2011). Nanostars shine bright for you: colloidal synthesis, properties and applications of branched metallic nanoparticles. *Colloid Interface Sci.* 16, 118–127. doi: 10.1016/j.cocis.2010.12.007

Hafner, J. (2008). Ab-initio simulations of materials using VASP: density-functional theory and beyond. *J. Comput. Chem.* 29, 2044–2078. doi: 10.1002/jcc.21057

Hao, E., Bailey, R. C., Schatz, G. C., Hupp, J. T., and Li, S. (2004). Synthesis and optical properties of "branched" gold nanocrystals. *Nano Lett.* 4, 327–330. doi: 10.1021/nl0351542

Hoggard, A., Wang, L. Y., Ma, L., Fang, Y., You, G., Olson, J., et al. (2013). Using the plasmon linewidth to calculate the time and efficiency of electron transfer between gold nanorods and graphene. *ACS Nano* 7, 11209–11217. doi: 10.1021/nn404985h

Indrasekara, A. S. D. S., Meyers, S., Shubeita, S., Feldman, L. C., Gustafsson, T., and Fabris, L. (2014). Gold nanostar substrates for SERS-based chemical sensing in the femtomolar regime. *Nanoscale* 6, 8891–8899. doi: 10.1039/C4NR02513J

Jana, N. R., Gearheart, L., and Murphy, C. J. (2001). Wet chemical synthesis of high aspect ratio cylindrical gold nanorods. *J. Phys. Chem. B* 105, 4065–4067. doi: 10.1021/jp0107964

Kelly, K. L., Coronado, E., Zhao, L. L., and Schatz, G. C. (2003). The optical properties of metal nanoparticles: the influence of size, shape, and dielectric environment. *J. Phys. Chem. B* 107, 668–677. doi: 10.1021/jp026731y

Khoury, C. G., and Vo-Dinh, T. (2008). Gold nanostars for surface-enhanced Raman scattering: synthesis, characterization and optimization. *J. Phys. Chem. C* 112, 18849–18859. doi: 10.1021/jp8054747

Kim, F., Connor, S., Song, H., Kuykendall, T., and Yang, P. (2004). Platonic gold nanocrystals. *Angew. Chem.* 116, 3759–3763. doi: 10.1002/ange.200454216

Kumar, P. S., Pastoriza-Santos, I., Rodríguez-González, B., García de Abajo, F. J., and Liz-Marzán L. M. (2007). High-yield synthesis and optical response of gold nanostars. *Nanotechnology* 19, 015606–015611. doi: 10.1088/0957-4484/19/01/015606

Kundu, S. (2013). A new route for the formation of Au nanowires and application of shape-selective Au nanoparticles in SERS studies. *J. Mater. Chem. C* 1, 831–842. doi: 10.1039/C2TC00315E

Li, N., Zhao, P., and Astruc, D. (2014). Anisotropic gold nanoparticles: synthesis, properties, applications, and toxicity. *Angew. Chem. Int. Ed.* 53, 1756–1789. doi: 10.1002/anie.201300441

Lim, B., and Xia, Y. (2011). Metal nanocrystals with highly branched morphologies. *Angew. Chem. Int. Ed.* 50, 76–85. doi: 10.1002/anie.201002024

Link, S., and El-Sayed, M. A. (2000). Shape and size dependence of radiative, non-radiative and photothermal properties of gold nanocrystals. *Int. Rev. Phys. Chem.* 19, 409–453. doi: 10.1080/01442350050034180

Liu, K., Zhao, N., and Kumacheva, E. (2011). Self-assembly of inorganic nanorods. *Chem. Soc. Rev.* 40, 656–671. doi: 10.1039/c0cs00133c

Liu, M., and Guyot-Sionnest, P. (2005). Mechanism of silver (I)-assisted growth of gold nanorods and bipyramids. *J. Phys. Chem. B* 109, 22192–22200. doi: 10.1021/jp054808n

Malikova, N., Pastoriza-Santos, I., Schierhorn, M., Kotov, N. A., and Liz-Marzán, L. M. (2002). Layer-by-layer assembled mixed spherical and planar gold nanoparticles: control of interparticle interactions. *Langmuir* 18, 3694–3697. doi: 10.1021/la025563y

Mayer, K. M., and Hafner, J. H. (2011). Localized surface plasmon resonance sensors. *Chem. Rev.* 111, 3828–3857. doi: 10.1021/cr100313v

Mets, O. M., de Jong, P. A., van Ginneken, B., Gietema, H. A., and Lammers, J. W. J. (2012). Quantitative computed tomography in COPD: possibilities and limitations. *Lung* 190, 133–145. doi: 10.1007/s00408-011-9353-9

Monkhorst, H. J., and Pack, J. D. (1976). Special points for Brillouin-zone integrations. *Phys. Rev. B* 13, 5188–5192. doi: 10.1103/PhysRevB.13.5188

Nehl, C. L., Liao, H., and Hafner, J. H. (2006). Optical properties of star-shaped gold nanoparticles. *Nano Lett.* 6, 683–688. doi: 10.1021/nl052409y

Newman, J. D. S., and Blanchard, G. J. (2006). Formation of gold nanoparticles using amine reducing agents. *Langmuir* 22, 5882–5887. doi: 10.1021/la060045z

Nikoobakht, B., and El-Sayed, M. A. (2003). Preparation and growth mechanism of gold nanorods (NRs) using seed-mediated growth method. *Chem. Mater.* 15, 1957–1962. doi: 10.1021/cm020732l

Niu, W., Chua, Y. A. A., Zhang, W., Huang, H., and Lu, X. (2015). Highly symmetric gold nanostars: crystallographic control and surface-enhanced Raman scattering property. *J. Am. Chem. Soc.* 137, 10460–10463. doi: 10.1021/jacs.5b05321

Park, K., Drummy, L. F., Wadams, R. C., Koerner, H., Nepal, D., Fabris, L., et al. (2013). Growth mechanism of gold nanorods. *Chem. Mater.* 25, 555–563. doi: 10.1021/cm303659q

Perdew, J. P., Burke, K., and Ernzerhof, M. (1996). Generalized gradient approximation made simple. *Phys. Rev. Lett.* 77, 3865–3868. doi: 10.1103/PhysRevLett.77.3865

Roper, D. K., Ahn, W., and Hoepfner, M. (2007). Microscale heat transfer transduced by surface plasmon resonant gold nanoparticles. *J. Phys. Chem. C* 111, 3636–3641. doi: 10.1021/jp064341w

Shankar, S. S., Rai, A., Ankamwar, B., Singh, A., Ahmad, A., and Sastry, M. (2004). Biological synthesis of triangular gold nanoprisms. *Nat. Mater.* 3, 482–488. doi: 10.1038/nmat1152

Shao, J., Xie, H., Huang, H., Li, Z., Sun, Z., Xu, Y. et al. (2016). Biodegradable black phosphorus-based nanospheres for *in vivo* photothermal cancer therapy. *Nat. Commun.* 7, 12967–12979. doi: 10.1038/ncomms12967

Skrabalak, S. E., Chen, J., Sun, Y., Lu, X., Au, L., Cobley, C. M., et al. (2008). Gold nanocages: synthesis, properties, and applications. *Acc. Chem. Res.* 41, 1587–1595. doi: 10.1021/ar800018v

Smith, A. F., Weiner, R. G., and Skrabalak, S. E. (2016). Symmetry-dependent optical properties of stellated nanocrystals. *J. Phys. Chem. C* 120, 20563–20571. doi: 10.1021/acs.jpcc.5b12280

Sönnichsen, C., Franzl, T., Wilk, T., von Plessen, G., Feldmann, J., Wilson, O., et al. (2002). Drastic reduction of plasmon damping in gold nanorods. *Phys. Rev. Lett.* 88, 077402. doi: 10.1103/PhysRevLett.88.077402

Sun, Y., and Xia, Y. (2002). Shape-controlled synthesis of gold and silver nanoparticles. *Science* 298, 2176–2179. doi: 10.1126/science.1077229

Wang, Y., Black, K. C. L., Luehmann, H., Li, W., Zhang, Y., Cai, X., et al. (2013). Comparison study of gold nanohexapods, nanorods, and nanocages for photothermal cancer treatment. *ACS Nano* 7, 2068–2077. doi: 10.1021/nn304332s

Wang, Y., He, J., Liu, C., Chong, W. H., and Chen, H. (2015a). Thermodynamics versus kinetics in nanosynthesis. *Angew. Chem. Int. Ed.* 54, 2022–2051. doi: 10.1002/anie.201402986

Wang, Y., Serrano, A. B., Sentosun, K., Bals, S., and Liz-Marzán, L. M. (2015b). Stabilization and encapsulation of gold nanostars mediated by dithiols. *Small* 11, 4314–4320. doi: 10.1002/smll.201500703

Wei, Q., Song, H. M., Leonov, A. P., Hale, J. A., Oh, D., Ong, Q. K., et al. (2009). Gyromagnetic imaging: dynamic optical contrast using gold nanostars with magnetic cores. *J. Am. Chem. Soc.* 131, 9728–9734. doi: 10.1021/ja901562j

Xia, X., Xie, S., Liu, M., Peng, H. C., Lu, N., Wang, J., et al. (2013). On the role of surface diffusion in determining the shape or morphology of noble-metal nanocrystals. *Proc. Natl. Acad. Sci. U.S.A.* 110, 6669–6673. doi: 10.1073/pnas.1222109110

Xia, Y., Xia, X., and Peng, H. C. (2015). Shape-controlled synthesis of colloidal metal nanocrystals: thermodynamic versus kinetic products. *J. Am. Chem. Soc.* 137, 7947–7966. doi: 10.1021/jacs.5b04641

Ye, E., Regulacio, M. D., Zhang, S. Y., Loh, X. J., and Han, M. Y. (2015). Anisotropically branched metal nanostructures. *Chem. Soc. Rev.* 44, 6001–6017. doi: 10.1039/C5CS00213C

Yuan, H., Fales, A. M., and Vo-Dinh, T. (2012). TAT peptide-functionalized gold nanostars: enhanced intracellular delivery and efficient NIR photothermal therapy using ultralow irradiance. *J. Am. Chem. Soc.* 134, 11358–11361. doi: 10.1021/ja304180y

Zhang, H., Li, W., Jin, M., Zeng, J., Yu, T., Yang, D., et al. (2010). Controlling the morphology of rhodium nanocrystals by manipulating the growth kinetics with a syringe pump. *Nano Lett.* 11, 898–903. doi: 10.1021/nl104347j

Zhang, J., Langille, M. R., Personick, M. L., Zhang, K., Li, S., and Mirkin, C. A. (2010). Concave cubic gold nanocrystals with high-index facets. *J. Am. Chem. Soc.* 132, 14012–14014. doi: 10.1021/ja106394k

Zhu, X., Zhuo, X., Li, Q., Yang, Z., and Wang, J. (2016). Gold nanobipyramid-supported silver nanostructures with narrow plasmon linewidths and improved chemical stability. *Adv. Funct. Mater* 26, 341–352. doi: 10.1002/adfm.201503670

Zijlstra, P., Paulo, P. M. R., Yu, K., Xu, Q. H., and Orrit, M. (2012). Chemical interface damping in single gold nanorods and its near elimination by tip-specific functionalization. *Angew. Chem. Int. Ed.* 51, 8352–8355. doi: 10.1002/anie.201202318

Conflict of Interest Statement: The authors declare that the research was conducted in the absence of any commercial or financial relationships that could be construed as a potential conflict of interest.

frontiers in Chemistry

ORIGINAL RESEARCH
published: 10 September 2018
doi: 10.3389/fchem.2018.00411

Light-Mediated Growth of Noble Metal Nanostructures (Au, Ag, Cu, Pt, Pd, Ru, Ir, Rh) From Micro- and Nanoscale ZnO Tetrapodal Backbones

Trevor B. Demille[1], **Robert A. Hughes**[1], **Arin S. Preston**[1], **Rainer Adelung**[2], **Yogendra Kumar Mishra**[2] and **Svetlana Neretina**[1,3,4]*

[1] Department of Aerospace and Mechanical Engineering, College of Engineering, University of Notre Dame, Notre Dame, IN, United States, [2] Functional Nanomaterials, Institute for Materials Science, Kiel University, Kiel, Germany, [3] Department of Chemistry and Biochemistry, University of Notre Dame, Notre Dame, IN, United States, [4] Center for Sustainable Energy at Notre Dame, Notre Dame, IN, United States

Micro- and nanoscale ZnO tetrapods provide an attractive support for metallic nanostructures since they can be inexpensively produced using the flame transport method and nanoparticle synthesis schemes can take advantage of a coupled response facilitated by the formation of a semiconductor-metal interface. Here, we present a light-mediated solution-based growth mode capable of decorating the surface of ZnO tetrapods with nanostructures of gold, silver, copper, platinum, palladium, ruthenium, iridium, and rhodium. It involves two coupled reactions that are driven by the optical excitation of electron-hole pairs in the ZnO semiconductor by ultraviolet photons where the excited electrons are used to reduce aqueous metal ions onto the ZnO tetrapod as excited holes are scavenged from the surface. For the most part, the growth mode gives rise to nanoparticles with a roundish morphology that are uniformly distributed on the tetrapod surface. Larger structures with irregular shapes are, however, obtained for syntheses utilizing aqueous metal nitrates as opposed to chlorides, a result that suggests that the anion plays a role in shape determination. It is also demonstrated that changes to the molarity of the metal ion can influence the nanostructure nucleation rate. The catalytic activity of tetrapods decorated with each of the eight metals is assessed using the reduction of 4-nitrophenol by borohydride as a model reaction where it is shown that those decorated with Pd, Ag, and Rh are the most active.

Keywords: ZnO, tetrapod, light-mediated, catalysis, synthesis, nanoparticle, 4-nitrophenol

Edited by:
Jing Zhao,
University of Connecticut,
United States

Reviewed by:
Sravan Thota,
Intel, United States
Yijin Kang,
University of Electronic Science and
Technology of China, China

***Correspondence:**
Svetlana Neretina
sneretina@nd.edu

Specialty section:
This article was submitted to
Nanoscience,
a section of the journal
Frontiers in Chemistry

Received: 24 July 2018
Accepted: 21 August 2018
Published: 10 September 2018

Citation:
Demille TB, Hughes RA, Preston AS, Adelung R, Mishra YK and Neretina S (2018) Light-Mediated Growth of Noble Metal Nanostructures (Au, Ag, Cu, Pt, Pd, Ru, Ir, Rh) From Micro- and Nanoscale ZnO Tetrapodal Backbones. Front. Chem. 6:411. doi: 10.3389/fchem.2018.00411

INTRODUCTION

As a wide bandgap (3.37 eV) semiconductor exhibiting high electron mobility, room temperature luminescence, and piezoelectricity, ZnO has garnered intense interest (Kumar et al., 2017; Laurenti and Valentina, 2017; Chaudhary et al., 2018; Vishnukumar et al., 2018). Its relevance has been further heightened by the ability to synthesize intricate geometries on both the nanoscale and microscale (Janotti and Van de Walle, 2009). A geometry of particular interest is the ZnO tetrapod, which has four arms connected to a central core. Tetrapods are typically formed using a non-catalytic growth mode that sees the nucleation of a zinc blende crystal core from which four wurtzite crystal arms emerge, a growth mode that is common to II–VI semiconductors (Newton and Warburton, 2007). Such structures are of intense interest due to potential applications in electronics, sensing, biomedicine, catalysis, and composites (Bai et al., 2008; Abdulgafour et al., 2012; Castillejos et al., 2012; Papavlassopoulos et al., 2014; Naghizadeh-Alamdari et al., 2015; Picciolini et al., 2015; Alsultany et al., 2016; Gröttrup et al., 2017a; Mishra and Adelung, 2017). With a high Young's modulus, the ability to withstand high temperatures, and the capability to be produced in bulk quantities from earth abundant materials, ZnO tetrapods can also act as inexpensive structural backbones (Newton and Warburton, 2007; Janotti and Van de Walle, 2009; Mecklenburg et al., 2012; Silva et al., 2017). Decorating micro- and nanoscale ZnO tetrapods with metal nanostructures is a particularly intriguing prospect in the respect that the tetrapod provides a retrievable support for use in liquid-phase heterogeneous catalysis while simultaneously providing the potential for a coupled response at the semiconductor-nanometal interface.

ZnO tetrapods decorated with noble metal nanostructures (e.g., Au, Ag, and Pt) and metal-oxides are known to enhance various sensing modalities and optoelectronic responses (Ammari et al., 2004; Zhang et al., 2007; Tan et al., 2008; Wang et al., 2011b; Rackauskas et al., 2015; Bertoni et al., 2016; Sun et al., 2016; Schütt et al., 2017; Wu et al., 2017). In particular, methods for synthesizing Au nanostructures on the ZnO tetrapod surface have been successfully demonstrated through liquid-phase deposition-precipitation (Castillejos et al., 2012), light-mediation (Picciolini et al., 2015), and physical vapor phase techniques (Silva et al., 2017). Coupled with Au nanostructures, ZnO tetrapods have been shown to increase the sensitivity of SERS (surface-enhanced Raman spectroscopy) surfaces (Picciolini et al., 2015). ZnO tetrapods decorated with noble metals have also been investigated as a tool in the assessment of plasma concentrations, food processing, biomolecular sensing, high energy imaging, and radiation detection (Tarrago-Trani et al., 2006; Podila et al., 2011; Castillejos et al., 2012; Picciolini et al., 2015; Sun et al., 2016). Ag-decorated ZnO tetrapods are valued because of the intense plasmonic resonances exhibited by Ag nanoparticles in the visible spectrum. Such structures have been demonstrated as highly efficient photocatalysts in model reactions such as the degradation of methylene blue and methylene orange (Wang et al., 2011a; Li et al., 2013; Naghizadeh-Alamdari et al., 2015; Rackauskas et al., 2015; Bertoni et al., 2016). There have also been demonstrations employing thin film evaporation to produce surface structures and even hybrid synthesis techniques that introduce metallic precursors during the tetrapod assembly stage (Giorgio et al., 1995; Ammari et al., 2004; Fouad et al., 2011; Gröttrup et al., 2017b). These techniques, however, rarely produce high nanostructure number densities, monodisperse metal nanoparticles, or consistent nanostructure geometries.

Solution-based chemistry provides the most versatile route for forming supported noble metal nanostructures on oxide supports (Lee et al., 2014; Li and Tang, 2014; Munnik et al., 2015; Neretina et al., 2016). Such routes can, however, prove challenging when using ZnO tetrapods since the chemical environments used in many of these liquid-phase syntheses attack the ZnO surface. Light-mediated solution-based growth modes present a possible means for mitigating this concern since they can be carried out at room temperature under relatively mild reaction conditions. While light-mediated growth modes have been successfully demonstrated for Au (Castillejos et al., 2012; Picciolini et al., 2015; Bertoni et al., 2016) and Ag (Wang et al., 2011b; Wu et al., 2017), a single-step light-driven synthesis has not yet been demonstrated for decorating ZnO tetrapods with a wide variety of metallic nanostructures. Here, we demonstrate the surface decoration of ZnO tetrapods with Au, Ag, Pt, Cu, Pd, Ir, Rh, and Ru using a liquid-phase UV light-mediated synthetic pathway. The so-formed structures are then assessed as catalysts using the model reaction that sees 4-nitrophenol (4-NP) reduced to 4-aminophenol (4-AP) by borohydride.

RESULTS AND DISCUSSION

Synthesis

Figure 1 schematically shows the chemical processes used to generate ZnO tetrapods decorated with metal nanostructures. The synthesis was adapted from a previously reported optically-driven growth mode (Picciolini et al., 2015; Bertoni et al., 2016). It is reliant on ZnO tetrapods being suspended in liquid reactants that support two coupled reactions that are driven by UV photons. The reaction is initiated by the optical excitation of electron-hole pairs in the ZnO semiconductor. With electrons excited above the band gap into the conduction band and Au^{3+} ions in the adjacent solution, the conditions exist for a reaction that sees the ions reduced to Au^0, a neutral species which deposits on the surface and acts as a favorable nucleation site for continued deposition. The reduction of each Au^{3+} ion leaves behind three holes in the valence band and the overall Au/ZnO structure with a charge of 3^+. At the same time, the adjacent solution has a corresponding negative charge. Such a charge build-up would ultimately prevent the reduction and deposition of further Au^{3+} ions due to Coulombic repulsion. This situation is, however, remedied by a second reaction that sees the oxidative reduction of isopropyl alcohol to acetone (Ait-Ichou et al., 1984; Yamakata et al., 2002, 2003). In this reaction, electrons are injected into the ZnO while positive H^+ ions enter the liquid phase. With this reaction giving rise to a charge imbalance that is opposite to the Au^{3+} reduction reaction, the electro-neutrality of both the structure and the solution is preserved. (Picciolini et al., 2015) The various chemical processes occurring at the ZnO surface are illustrated in **Figure 1A**.

The tetrapods used in the light-mediated growth mode were synthesized using the flame transport method, the details of which can be found elsewhere (Mishra et al., 2013). Briefly, micrometer-scale metallic precursors, sacrificial polymer polyvinyl butyral (PVB), and ethanol in a specific weight ratio are heated in a muffle furnace (open-air) where the oxygen concentration required for ZnO tetrapod growth is tuned by adjusting the amount O_2 consumed in the combustion of PVB and ethanol. Decreasing the concentration of these reactants, hence, results in greater quantities of oxygen available for the

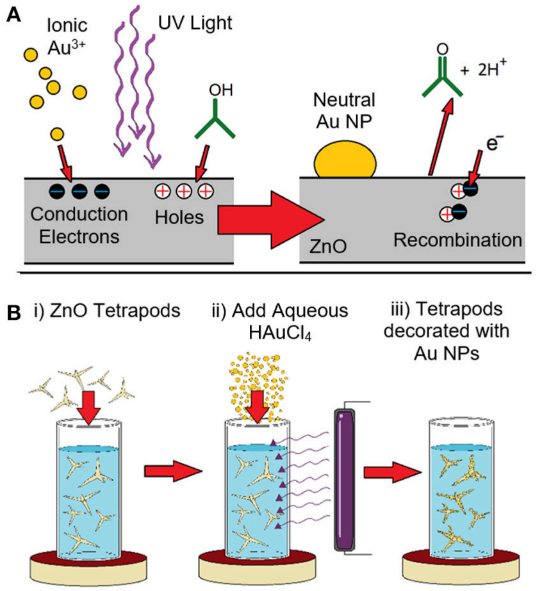

FIGURE 1 | (A) Schematic representation of the light-mediated growth mode used to decorate ZnO tetrapods with Au nanoparticles. The incident UV light excites electron-hole pairs in the ZnO. The electrons excited to the conduction band reduce Au^{3+} ions which leads to Au deposition. The holes in the valence band are scavenged through recombination with electrons derived from a reaction which sees the oxidative reduction of isopropyl alcohol to acetone as well as the release of H^{+} ions into the solution. **(B)** Schematic showing the synthesis process in which (i) ZnO tetrapods are added to isopropyl alcohol and stirred, (ii) the reaction is initiated through the addition of aqueous $HAuCl_4$ and the application of UV light, and (iii) Au nanoparticles (NPs) form on the ZnO tetrapods.

ZnO synthesis. As the reactants are transported through the furnace by convection, ZnO nanoparticles first nucleate and, with time, evolve into tetrapods with micro and nanoscale dimensions. The tetrapods are then collected on substrates or from the inside of the furnace. The as-synthesized tetrapods are then readied for nanoparticle decoration by suspending them in isopropyl alcohol that is rapidly stirred to inhibit their precipitation. The reaction is initiated by exposing the solution to 4 W 365 nm UV light as a small quantity of aqueous metal ions is injected. In addition to the ZnO tetrapod preparation method, the use of a low wattage UV light source marks a key difference between this work and the prior study (Bertoni et al., 2016) which utilized a broadband 300 W halogen lamp. Metal nanostructure growth is allowed to proceed over a 2 h interval where the metal ion supply is periodically replenished though additional injections. The reaction is terminated by turning off the UV light source. In the absence of stirring, the metal decorated ZnO tetrapods readily precipitate and are easily harvested. These structures are then cleaned and re-suspended in fresh isopropyl alcohol, and stored as such. The synthesis procedure is schematically depicted in **Figure 1B**.

Au Nanoparticle Decoration

Figure 2A shows an SEM image of ZnO tetrapods produced using the flame transport method. The structures, which vary widely in size, have tapered arms that can extend tens of micrometers in length and exhibit a solid or hollow interior. **Figures 2B–E** shows a series of SEM images of Au-decorated tetrapods derived from the light-mediated synthesis. For all cases, the ZnO tetrapods appear structurally intact, showing no indication of any chemical attack due to the light-mediated synthesis. The Au nanostructures that decorate the ZnO surface appear as unfaceted roundish nanoparticles. The separation and size of the nanostructures is dependent on the molarity of $HAuCl_4$ used. **Figures 2D–E** compares ZnO tetrapods decorated with Au nanoparticles derived from $HAuCl_4$ molarities of 1 and 0.5 mM, respectively. The lower molarity gives rise to a more densely decorated ZnO surface, a result that is highly reproducible. Histograms of the size distribution for the two cases (**Figure 2F**) indicate mean nanoparticle diameters of 47.5 and 31.8 nm for the 1 and 0.5 mM concentrations where, in both cases, the standard deviation is ∼14 nm. At the lower concentration, the number density of Au^{3+} ions available at the ZnO tetrapod surface is a factor of two less. The number of available conduction band electrons, however, is the same since the incident light intensity is maintained at the same value for all syntheses. The result indicates that, under these conditions, a lower Au^{3+} concentration in the adjacent solution provides a more favorable condition for the nucleation of additional Au nanoparticles as opposed to continued deposition onto preexisting structures. While the higher density of nanoparticles gives the impression that more Au is deposited on the ZnO tetrapods for 0.5 mM concentration, this is not the case. An analysis of the volume of Au deposited per unit area over the course of the 2 h synthesis indicates that 1.7× more Au is deposited when using the 1 mM concentration. This estimate was made by analyzing the size distribution over representative areas imaged in SEM from which the total volume of Au was calculated. XRD characterization of the Au-decorated ZnO tetrapods using the Bragg-Brentano $\Theta-2\Theta$ configuration is shown in **Figure 2G**. With all reflections being attributed to ZnO or Au, the result confirms that no unexpected phases originate from the flame transport method or the light-mediated growth mode.

Nanoparticle Decoration With Pt-Group Metals

Light-mediated syntheses of Pt-group metals were carried out in an analogous manner using aqueous K_2PtCl_4, Na_2PdCl_4, $RuCl_3$, H_2IrCl_6, and Na_3RhCl_6, to obtain Pt-, Pd-, Ru-, Ir-, and Rh-decorated tetrapods, respectively. **Figure 3** shows SEM images of the Pt-, Pd-, Ru-, and Ir-decorated tetrapods and their corresponding size distributions. For all cases, the nanoparticles have a roundish geometry similar to that observed for Au. The structures are, however, smaller in size, more densely spaced, show greater monodispersity, and grow at a slower rate. For the Pt, Pd, Ru, and Ir nanoparticles the size distribution histograms indicate mean particle diameters of 20.91, 17.29, 25.34, and 14.12 nm with standard deviations of 7.03, 4.67, 6.99, and 4.68 nm, respectively. These characteristically smaller and more monodisperse nanoparticles form at a high density which indicates a greater propensity for the reduced metallic

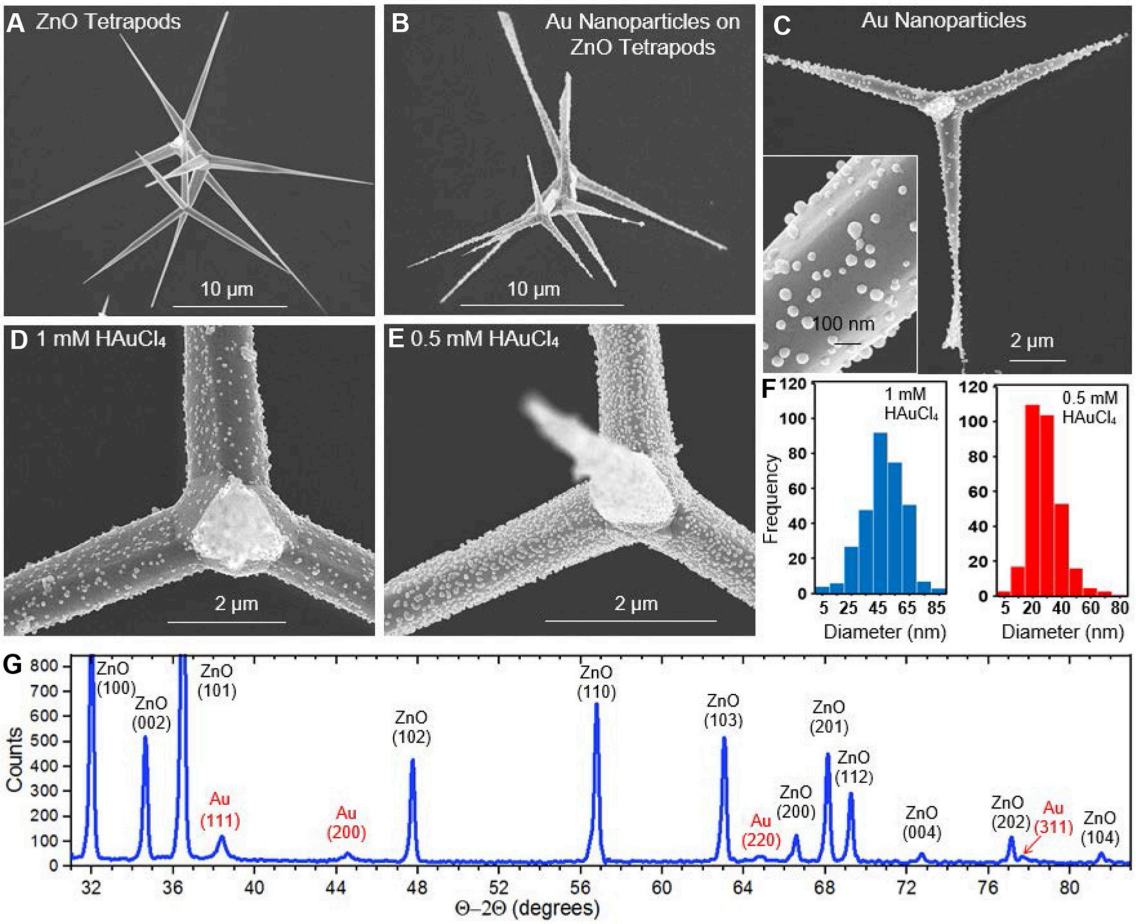

FIGURE 2 | SEM images showing **(A)** bare ZnO tetrapods **(B–D)**, Au nanoparticles synthesized on ZnO tetrapods from 1 mM $HAuCl_4$ **(E)**, Au nanoparticles synthesized on ZnO tetrapod from 0.5 mM $HAuCl_4$ **(F)**, histograms showing the Au nanoparticle size distribution derived from 1 mM (blue) and 0.5 mM (red) $HAuCl_4$. **(G)** XRD data showing the Au and ZnO reflections.

ions to nucleate at a new site on the ZnO tetrapod surface as opposed to their deposition onto pre-existing nanoparticles—an effect similarly seen for Au nanoparticle syntheses employing lower $HAuCl_4$ concentrations (**Figure 2E**). The Ir synthesis is unique in that nanostructures preferentially nucleate on the tetropod arms as opposed to the core (**Supplementary Figure 1**). The Rh synthesis was also unique in that it was difficult to resolve a significant number of nanoparticles on the tertrapod surface with SEM. A small Rh signature was, however, obtained using Energy-dispersive X-ray spectroscopy (EDS). Moreover, the Rh-decorated tetrapods showed significant catalytic activity (*vida infra*). Together these results suggest that Rh nanoparticles are present on the tetrapod in numbers of significance, but where their size is below the resolution limit of the SEM. Characterization of the Rh-decorated tetrapods is presented as Supplementary Material (**Supplementary Figure 2**) along with EDS data for the other metals (**Supplementary Figure 3**).

Nanoparticle Decoration With Cu and Ag

Aqueous solutions of $CuCl_2$ and $Cu(NO_3)_2$ were both investigated as a means to decorate ZnO tetrapods with Cu nanoparticles. The $CuCl_2$ results, shown in **Figure 4A**, were largely in line with those obtained for other metals in that it yielded a rounded nanoparticle geometry with an average diameter of 11.53 nm. In stark contrast, $Cu(NO_3)_2$ yielded a distinct morphology characterized by micrometer-scale plates that extend radially outward from the arms of the ZnO tetrapod (**Figure 4B**). It is noted that Wei et al. (2014) observed markedly different morphologies when depositing Cu nanostructures on ZnO nanowires using the same two salts, yielding small nanoparticles for $CuCl_2$ and leaf-shaped structures for $Cu(NO_3)_2$. The growth of large plate-like structures off preexisting structures is not unprecedented. It has, for example, been observed for both Cu and Ag when deposited on Au templates (Gilroy et al., 2014; Mettela and Kulkarni, 2015; Zhu et al., 2018). Markedly different morphologies are also observed when the light-mediated growth mode is used to decorate the tetrapods with Ag using aqueous $AgNO_3$. For this case, Ag structures form with a jagged shape (**Figure 4C**). It is conceivable that the NO_3^- counterion derived from $Cu(NO_3)_2$ and $AgNO_3$ is crucial to the formation of these anomalously shaped structures since all the chloride-based salts used in this study give rise to small rounded nanostructures.

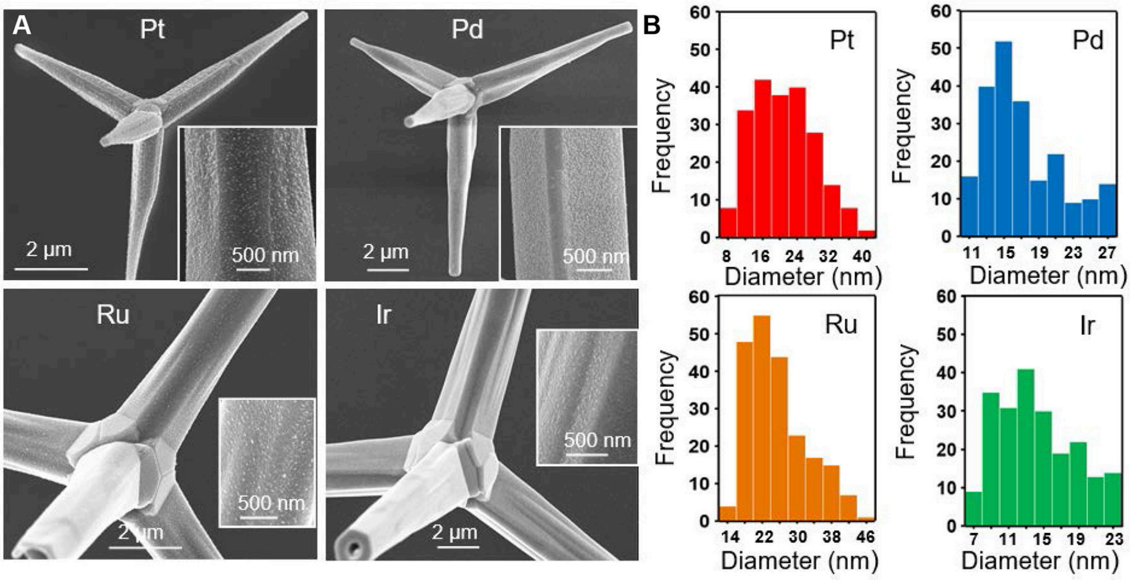

FIGURE 3 | (A) SEM images of ZnO tetrapods decorated with Pt, Pd, Ru, and Ir nanoparticles and **(B)** their corresponding size distribution histograms.

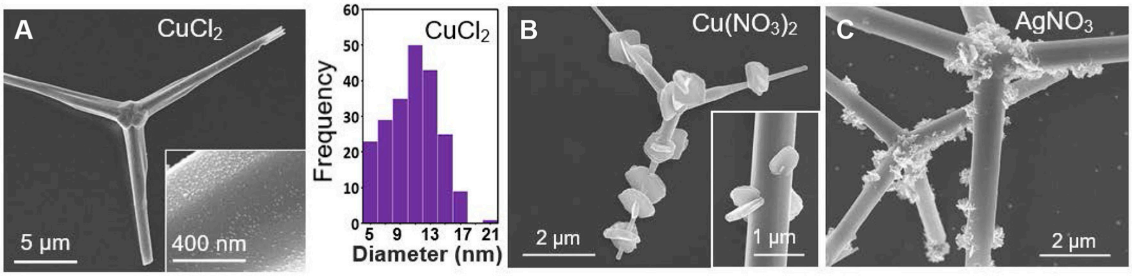

FIGURE 4 | (A) SEM images of Cu-decorated ZnO tetrapods derived from aqueous $CuCl_2$ and the corresponding nanoparticle size distribution histogram. SEM images of **(B)** Cu- and **(C)** Ag-decorated ZnO tetrapods derived from aqueous $Cu(NO_3)_2$ and $AgNO_3$, respectively.

Catalysis

The catalytic reduction of 4-NP is widely recognized as a trusted model reaction for gauging the catalytic efficacy of nanoscale materials (Hervés et al., 2012; Aditya et al., 2015; Zhao et al., 2015). In this reaction, aqueous 4-NP is reduced to 4-AP by borohydride on the surface of a catalyst. A 4-NP absorbance peak at 400 nm is used to spectroscopically monitor the progress of the reaction in real-time. In the presence of a catalyst, the time dependence of the 400 nm absorbance takes the form of an exponential decay. An apparent reaction rate constant, k_{app}, can be extracted from the data using the expression:

$$\ln\left(\frac{A}{A_0}\right) = k_{app}t \tag{1}$$

where A/A_0 is the absorbance at time t normalized to its initial value. A plot of the natural logarithm of the normalized absorbance vs. time, therefore, yields a straight line with a slope of k_{app} where larger values indicate a better performing catalyst. When assessing catalytic performance, it is imperative that the dissolved oxygen be purged from all aqueous reactants since its presence (i) gives rise to an induction time (Menumerov et al., 2016), (ii) diminishes k_{app} values (Menumerov et al., 2017), (iii) can result in the oxidative etching of catalytically active sites (Menumerov et al., 2018), and (iv) lead to the misidentification of the true catalyst (Menumerov et al., 2018).

The catalytic activity of ZnO tetrapods decorated with metal nanostructures were assessed using solutions of 30 μM 4-NP and 3 mM $NaBH_4$. Bare ZnO tetrapods (i.e., those without metallic decoration) exhibited no catalytic activity toward the reduction of 4-NP. Of the eight different metals tested, significant catalytic activity was observed for ZnO tetrapods decorated with Pd, Ag, and Rh. **Figure 5** shows the time dependent absorbance obtained for these metals as well as the plot used to extract k_{app}. The k_{app} values determined for ZnO tetrapod decorated with Ag, Pd, and Rh are 5.9×10^{-3} s^{-1}, $5.7 \times$

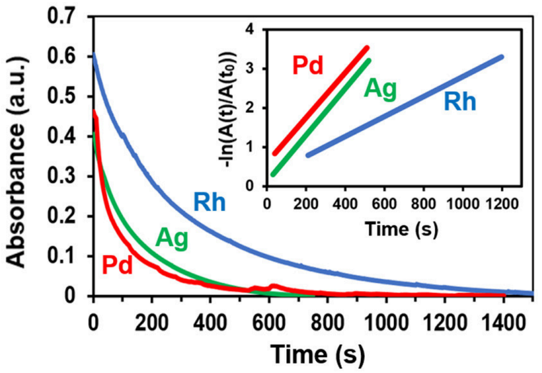

FIGURE 5 | The time-dependence of the 400 nm 4-NP absorbance when using Rh-, Ag-, and Pd-decorated tetrapods as catalysts. The inset depicts the linear region of the normalized logarithmic plot of the absorbance from which the reaction rate is extracted.

10^{-3} s^{-1}, and 2.5 × 10^{-3} s^{-1}, respectively. While Ag and Pd are well-known for their catalytic activity toward the reduction of 4-nitrophenol, Rh has received little attention. Sub 10-nm nanoparticles of Ag are particularly catalytic due to a high density of low coordination surface sites (Menumerov et al., 2016). The catalytic activity of the comparatively large Ag structures shown in **Figure 4C** is likely attributable to their jagged shape since such a morphology is characterized by surfaces with numerous steps, kinks, and terraces that inevitably express numerous undercoordinated sites from which the catalytic activity is likely derived (Menumerov et al., 2018).

CONCLUSION

In summary, we have demonstrated a light-mediated growth mode for decorating ZnO tetrapods with nanostructures of eight different elemental metals. By employing a room temperature reaction under relatively mild reaction conditions, we have avoided pitfalls associated with practicing common solution-based protocols that show chemical incompatibility with the ZnO surface. This study has, hence, forwarded the use of ZnO tetrapods as a support for metal nanostructures, with the potential to motivate new light-mediated synthesis schemes and provide a new platform for advancing applications in sensing, optoelectronic, catalysis, and photocatalysis that are reliant on a coupled response at the semiconductor-nanometal interface.

MATERIALS AND METHODS

Chemicals

Solution-based syntheses were carried out using 99.99% hydrogen tetrachloroaurate(III) trihydrate (Alfa Aesar), 99.9999% silver nitrate (Sigma-Aldrich), 99.99% copper (II) nitrate trihydrate (Sigma-Aldrich), 99.99% potassium tetrachloroplatinate(II) (Sigma-Aldrich), 99.999% sodium tetrachloropalladate(II) (Sigma-Aldrich), 99.98% ruthenium(III) chloride hydrate (Sigma-Aldrich), 99.98% hydrogen hexachloroiridate(IV) hydrate (Sigma-Aldrich), 99.98% sodium hexachlororhodate(III) (Sigma-Aldrich), and 100% isopropyl alcohol (Honeywell). Solutions for catalysis were prepared using 4-NP (Fluka), $NaBH_4$ (Fluka), and DI water with a resistivity of 18.2 MΩ cm^{-1}. All chemicals were used as received.

Tetrapod Synthesis

ZnO tetrapods were prepared in bulk by the flame transport synthesis method (Mishra et al., 2013). Micrometer-scale (typically 3–10 µm) Zn precursor particles, polymer polyvinyl butyral, and ethanol are heated in a muffle-type furnace, in air, above 800°C at a rate >100°C min^{-1}. The heated atmosphere within the furnace results in laminar convection that is utilized for the transportation and oxidation of the metallic particles and provides the emerging tetrapods with enough local space for uninterrupted growth as they continue to transit upward through the furnace. The size and geometry of the ZnO structure is dependent on the time spent in transit as well as the component material ratios and oven temperature, granting tunablility to the procedure. Once the reaction is complete, the ZnO tetrapods are collected from the inside the furnace.

Light-Mediated Growth Modes

Ten milligrams of ZnO tetrapods were weighed and added to a 50 mL polypropylene tube into which 48.8 mL of isopropyl alcohol was added and stirred at 680 rpm using a magnetic stirrer. A 100 µL of aqueous 1 mM metallic salt was added every 10 min for 2 h (for a total of 1.2 mL) while under a 365 nm, 4 W mercury vapor lamp. After 2 h the tetrapods were allowed to precipitate out of solution, where they were then rinsed twice with isopropyl alcohol. For SEM imaging, the decorated ZnO tetrapods were then dropcast onto sapphire heated to 90°C.

4-Nitrophenol Reduction

The catalytic reduction of 4-NP to 4-AP was carried out in a 3 mL quartz cuvette with a 1 cm path length and monitored using a UV-Vis spectrometer. The metal decorated ZnO tetrapods were first dried and then 2 mg were added to the empty cuvette. A 2 mL aqueous solution of 3 mM $NaBH_4$ and 30 µM 4-NP was then prepared and purged with N_2 gas for 10 min to remove dissolved oxygen. The cuvette was then filled with the purged solution and covered with Parafilm such that two small openings allowed for N_2 gas to be flowed over the solution (Menumerov et al., 2016) to further prevent oxygen from dissolving into the reactants during data collection. The time dependent absorbance was measured at 400 nm for metal-decorated tetrapods investigated.

INSTRUMENTATION

SEM and EDS measurements were carried out using a Magellan 400 FEI field emission scanning electron microscope. XRD scans were obtained using a Bruker D8 Advance Davinci diffractometer using Cu Kα1 radiation. Absorbance spectra were acquired with a Jasco V-730 UV-Vis Spectrophotometer. The nanoparticle size distributions presented in **Figures 2F**, **3B**, **4A** were processed with ImageJ software using 312, 215, and 215 nanoparticles, respectively.

AUTHOR CONTRIBUTIONS

TD, RH, and SN designed the experiments and prepared the manuscript. RA and YM performed tetrapod synthesis. TD performed the light-mediated growth syntheses and catalysis experiments. AP carried out XRD characterization.

FUNDING

The Notre Dame work was funded by a National Science Foundation award (DMR-1803917) to SN and the Kiel work was funded by Deutsche Forschungsgemeinschaft (DFG) under schemes: AD 183/17-1, SFB 1261 TP (A05, RA), and SFB 677 (C14).

ACKNOWLEDGMENTS

TD acknowledges support received through the University of Notre Dame's Remick Graduate Fellowship. The authors have benefited from the facilities available through the Notre Dame Integrated Imaging Facility (NDIIF) and the ND Energy Materials Characterization Facility.

SUPPLEMENTARY MATERIAL

The Supplementary Material for this article can be found online at: https://www.frontiersin.org/articles/10.3389/fchem.2018.00411/full#supplementary-material

REFERENCES

Abdulgafour, H., Hassan, Z., Ahmed, N., and Yam, F. (2012). Comparative study of ultraviolet detectors based on zno nanostructures grown on different substrates. *J. Appl. Phys.* 112:074510. doi: 10.1063/1.4757619

Aditya, T., Pal, A., and Pal, T. (2015). Nitroarene reduction: a trusted model reaction to test nanoparticle catalysts. *Chem. Commun.* 51, 9410–9431. doi: 10.1039/C5CC01131K

Ait-Ichou, A., Formenti, M., Pommier, B., and Teichner, S. J. (1984). Photocatalytic dehydrogenation of lsopropanol on Pt/Ti02 catalysts. *J. Catal.* 91, 293–307. doi: 10.1016/0021-9517(85)90343-4

Alsultany, F., Hassan, Z., and Ahmed, N. (2016). Low-Power UV photodetection characteristics of zno tetrapods grown on catalyst-free glass substrate. *Sensors Actuat. A Phys.* 250, 187–194. doi: 10.1016/j.sna.2016.09.039

Ammari, F., Lamotte, J., and Touroude, R. (2004). An emergent catalytic material: Pt/ZnO catalyst for selective hydrogenation of crotonaldehyde. *J. Catal.* 221, 32–42. doi: 10.1016/S0021-9517(03)00290-2

Bai, Z., Xie, C., Hu, M., Zhang, S., and Zeng, D. (2008). Effect of humidity on the gas sensing property of the tetrapod-shaped Zno nanopowder sensor. *Mat. Sci. Eng. B* 149, 12–17. doi: 10.1016/j.mseb.2007.11.020

Bertoni, G., Fabbri, F., Villani, M., Lazzarini, L., Turner, S., Van Tendeloo, G., et al. (2016). Nanoscale mapping of plasmon and exciton in zno tetrapods coupled with au nanoparticles. *Sci. Rep.* 6:19168. doi: 10.1038/srep19168

Castillejos, E., Gallegos-Suarez, E., Bachiller-Baeza, B., Bacsa, R., Serp, P., Guerrero-Ruiz, A., et al. (2012). Deposition of gold nanoparticles on ZnO and their catalytic activity for hydrogenation applications. *Catal. Commun.* 22, 79–82. doi: 10.1016/j.catcom.2012.02.016

Chaudhary, S., Umar, A., Bhasin, K. K., and Baskoutas, K. (2018). Chemical sensing applications of ZnO nanomaterials. *Materials* 11:287. doi: 10.3390/ma11020287

Fouad, O. A., El Rahman, A., Khder, S., Dai, Q., and El-Shall, M. S. (2011). Structural and catalytic properties of ZnO and Al_2O_3 nanostructures loaded with metal Nanoparticles. *J. Nanopart. Res.* 13, 7075–7083. doi: 10.1007/s11051-011-0620-8

Gilroy, K. D., Hughes, R. A., and Neretina, S. (2014). Kinetically controlled nucleation of silver on surfactant-free gold seeds. *J. Am. Chem. Soc.* 136, 15337–15345. doi: 10.1021/ja5081635

Giorgio, S., Henry, C., and Chapon, C. (1995). HRTEM studies of the epitaxial growth of Pd particles (1-6 Nm) on ZnO micro-prisms. *Microsc. Microanal. Microstruct.* 6, 237–248.

Gröttrup, J., Postica, V., Smazna, D., Hoppe, M., Kaidas, V., Mishra, Y. K., et al. (2017a). UV Detection properties of hybrid ZnO tetrapod 3-D networks. *Vacuum* 146, 492–500. doi: 10.1016/j.vacuum.2017.03.017

Gröttrup, J., Schutt, F., Smazna, D., Lupan, O., Adelung, R., and Mishra, Y. K. (2017b). Porous ceramics based on hybrid inorganic tetrapodal networks for efficient photocatalysis and water purification. *Ceram. Int.* 43, 14915–14922. doi: 10.1016/j.ceramint.2017.08.008

Hervés, P., Pérez-Lorenzo, M., Liz-Marzán, L. M., Dzubiella, J., Lu, Y., and Ballauff, M. (2012). Catalysis by metallic nanoparticles in aqueous solution: model reactions. *Chem. Soc. Rev.* 41, 5577–5587. doi: 10.1039/C2CS35029G

Janotti, A., and Van de Walle, C. G. (2009). Fundamentals of zinc oxide as a semiconductor. *Rep. Prog. Phys.* 72:126501. doi: 10.1088/0034-4885/72/12/126501

Kumar, R., Umar, A., Kumar, G., and Nalwa, H. (2017). Antimicrobial Properties of ZnO Nanomaterials: a review. *Ceram. Int.* 43, 3940–3961. doi: 10.1016/j.ceramint.2016.12.062

Laurenti, M., and Valentina, C. (2017). ZnO nanostructures for tissue engineering applications. *Nanomaterials* 7:374. doi: 10.3390/nano7110374

Lee, J., Kim, S. M., and Lee, I. S. (2014). Functionalization of hollow nanoparticles for nanoreactor applications. *Nano Today* 9, 631–667. doi: 10.1016/j.nantod.2014.09.003

Li, G., and Tang, Z. (2014). Noble Metal Nanoparticle@Metal Oxide Core/Yolk–shell nanostructures as catalysts: recent progress and perspective. *Nanoscale* 6, 3995–4011. doi: 10.1039/C3NR06787D

Li, W., Hua, F., Yue, J., and Li, J. (2013). Ag@AgCl Plasmon-induced sensitized zno particle for high-efficiency photocatalytic property under visible light. *Appl. Surf. Sci.* 285, 490–497. doi: 10.1016/j.apsusc.2013.08.082

Mecklenburg, M., Schuchardt, A., Mishra, Y. K., Kaps, S., Adelung, R., Lotnyk, A., et al. (2012). Aerographite: ultra lightweight, flexible nanowall, carbon microtube material with outstanding mechanical performance. *Adv. Mater.* 24, 3486–3490. doi: 10.1002/adma.201200491

Menumerov, E., Hughes, R. A., Golze, S., Neal, R., Demille, T., Campanaro, J., et al. (2018). Identifying the true catalyst in the reduction of 4-nitrophenol: a case study showing the effect of leaching and oxidative etching using ag catalysts. *ACS Catal.* 8, 8879–8888. doi: 10.1021/acscatal.8b02325

Menumerov, E., Hughes, R. A., and Neretina, S. (2016). Catalytic Reduction of 4-nitrophenol: a quantitative assessment of the role of dissolved oxygen in determining the induction time. *Nano Lett.* 16, 7791–7797. doi: 10.1021/acs.nanolett.6b03991

Menumerov, E., Hughes, R. A., and Neretina, S. (2017). One-step catalytic reduction of 4-nitrophenol through the direct injection of metal salts into oxygen-depleted reactants. *Catal. Sci. Technol.* 7, 1460–1464. doi: 10.1039/C7CY00260B

Mettela, G., and Kulkarni, G. U. (2015). Site selective cu deposition on au microcrystallites: corners, edges versus planar surfaces. *Cryst. Eng. Commun.* 17, 9459–9465. doi: 10.1039/C5CE01574J

Mishra, Y. K., and Adelung, R. (2017). ZnO tetrapod materials for functional applications. *Mater. Today* 21, 631–651. doi: 10.1016/j.mattod.2017.11.003

Mishra, Y. K., Kaps, S., Schuchardt, A., Paulowicz, I., Jin, X., Gedamu, D., et al. (2013). Fabrication of macroscopically flexible and highly porous

3D semiconductor networks from interpenetrating nanostructures by a simple flame transport approach. *Part. Part. Syst. Charact.* 30, 775–783. doi: 10.1002/ppsc.201300197

Munnik, P., de Jongh, P. E., and de Jong, K. P. (2015). Recent developments in the synthesis of supported catalysts. *Chem. Rev.* 115, 6687–6718. doi: 10.1021/cr500486u

Naghizadeh-Alamdari, S., Habibi-Yangjeh, A., and Pirhashemi, M. (2015). One-pot ultrasonic-assisted method for preparation of Ag/AgCl Sensitized ZnO nanostructures as visible-light-driven photocatalysts. *Solid State Sci.* 40, 111–120. doi: 10.1016/j.solidstatesciences.2015.01.007

Neretina, S., Hughes, R. A., Gilroy, K. D., and Hajfathalian, M. (2016). Noble metal nanostructure synthesis at the liquid-substrate interface: new structures, new insights and new possibilities. *Acc. Chem. Res.* 49, 2243–2250. doi: 10.1021/acs.accounts.6b00393

Newton, M. C., and Warburton, P. A. (2007). ZnO tetrapod nanocrystals. *Mater. Today* 10, 50–54. doi: 10.1016/S1369-7021(07)70079-2

Papavlassopoulos, H., Mishra, Y. K., Kaps, S., Paulowicz, I., Abdelaziz, R., Elbahry, M., et al. (2014). Toxicity of functional nano-micro zinc oxide tetrapods: impact of cell culture conditions, cellular age and material properties. *PLoS ONE* 9:e84983. doi: 10.1371/journal.pone.0084983

Picciolini, S., Castagnetti, N., Vanna, R., Mehn, D., Bedoni, M., Gramatica, F., et al. (2015). Branched gold nanoparticles on ZnO 3D architecture as biomedical SERS sensors. *RSC Adv.* 5, 93644–93651. doi: 10.1039/C5RA13280K

Podila, R., Chen, P., Reppert, J., Rao, A., and Ke, P. (2011). Biomolecular sensing using gold nanoparticle-coated ZnO nanotetrapods. *J. Mater. Res.* 26, 2328–2333. doi: 10.1557/jmr.2011.147

Rackauskas, S., Klimova, O., Jiang, H., Nikitenko, A., Chernenko, K., Shandakov, S., et al. (2015). A novel method for continuous synthesis of Zno tetrapods. *J. Phys. Chem. C* 119, 1345–1352. doi: 10.1021/acs.jpcc.5b03702

Schütt, F., Signetti, S., Krüger, H., Röder, S., Smazna, D., Kaps, S., et al. (2017). Hierarchal self-entangled carbon nanotube tube networks. *Nat. Commun.* 8:1215. doi: 10.1038/s41467-017-01324-7

Silva, E. L., Mishra, Y. K., Fernandes, A. J. S., Silva, R. F., Strobel, J., Kienle, L., et al. (2017). Direct synthesis of electrowettable carbon nanowall-diamond hybrid materials from sacrificial ceramic templates using HFCVD. *Adv. Mater. Int.* 4:1700019. doi: 10.1002/admi.201700019

Sun, C., Fu, Y., Wang, Q., Xing, L., Liu, B., and Xue, X. (2016). Ultrafast Piezo-photocatalytic degradation of organic pollutions by Ag_2O/Tetrapod-ZnO nanostructures under ultrasonic/UV exposure. *RSC Adv*. 6, 87446–87453. doi: 10.1039/C6RA13464E

Tan, T., Li, Y., Liu, Y., Wang, B., Song, X., Li, E., et al. (2008). Two-step preparation of Ag/tetrapod-like ZnO with photocatalytic activity by thermal evaporation and sputtering. *Mater. Chem. Phys.* 111, 305–308. doi: 10.1016/j.matchemphys.2008.04.013

Tarrago-Trani, M., Phillips, K., Lemar, L., and Holden, J. (2006). New and existing oils and fats used in products with reduced trans-fatty acid Content. *J. Am. Diet. Assoc.* 106, 867–880. doi: 10.1016/j.jada.2006.03.010

Vishnukumar, P., Vivekanandhan, S., Misha, M., and Mohanty, A. K. (2018). Recent advances and emerging opportunities in phytochemical synthesis of zno nanostructures. *Mat. Sci. Semicond. Process.* 80, 143–161. doi: 10.1016/j.mssp.2018.01.026

Wang, J., Fan, X. M., Tian, K., Zhou, Z. W., and Wang, Y. (2011a). Largely Improved photocatalytic properties of Ag/Tetrapod-like ZnO nanocompounds prepared with different peg contents. *Appl. Surf. Sci.* 257, 7763–7770. doi: 10.1016/j.apsusc.2011.04.026

Wang, J., Fan, X. M., Zhou, Z. W., and Tian, K. (2011b). Preparation of Ag Nanoparticles coated tetrapod-like ZnO whisker photocatalysts using photoreduction. *Mater. Sci. Eng. B* 176, 978–983. doi: 10.1016/j.mseb.2011.05.027

Wei, F., Liu, L., and Li, G. (2014). "Zinc oxide/copper oxide heterogeneous nanowire preparation and application in uv sensor," in *14th IEEE International Conference on Nanotechnology* (Toronto, ON).

Wu, M., Yan, L., Li, J., and Wang, L. (2017). Synthesis and photocatalytic performance of Ag/AgCl/ZnO tetrapod composites. *Res. Chem. Int.* 43, 6407–6419. doi: 10.1007/s11164-017-2997-1

Yamakata, A., Ishibashi, T., and Onishi, H. (2002). Electron- and hole-capture reactions on pt/tio$_2$ photocatalyst exposed to methanol vapor studied with time-resolved infrared absorption spectroscopy. *J. Phys. Chem. B* 106, 9122–9125. doi: 10.1021/jp025993x

Yamakata, A., Ishibashi, T., and Onishi, H. (2003). Microsecond kinetics of photocatalytic oxidation on Pt/TiO_2traced by vibrational spectroscopy. *Chem. Phys. Lett.* 376, 5–6. doi: 10.1016/S0009-2614(03)01034-0

Zhang, Q., Fan, W., and Gao, L. (2007). Anatase TiO_2 nanoparticles immobilized on ZnO tetrapods as a highly efficient and easily recyclable photocatalyst. *Appl. Catal. B Environ.* 76, 168–173. doi: 10.1016/j.apcatb.2007.05.024

Zhao, P., Feng, X., Huang, D., Yang, G., and Astruc, D. (2015). Basic concepts and recent advances in nitrophenol reduction by gold- and other transition metal nanoparticles. *Coord. Chem. Rev.* 287, 114–136. doi: 10.1016/j.ccr.2015.01.002

Zhu, M., Sun, Z., Fujitsuka, M., and Majima, T. (2018). Z-Scheme photocatalytic water splitting on a 2D heterostructure of black phosphorous/bismuth vanadate using visible light. *Angew. Chem. Int. Ed.* 1, 2160–2164. doi: 10.1002/anie.201711357

Conflict of Interest Statement: The authors declare that the research was conducted in the absence of any commercial or financial relationships that could be construed as a potential conflict of interest.

frontiers in Chemistry

ORIGINAL RESEARCH
published: 26 September 2018
doi: 10.3389/fchem.2018.00444

Gram-Scale Synthesis of Blue-Emitting $CH_3NH_3PbBr_3$ Quantum Dots Through Phase Transfer Strategy

Feng Zhang[1], Changtao Xiao[1], Yunfei Li[2], Xin Zhang[1], Jialun Tang[1], Shuai Chang[1], Qibing Pei[2] and Haizheng Zhong[1]*

[1] Beijing Key Laboratory of Nanophotonics and Ultrafine Optoelectronic Systems, School of Materials Science and Engineering, Beijing Institute of Technology, Beijing, China, [2] Department of Materials Sciences and Engineering, California NanoSystems Institute, Henry Samuli School of Engineering and Applied Science, University of California, Los Angeles, Los Angeles, CA, United States

Reprecipitation synthesis has been demonstrated to be a simple and convenient route to fabricate high quality perovskite quantum dots toward display applications, whereas the limited chemical yields (<10%) and difficulty of purification limited its further application. In order to overcome this issue, we here report a modified emulsion synthesis by introducing phase transfer strategy, which achieving effective extraction of newly formed perovskite quantum dots into non-polar solvent and avoiding the degradation of perovskite quantum dots to a large extent. Based on this strategy, gram-scale $CH_3NH_3PbBr_3$ quantum dots were fabricated in 10 mL (∼0.02 mol/L) colloidal solution with chemical yields larger than 70%. The as fabricated $CH_3NH_3PbBr_3$ quantum dots exhibit an emission peak of 453 nm and a full width at half maximum of only 14 nm. Moreover, electroluminescent devices based on blue emitting $CH_3NH_3PbBr_3$ quantum dots were also explored with a maximum luminance of 32 cd/m^2, showing potential applications in blue light emitting devices.

Keywords: emulsion synthesis, $CH_3NH_3PbBr_3$, quantum dots, blue-emitting, phase transfer

Edited by:
Jing Zhao,
University of Connecticut,
United States

Reviewed by:
Angang Dong,
Fudan University, China
Huaibin Shen,
Henan University, China

****Correspondence:***
Shuai Chang
schang@bit.edu.cn

Specialty section:
This article was submitted to Nanoscience,
a section of the journal
Frontiers in Chemistry

Received: *30 July 2018*
Accepted: *07 September 2018*
Published: *26 September 2018*

Citation:
Zhang F, Xiao C, Li Y, Zhang X, Tang J, Chang S, Pei Q and Zhong H (2018) Gram-Scale Synthesis of Blue-Emitting $CH_3NH_3PbBr_3$ Quantum Dots Through Phase Transfer Strategy. Front. Chem. 6:444. doi: 10.3389/fchem.2018.00444

INTRODUCTION

The development of lighting and display technologies demand luminescent materials with high color quality (Lin and Liu, 2011; Shirasaki et al., 2013; Pust et al., 2014). In the past 3 years, halide perovskite quantum dots (QDs) have emerged as a new generation of luminescent materials with excellent photoluminescent (PL) properties such as high quantum yields (QYs), panchromatic wavelength tunability and narrow emission line width (Protesescu et al., 2015; Stranks and Snaith, 2015; Zhang et al., 2015), which make them promising candidates for wide color gamut displays (Bai and Zhong, 2015; Kim et al., 2016; Li et al., 2017). To further promote their potential commercialization applications, efficient mass production of colloidal perovskite QDs has become an important research topic (Huang H. et al., 2016; Xing et al., 2016; Ha et al., 2017; Zhang et al., 2017a). Great progress has been made on the colloidal synthesis of perovskite QDs

(Huang et al., 2015a; Leng et al., 2016; Wang et al., 2016; Polavarapu et al., 2017; Protesescu et al., 2017) where two main synthesis strategies have been established, namely, high temperature hot-injection and room temperature reprecipitation. Currently room temperature reprecipitation methods including ligand-assisted reprecipitation (LARP) (Zhang et al., 2015) and emulsion reprecipitation (Huang et al., 2015a) have been more universally applied owing to their simple and low temperature synthesis process and feasibility for both organic-inorganic hybrid and all-inorganic perovskite materials (Lignos et al., 2016; Wei et al., 2016; Levchuk et al., 2017a,b; Minh et al., 2017). However, there still exist many challenges that hinder the development of perovskite QDs for display applications. In 2015, our group fabricated $CH_3NH_3PbBr_3$ QDs by applying the conventional emulsion strategy (Huang et al., 2015a). However, the obtained $CH_3NH_3PbBr_3$ QDs through this strategy were precipitated in the mixture of polar and non-polar solvents. It is widely recognized that perovskite QDs can be destroyed by even trace amount of polar solvent, which leads to limited chemical yields (Huang H. et al., 2016; Zhang et al., 2017a). On the other hand, the conventional emulsion process normally generate multiple products from nano-sized QDs to micro-sized crystals, thus the purification process by centrifuging will inevitably lead to material loss. Therefore, the extraction of the perovskite QDs from polar solvent as well as the reduction of side products is a crucial step to enhance the chemical yield. From the perspective of electroluminescent (EL) device integration, the reported green emission EL device based on halide perovskite QDs or nanocrystals has achieved an EQE over 16%, (Han et al., 2018; Yang et al., 2018) however, there still lacks high quality blue emission perovskite materials, especially the ones with controlled emission wavelength within the pure blue range of 450–470 nm. On the other hand, the reported blue EL emission perovskite materials so far are all based on 2D or quasi 2D structure with the assistance of large organic ammonium molecules, (Kumar et al., 2016; Wang et al., 2017) no blue EL result based on pure 3D structured $CH_3NH_3PbBr_3$ QDs was reported. Therefore, further exploration of colloidal chemistry to overcome these issues is imperative.

Here, for the first time we report the gram scale fabrication of 3D structured blue emitting $CH_3NH_3PbBr_3$ QDs through a modification of the conventional emulsion synthesis method. The main alteration is that acetonitrile (ACN) is used as demulsifier instead of acetone. As ACN is miscible with N, N-dimethylformamide (DMF) but immiscible with hexane, the addition of ACN initiates the crystallization for $CH_3NH_3PbBr_3$ QDs and also induces phase separation at the same time. As a result, the as-formed $CH_3NH_3PbBr_3$ QDs in DMF and ACN phase spontaneously transferred into hexane phase, leading to enhanced chemical yields and simplified purification process by stratification. Based on the modified emulsion route, strong blue-emitting $CH_3NH_3PbBr_3$ QDs with an average diameter of 2.4 nm was successfully fabricated. The obtained $CH_3NH_3PbBr_3$ QDs exhibit an emission peak of 454 nm and full width at half maximum (FWHM) of only 14 nm. Furthermore, LED devices based on the blue perovskite QDs were explored, demonstrating their potential in display applications.

MATERIALS AND METHODS

Chemicals

$PbBr_2$ [lead(II) bromide, 99%, alfa aesar],methylamine (CH_3NH_2, 33 wt. % in absolute ethanol, aladdin), n-octylamine (≥99%, aladdin), hydrobromic acid(HBr, 49 wt.% in water, alfa aesar),oleic acid (≥90%, Alfa aser), N, N-dimethylformamide (DMF, analytical grade, Beijing Chemical Reagent Co., Ltd., China), acetronitrile (ACN, analytical grade, Beijing Chemical Reagent Co., Ltd., China), toluene (analytical grade, Beijing Chemical Reagent Co., Ltd., China).

Fabrication of Hybrid $CH_3NH_3PbBr_3$ QDs

CH_3NH_3Br was synthesized according to the literature (Zhang et al., 2015). Colloidal $CH_3NH_3PbBr_3$ QDs was fabricated by a modification of the reported emulsion synthesis. Firstly, $PbBr_2$ (0.2 mmol, 0.0734 g) and CH_3NH_3Br (0.2 mmol, 0.0224 g) were dissolved in 0.5 mL DMF and sonicated for 10 min to form solution A. Solution B was prepared by mixing of n-hexane (10 mL), n-octylamine (30 μL) and oleic acid (35 μL). Then, the solution A was dropwise added into solution B under vigorous stirring. With the addition of solution A, the color of mixed solution gradually turned from clear to slight milky indicating the formation of emulsion system. Then, 6 mL of ACN was added into the emulsion system as demulsifier to initiate demulsion process. The limited solubility of $CH_3NH_3PbBr_3$ precursors in ACN drives the formation of $CH_3NH_3PbBr_3$ QDs. The mixture stratified into two phases after removing the stir. The top layer was collected as dispersion of $CH_3NH_3PbBr_3$ QDs in hexane for further characterization. Furthermore, $CH_3NH_3PbBr_3$ QD powder can be obtained by collecting the precipitates after adding a fixed amount of ethyl acetate into the QDs dispersion in hexane solution.

Fabrication and Characterization of EL Devices

ITO substrate was sequentially washed with acetone, ethanol and deionized water, followed by plasma treatment for 5 min. Poly(3,4-ethylenedioxythiophene):poly(styrenesulfonate) (PEDOT:PSS) solution was spin coated on the ITO film at 4000 rpm, then annealed at 150°C for 15 min. $CH_3NH_3PbBr_3$ QDs dispersed in hexane (2.5 mg/mL) was spin-coated on the PVK film, followed by thermal annealing at 70°C for 15 min, then (2,2,2-(1,3,5-benzinetrily)tris(1-phenyl-1-Hbenzimidazole) (TPBi) (40 nm), CsF (1 nm) and Al (80 nm) were thermally deposited in sequence in a high-vacuum chamber with a deposition rate of 1, 0.1, and 5 Å/s, respectively ($<10^{-6}$ mbar). Keithley 2400 and Keithley 2000 SourceMeter unit linked to a calibrated silicon photodiode were used to measure the current-voltage-brightness characteristics. A spectrophotometer PR-655 (Photo Research, Inc.) was used to measure the electroluminescence spectrum.

Characterizations

UV-Vis absorption spectra were measured on a UV-6100 UV-Vis spectrophotometer (Shanghai Mapada Instruments Co.,Ltd., China). X-ray diffraction patterns (XRD) were measured on a Bruker/D8 FOCUS X-ray diffractometer with Cu Kα radiation source (wavelength at 1.5406 Å). The samples were scanned from $3° < 2\theta < 60°$ at an increment of 2°/min. Liquid samples of toluene solutions deposited on amorphous carbon-coated copper grids were analyzed using a JEOL-JEM 2100F transmission electron microscopy (TEM)operating at an acceleration voltage of 200 kV. PL spectra were taken using a F-380 fluorescence spectrometer (Tianjin Gangdong Sci. & Tech. Development. Co., Ltd., China). Time-resolved PL was collected using fluorescence lifetime measurement system (C11367-11, Hamamatsu Photonics, Japan) with excitation wavelength of 405 nm. The absolute PLQYs of diluted QDs solutions were determined using a fluorescence spectrometer with integrated sphere (C9920-02, Hamamatsu Photonics, Japan) under blue light emitting diodes (LED) excited at a wavelength of 450 nm.

RESULTS AND DISCUSSION

Modified Emulsion Synthesis Process With Phase Transfer Strategy

Emulsion system, first proposed by Schulman and co-workers in 1959, consists of at least three components namely polar solvent, non-polar solvent and surfactant (Schulman et al., 1959). After developing for over 50 years, emulsion strategy has become one of the versatile preparation techniques for the synthesis of numerous organic and inorganic nanoparticles (Malik et al., 2012). The physical model of an emulsion is that the surfactant forms an interfacial layer between the polar and the non-polar solvents and let the polar solvent dispersed in non-polar solvent as small droplets at microscopic level. These micrometer-sized small droplets can act as small nanoreactors and control the

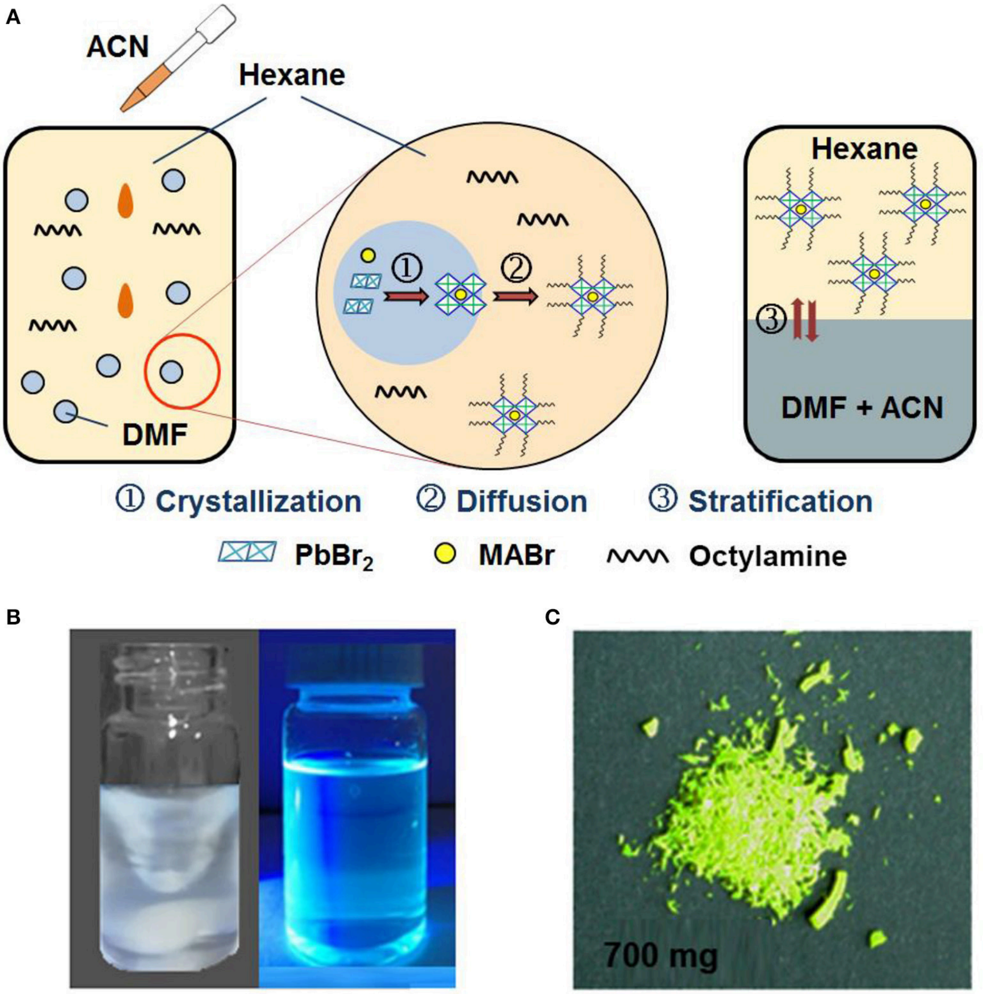

FIGURE 1 | (A) Schematically illustration of the modified emulsion synthesis process with phase transfer strategy. **(B)** Optical photographs of the established emulsion system after addition of ACN (left) and obtained $CH_3NH_3PbBr_3$ QDs dissolved in hexane under UV 365 nm radiation. **(C)** Optical photograph of resultant $CH_3NH_3PbBr_3$ QDs powder in one pot synthesis.

size, morphology, and surface area of nanoparticles (Lopez-Perez et al., 1997).

The fabrication of blue emitting $CH_3NH_3PbBr_3$ QDs was based on the modification of our reported emulsion synthesis (Huang et al., 2015a). In a typical emulsion synthesis process, DMF and hexane are selected as good and poor solvent for $CH_3NH_3PbBr_3$ precursors. Oleic acid and octylamine act as surfactants and *t*-butanol or acetone is used as demulsifier. Owing to the immiscibility between DMF and hexane, $CH_3NH_3PbBr_3$ precursors in DMF can be dispersed as microscopic droplets in hexane under vigorous stirring. The subsequent addition of demulsifier (acetone) provides the driving force for crystallization of $CH_3NH_3PbBr_3$ QDs. However, the chemical yields of $CH_3NH_3PbBr_3$ QDs through this emulsion system is lower than 10%. In fact, the conventional emulsion synthesis method also produces micrometer-sized and even larger $CH_3NH_3PbBr_3$ particles which occupy a large proportion of the overall products, as shown in **Figure S1**. This is because that the addition of acetone induces instant solvent mixing process, leading to a large degree of supersaturation for $CH_3NH_3PbBr_3$ precursors. From the viewpoints of classical nucleation and growth theory, the high supersaturation degree will bring fast nucleation and growth rates for $CH_3NH_3PbBr_3$ precursors, which lacks feasibility to control the crystallization process (Barlow et al., 2004; Leite and Ribeiro, 2011; Thanh et al., 2014; Zhang et al., 2017b). On the other hand, the residual

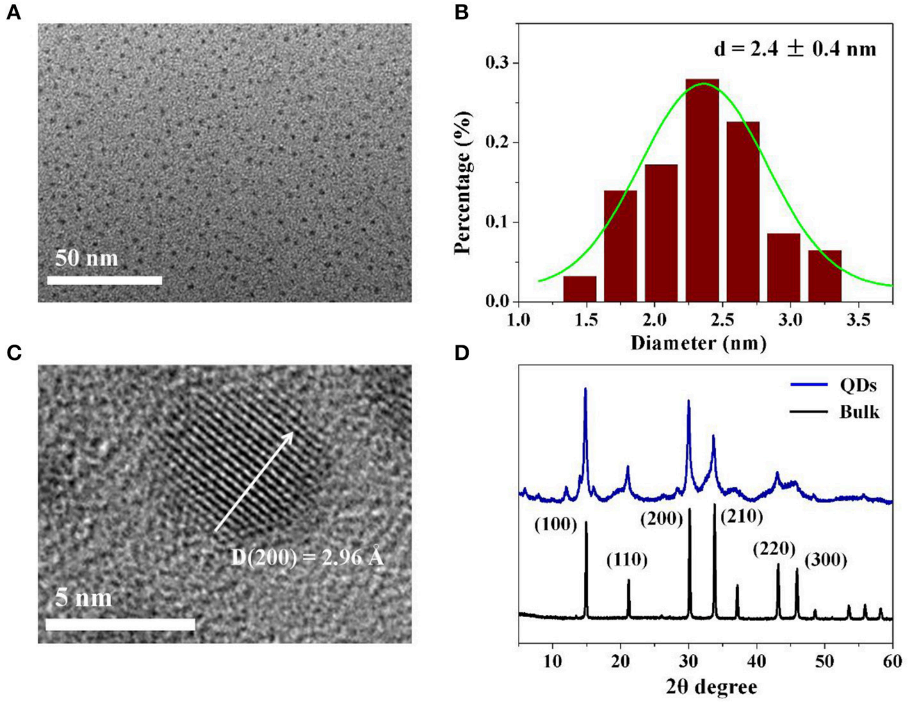

FIGURE 2 | (A) TEM image of as-synthesized colloidal $CH_3NH_3PbBr_3$ QDs. **(B)** Statistical analysis of **(A)**. **(C)** High resolution TEM image of single $CH_3NH_3PbBr_3$ QD. **(D)** XRD spectra of colloidal $CH_3NH_3PbBr_3$ QDs and the corresponding $CH_3NH_3PbBr_3$ bulk.

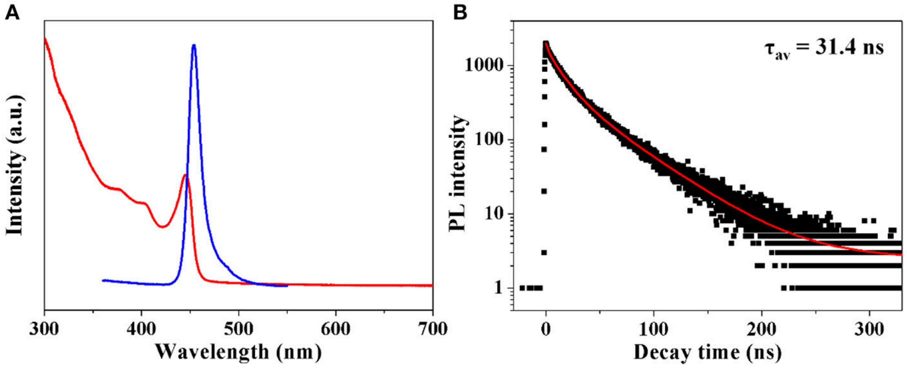

FIGURE 3 | (A) Absorption and PL spectra of as fabricated $CH_3NH_3PbBr_3$ QDs. **(B)** Time-resolved PL spectrum of $CH_3NH_3PbBr_3$ QDs.

solvents (DMF and acetone) after solvent mixing can degrade the as-formed $CH_3NH_3PbBr_3$ QDs, (Huang S. et al., 2016; Vybornyi et al., 2016; Chiba et al., 2017) resulting in even lower chemical yields.

It can be suggested that if the newly formed $CH_3NH_3PbBr_3$ QDs can be separated from their nucleation area and promptly transferred into another phase, the degradation of $CH_3NH_3PbBr_3$ QDs by contacting good solvent can be avoided. Here, we replaced the demulsifier acetone with ACN and modified the emulsion synthesis through a phase transfer strategy accordingly. **Figure 1** schematically illustrate the synthetic process of $CH_3NH_3PbBr_3$ QDs by emulsion synthesis with phase transfer strategy. Typically, ACN instead of acetone is added into the emulsion system to induce the demulsion process. As ACN is miscible with DMF but immiscible with hexane, the added ACN mixes with the DMF droplet and drives the nucleation and growth process of $CH_3NH_3PbBr_3$ QDs due to the limited solubility of $CH_3NH_3PbBr_3$ precursors in ACN. The formed $CH_3NH_3PbBr_3$ QDs spontaneously diffuses into hexane solvent phase. Such phase separation process greatly impede the further growth and aggregation of the QDs into large particles, which is the primary cause of the enhanced chemical yields. Finally, after removed from magnetic stirrer, the mixed solution can be stratified into two layers. As shown in the right most part of **Figure 1A**, the bottom layer is the mixture of DMF and ACN due to their relatively larger density, while the top layer is $CH_3NH_3PbBr_3$ QDs/hexane dispersion. Powdery $CH_3NH_3PbBr_3$ QDs can be easily obtained by adding ethyl acetate as precipitator without the further purification process as in the conventional emulsion synthesis (Protesescu et al., 2017). In a word, precise control for $CH_3NH_3PbBr_3$ QDs is achieved through this modified emulsion synthesis with phase transfer strategy and the chemical yield is calculated to be more than 70%, producing ~700 mg $CH_3NH_3PbBr_3$ QDs powder per batch in 10 mL (~0.02 mol/L) colloidal solution (the weight of the starting material in the solvent is about 1,000 mg). Moreover, this modified emulsion synthesis method can also be applied for the fabrication of other types of perovskite QDs. As shown in **Figure S2**, high quality $CH(NH_2)_2PbBr_3$ ($FAPbBr_3$) QDs were also fabricated, indicating the wide applicability of this method.

Structure and Optical Properties of As-prepared $CH_3NH_3PbBr_3$ QDs

The as fabricated $CH_3NH_3PbBr_3$ QDs were further characterized by applying TEM and XRD measurements. From the TEM image in **Figure 2A** and statistical analysis in **Figure 2B**, it is observed that the obtained $CH_3NH_3PbBr_3$ QDs have an average diameter of 2.4 nm with size deviation of ± 0.4 nm. The high resolution TEM image of a $CH_3NH_3PbBr_3$ QD in **Figure 2C** shows a interplanar distance of 2.96 Å, which is consistent with the (200) crystal face. In **Figure 2D**, $CH_3NH_3PbBr_3$ QDs show main diffraction peaks of 15.04, 21.29, 30.26, 33.92, 37.25, 43.30, and 45.98°, which can be well matched with corresponding bulk $CH_3NH_3PbBr_3$ in cubic phase (Pm3m) (Stoumpos et al., 2013). The XRD and TEM results demonstrate the formation of highly crystalline $CH_3NH_3PbBr_3$ QDs.

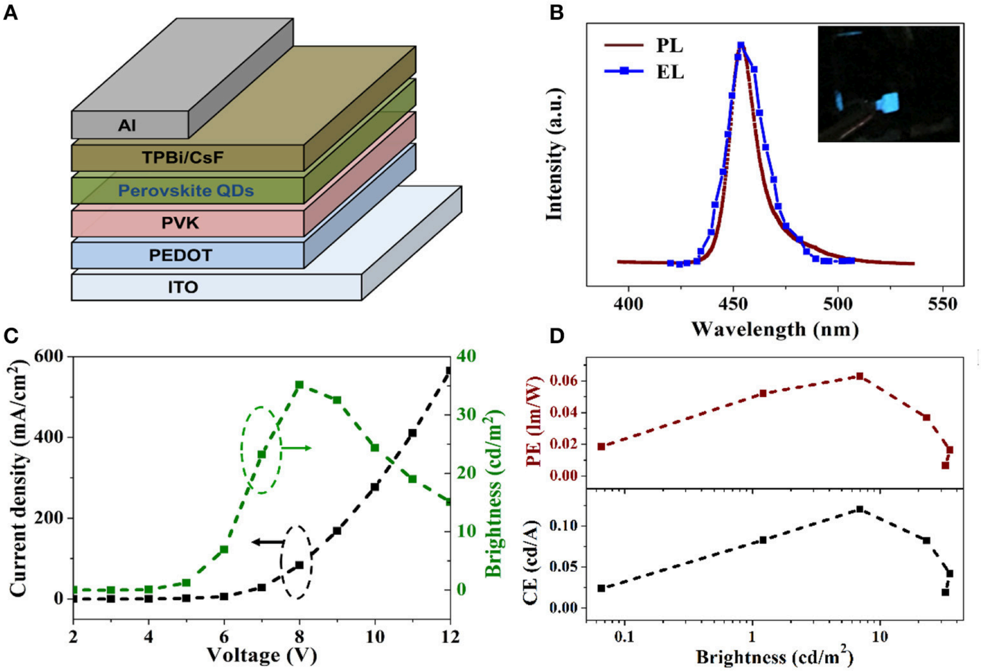

FIGURE 4 | (A) Schematically illustration of the device structure employed in the QD-LED. **(B)** Comparison of normalized EL (solid red line) and PL (dashed blue line) spectra of $CH_3NH_3PbBr_3$ QDs. The inset is an optical photograph of a lit QD-LED. **(C)** Current density (black) and brightness (green) vs. voltage. **(D)** Current, power efficiency, and EQE as a function of brightness of the QD-LED.

UV-vis absorption, steady state and time-resolved PL are employed to investigate the optical properties of the as fabricated $CH_3NH_3PbBr_3$ QDs. From **Figure 3A**, it is observed that colloidal $CH_3NH_3PbBr_3$ QDs show a typical excitonic peak at 440 nm. An emission peak of 454 nm with a FWHM of 14 nm can also be identified. The absolute PLQYs of these obtained $CH_3NH_3PbBr_3$ QDs were determined to be ∼15%, which were comparable to the reported lead free $(CH_3NH_3)_3Bi_2Br_9$ QDs (Leng et al., 2016). Moreover, the emission wavelength can be tuned by varying the amount of ligands. As shown in **Figure S3**, the emission peak decreased from 510 to 430 nm with the amount of ligands varied from 10 to 100 μL. The blue-shift of emission peaks can be well explained by the quantum size effect in $CH_3NH_3PbBr_3$ QDs (Di et al., 2015; Huang et al., 2015b; Malgras et al., 2016). It has been demonstrated that $CH_3NH_3PbBr_3$ QDs with size close to 2 nm will exhibit strong quantum confinement effect (Tanaka et al., 2003; Sichert et al., 2015). The average diameters of literature reported green emissive $CH_3NH_3PbBr_3$ QDs are mostly larger than 3 nm. As shown in **Figure S4**, the blue emitting $CH_3NH_3PbBr_3$ QDs have relatively smaller sizes. The confirmed average particle size of 2.4 nm locates in strong quantum confinement range, which contributes to the blue shifted emission. To further acquire information on carrier recombination dynamics, time-resolved PL was conducted. The decay curve in **Figure 3B** was fitted by using multi-exponential functions (Equation 1) and the average lifetime (τ_{av}) was determined by Equation 2.

$$I = \sum_i A_i \exp(-t/\tau_i) \quad i = 1, 2, 3 \ \ldots \tag{1}$$

$$\tau_{av} = \sum_i \frac{A_i \tau_i^2}{A_i \tau_i} \quad i = 1, 2, 3 \ \ldots \tag{2}$$

Halide perovskites have been known to show tunable features from exciton to free carries (D'Innocenzo et al., 2014a; Stranks et al., 2014). It has been demonstrated that the free carrier recombination often gives an average lifetime from hundreds to thousands of nanoseconds while the exciton recombination exhibits an average lifetime of tens of nanoseconds (D'Innocenzo et al., 2014a,b; Stranks et al., 2014). The detected average lifetime of 31.4 ns from the fitting result implies that the exciton recombination would occupy a large fraction in as fabricated $CH_3NH_3PbBr_3$ QDs, which is consistent with their relatively high PL QYs.

Performance of $CH_3NH_3PbBr_3$ QDs Based EL Devices

EL devices based on blue emitting $CH_3NH_3PbBr_3$ QDs were also fabricated by applying a simple sandwich structure of ITO/PEDOT/PVK/$CH_3NH_3PbBr_3$ QDs/TPBi/CsF/Al, as shown in **Figure 4A**. Poly(3,4-ethylenedioxythiophene):polystyrenesulfonate (PEDOT:PSS) was used to enhance the hole injection. 1,3,5-tris (2-*N*-phenylbenzimidazolyl) benzene (TPBi) was used as electron transporting layer (ETL) with CsF as cathode buff layer. $CH_3NH_3PbBr_3$ QDs dissolved in hexane was deposited on the top of PVK layer by spin-coating. **Figure 4B** shows the comparison between PL spectrum of $CH_3NH_3PbBr_3$ QDs in hexane and EL spectrum of resulting LED devices. Compared with the previously reported deep blue (<440 nm) or sky blue (> 480 nm) perovskite EL devices, the 454 nm EL peak of our device is located in the pure blue range and thus more suitable for display integration. It is also noted that the EL spectrum exhibits the same emission peak with the PL spectrum, indicating that the EL is totally originated from the exciton recombination in $CH_3NH_3PbBr_3$ QDs film during device operation. The FWHM of the EL spectrum is slightly broadened to 16 nm, which is a common phenomena in LED devices (Lee et al., 2014; Zhang et al., 2016). **Figure 4C** presents the voltage-dependent curves of current density and luminance for $CH_3NH_3PbBr_3$ QDs based LEDs. The turn on voltage is identified to be 4 V. The current densities varies from 0 to 37 mA/cm^2 with voltage increased from 2 to 12 V. The as fabricated blue emitting LEDs reached its maximum brightness of 32 cd/m^2 at 8 V. The brightness dependent current efficiency and power efficiency were plotted in **Figure 4D**. The maximum current efficiency and maximum power efficiency are calculated as 0.12 cd/A and 0.063 lm/W, respectively. Further work is underway to improve the efficiencies, brightness and stability of $CH_3NH_3PbBr_3$ QDs based LEDs.

CONCLUSIONS

In summary, $CH_3NH_3PbBr_3$ QDs with average size of 2.4 nm were successfully fabricated via a modification of conventional emulsion synthesis process. Through introduction of phase transfer strategy, the chemical yields of the final product was greatly improved to larger than 70%, which contributes to achieve gram scale synthesis in a 10 mL emulsion system (0.02 mol/L). The obtained $CH_3NH_3PbBr_3$ QDs exhibit strong blue emission peaked at 454 nm with a FWHM of 14 nm. Moreover, EL devices based on blue emitting $CH_3NH_3PbBr_3$ QDs were also fabricated with a maximum luminance of 32 cd/m^2, demonstrating their potential applications as alternative blue-emitting materials for display applications.

AUTHOR CONTRIBUTIONS

FZ, CX, and XZ designed the experiments. FZ, SC, JT, and YL analyzed the results. FZ, SC, QP, and HZ wrote and revised the manuscript. All authors have approved the final revised manuscript.

ACKNOWLEDGMENTS

This study was supported by National Natural Sciences Foundation of China (No. 21603012), the National Natural Science Foundation of China/Research Grants Council Joint Research Project (51761165021) and BIT funds.

SUPPLEMENTARY MATERIAL

The Supplementary Material for this article can be found online at: https://www.frontiersin.org/articles/10.3389/fchem.2018.00444/full#supplementary-material

REFERENCES

Bai, Z., and Zhong, H. Z. (2015). Halide perovskite quantum dots: potential candidates for display technology. *Sci. Bull.* 60, 1622–1624. doi: 10.1007/s11434-015-0884-y

Barlow, D. A., Baird, J. K., and Su, C. H. (2004). Theory of the von weimarn rules governing the average size of crystals precipitated from a supersaturated solution. *J. Crystal Growth* 264, 417–423. doi: 10.1016/j.jcrysgro.2003.12.047

Chiba, T., Hoshi, K., Pu, Y. J., Takeda, Y., Hayashi, Y., Ohisa, S., et al. (2017). High-efficiency perovskite quantum-dot light-emitting devices by effective washing process and interfacial energy level alignment. *ACS Appl. Mater. Interfaces* 9, 18054–18060. doi: 10.1021/acsami.7b03382

Di, D., Musselman, K. P., Li, G., Sadhanala, A., Ievskaya, Y., Song, Q., et al. (2015). Size-dependent photon emission from organometal halide perovskite nanocrystals embedded in an organic matrix. *J. Phys. Chem. Lett.* 6, 446–450. doi: 10.1021/jz502615e

D'Innocenzo, V., Grancini, G., Alcocer, M. J., Kandada, A. R. S., Stranks, S. D., Lee, M. M., et al. (2014a). Excitons versus free charges in organo-lead trihalide perovskites. *Nat. Commun.* 5:3586. doi: 10.1038/ncomms4586

D'Innocenzo, V., Srimath Kandada, A. R., De Bastiani, M., Gandini, M., and Petrozza, A. (2014b). Tuning the light emission properties by band gap engineering in hybrid lead halide perovskite. *J. Am. Chem. Soc.* 136, 17730–17733. doi: 10.1021/ja511198f

Ha, S. T., Su, R., Xing, J., Zhang, Q., and Xiong, Q. (2017). Metal halide perovskite nanomaterials: synthesis and applications. *Chem. Sci.* 8, 2522–2536. doi: 10.1039/C6SC04474C

Han, D., Imran, M., Zhang, M., Chang, S., Wu, X. G., Zhang, X., et al. (2018). Efficient light-emitting diodes based on *in situ* fabricated FAPbBr3 nanocrystals: the enhancing role of ligand-assisted reprecipitation process. *ACS Nano* 12, 8808–8816. doi: 10.1021/acsnano.8b05172

Huang, H., Polavarapu, L., Sichert, J. A., Susha, A. S., Urban, A. S., and Rogach, A. L. (2016). Colloidal lead halide perovskite nanocrystals: synthesis, optical properties and applications. *NPG Asia Mater.* 8:e328. doi: 10.1038/am.2016.167

Huang, H., Susha, A. S., Kershaw, S. V., Hung, T. F., and Rogach, A. L. (2015b). Control of emission color of high quantum yield $CH_3NH_3PbBr_3$ perovskite quantum dots by precipitation temperature. *Adv. Sci.* 2:201500194. doi: 10.1002/advs.201500194

Huang, H., Zhao, F., Liu, L., Zhang, F., Wu, X. G., Shi, L., et al. (2015a). Emulsion synthesis of size-tunable $CH_3NH_3PbBr_3$ quantum dots: an alternative route toward efficient light-emitting diodes. *ACS Appl. Mater. Interfaces* 7, 28128–28133. doi: 10.1021/acsami.5b10373

Huang, S., Li, Z., Kong, L., Zhu, N., Shan, A., and Li, L. (2016). Enhancing the stability of $CH_3NH_3PbBr_3$ quantum dots by embedding *in silica* spheres derived from tetramethyl orthosilicate in"Waterless" toluene. *J. Am. Chem. Soc.* 138, 5749–5752. doi: 10.1021/jacs.5b13101

Kim, Y. H., Cho, H., and Lee, T. W. (2016). Metal halide perovskite light emitters. *Proc. Natl. Acad. Sci. U.S.A.* 113, 11694–11702. doi: 10.1073/pnas.1607471113

Kumar, S., Jagielski, J., Yakunin, S., Rice, P., Chiu, Y. C., Wang, M., et al. (2016). Efficient blue electroluminescence using quantum-confined two-dimensional perovskites. *ACS Nano* 10, 9720–9729. doi: 10.1021/acsnano.6b05775

Lee, K. H., Lee, J. H., Kang, H. D., Park, B., Kwon, Y., Ko, H., et al. (2014). Over 40 cd/A efficient green quantum dot electroluminescent device comprising uniquely large-sized quantum dots. *ACS Nano* 8, 4893–4901. doi: 10.1021/nn500852g

Leite, E. R., and Ribeiro, C. (2011). *Crystallization and Growth of Colloidal Nanocrystals*. New York, NY: Springer Science & Business Media.

Leng, M., Chen, Z., Yang, Y., Li, Z., Zeng, K., Li, K., et al. (2016). Lead-free, blue emitting bismuth halide perovskite quantum dots. *Angew. Chem. Int. Ed.* 55, 15012–15016. doi: 10.1002/anie.201608160

Levchuk, I., Herre, P., Brandl, M., Osvet, A., Hock, R., Peukert, W., et al. (2017a). Ligand-assisted thickness tailoring of highly luminescent colloidal $CH_3NH_3PbX_3$ (X = Br and I) perovskite nanoplatelets. *Chem. Commun.* 53, 244–247. doi: 10.1039/C6CC09266G

Levchuk, I., Osvet, A., Tang, X., Brandl, M., Perea, J. D., Hoegl, F., et al. (2017b). Brightly luminescent and color-tunable formamidinium lead halide perovskite $FAPbX_3$ (X = Cl, Br, I) colloidal nanocrystals. *Nano Lett.* 17, 2765–2770. doi: 10.1021/acs.nanolett.6b04781

Li, Q., Li, H., Shen, H., Wang, F., Zhao, F., Li, F., et al. (2017). Solid ligand-assisted storage of air-stable formamidinium lead halide quantum dots via restraining the highly dynamic surface toward brightly luminescent light-emitting diodes. *ACS Photonics* 4, 2504–2512. doi: 10.1021/acsphotonics.7b00743

Lignos, I., Stavrakis, S., Nedelcu, G., Protesescu, L., deMello, A. J., and Kovalenko, M. V. (2016). Synthesis of cesium lead halide perovskite nanocrystals in a droplet-based microfluidic platform: fast parametric space mapping. *Nano Lett.* 16, 1869–1877. doi: 10.1021/acs.nanolett.5b04981

Lin, C. C., and Liu, R. S. (2011). Advances in phosphors for light-emitting diodes. *J. Phys. Chem. Lett.* 2, 1268–1277. doi: 10.1021/jz2002452

Lopez-Perez, J. A., Lopez-Quintela, M. A., Mira, J., Rivas, J., and Charles, S. W. (1997). Advances in the preparation of magnetic nanoparticles by the microemulsion method. *J. Phys. Chem. B* 101, 8045–8047. doi: 10.1021/jp972046t

Malgras, V., Tominaka, S., Ryan, J. W., Henzie, J., Takei, T., Ohara, K., et al. (2016). Observation of quantum confinement in monodisperse methylammonium lead halide perovskite nanocrystals embedded in mesoporous silica. *J. Am. Chem. Soc.* 138, 13874–13881. doi: 10.1021/jacs.6b05608

Malik, M. A., Wani, M. Y., and Hashim, M. A. (2012). Microemulsion method: a novel route to synthesize organic and inorganic nanomaterials. *Arabian J. Chem.* 5, 397–417. doi: 10.1016/j.arabjc.2010.09.027

Minh, D. N., Kim, J., Hyon, J., Sim, J. H., Sowlih, H. H., Seo, C., et al. (2017). Room-temperature synthesis of widely tunable formamidinium lead halide perovskite nanocrystals. *Chem. Mater.* 29, 5713–5719. doi: 10.1021/acs.chemmater.7b01705

Polavarapu, L., Nickel, B., Feldmann, J., and Urban, A. S. (2017). Advances in quantum-confined perovskite nanocrystals for optoelectronics. *Adv. Energy Mater.* 7:1700267. doi: 10.1002/aenm.201700267

Protesescu, L., Yakunin, S., Bodnarchuk, M. I., Krieg, F., Caputo, R., Hendon, C. H., et al. (2015). Nanocrystals of cesium lead halide perovskites ($CsPbX_3$, X = Cl, Br, and I): novel optoelectronic materials showing bright emission with wide color gamut. *Nano Lett.* 15, 3692–3696. doi: 10.1021/nl5048779

Protesescu, L., Yakunin, S., Kumar, S., Bär, J., Bertolotti, F., Masciocchi, N., et al. (2017). Dismantling the "Red Wall" of colloidal perovskites: highly luminescent formamidinium and formamidinium-cesium lead iodide nanocrystals. *ACS Nano* 11, 3119–3134. doi: 10.1021/acsnano.7b00116

Pust, P., Weiler, V., Hecht, C., Tücks, A., Wochnik, A. S., Henß, A. K., et al. (2014). Narrow-band red-emitting $Sr[LiAl_3N_4]:Eu^{2+}$ as a next-generation LED-phosphor material. *Nat. Mater.* 13, 891–896. doi: 10.1038/nmat4012

Schulman, J. H., Stoekenius, W., and Prince, L. M. (1959). Mechanism of formation and structure of microemulsions by electron microscopy. *J. Phys. Chem.* 63, 1677–1680. doi: 10.1021/j150580a027

Shirasaki, Y., Supran, G. J., Bawendi, M. G., and Bulović, V. (2013). Emergence of colloidal quantum-dot light-emitting technologies. *Nat. Photonics* 7, 13–23. doi: 10.1038/nphoton.2012.328

Sichert, J. A., Tong, Y., Mutz, N., Vollmer, M., Fischer, S., Milowska, K. Z., et al. (2015). Quantum size effect in organometal halide perovskite nanoplatelets. *Nano Lett.* 15, 6521–6527. doi: 10.1021/acs.nanolett.5b02985

Stoumpos, C. C., Malliakas, C. D., and Kanatzidis, M. G. (2013). Semiconducting tin and lead iodide perovskites with organic cations: phase transitions, high mobilities, and near-infrared photoluminescent properties. *Inorg. Chem.* 52, 9019–9038. doi: 10.1021/ic401215x

Stranks, S. D., Burlakov, V. M., Leijtens, T., Ball, J. M., Goriely, A., and Snaith, H. J. (2014). Recombination kinetics in organic-inorganic perovskites: excitons, free charge, and subgap states. *Phys. Rev. Appl.* 2:034007. doi: 10.1103/PhysRevApplied.2.034007

Stranks, S. D., and Snaith, H. J. (2015). Metal-halide perovskites for photovoltaic and light-emitting devices. *Nat. Nanotechnol.* 10, 391–402. doi: 10.1038/nnano.2015.90

Tanaka, K., Takahashi, T., Ban, T., Kondo, T., Uchida, K., and Miura, N. (2003). Comparative study on the excitons in lead-halide based perovskite-type crystals $CH_3NH_3PbBr_3$ $CH_3NH_3PbI_3$. *Solid State Commun.* 127, 619–623. doi: 10.1016/S0038-1098(03)00566-0

Thanh, N. T., Maclean, N., and Mahiddine, S. (2014). Mechanisms of nucleation and growth of nanoparticles in solution. *Chem. Rev.* 114, 7610–7630. doi: 10.1021/cr400544s

Vybornyi, O., Yakunin, S., and Kovalenko, M. V. (2016). Polar-solvent-free colloidal synthesis of highly luminescent alkylammonium lead halide perovskite nanocrystals. *Nanoscale* 8, 6278–6283. doi: 10.1039/C5NR06890H

Wang, A., Yan, X., Zhang, M., Sun, S., Yang, M., Shen, W., et al. (2016). Controlled synthesis of lead-free and stable perovskite derivative Cs_2SnI_6 nanocrystals via a facile hot-injection process. *Chem. Mater.* 28, 8132–8140. doi: 10.1021/acs.chemmater.6b01329

Wang, Q., Ren, J., Peng, X. F., Ji, X. X., and Yang, X. H. (2017). Efficient sky-blue perovskite light-emitting devices based on ethylammonium bromide induced layered perovskites. *ACS Appl. Mater. Interfaces* 9, 29901–29906. doi: 10.1021/acsami.7b07458

Wei, S., Yang, Y., Kang, X., Wang, L., Huang, L., and Pan, D. (2016). Room-temperature and gram-scale synthesis of $CsPbX_3$ (X = Cl, Br, I) perovskite nanocrystals with 50–85% photoluminescence quantum yields. *Chem. Commun.* 52, 7265–7268. doi: 10.1039/C6CC01500J

Xing, J., Yan, F., Zhao, Y., Chen, S., Yu, H., Zhang, Q., et al. (2016). High-efficiency light-emitting diodes of organometal halide perovskite amorphous nanoparticles. *ACS Nano* 10, 6623–6630. doi: 10.1021/acsnano.6b01540

Yang, X., Zhang, X., Deng, J., Chu, Z., Jiang, Q., Meng, J., et al. (2018). Efficient green light-emitting diodes based on quasi-two-dimensional composition and phase engineered perovskite with surface passivation. *Nat. Commun.* 9:570. doi: 10.1038/s41467-018-02978-7

Zhang, F., Chen, C., Kershaw, S. V., Xiao, C., Han, J., Zou, B., et al. (2017b). Ligand-controlled formation and photoluminescence properties of $CH_3NH_3PbBr_3$ nanocubes and nanowires. *Chem. Nano. Mat.* 3, 303–310. doi: 10.1002/cnma.201700034

Zhang, F., Huang, S., Wang, P., Chen, X., Zhao, S., Dong, Y., et al. (2017a). Colloidal synthesis of air-stable $CH_3NH_3PbI_3$ quantum dots by gaining chemical insight into the solvent effects. *Chem. Mater.* 29, 3793–3799. doi: 10.1021/acs.chemmater.7b01100

Zhang, F., Zhong, H., Chen, C., Wu, X. G., Hu, X., Huang, H., et al. (2015). Brightly luminescent and color-tunable colloidal $CH_3NH_3PbX_3$ (X= Br, I, Cl) quantum dots: potential alternatives for display technology. *ACS Nano* 9, 4533–4542. doi: 10.1021/acsnano.5b01154

Zhang, X., Lin, H., Huang, H., Reckmeier, C., Zhang, Y., Choy, W. C. H., et al. (2016). Enhancing the brightness of cesium lead halide perovskite nanocrystal based green light-emitting devices through the interface engineering with perfluorinated ionomer. *Nano Lett.* 16, 1415–1420. doi: 10.1021/acs.nanolett.5b04959

Conflict of Interest Statement: The authors declare that the research was conducted in the absence of any commercial or financial relationships that could be construed as a potential conflict of interest.

frontiers in Chemistry

ORIGINAL RESEARCH
published: 04 October 2018
doi: 10.3389/fchem.2018.00468

Controlled Synthesis of PtNi Hexapods for Enhanced Oxygen Reduction Reaction

*Xing Song, Shuiping Luo, Xiaokun Fan, Min Tang, Xixia Zhao, Wen Chen, Qi Yang and Zewei Quan**

Department of Chemistry, Southern University of Science and Technology (SUSTech), Shenzhen, China

Well-defined PtNi nanocrystals represent one of the most efficient electrocatalysts to boost the oxygen reduction reaction (ORR), especially in the shape of octahedrons, nanoframes, and nanowires. However, the synthesis of complex PtNi nanostructure is still a great challenge. Herein, we report a new class of PtNi hexapods with high activity and stability toward ORR. The hexapods are prepared by selective capping and simultaneous corrosion. By controlling the oxidative etching, PtNi polyhedrons and nanoparticles are obtained, respectively. The intriguing hexapods are composed of six nanopods with an average length of 12.5 nm. Due to their sharp tips and three-dimensional (3D) accessible surfaces, the PtNi hexapods show a high mass activity of 0.85 A mg_{Pt}^{-1} at 0.9 V vs. RHE, which are 5.4-fold higher than commercial Pt/C, also outperforming PtNi polyhedrons and PtNi nanoparticles. In addition, the mass activity of PtNi hexapods maintains 92.3% even after 10,000 potential cycles.

Keywords: hexapod, platinum-nickel alloy, nanocrystal, oxidative etching, oxygen reduction reaction

OPEN ACCESS

Edited by:
Jing Zhao,
University of Connecticut,
United States

Reviewed by:
Ben Liu,
Nanjing Normal University, China
Shutang Chen,
Honda Research Institute USA
Mountain View, United States

****Correspondence:***
Zewei Quan
quanzw@sustc.edu.cn

Specialty section:
This article was submitted to
Nanoscience,
a section of the journal
Frontiers in Chemistry

Received: *24 August 2018*
Accepted: *18 September 2018*
Published: *04 October 2018*

Citation:
Song X, Luo S, Fan X, Tang M,
Zhao X, Chen W, Yang Q and Quan Z
(2018) Controlled Synthesis of PtNi
Hexapods for Enhanced Oxygen
Reduction Reaction.
Front. Chem. 6:468.
doi: 10.3389/fchem.2018.00468

INTRODUCTION

Proton exchange membrane fuel cells (PEMFCs) represent as one of the most promising clean energy technologies for electric vehicles, but the high cost of components and the sluggish kinetics of oxygen reduction reaction (ORR) hinder its broad deployment, especially when the expensive and scarce Platinum (Pt) is used as catalyst (Gasteiger et al., 2005). Thus, intensive efforts have been focused on improving the activity, stability and utilization of Pt catalyst (Huang et al., 2015; Zhang et al., 2015a; Wang et al., 2018). Specially, controlling the composition and morphology of Pt-based nanocrystals is demonstrated to be one of the most efficient strategies (Stamenkovic et al., 2006; Yin et al., 2012; Porter et al., 2013; Li and Sun, 2016). Marković and co-workers have reported that the bulk alloy of Pt_3Ni composition with Pt (111)-skin exhibits greatly enhanced ORR activity compared with Pt. Pt_xNi alloy nanocrystals have been widely developed and which show the best catalytic performance toward ORR, outperforming the commercial Pt/C and other Pt-based catalysts with different component (Stamenkovic et al., 2007a,b; Choi et al., 2013). Therefore, engineering PtNi nanocrystals with well-defined shape, phase and composition is the subject of intensive interest to exploit their possible properties and applications (Cao et al., 2017; Zhang et al., 2018).

Apart from its composition, it is well known that the catalytic properties of Pt-based nanocrystals are closely related to their morphology, which determines the utilization efficiency and atomic arrangement of the active Pt atoms (Lim et al., 2009; Wu et al., 2012b; Quan et al., 2013; Li et al., 2014). Therefore, many research groups have synthesized Pt-based nanocrystals with various shapes, including polyhedrons (Chen et al., 2009), nanowires (Li et al., 2016; Jiang et al., 2017), nanodendrites (Huang et al., 2013), nanoplates (Bu et al., 2016), nanoframes (Chen et al., 2014; Luo et al., 2017) and so on. In particular, nanodendrites with porous structure or multi-branches possess high utilization of Pt atoms and high catalytic performance, benefiting from their three-dimensional (3D) accessible active sites and the tip-effect (Huang et al., 2013; Khan et al., 2016). Notably, multi-pod structure (tripod, tetrapod, pentapod, hexapod, octopod, etc.) with specific branches combines the advantages of nanodendrites and nanowires, possessing larger accessible surface areas (Teng and Yang, 2005; Zhang et al., 2010a; Lim and Xia, 2011). However, the controlled synthesis of well-defined PtNi multi-pod nanocrystals is still a great challenge.

Herein, we report the facile synthesis of well-defined PtNi hexapods through selective capping and oxidative etching. The as-prepared PtNi hexapods possess six pods with a length of 12.5 nm and 3D accessible surfaces. For comparison, PtNi polyhedrons and near-spherical nanoparticles are synthesized by controlling the oxidative etching. Electrochemical characterizations show that the PtNi hexapods exhibit enhanced catalytic activity toward ORR, compared with the PtNi polyhedrons, PtNi nanoparticles and commercial Pt/C. In addition, the PtNi hexapods show impressive stability, with negligible loss of activity after 10,000 cycles.

MATERIALS AND METHODS

Chemicals

Platinum(II) acetylacetonate [Pt(acac)$_2$, 98%] and nickel(II) acetylacetonate [Ni(acac)$_2$, 98%] were purchased from Energy Chemical. Oleylamine (OAm, 70%) was purchased from Sigma-Aldrich. Hexacarbonyl tungsten [W(CO)$_6$, 97%] was purchased from Alfa Aesar. Ammonium bromide (NH$_4$Br) was purchased from Aladdin. Solvents such as hexane, ethanol, methanol, and n-butylamine were analytical grade and used as received without further purification. The water used in all experiments was deionized (18.2 MΩ).

Synthesis of PtNi Hexapods

In a typical synthesis of PtNi hexapod nanocrystals, 0.05 mmol Pt(acac)$_2$, 0.04 mmol Ni(acac)$_2$ and 0.34 mmol NH$_4$Br were dissolved in 8.0 mL OAm. The mixture was loaded into a three-neck flask equipped with a condenser and a thermometer under argon flow. When heated to 130°C under Ar atmosphere with gentle magnetic stirring, 0.14 mmol W(CO)$_6$ powder was quickly added into the homogeneous solution. Afterwards, the reaction temperature was increased to 240°C at a rate of ∼10°C/min and kept for 45 min. After the solution was cooled down to room temperature, the final products were precipitated by centrifugation, washed twice with ethanol and hexane, and further dispersed in hexane.

Synthesis of PtNi Polyhedrons

In a typical synthesis of PtNi polyhedrons, 0.05 mmol Pt(acac)$_2$, 0.04 mmol Ni(acac)$_2$, 0.34 mmol NH$_4$Br, and 0.14 mmol W(CO)$_6$ powder were dissolved in 8.0 mL OAm. After being degassed under vacuum, the mixture was heated to 240°C and kept for 45 min under argon flow. The final products were precipitated by centrifugation, washed twice with ethanol and hexane, and further dispersed in hexane.

Synthesis of PtNi Nanoparticles

The procedure was exactly the same as that for PtNi hexapods, except exposing the reaction system to air after adding 0.14 mmol W(CO)$_6$ powder.

Characterizations

X-ray diffraction (XRD) patterns were recorded on an X-ray diffractometer (Rigaku SmartLab) with Cu Kα radiation (λ = 0.15418 nm) at a voltage of 45 kV and a current of 200 mA. Transmission electron microscope (TEM) images were obtained by using FEI Tecnai F30 electron microscope (300 kV). High-angle annular dark-field scanning TEM (HAADF-STEM) and energy-dispersive X-ray (EDX) elemental mapping were obtained by using FEI Talos TEM. TEM samples were prepared by placing a drop of the nanoparticle colloidal solution onto a carbon-coated Cu grid under ambient conditions. The metal compositions and loading of catalysts were measured by inductively coupled plasma mass spectrometry (ICP-MS, Agilent 7700x).

Electrochemical Study

As for the electrochemical tests, the Pt loading of the PtNi nanocrystals loaded on carbon powders was controlled in the range of ∼15%. The actual loadings of Pt were determined by ICP-MS. In a standard preparation, the PtNi nanocrystals were dispersed in 10 mL of hexane and Vulcant-72 carbon was dispersed in 15 mL of ethanol, then they were mixed and ultrasonicated for 30 min. Then, the carbon supported PtNi nanocrystals were collected by centrifugation and redispersed in 20 mL of n-butylamine. The mixtures were ultrasonicated for 30 min and then stirred at room temperature for 12 h. The products were collected by centrifugation and then washed with 20 mL methanol two times. The prepared catalysts were dried in vacuum at 80°C for 12 h. Finally, the pulverized samples were placed in a furnace preheated at 200°C and then heated for 1 h in air. The final catalyst suspension was prepared by mixing 4.0 mg of catalysts in 2.0 mL solution containing 1.8 mL ethanol and 0.2 mL 0.5 wt.% Nafion solution followed by ultrasonication for 30 min. Five Microliter catalyst suspension was dropped onto the clean Glassy carbon (GC) surface by using a micropipette and dried to form a uniform thin film at room temperature.

The electrochemical measurements were conducted in a three-electrode electrochemical cell with a Pine rotational disk electrode system connected with a biopotentiostat (AFCBP1E, Pine Instrument Co., USA) at 25°C. GC electrode (5 mm in diameter) covered with catalysts was served as a working electrode. A reversible hydrogen electrode (RHE) was used as a reference electrode and a Pt wire was used as a counter electrode. Cyclic voltamogram (CV) curves of catalysts in Ar-saturated 0.1 M HClO$_4$ solution recorded at a scan rate of 50 mV

s^{-1}. The electrochemical surface areas (ECSAs) were measured by integrating the electric charges of hydrogen desorption region from 0.05 to 0.4 V on the CV curves carried out in Ar-saturated 0.1 M $HClO_4$ solution. ORR measurements were conducted in O_2-saturated 0.1 M $HClO_4$ solution. The ORR polarization curves were collected at 1600 rpm with scan rate of 10 mV s^{-1}. The durability tests were performed at 25°C in O_2-saturated 0.1 M $HClO_4$ solution by applying cyclic potential sweeps between 0.6 and 1.1 V vs. RHE at a scan rate of 100 mV s^{-1} for 10,000 cycles.

RESULTS AND DISCUSSION

Figures 1a,b show the TEM image and HAADF-STEM image of the as-obtained nanocrystals. The TEM image indicates that the well-dispersed nanocrystals are multi-branched nanostructure in high yield. The pod-like features in the nanocrystals can be clearly observed by TEM and STEM. **Figure 1c** shows the TEM images of typical PtNi nanostructures at different projections, including tripod, tetrapod, pentapod and hexapod, corresponding to the hexapod nanostructures oriented at different angles. To confirm the hexapod morphology in more details, we acquired a set of tilted TEM images at different α direction and illustrated their structure models. The TEM images of a typical hexapod tilted from 0° to 40° and their corresponding tilted 3D hexapod models shown in **Figure S1**. In particular, the projection of nanocrystal transforms from pentapod to hexapod through rotating a certain angle, which proves the hexapod structure of PtNi nanocrystals.

The high-resolution TEM (HRTEM) image of an individual PtNi hexapod oriented along the [001] zone axes (tetrapod) and its corresponding fast Fourier transform (FFT) pattern are shown in **Figure S2**, indicating the nanocrystals are highly crystallized. The lattice spacing (0.193 nm) in the pod region can be clearly observed, which demonstrates that the pod grows

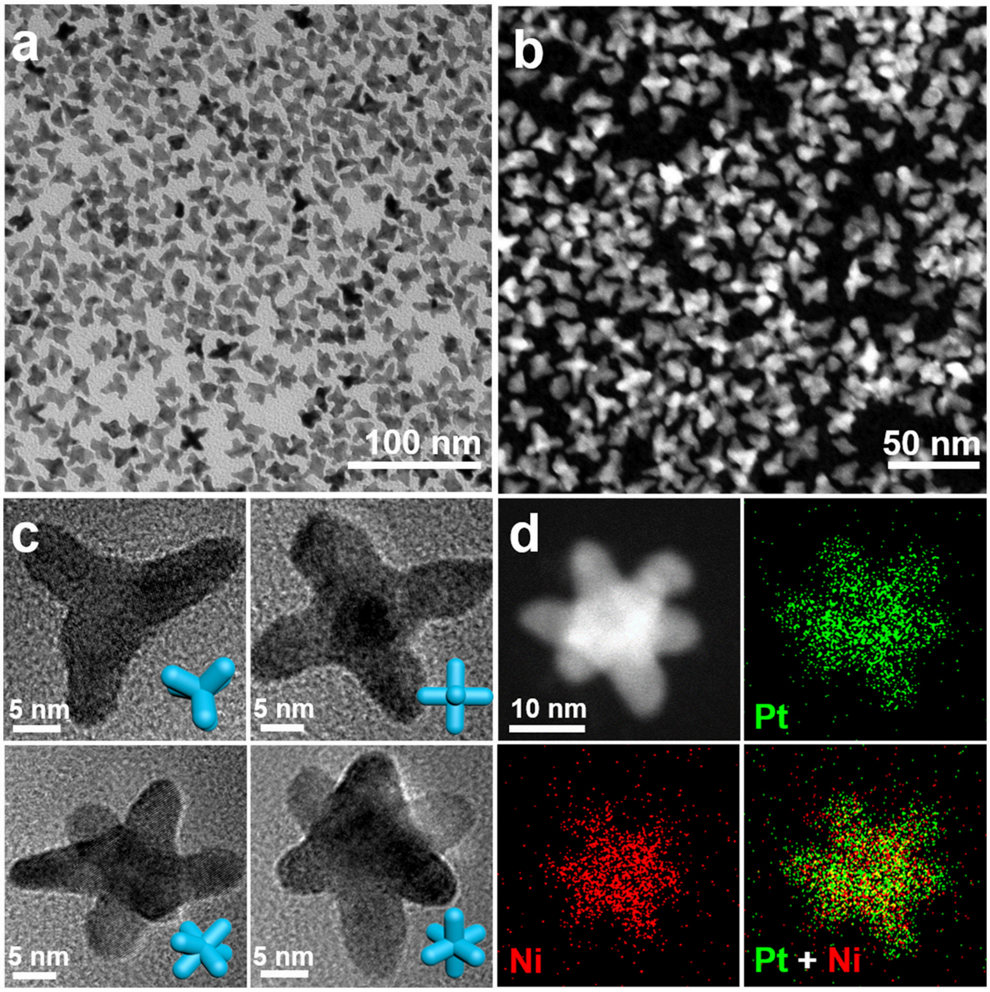

FIGURE 1 | (a) Low-magnification TEM image and **(b)** HAADF-STEM image of PtNi hexapods. **(c)** The representative TEM images of nanocrystal obtained at different projection directions. **(d)** HAADF-STEM image and elemental mapping images of an individual PtNi hexapod. The insets of **(c)** show the corresponding 3D structure models of the nanocrystals.

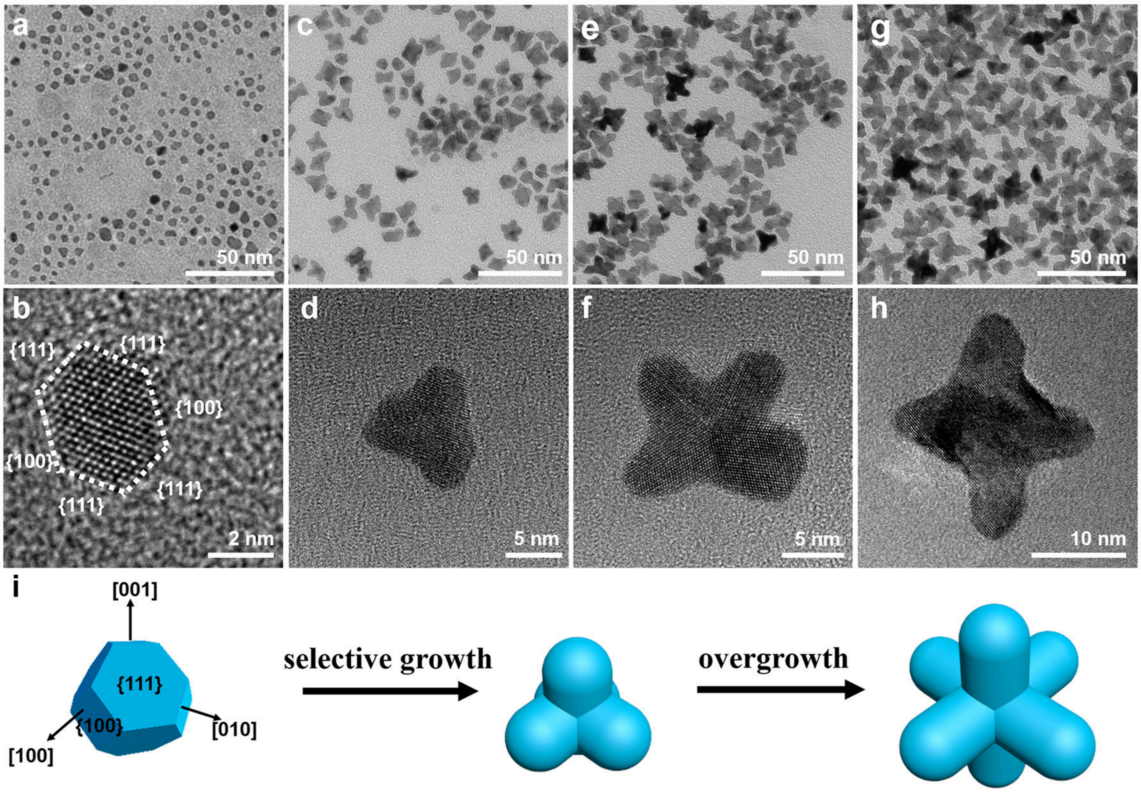

FIGURE 2 | Representative TEM and HRTEM images of PtNi nanocrystals obtained at different reaction stages: **(a,b)** 140°C, **(c,d)** 150°C, **(e,f)** 160°C, **(g,h)** 200°C. **(i)** Schematic of growth mechanism illustrating the morphological evolution of the PtNi hexapods.

along the <100> directions. As shown in the XRD pattern of hexapod nanocrystals (**Figure S3**), the typical diffraction peaks locate between monometallic face-centered-cubic (*fcc*) Pt and Ni, demonstrating that the PtNi hexapods with a pure alloy phase are obtained. **Figure 1d** shows the STEM image and EDX elemental mapping images of an individual hexapod nanocrystal. The result indicates that Pt and Ni atoms are homogeneously distributed in this nanostructure. The overall Pt/Ni atomic ratio is determined to be 2.2/1.0 by the ICP-MS.

To understand the growth mechanism of PtNi hexapods, the intermediate products obtained at different reaction stages were characterized by TEM (**Figure 2**). During the heat-up synthesis, the solution turned brown at 140°C, and the products were separated immediately. As shown in the TEM image (**Figure 2a**), small nanoparticles with a diameter of 5.0 nm were formed at this stage. It is clearly observed in the HRTEM image (**Figure 2b**) that the nanoparticle possesses the shape of truncated octahedron, which is surrounded by {100} and {111} facets. As known, due to the low surface energy, polyhedron consisting of mixed {100} and {111} facets is a typical thermodynamically stable shape at the nucleation stage (Wu et al., 2012a; Gan et al., 2014). When the temperature was further raised to 150°C (**Figures 2c,d**), the pods with a length of ~5.0 nm can be observed, which is much shorter than that for the final product. The six pods are formed by the selective growth along the <100> directions on truncated octahedral seeds (Gan et al., 2014). At 160°C, most nanoparticles transform into multi-branched nanostructure through rapid growth along the <100> directions, and the length of pods increases to ~8.0 nm, as shown in **Figures 2e,f**. By further increasing the temperature to 200°C, the length of pods reached to ~12.0 nm, indicating the continuous growth of hexapod with increasing temperature (**Figures 2g,h**). It is clear to illustrate the growth trajectory of PtNi hexapods as schematically represented in **Figure 2i**. Based on above observations, the growth of PtNi hexapod nanocrystals follows the classic nucleation-growth mechanism, including the formation of stable polyhedral seeds and the selective growth along the <100> directions.

During this synthesis, NH_4Br and $W(CO)_6$ play key roles in the formation of PtNi hexapods. It has been reported that Br ions (Br^-) can selectively adsorb on {100} surfaces (Li et al., 2015; Luo and Shen, 2017), and carbon monoxide (CO) produced by the decomposition of $W(CO)_6$ can selectively adsorb on the {111} facets of PtNi nanocrystals (Zhang et al., 2010b). Thus, the truncated octahedron consisting of mixed {100} and {111} facets are expected to produce. In addition, the Br^-/O_2 pairs are the most common reagent for etching transition metals, such as Ni (Wiley et al., 2004; Chen et al., 2012). The Br^- capped on the {100} facets in presence of O_2 would cause the etching of {100} facets and exposing of specific active sites. As a result, the unstable Ni atoms can be partially dissolved by the Br^-/O_2 pairs, leading to the activated {100} facets. Then, the newly formed atoms prefer to deposit on these sites, and keep growing along the <100> directions (Wang et al., 2016; Tang et al., 2018). At the same time, the adsorption of CO on the {111} facets is stronger than the adsorption of Br^- on the {100} facets, hindering the growth along <111> directions (Huang et al., 2010). Thus, we propose that the formation of PtNi hexapod nanocrystals is ascribed to the selective capping and oxidative etching (Luo and Shen, 2017).

To confirm above selective capping and oxidative etching formation mechanism of PtNi hexapods, we designed a set of control experiments. As shown in **Figure S4**, PtNi nanocrystals can be produced in the absence of $W(CO)_6$, but their morphology is irregular with larger size. Such result indicates that the presence of $W(CO)_6$ is essential for the size and shape control of the PtNi hexapod nanocrystals. In the absence of NH_4Br, the PtNi polyhedral nanocrystals are obtained (**Figure 3a**), indicating that the NH_4Br is indispensable to form the pod-like nanostructure.

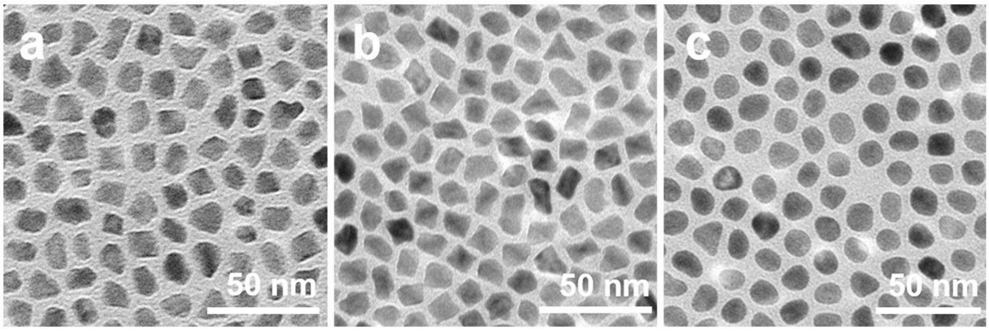

FIGURE 3 | TEM images of PtNi nanocrystals obtained by using the standard procedures **(a)** in the absence of NH_4Br, **(b)** in the absence of O_2, and **(c)** with the system exposed to air.

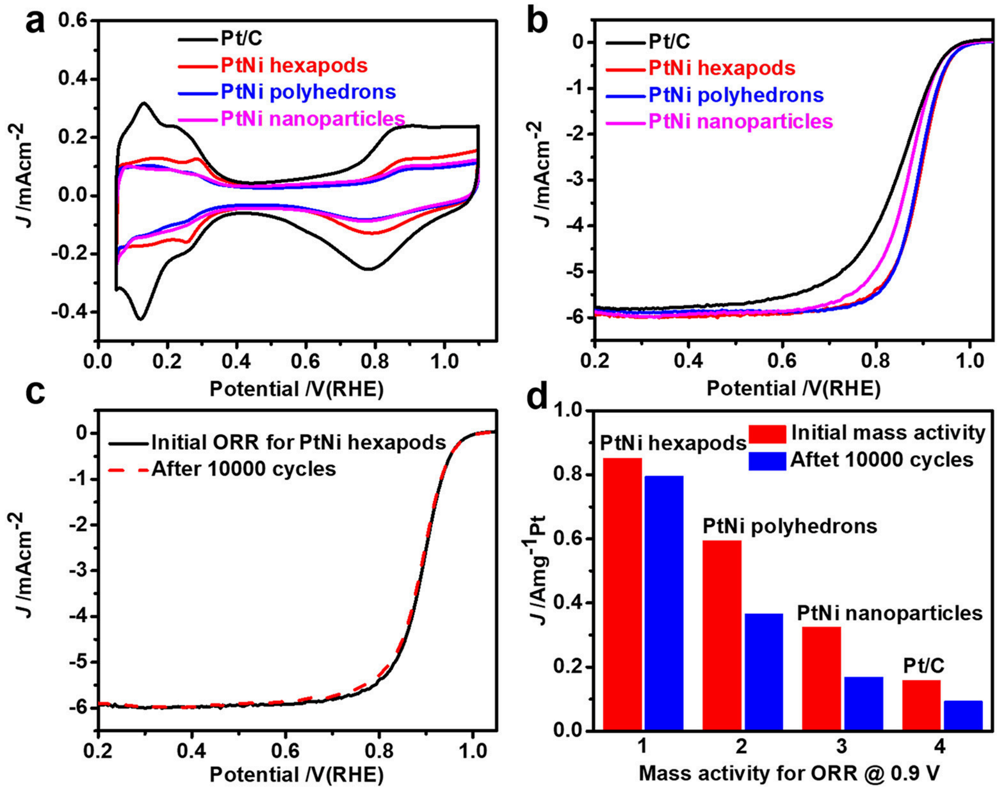

FIGURE 4 | (a) CV curves of PtNi hexapods, polyhedrons, nanoparticles and commercial JM Pt/C catalyst recorded at a scan rate of 50 mV s^{-1} in Ar-saturated 0.1 M $HClO_4$ solution; **(b)** ORR polarization curve of these catalysts at a scan rate of 10 mV s^{-1} in O_2-saturated 0.1 M $HClO_4$ solution; **(c)** ORR polarization curve of PtNi hexapods before and after 10,000 potential cycles; **(d)** Mass activity of different catalysts before and after 10,000 potential cycles.

Without NH_4Br, the capping and etching effects of Br^- are eliminated, therefore, the morphology of polyhedron is regulated by the $W(CO)_6$. On the other hand, during the synthesis of PtNi hexapod nanocrystals, O_2 could be introduced into the solution along with the addition of $W(CO)_6$. As a comparison, we completely removed O_2 in the system by degassing the sealed three-necked flask for 30 min at room temperature. As shown in **Figure 3b**, PtNi polyhedron nanocrystals are obtained. The oxidative etching effect on the nanocrystals disappears when O_2 is absent. This result indicates that the oxidative etching is necessary to the formation of hexapod nanocrystals by inducing the selective growth along <100> directions. In addition, when the system is exposed to air (**Figure 3c**), PtNi nanoparticles with near-spherical shapes without sharp tips and extended surfaces are obtained, due to the stronger oxidative etching ability of Br^-/O_2 in the presence of excessive O_2. Thus, the successful formation of PtNi hexapods is attributed to the selective capping and moderate oxidative etching.

ELECTROCHEMICAL PROPERTIES

The electrochemical properties of the as-prepared PtNi hexapods, PtNi polyhedrons, PtNi nanoparticles and commercial Pt/C from the Johnson Matthey (20% Pt, JM) were investigated and compared under the same conditions. Before the electrochemical measurements, the products were treated with n-butylamine to exchange shorter ligands around the nanocrystals (Cargnello et al., 2015) and heated in air at 200°C for 1 h. Finally, the carbon supported products were dissolved in the mixed nafion and ethanol solution by ultrasonication. **Figure 4a** shows CV curves of the PtNi hexapods, PtNi polyhedrons, PtNi nanoparticles and commercial Pt/C in Ar-saturated 0.1 M $HClO_4$ solution at a scan rate of 50 mV s^{-1}. The electrochemical surface areas (ECSAs), measured by integrating the electric charges of hydrogen desorption region from 0.05 to 0.4 V, are 47.2 m^2 g^{-1} for PtNi hexapods, 23.9 m^2 g^{-1} for PtNi polyhedrons and 21.4 m^2 g^{-1} for PtNi nanoparticles, respectively. Although the size of PtNi hexapods is far larger than the commercial Pt/C, the ECSA is approximate to it (48.4 m^2 g^{-1}), which is due to the presence of sharp tips in these PtNi hexapods.

The ORR polarization curves of different electrocatalysts (**Figure 4b**) were performed at a scan rate of 10 mV s^{-1} in O_2-saturated 0.1 M $HClO_4$ solution via rotating disk electrode approach. The half-wave potential of PtNi hexapods is positively shifted by 49 mV than that of commercial Pt/C. Additionally, the PtNi hexapods exhibit the greatest mass activity of 0.85 A mg_{Pt}^{-1} at 0.9 V vs. RHE, which is 5.4 times higher than that of commercial Pt/C (0.16 A mg_{Pt}^{-1}), which is attributed to the synergistic effect of Pt-Ni alloy (Zhang et al., 2015b) and 3D accessible surfaces. Furthermore, the mass activity of PtNi hexapods is 1.4 and 2.6 times higher than PtNi polyhedrons (0.59 A mg_{Pt}^{-1}) and PtNi nanoparticles (0.32 A mg_{Pt}^{-1}), respectively.

The electrochemical durability tests of these three PtNi catalysts and commercial Pt/C were recorded by sweeping from 0.6 to 1.1 V vs. RHE for 10,000 cycles at a scan rate of 100 mV s^{-1}. As shown in **Figure 4c**, the half-wave potential of PtNi hexapods is negligibly degraded. **Figure 4d** indicates that the mass activity for PtNi hexapods after durability tests remains 92.3% of its initial value. However, under the same conditions, the mass activity of PtNi polyhedrons, PtNi nanoparticles and commercial Pt/C only remain 61.5, 52.0, and 58.9%, respectively, and exhibit a large negative shifting compared with the initial ORR polarization curves (**Figure 4d**, **Figure S5**). The TEM images reveal the structures of catalysts before and after the durability tests (**Figure S6**), which indicates that PtNi hexapods have negligible change on the morphology. After detailed EDX analysis (**Figure S7**), the average molar ratio of Pt/Ni before and after durability test are determined to be 2.12/1.0 and 2.26/1.0, respectively. The results demonstrate that the molar ratios of Pt and Ni are well maintained after 10,000 cycles, further confirming the stability of PtNi hexapods. However, under the same conditions, the PtNi polyhedrons and PtNi nanoparticles exhibit obvious changes on the morphology, while the Pt/C catalysts are changed to larger particles and seriously aggregated after 10,000 cycles. The results indicate that these PtNi hexapods have an impressive electrochemistry stability compared with the commercial Pt/C.

CONCLUSION

In summary, we have successfully synthesized the well-defined PtNi hexapod nanocrystals with 3D accessible surfaces. The formation of truncated octahedron seeds, selective growth and moderate oxidative etching synergistically govern the synthesis of PtNi hexapods. Notably, the PtNi hexapods exhibit much enhanced electrocatalytic activity for ORR. In addition, the PtNi hexapods retain high activity and stability after 10,000 cycles. Our work provides a facile route to engineer multi-pod nanostructure with high catalytic performance, which advances the understanding of the relationship between nanoparticle geometry and catalytic performance.

AUTHOR CONTRIBUTIONS

ZQ conceived the project. XS carried out the experiments and collected the data. SL performed the electrochemical tests. XF, MT, XZ, WC, and QY made contribution to the analysis and discussion of the results. XS drafted the manuscript, and all authors contributed to the final version of the manuscript.

FUNDING

This work was supported by the National Natural Science Foundation of China (NSFC) (No. 51772142), Shenzhen Science and Technology Innovation Committee including fundamental research projects (Nos. JCYJ20170412152528921, JCYJ20160530190842589), Shenzhen Peacock Plan (KQTD2016053019134356) and peacock technology innovation project (KQJSCX20170328155428476), Development and Reform

Commission of Shenzhen Municipality (Novel Nanomaterial Discipline Construction Plan), and Special Funds for the Cultivation of Guangdong College Students' Scientific and Technological Innovation ("Climbing Program" Special Funds).

SUPPLEMENTARY MATERIAL

The Supplementary Material for this article can be found online at: https://www.frontiersin.org/articles/10.3389/fchem.2018.00468/full#supplementary-material

REFERENCES

Bu, L., Zhang, N., Guo, S., Zhang, X., Li, J., Yao, J., et al. (2016). Biaxially strained PtPb/Pt core/shell nanoplate boosts oxygen reduction catalysis. *Science* 354, 1410–1414. doi: 10.1126/science.aah6133

Cao, Z., Chen, Q., Zhang, J., Li, H., Jiang, Y., Shen, S., et al. (2017). Platinum-nickel alloy excavated nano-multipods with hexagonal close-packed structure and superior activity towards hydrogen evolution reaction. *Nat. Commun.* 8, 15131–15137. doi: 10.1038/ncomms15131

Cargnello, M., Chen, C., Diroll, B. T., Doan-Nguyen, V. V. T., Gorte, R. J., and Murray, C. B. (2015). Efficient removal of organic ligands from supported nanocrystals by fast thermal annealing enables catalytic studies on well-defined active phases. *J. Am. Chem. Soc.* 137, 6906–6911. doi: 10.1021/jacs.5b03333

Chen, C., Kang, Y., Huo, Z., Zhu, Z., Huang, W., Xin, H. L., et al. (2014). Highly crystalline multimetallic nanoframes with three-dimensional electrocatalytic surfaces. *Science* 343, 1339–1343. doi: 10.1126/science.1249061

Chen, J., Lim, B., Lee, E. P., and Xia, Y. (2009). Shape-controlled synthesis of platinum nanocrystals for catalytic and electrocatalytic applications. *Nano Today* 4, 81–95. doi: 10.1016/j.nantod.2008.09.002

Chen, M., Wu, B., Yang, J., and Zheng, N. (2012). Small adsorbate-assisted shape control of Pd and Pt nanocrystals. *Adv. Mater.* 24, 862–879. doi: 10.1002/adma.201104145

Choi, S. I., Xie, S., Shao, M., Odell, J. H., Lu, N., Peng, H. -C., et al. (2013). Synthesis and characterization of 9 nm Pt-Ni Octahedra with a record high activity of 3.3 A/mg$_{Pt}$ for the oxygen reduction reaction. *Nano Lett.* 13, 3420–3425. doi: 10.1021/nl401881z

Gan, L., Cui, C., Heggen, M., Dionigi, F., Rudi, S., and Strasser, P. (2014). Element-specific anisotropic growth of shaped platinum alloy nanocrystals. *Science* 346, 1502–1506. doi: 10.1126/science.1261212

Gasteiger, H. A., Kocha, S. S., Sompalli, B., and Wagner, F. T. (2005). Activity benchmarks and requirements for Pt, Pt-alloy, and non-Pt oxygen reduction catalysts for PEMFCs. *Appl. Catal. B* 56, 9–35. doi: 10.1016/j.apcatb.2004.06.021

Huang, X., Tang, S., Mu, X., Dai, Y., Chen, G., Zhou, Z., et al. (2010). Freestanding palladium nanosheets with plasmonic and catalytic properties. *Nat. Nanotechnol.* 6, 28–32. doi: 10.1038/nnano.2010.235

Huang, X., Zhao, Z., Cao, L., Chen, Y., Zhu, E., Lin, Z., et al. (2015). High-performance transition metal-doped Pt3Ni octahedra for oxygen reduction reaction. *Science* 348, 1230–1234. doi: 10.1126/science.aaa8765

Huang, X., Zhu, E., Chen, Y., Li, Y., Chiu, C.-Y., Xu, Y., et al. (2013). A facile strategy to Pt_3Ni nanocrystals with highly porous features as an enhanced oxygen reduction reaction catalyst. *Adv. Mater.* 25, 2974–2979. doi: 10.1002/adma.201205315

Jiang, K., Zhao, D., Guo, S., Zhang, X., Zhu, X., Guo, J., et al. (2017). Efficient oxygen reduction catalysis by subnanometer Pt alloy nanowires. *Sci. Adv.* 3:e1601705. doi: 10.1126/sciadv.1601705

Khan, M. U., Wang, L., Liu, Z., Gao, Z., Wang, S., Li, H., et al. (2016). Pt_3Co octapods as superior catalysts of CO_2 hydrogenation. *Angew. Chem.* 55, 9548–9552. doi: 10.1002/anie.201602512

Li, C., Imura, M., and Yamauchi, Y. (2014). Displacement plating of a mesoporous Pt Skin onto Co nanochains in a low-concentration surfactant solution. *Chem. Eur. J.* 20, 3277–3282. doi: 10.1002/chem.201303250

Li, M., Zhao, Z., Cheng, T., Fortunelli, A., Chen, C. -Y., Yu, R., et al. (2016). Ultrafine jagged platinum nanowires enable ultrahigh mass activity for the oxygen reduction reaction. *Science* 354, 1414–1419. doi: 10.1126/science.aaf9050

Li, Q., and Sun, S. (2016). Recent advances in the organic solution phase synthesis of metal nanoparticles and their electrocatalysis for energy conversion reactions. *Nano Energy* 29, 178–197. doi: 10.1016/j.nanoen.2016.02.030

Li, Y., Wang, W., Xia, K., Zhang, W., Jiang, Y., Zeng, Y., et al. (2015). Ultrathin two-dimensional Pd-based nanorings as catalysts for hydrogenation with high activity and stability. *Small* 11, 4745–4752. doi: 10.1002/smll.201500769

Lim, B., Jiang, M., Camargo, P. H. C., Cho, E. C., Tao, J., Lu, X., et al. (2009). Pd-Pt bimetallic nanodendrites with high activity for oxygen reduction. *Science* 324, 1302–1305. doi: 10.1126/science.1170377

Lim, B., and Xia, Y. (2011). Metal nanocrystals with highly branched morphologies. *Angew. Chem.* 50, 76–85. doi: 10.1002/anie.201002024

Luo, S., and Shen, P. K. (2017). Concave platinum-copper octopod nanoframes bounded with multiple high-index facets for efficient electrooxidation catalysis. *ACS Nano* 11, 11946–11953. doi: 10.1021/acsnano.6b04458

Luo, S., Tang, M., Shen, P. K., and Ye, S. (2017). Atomic-scale preparation of octopod nanoframes with high-index facets as highly active and stable catalysts. *Adv. Mater.* 29:1601687. doi: 10.1002/adma.201601687

Porter, N. S., Wu, H., Quan, Z., and Fang, J. (2013). Shape-control and electrocatalytic activity-enhancement of Pt-based bimetallic nanocrystals. *Acc. Chem. Res.* 46, 1867–1877. doi: 10.1021/ar3002238

Quan, Z. W., Wang, Y. X., and Fang, J. Y. (2013). High-index faceted noble metal nanocrystals. *Acc. Chem. Res.* 46, 191–202. doi: 10.1021/ar200293n

Stamenkovic, V., Mun, B. S., Mayrhofer, K. J. J., Ross, P. N., Markovic, N. M., Rossmeisl, J., et al. (2006). Changing the activity of electrocatalysts for oxygen reduction by tuning the surface electronic structure. *Angew. Chem.* 118, 2963–2967. doi: 10.1002/ange.200504386

Stamenkovic, V. R., Fowler, B., Mun, B. S., Wang, G., Ross, P. N., Lucas, C. A., et al. (2007a). Improved oxygen reduction activity on Pt_3Ni(111) via increased surface site availability. *Science* 315, 493–497. doi: 10.1126/science.1135941

Stamenkovic, V. R., Mun, B. S., Arenz, M., Mayrhofer, K. J. J., Lucas, C. A., Wang, G., et al. (2007b). Trends in electrocatalysis on extended and nanoscale Pt-bimetallic alloy surfaces. *Nat. Mater.* 6, 241–247. doi: 10.1038/nmat1840

Tang, M., Luo, S., Wang, K., Du, H., Sriphathoorat, R., and Shen, P. (2018). Simultaneous formation of trimetallic Pt-Ni-Cu excavated rhombic dodecahedrons with enhanced catalytic performance for the methanol oxidation reaction. *Nano. Res.* 11, 4786–4795. doi: 10.1007/s12274-018-2063-3

Teng, X., and Yang, H. (2005). Synthesis of platinum multipods: an induced anisotropic growth. *Nano Lett.* 5, 885–891. doi: 10.1021/nl0503072

Wang, K., Sriphathoorat, R., Luo, S., Tang, M., Du, H., and Shen, P. K. (2016). Ultrathin PtCu hexapod nanocrystals with enhanced catalytic performance for electro-oxidation reactions. *J. Mater. Chem. A* 4, 13425–13430. doi: 10.1039/C6TA05230D

Wang, X. X., Hwang, S., Pan, Y. -T., Chen, K., He, Y., Karakalos, S., et al. (2018). Ordered Pt_3Co intermetallic nanoparticles derived from metal-organic frameworks for oxygen reduction. *Nano Lett.* 18, 4163–4171. doi: 10.1021/acs.nanolett.8b00978

Wiley, B., Herricks, T., Sun, Y., and Xia, Y. (2004). Polyol synthesis of silver nanoparticles: use of chloride and oxygen to promote the formation of single-crystal, truncated cubes and tetrahedrons. *Nano Lett.* 4, 1733–1739. doi: 10.1021/nl048912c

Wu, J., Li, P., Pan, Y. -T., Warren, S., Yin, X., and Yang, H. (2012a). Surface lattice-engineered bimetallic nanoparticles and their catalytic properties. *Chem. Soc. Rev.* 41, 8066–8074. doi: 10.1039/C2CS35189G

Wu, Y., Cai, S., Wang, D., He, W., and Li, Y. (2012b). Syntheses of water-soluble octahedral, truncated octahedral, and cubic Pt-Ni nanocrystals and their structure-activity study in model hydrogenation reactions. *J. Am. Chem. Soc.* 134, 8975–8981. doi: 10.1021/ja302606d

Yin, A. -X., Min, X. -Q., Zhu, W., Liu, W. -C., Zhang, Y. -W., and Yan, C. -H. (2012). Pt-Cu and Pt-Pd-Cu concave nanocubes with high-index facets and superior electrocatalytic activity. *Chem. Eur. J.* 18, 777–782. doi: 10.1002/chem.201102632

Zhang, H., Xia, X., Li, W., Zeng, J., Dai, Y., Yang, D., et al. (2010a). Facile synthesis of five-fold twinned, starfish-like rhodium nanocrystals by eliminating oxidative etching with a chloride-free precursor. *Angew. Chem.* 122, 5424–5428. doi: 10.1002/ange.201002546

Zhang, J., Yang, H., Fang, J., and Zou, S. (2010b). Synthesis and oxygen reduction activity of shape-controlled Pt_3Ni nanopolyhedra. *Nano Lett.* 10, 638–644. doi: 10.1021/nl903717z

Zhang, L., Roling, L. T., Wang, X., Vara, M., Chi, M., Liu, J., et al. (2015a). Platinum-based nanocages with subnanometer-thick walls and well-defined, controllable facets. *Science* 349, 412–416. doi: 10.1126/science.aab0801

Zhang, P., Dai, X., Zhang, X., Chen, Z., Yang, Y., Sun, H., et al. (2015b). One-pot synthesis of ternary Pt-Ni-Cu nanocrystals with high catalytic performance. *Chem. Mater.* 27, 6402–6410. doi: 10.1021/acs.chemmater.5b02575

Zhang, Z., Liu, G., Cui, X., Chen, B., Zhu, Y., Gong, Y., et al. (2018). Crystal phase and architecture engineering of lotus-thalamus-shaped Pt-Ni anisotropic superstructures for highly efficient electrochemical hydrogen evolution. *Adv. Mater.* 30:1801741. doi: 10.1002/adma.201801741

Conflict of Interest Statement: The authors declare that the research was conducted in the absence of any commercial or financial relationships that could be construed as a potential conflict of interest.

frontiers in Chemistry

ORIGINAL RESEARCH
published: 16 October 2018
doi: 10.3389/fchem.2018.00494

Geometric Symmetry of Dielectric Antenna Influencing Light Absorption in Quantum-Sized Metal Nanocrystals: A Comparative Study

Xinyan Dai[†]*, Kowsalya Devi Rasamani*[†]*, Gretchen Hall, Rafaela Makrypodi and Yugang Sun*[*]

Department of Chemistry, Temple University, Philadelphia, PA, United States

Edited by:
Ou Chen,
Brown University, United States

Reviewed by:
Hongbo Li,
Beijing Institute of Technology, China
Gang Chen,
University of Central Florida, United States
Hongyou Fan,
Sandia National Laboratories (SNL), United States

****Correspondence:***
Yugang Sun
ygsun@temple.edu

[†] *These authors have contributed equally to this work*

Specialty section:
This article was submitted to Nanoscience, a section of the journal Frontiers in Chemistry

Received: *24 August 2018*
Accepted: *27 September 2018*
Published: *16 October 2018*

Citation:
Dai X, Rasamani KD, Hall G, Makrypodi R and Sun Y (2018) Geometric Symmetry of Dielectric Antenna Influencing Light Absorption in Quantum-Sized Metal Nanocrystals: A Comparative Study. Front. Chem. 6:494. doi: 10.3389/fchem.2018.00494

Silica nanoparticles, optically transparent in the visible spectral region, represent a class of dielectric antenna to tune the propagation and local field distribution of the visible light through surface scattering while the energy loss is minimized. The light scattering on the surface of silica nanoparticles include resonant scattering and random scattering that strongly depend on their geometry: spherical silica nanoparticles with the highest geometrical symmetry favors the light scattering resonances on the nanoparticle surfaces to promote resonant scattering while non-spherical silica nanoparticles mainly support random scattering. Both resonant scattering and random scattering of light on the silica nanoparticles are capable of enhancing the light absorption in quantum-sized metal nanocrystals attached to the surfaces of the silica nanoparticles. The contributions of resonant scattering and random scattering to the enhancement of light absorption have been compared and discussed. The understanding highlights the importance of the geometry of the silica nanoparticle antenna on the design and synthesis of composite materials for efficient light harvesting.

Keywords: light scattering, resonant scattering, random scattering, enhanced optical absorption, dielectric antenna

INTRODUCTION

A dielectric antenna consisting of a block of ceramic material of varying shapes interacts with electromagnetic waves while loses much less energy than the metal counterparts, resulting in an efficient modulation of the incident waves (Ashkin and Dziedzic, 1981; Ausman and Schatz, 2008; Matheu et al., 2008; Anderson, 2010; Grandidier et al., 2013; Yin et al., 2013; Kuznetsov et al., 2016; Huang et al., 2018). For instance, a dielectric resonator antenna with an appropriate geometry can allow the incident electromagnetic wave to bounce back and forth against the antenna surface, supporting scattering resonances to form new standing waves near the antenna surface, behaving as resonant scattering. The new surface standing waves can possibly radiate and propagate into space if the antenna surface is leaky. In contrast, an incident electromagnetic wave can also (elastically) scatter away from the antenna surface into space regardless of the geometry of the antenna, behaving as random scattering. Therefore, a dielectric antenna supporting different scattering modes leads to a difference in influencing the absorption spectrum of a material that can absorb the incident electromagnetic energy when it is placed near the antenna. The random scattering usually does not alter the absorption spectrum profile of the energy-absorbing material while the resonant scattering does. A typical example extensively reported in literature is the use of silica particles with sizes of several hundreds of nanometers and larger as a class of dielectric antenna to improve the capability of light absorption in active materials of light-harvesting devices such as solar cells (Matheu et al., 2008; Matsko, 2009; Grandidier et al., 2011; Gupta et al., 2018). Since silica is transparent in the visible spectral region and silica nanoparticles do not absorb visible light, the enhanced light absorption in active materials is attributed to the strong light scattering (both resonant scattering and random scattering) on the surfaces of the silica nanoparticles. When the silica nanoparticles are mixed with the light-absorbing active materials to form a composite in a given volume, the light scattering from the surface of the silica nanoparticles elongates the light traveling path to benefit light absorption in the active materials (Matheu et al., 2008; Kumari and Narayana, 2012; Son et al., 2013; Ullah et al., 2015; Rahman et al., 2016). In addition to the light scattered away from the surface of the silica nanoparticles, the light scattering resonances on the surface of the silica nanoparticles also influence the optical response of active materials attached to the silica nanoparticles (Ausman and Schatz, 2008; Grandidier et al., 2011; Liu et al., 2015). The surface scattering resonances usually create electrical fields much stronger than the incident light near the surface of the silica nanoparticles, significantly enhancing the light absorption of active materials attached to the surface of the silica nanoparticles (Zhang et al., 2016; Codrington et al., 2017; Rasamani et al., 2017, 2018; Dai et al., 2018b). Herein, we study the influence of geometry of silica nanoparticles on their light scattering behavior as well as the corresponding enhanced light absorption in quantum-sized metal nanocrystals attached to the silica nanoparticles. Using the quantum-sized metal nanocrystals as the unique probe, the contributions of resonant scattering and random scattering to the enhanced light absorption are compared. The enhanced light absorption in quantum-sized metal nanocrystals, for example, the nanocrystal catalysts made of platinum group metals (PGMs), is beneficial for more efficiently exciting hot electrons in the quantum-sized metal nanocrystals to drive chemical transformations as discussed elsewhere (Wei et al., 2018).

MATERIALS AND METHODS

Synthesis of Silica Nanospheres (SiO_x NSs)

Silica nanospheres (SiO_x NSs) were prepared through a sol-gel process relying on a controlled hydrolysis and condensation of tetraethyl orthosilicate (TEOS, 98%, Sigma-Aldrich) (Green et al., 2003). An appropriate amount (1.7 mL) of TEOS was added to a solution containing 29.1 mL of absolute ethanol (Pharmco-Aaper), 3.21 mL of deionized (DI) water, and 1.96 mL of ammonia hydroxide (28–30 wt.% in water, Fisher Scientific). The reaction proceeded for 2 h at a stirring rate of 600 rpm to complete the growth of SiO_x NSs. Changing the amount of water and TEOS could tune the size of the synthesized SiO_x NSs. The resultant SiO_x NSs were collected through two cycles of centrifugation and washing with ethanol, and then dried overnight in an oven set at 60°C.

Synthesis of Truncated Silica Nanospheres (t-SiO_x NSs) and Ellipsoidal Silica Nanoparticles (e-SiO_x NPs)

The t-SiO_x NSs and e-SiO_x NPs were synthesized by following the procedure reported in literature with slight modifications (Rahmani et al., 2017). A desirable amount (50–300 mg) of cetyl trimethylammonium bromide (CTAB, 99.5%, Chem-Impex Int'l Inc.) was added to a mixed solvent containing 50 mL of deionized water and 5 mL of ethanol. The temperature of the solution was maintained at 50°C and stirred at 800 rpm for 30 min. To this solution was added 350 μL of NaOH aqueous solution (3 M, Fisher Scientific) to dissolve CTAB completely. While the temperature and magnetic stirring was maintained, adding 575 μL of TEOS to the CTAB solution initiated the nucleation and growth of silica nanoparticles. Continuous reaction for 2 h completed the synthesis of silica nanoparticles. The geometry of the silica nanoparticles was determined by the concentration of CTAB, i.e., 100 mg of CTAB for t-SiO_x NSs and 200 mg of CTAB for e-SiO_x NPs. The resulting SiO_x nanoparticles were collected through multiple cycles of centrifugation (at 6,000 rpm for 10 min) and washing with ethanol. The collected particles were dried overnight in an oven set at 60°C.

Synthesis of Rodlike Silica Nanoparticles (r-SiO_x NPs)

Rodlike silica nanorods (r-SiO_x NPs) with different aspect ratios were synthesized and purified based on the method reported in previous studies (Kuijk et al., 2011; Murphy et al., 2016). In a typical synthesis of r-SiO_x NPs with an aspect ratio of 0.8, 30 g of polyvinylpyrrolidone (PVP, molecular weight ∼55,000, Sigma-Aldrich) was first dissolved in 30 mL of 1-pentanol (99%, Acros Organics) with assistance of sonication in a 50-mL centrifuge tube. To this PVP solution was sequentially added 0.5 mL of absolute ethanol, 1.2 mL of DI water, and 0.3 mL of 0.18 M aqueous sodium citrate dehydrate (Fisher Scientific). The solution was homogenized via vortex for 30 s. 0.4 mL of ammonium hydroxide was then added to the solution followed by vortex for 30 s. To the solution was finally added 0.3 mL of TEOS. The solution was then vortexed for 1 min and maintained still for 1.5 h, forming r-SiO_x NPs with the aspect ratio of 0.8. The length and radius (thus the aspect ratio) of r-SiO_x NPs could be tuned by changing the amount of ethanol, water, sodium citrate, ammonium hydroxide, TEOS, and reaction time. The synthesized r-SiO_x NPs were collected by three cycles of centrifugation (at 6,000 rpm for 20 min) and washing with ethanol and water. The rods were then re-dispersed in ethanol with assistance of sonication for 2 h. The dispersion was centrifuged at 800 rpm to remove larger rods in the sediment, leaving nearly mono-dispersed r-SiO_x NPs in the supernatant.

Synthesis of Quantum-Sized Pt and Rh Nanocrystals

Colloidal Pt nanocrystals were synthesized through reduction of hexachloroplatinate anions in an aqueous solution at ambient condition. In a typical synthesis, 26 mL of aqueous solution of trisodium citrate (4 mM, Alfa Aesar) was added to 50 mL of aqueous solution of hexachloroplatinic acid hexahydrate (0.4 mM, Acros Organics) while the solution was stirred at 800 rpm. To this solution was added 5 mL of aqueous solution of 4 mM sodium borohydride (98%, Sigma-Aldrich) slowly, triggering the reduction of hexachloroplatinate anions to immediately turn the solution from yellow to brown. The reaction lasted 2 h under a continuous stirring, forming a black dispersion containing Pt nanocrystals.

Colloidal Rh nanocrystals were synthesized through a polyol process involving sequential reactions at two different temperatures (Biacchi and Schaak, 2015). In a typical synthesis, 0.238 g of potassium bromide (KBr, Alfa Aesa), 0.088 g of PVP, 0.024 g of sodium hexachlororhodate (III) dodecahydrate ($Na_3RhCl_6 \cdot 12\ H_2O$, Alfa Aesa) were mixed with 7 mL of ethylene glycol (EG, Fisher Scientific) in a 20-mL glass vial. Warming up the solution at 40°C for 1 h dissolved the reagent powders completely. The solution was then heated up to 90°C and this temperature was maintained for 15 min to initiate nucleation. The reaction was heated to 150°C and maintained for 1 h, facilitating the growth of colloidal Rh nanocrystals. The resulting dispersion of Rh nanocrystals was mixed with 3 mL of acetone/water (9/1 in V/V), followed by centrifugation at 13,400 rpm for 10 min. The settled powders were then re-dispersed with 3 mL of acetone/water (9/1 in V/V). Repeating the centrifugation/re-dispersion cycles for 5 times removed PVP and ions from the dispersion of the Rh nanocrystals.

Functionalization of Silica (SiO_X) Nanoparticles

The synthesized SiO_x nanoparticles were functionalized with (3-amniopropyl) triethoxysilane (APTES, 98%, Acros Organics) to introduce positively charged surfaces. An ethanolic dispersion of 2 mg mL^{-1} of silica nanoparticles was first prepared with assistance of ultrasonication. To 10 mL of the silica nanoparticle dispersion was dropwise added 0.1 mL of APTES while the temperature of the dispersion was maintained at 60°C. It took 30 s to complete the addition of APTES. The dispersion was continuously stirred for 8 h, leading to the conjugation of APTES to the surface of the silica nanoparticles. The functionalized silica nanoparticles were collected through centrifugation and washing with ethanol, followed by drying in an oven set at 60°C. As for r-SiO_x NPs, the corresponding powders were calcined at 500°C for 3 h to burn off PVP from the r-SiO_x NPs. An appropriate amount of the calcinated r-SiO_x NPs were then added to ethanol, forming a dispersion with a silica concentration of 2 mg mL^{-1}. To 12 mL of the r-SiO_x NP dispersion was added 7 mL of aqueous solution of hydrochloric acid (37 wt.%, Fisher Scientific). The dispersion was constantly stirred overnight at room temperature. The pre-treated r-SiO_x NPs were then collected by centrifugation and washing with ethanol for further surface modification with APTES.

The APTES-modified silica nanoparticles exhibited positively charged surfaces, to which metal nanocrystals with negatively charged surfaces could be attached through strong electrostatic attractions (Zhang et al., 2016; Rasamani et al., 2017, 2018). In a process of loading 1 wt.% Pt nanocrystals to the silica NPs, 4.21 mL of the as-synthesized Pt nanocrystal solution was slowly added to 10 mL aqueous dispersion of the silica nanoparticles with a concentration of 2 mg mL^{-1}. Constantly stirring the dispersion of two types of nanoparticles at 600 rpm for 15 min resulted in the attachment of the Pt nanocrystals to the surface of the silica nanoparticles, forming composite SiO_x-NP/Pt particles. The obtained SiO_x-NP/Pt particles were collected via centrifugation for 10 min at 6,000 rpm, followed by drying in an oven set at 60°C for 2 h. The same method was also used to load the synthesized Rh nanocrystals to the APTES-modified silica nanoparticles. The loading of metal nanocrystals was tuned by controlling the amount of metal nanocrystals and silica nanoparticles used in the synthesis.

MATERIALS CHARACTERIZATION

Transmission electron microscopy (TEM) images of metal nanocrystals were recorded on a microscope (JEOL JEM-1400). Scanning electron microscopy (SEM) images of silica nanoparticles and silica/metal composite particles were characterized with a field-emission microscope (FEI Quanta FEG 450) that was operated at an acceleration voltage of 20 kV. Inductively coupled plasma atomic emission spectroscopy (ICP-OES, Thermo Scientific 7000 Series) was used to determine the loading contents of metal nanocrystals on the silica/metal composite particles. Diffuse reflectance spectroscopy (DRS) was analyzed by an ultraviolet–visible (UV–vis) spectrophotometer (Thermo Scientific, Evolution 220) equipped with an integration sphere.

RESULTS AND DISCUSSION

Silica nanoparticles with large enough sizes can always produce random scattering in the visible spectral region regardless of their morphology, but generating resonant scattering strongly depends on their morphology. For instance, theoretical modeling and calculations have shown that spherical SiO_2 particles of several microns supports Fabry-Perot or Whispering Gallery resonances, forming electrical fields near the SiO_2 surfaces much stronger than that of the incident light (Ausman and Schatz, 2008). Varying the size of the SiO_2 particles tunes the resonant wavelengths and the enhancement of electrical fields near the particle surfaces. Decreasing the size of silica spheres down to the sub-micrometer scale still supports surface scattering resonances despite the broadness of the resonance peaks. The light scattering resonances on the surfaces of silica nanospheres (SiO_x NSs) significantly enhance the optical absorbance and change the spectral profile of absorption in quantum-sized Pt nanocrystals (with size <10 nm) that are attached to the surface of the SiO_x NSs (Zhang et al., 2016). An aqueous dispersion of well-dispersed Pt nanocrystals with an average size of 3.2 nm exhibits a brown color and a peakless absorption spectrum in the range of 300–800 nm (**Figure 1A**). The Pt nanocrystals have negatively charged surfaces, which allows them to attach to the surfaces of positively charged SiO_x NSs through the strong electrostatic attraction. This hybridization process results in a uniform distribution of the Pt nanocrystals on the SiO_x NSs, forming SiO_x-NS/Pt composite particles (**Figure S1**). A powder of the SiO_x-NS/Pt particles is greenish (inset, **Figure 1B**), corresponding to the strong light absorption around 530 nm. **Figure 1B** compares the SiO_x-NS/Pt particles and the SiO_x NSs with regard to the DRS spectra, which exclude the contribution of scattering and are only sensitive to the absorption. The negligible signal of the SiO_x NSs indicates that the absorption signal of the SiO_x-NS/Pt particles originates only from the Pt nanocrystals. Different from the freestanding Pt nanocrystals dispersed in an aqueous solution, the SiO_x-NS/Pt particles exhibit well-defined peaks, which are consistent with the light scattering resonances on the surface of the SiO_x NSs with the highest geometric symmetry (R_3) (Zhang et al., 2016). The DRS spectrum of the SiO_x-NS/Pt particles also exhibits a non-zero baseline, more likely independent of the wavelength, which agrees with the feature of random scattering. The comparisons indicate that both resonant scattering and random scattering of the dielectric SiO_x NSs are responsible for enhancing the light absorption in the quantum-sized Pt nanocrystals. The respective contribution of resonant scattering and random scattering to the enhanced light absorption is not distinguished.

Theoretical modeling and calculations indicate that the spherical geometry of dielectric particles favors resonant scattering and reducing the geometrical symmetry of the dielectric particles weakens resonant scattering (Gupta et al., 2018). **Figure 2A** highlights that the geometrical symmetry of silica nanoparticles can be lowered by tuning the concentration of CTAB in the sol-gel reaction as described elsewhere (**Figure S2**) (Hao et al., 2015; Rahmani et al., 2017). Highly symmetrical SiO_x NSs are formed by using the modified Stöber method (**Figure S1**). Adopting a different synthetic procedure with addition of CTAB yields SiO_x with varied morphologies. Addition of a low concentration (4.9 mM) of CTAB to the reaction solution slightly truncates the two poles of SiO_x NSs, forming silica nanoparticles (labeled as t-SiO_x NSs shown in **Figure 2B**) with a lower geometric symmetry than the SiO_x NSs. Adding more CTAB further truncates the silica nanoparticles and silica nanoparticles with an ellipsoidal shape (labeled as e-SiO_x NPs, **Figure 2C**) are formed with an extremely high concentration (9.8 mM) of CTAB. Same as the SiO_x NSs, both the t-SiO_x NSs and e-SiO_x NPs also exhibit negligible absorption signal in the corresponding DRS spectra (purple and pink curves, **Figure 2D**). In contrast, the Pt nanocrystals on the t-SiO_x NSs and e-SiO_x NPs exhibit strong light absorption (red and blue curves, **Figure 2D**), indicating that both the t-SiO_x NSs and e-SiO_x NPs are still capable of enhancing light absorption of the Pt nanocrystals due to light scattering of the silica nanoparticles. The corresponding DRS spectra become essentially peakless, implying the absence of resonant light scattering on the t-SiO_x NSs and e-SiO_x NPs with lowered geometric symmetry of $D_{\infty h}$. The spectral difference of the Pt nanocrystals on the differently shaped silica nanoparticles highlights the importance of geometric symmetry of the silica nanoparticles on determining their light scattering mode. Resonant scattering, which is responsible for the appearance of well-defined intense absorption peaks in the DSR spectra, is very sensitive to the geometric symmetry of silica nanoparticles. Only the SiO_x NSs with the highest geometrical symmetry of R_3 supports strong surface scattering resonances. Lowering the geometric symmetry of the silica nanoparticles drastically suppresses the resonant scattering while random scattering is barely influenced (**Figure 2D**). The difference in the DRS intensity shows that the resonant scattering and random scattering of SiO_x NSs make approximately equal contributions to enhance the light absorption in the Pt nanocrystals at the resonance frequencies. At the non-resonance frequencies, the random scattering dominates the enhancement of light absorption in the Pt nanocrystals.

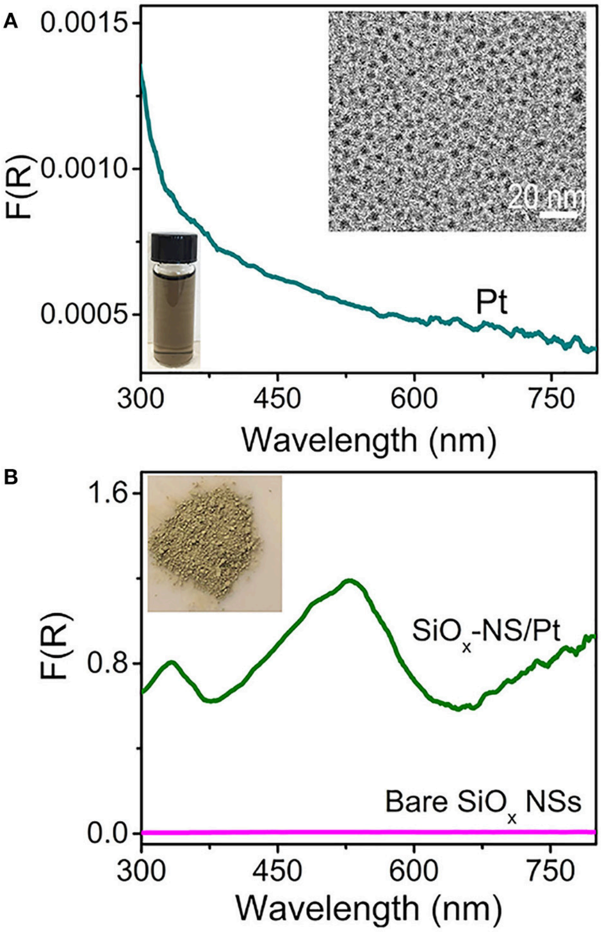

FIGURE 1 | DRS spectra of **(A)** an aqueous dispersion of Pt nanocrystals and **(B)** a powder film of SiO_x-NS/Pt composite particles. The DRS spectrum of a powder film of SiO_x NSs is presented in **(B)** for reference. A representative TEM image of the Pt nanocrystals and a digital photograph of an aqueous dispersion of the Pt nanocrystals are presented as insets in **(A)**. A digital photo of the powders of SiO_x-NS/Pt composite particles is shown as inset in **(B)**.

Light scattering on the SiO_x NSs can enhance optical absorption in any nanoparticles attached to the SiO_x NSs (Zhang et al., 2016; Rasamani et al., 2017, 2018; Dai et al., 2018b). For example, quantum-sized Rh nanocrystals with sizes of ~3 nm exhibit a peakless absorption spectrum while strong light absorption with well-defined peaks is observed from the Rh nanocrystals loaded to the SiO_x NSs (with an average

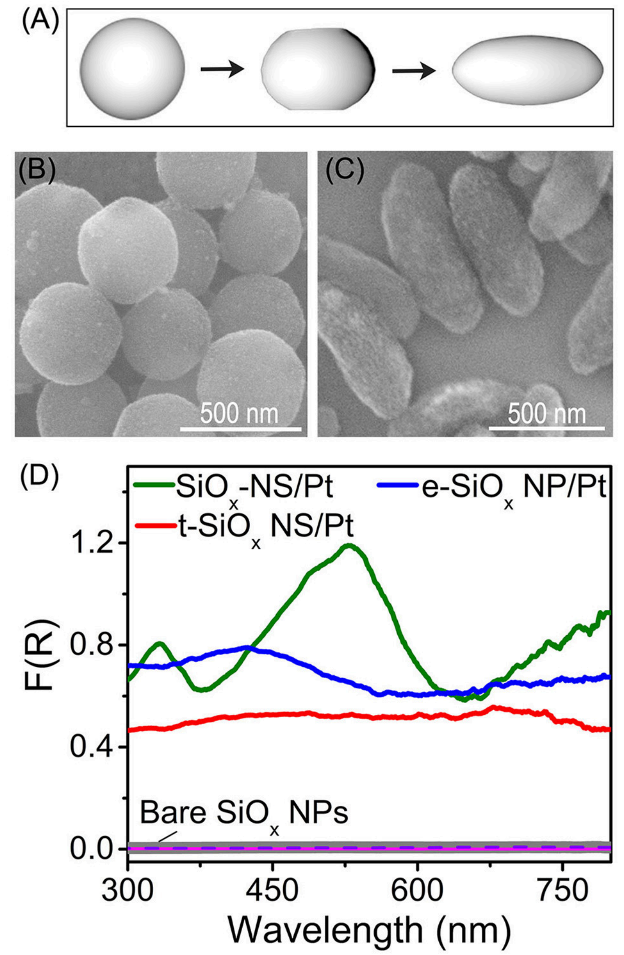

FIGURE 2 | (A) Schematic illustration of geometry of SiO_X NSs (left), t-SiO_X NSs (middle), and e-SiO_X NPs (right), highlighting the difference of their geometric symmetries. **(B,C)** SEM images of t-SiO_X NSs **(B)** and e-SiO_X NPs with Pt nanocrystals loaded on their surfaces. **(D)** DRS spectra of powders of bare silica nanoparticles (SiO_X NSs, t-SiO_X NSs and e-SiO_X NPs) and the corresponding SiO_X/Pt composite particles with 1 wt.% loading of Pt nanocrystals on the silica nanoparticles.

diameter of 356 nm, **Figure S3**). To further verify the importance of spherical symmetry of the silica nanoparticles on resonant scattering, another set of silica nanoparticles with reduced geometrical symmetry are synthesized by controlling the aspect ratio of the rodlike particles. The silica nanoparticles start nucleation at nanosized water-rich emulsion droplets followed by anisotropic growth along the direction away from emulsion droplets, forming rodlike nanoparticles with one flat end and one rounded end (**Figure 3A**, **Figure S4**). These rodlike silica nanoparticles (r-SiO_x NPs) exhibit a geometric symmetry of $C_{\infty V}$ and their geometric aspect ratio is determined by the lateral dimensions shown in **Figure 3A**. Similar to the SiO_x NSs, these r-SiO_x NPs are also feasible to attract the quantum-sized Rh nanocrystals to their surfaces, forming SiO_x/Rh composites. **Figures 3B,C** show the SEM images of bare silica and composite samples (insets) formed from the r-SiO_x NPs with aspect ratios

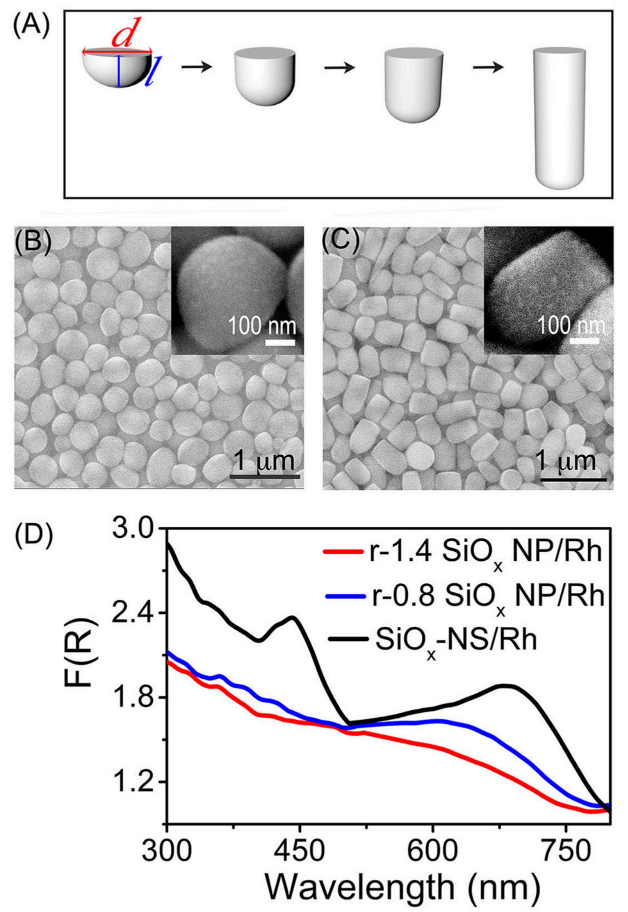

FIGURE 3 | (A) Schematic illustration of the geometry of r-SiO_X NPs with different aspect ratios. The aspect ratio is defined by the ratio of the length (*l*) to the width (*d*) of an r-SiO_X NP. **(B,C)** SEM images of the r-SiO_X NPs with aspect ratios of 0.8 (denoted as r-0.8 SiO_X NPs) **(B)** and 1.4 (denoted as r-1.4 SiO_X NPs) **(C)**. The insets present the SEM images of the r-SiO_X NPs covered with Rh nanocrystals. **(D)** DRS spectra of powders of the silica nanoparticles (SiO_X NSs, r-0.8 SiO_X NPs, and r-1.4 SiO_X NPs) with 2 wt.% loading of Rh nanocrystals.

of 0.8 and 1.4, respectively. The corresponding powders of these composite particles exhibit strong optical absorption although their DSR spectra are different from that of the SiO_x-NS/Rh composite particles (**Figure 3D**). The spectral difference shows that the intensity of the absorption peaks decreases as the aspect ratio of the r-SiO_x NPs deviates from the unity (i.e., 1) that corresponds to the aspect ratio of the SiO_x NSs. This relationship can be quantitatively compared by integrating these DRS spectra in the range of 300–800 nm, and the integrated values are shown in **Figure S5** as a function of aspect ratio of the supporting SiO_x NPs. The volcano shape with a maximum at the aspect ratio of 1 (corresponding to spherical SiO_x NPs) again highlights that the SiO_x NSs are more effective in enhancing light absorption in the Rh nanocrystals than the rodlike silica nanoparticles regardless of the aspect ratios >1 or <1. A more deviation of the aspect ratio weakens the absorption peaks more, further confirming that high geometric symmetry of the SiO_x

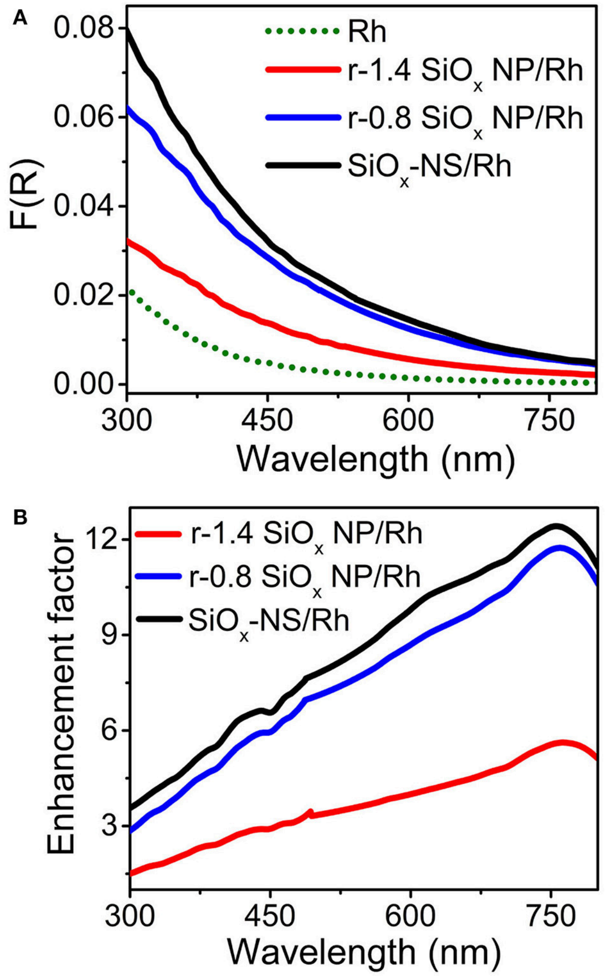

FIGURE 4 | (A) DRS spectra of aqueous dispersions of well-dispersed Rh nanocrystals (green dotted) and SiO$_X$/Rh composite particles formed from SiO$_X$ NSs (black), r-0.8 SiO$_X$ NPs (blue), and r-1.4 SiO$_X$ NPs (red). The intensity of these DRS spectra were normalized against the mass concentration of Rh nanocrystals. **(B)** Calculated enhancement spectra for the SiO$_X$ NSs (black), r-0.8 SiO$_X$ NPs (blue), and r-1.4 SiO$_X$ NPs (red).

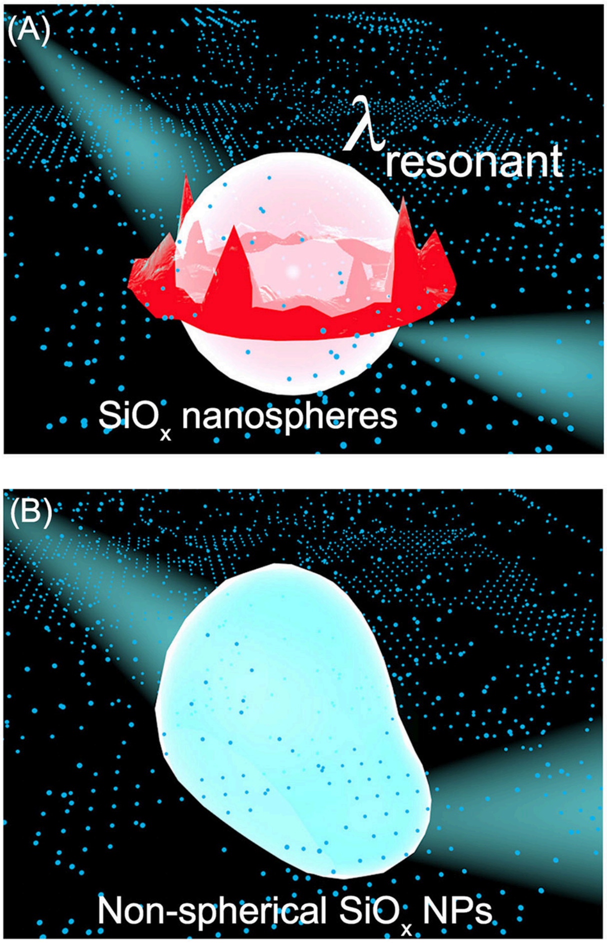

FIGURE 5 | Schematic illustration highlighting the difference of light scattering on silica nanoparticles with different geometric symmetries. **(A)** A SiO$_X$ NS with the highest geometric symmetry of R$_3$ supports both strong resonant scattering, which generates new standing waves with stronger electric fields near the surface of the SiO$_X$ NS, and random scattering, which scatters the incident light off the surface of the SiO$_X$ NS in directions different from its original propagation direction. **(B)** A SiO$_X$ NP with non-spherical shape, corresponding to a geometric symmetric lower than R$_3$, merely supports random scattering. The influence of geometry of SiO$_X$ NPs on the light scattering mode can be transferred to the enhanced optical absorption of quantum-sized metal nanocrystals attached to the SiO$_X$ NPs as presented in **Figures 1–4**. The red and blue colors denote high and low electric field intensity, respectively.

NSs is crucial to support strong resonant scattering on the dielectric silica nanoparticles. Regardless of the aspect ratio of the silica nanoparticles, the featureless baselines of these DRS spectra remain essentially consistent, indicating that the random scattering of the silica nanoparticles makes an approximately constant contribution to enhance the light absorption in the Rh nanocrystals. At the resonance frequencies, the light absorption in the Rh nanocrystals enhanced by the resonant scattering of the SiO$_x$ NSs is comparable to the absorption enhanced by the random scattering. The light absorption is dominated by the enhancement originated from the random scattering at the non-resonance frequencies. The DRS spectra shown in **Figures 2D, 3D** consistently highlight that both resonant scattering and random scattering of the silica nanoparticles are capable of enhancing the light absorption in the quantum-sized metal nanocrystals attached to the silica nanoparticles. The occurrence of resonant scattering strongly depends on the geometric symmetry of the silica nanoparticles. The SiO$_x$ NSs with the highest geometric symmetry supports the strongest resonant scattering while the resonant scattering weakens with decrease of their geometric symmetry. In contrast, the random scattering is independent of the geometry of the silica nanoparticles.

The light scattering efficiency of the dielectric silica nanoparticles also relies on the refractive index (n) of the surrounding environment (Mishchenko et al., 2002; Zhu et al., 2010). A large difference of refractive indexes between the surround medium and the silica nanoparticles (n_{silica} ≈1.4–1.45

for the sol-gel silica) promotes light scattering. Therefore, the silica nanoparticles dispersed in water ($n_{\text{water}} = 1.33$ at room temperature) exhibit a much lower light scattering efficiency compared to the dry powder of the silica nanoparticles in air ($n_{\text{air}} = 1$). The variation of refractive index of the surround medium also influences the scattering resonance frequencies of the SiO_x NSs. **Figure 4A** compares the DRS spectra of aqueous dispersions of freestanding Rh nanocrystals and SiO_x/Rh composite particles formed with varying silica nanoparticles, which exhibit profiles different from the DRS spectra of the corresponding SiO_x/Rh dry powders (**Figure 3D**). However, the light absorption in the Rh nanocrystals is always enhanced when the Rh nanocrystals are attached to the silica nanoparticles. The good dispersion of the Rh nanocrystals in water and on the surfaces of the silica nanoparticles ensures that the measured DRS signals represent the accumulation of optical absorption of individual Rh nanocrystals with exclusion of possible interparticular coupling between the adjacent Rh nanocrystals. As a result, the enhancement spectrum, i.e., enhancement factor as a function of wavelength, enabled by the silica nanoparticles can be calculated by dividing the DRS spectrum of a dispersion of the corresponding SiO_x/Rh composite particles against the DRS spectrum of the dispersion of the freestanding Rh nanocrystals (green dotted curve, **Figure 4A**). **Figure 4B** presents the calculated enhancement spectra enabled by the SiO_x NSs and the r-SiO_x NPs with aspect ratios of 0.8 and 1.4, showing that the maximum enhancement factor can reach ∼12 around 750 nm for the SiO_x NSs. In the visible spectral region (i.e., at $\lambda > 450$ nm), the enhancement factor is always higher than 7 for the SiO_x NSs although it is lower for the r-SiO_x NPs. Since the light scattering efficiency of the dry SiO_x NSs in air is much higher than that of the wet SiO_x NSs in solvents (e.g., ethanol, water, etc.), the optical absorption power of the Rh nanocrystals attached to the SiO_x NSs could be enhanced by a higher factor when SiO_x-NS/Rh composite particles are used in gas atmospheres. In order to achieve the maximum scattering-enhanced light absorption in quantum-sized metal nanoparticles, the synthesis of SiO_x NSs has to be carefully controlled to ensure the refractive index of the SiO_x NSs to reach the possible maximum value (Li et al., 2014; Zulfiqar et al., 2016; Dai et al., 2018a).

CONCLUSION

In conclusion, silica nanoparticles with lateral dimensions of hundreds of nanometers and larger represent a class of dielectric antenna that does not absorb visible light, exhibiting strong light scattering in the visible spectral region with a minimum energy loss. Regardless of the geometry of the silica nanoparticle antenna, random scattering of the incident light is always observed while the wave function is not altered. When the geometry of the silica nanoparticles exhibits a high enough symmetry, the nanoparticle antenna can also support surface scattering resonances that generate new standing waves with wave functions different from the incident light. For example, light scattering resonances on the surface of SiO_x NSs with the highest geometric symmetry result in the formation surface "hot spots," at which the new electromagnetic waves exhibit higher power density than the incident light. **Figure 5** schematically highlights the dependence of scattering mode on the geometry of the silica nanoparticles. The highly symmetric SiO_x NSs support both resonant scattering and random scattering while the silica nanoparticles with low geometric symmetry (e.g., r-SiO_x NPs with large aspect ratios shown in **Figure S4**) support merely random scattering. When light-absorbing species are attached to the surface of the silica nanoparticles, their optical absorption power can be enhanced by both random scattering and resonant scattering. The DRS spectra of the SiO_x/Pt and SiO_x/Rh composite particles shown in **Figures 2D**, **3D** represent the typical examples highlighting that the optical absorption of quantum-sized metal nanocrystals is significantly enhanced by light scattering (including both random scattering and resonant scattering) on the silica nanoparticles. The random scattering of light from the silica nanoparticles propagates in directions different from that of the incident light, elongating the propagation pathway of light in a material block made of silica/metal composite particles. The longer light pathway allows more incident light to be absorbed by the metal nanocrystals attached on the silica nanoparticles, resulting in an enhancement of overall light absorption. It is worth pointing out that the random scattering does not change the spatial power density of the scattered light. In contrast, resonant scattering of the incident light creates "hot spots" on the surface of SiO_x NSs to significantly increase the local electrical fields (corresponding to power density), which enhance the optical (energy) absorption in the metal nanocrystals attached to the surface of the SiO_x NSs. The mechanistic difference in enhancing light absorption in quantum-sized metal nanocrystals for random scattering and resonant scattering might be more influential toward non-linear optical properties, for example, photo-excited hot electron generation in the quantum-sized metal nanocrystals (Wei et al., 2018). The understanding sheds light on designing composite materials with the dielectric silica nanoparticle antenna to promote performance of applications.

AUTHOR CONTRIBUTIONS

YS, XD, and KR: experimental design, data analysis and interpretation, manuscript writing, and manuscript revision; XD, KR, GH, and RM: material synthesis and characterizations, data acquisition.

ACKNOWLEDGMENTS

This work is supported by the startup from Temple University.

SUPPLEMENTARY MATERIAL

The Supplementary Material for this article can be found online at: https://www.frontiersin.org/articles/10.3389/fchem.2018.00494/full#supplementary-material

REFERENCES

Anderson, M. S. (2010). Nonplasmonic surface enhanced raman spectroscopy using silica microspheres. *Appl. Phys. Lett.* 97:131116. doi: 10.1063/1.3493657

Ashkin, A., and Dziedzic, J. (1981). Observation of optical resonances of dielectric spheres by light scattering. *Appl. Opt.* 20, 1803–1814. doi: 10.1364/AO.20.001803

Ausman, L. K., and Schatz, G. C. (2008). Whispering-gallery mode resonators: surface enhanced raman scattering without plasmons. *J. Chem. Phys.* 129:054704. doi: 10.1063/1.2961012

Biacchi, A. J., and Schaak, R. E. (2015). Ligand-induced fate of embryonic species in the shape-controlled synthesis of rhodium nanoparticles. *ACS Nano* 9, 1707–1720. doi: 10.1021/nn506517e

Codrington, J., Eldabagh, N., Fernando, K., and Foley, J. J, IV. (2017). Unique hot carrier distributions from scattering-mediated absorption. *ACS Photon.* 4, 552–559. doi: 10.1021/acsphotonics.6b00773

Dai, X., Rasamani, K. D., Hu, F., and Sun, Y. (2018a). Mesoporous SiO_2 nanoparticles: a unique platform enabling sensitive detection of rare earth ions with smartphone camera. *Nano-Micro Lett.* 10:55. doi: 10.1007/s40820-018-0208-2

Dai, X., Rasamani, K. D., Wu, S., and Sun, Y. (2018b). Enabling selective aerobic oxidation of alcohols to aldehydes by hot electrons in quantum-sized Rh nanocubes. *Mater. Today Energy* 10, 15–22. doi: 10.1016/j.mtener.2018.08.003

Grandidier, J., Callahan, D. M., Munday, J. N., and Atwater, H. A. (2011). Light absorption enhancement in thin-film solar cells using whispering gallery modes in dielectric nanospheres. *Adv. Mater.* 23, 1272–1276. doi: 10.1002/adma.201004393

Grandidier, J., Weitekamp, R. A., Deceglie, M. G., Callahan, D. M., Battaglia, C., Bukowsky, C. R., et al. (2013). Solar cell efficiency enhancement via light trapping in printable resonant dielectric nanosphere arrays. *Phys. Status Solid A* 210, 255–260. doi: 10.1002/pssa.201228690

Green, D., Lin, J., Lam, Y.-F., Hu, M.-C., Schaefer, D. W., and Harris, M. (2003). Size, volume fraction, and nucleation of stöber silica nanoparticles. *J. Colloid Interface Sci.* 266, 346–358. doi: 10.1016/S0021-979700610-6

Gupta, M. C., Ungaro, C., Foley, J. J., and Gray, S. K. (2018). Optical nanostructures design, fabrication, and applications for solar/thermal energy conversion. *Solar Energy* 165, 100–114. doi: 10.1016/j.solener.2018.01.010

Hao, N., Chen, X., Jayawardana, K. W., Wu, B., Sundhoro, M., and Yan, M. (2015). Shape control of mesoporous silica nanomaterials templated with dual cationic surfactants and their antibacterial activities. *Biomater. Sci.* 4, 87–91. doi: 10.1039/C5BM00197H

Huang, S. H., Jiang, X., Peng, B., Janisch, C., Cocking, A., Özdemir, S. K., et al. (2018). Surface-enhanced Raman scattering on dielectric microspheres with whispering gallery mode resonance. *Photon. Res.* 6, 346–356. doi: 10.1364/PRJ.6.000346

Kuijk, A., van Blaaderen, A., and Imhof, A. (2011). Synthesis of monodisperse, rodlike silica colloids with tunable aspect ratio. *J. Am. Chem. Soc.* 133, 2346–2349. doi: 10.1021/ja109524h

Kumari, G., and Narayana, C. (2012). New nano architecture for SERS applications. *J. Phys. Chem. Lett.* 3, 1130–1135. doi: 10.1021/jz3001344

Kuznetsov, A. I., Miroshnichenko, A. E., Brongersma, M. L., Kivshar, Y. S., and Luk'yanchuk, B. (2016). Optically resonant dielectric nanostructures. *Science* 354:aag2472. doi: 10.1126/science.aag2472

Li, X., Zhou, L., Wei, Y., El-Toni, A. M., Zhang, F., and Zhao, D. (2014). Anisotropic growth-induced synthesis of dual-compartment Janus mesoporous silica nanoparticles for bimodal triggered drugs delivery. *J. Am. Chem. Soc.* 136, 15086–15092. doi: 10.1021/ja508733r

Liu, R.-S., Jin, W.-L., Yu, X.-C., Liu, Y.-C., and Xiao, Y.-F. (2015). Enhanced Raman scattering of single nanoparticles in a high-*Q* whispering-gallery microresonator. *Phys. Rev. A* 91:43836. doi: 10.1103/PhysRevA.91.043836

Matheu, P., Lim, S., Derkacs, D., McPheeters, C., and Yu, E. (2008). Metal and dielectric nanoparticle scattering for improved optical absorption in photovoltaic devices. *Appl. Phys. Lett.* 9311:113108. doi: 10.1063/1.2957980

Matsko, A. B. (2009). *Practical Applications of Microresonators in Optics and Photonics*. Boca Raton, FL: CRC Press.

Mishchenko, M. I., Travis, L. D., and Lacis, A. A. (2002). *Scattering, Absorption, and Emission of Light by Small Particles*. Cambridge: Cambridge University Press.

Murphy, R. P., Hong, K., and Wagner, N. J. (2016). Thermoreversible gels composed of colloidal silica rods with short-range attractions. *Langmuir* 32, 8424–8435. doi: 10.1021/acs.langmuir.6b02107

Rahman, M. M., Younes, H., Lu, J. Y., Ni, G., Yuan, S., Fang, N. X., et al. (2016). Broadband light absorption by silver nanoparticle decorated silica nanospheres. *RSC Adv.* 6, 107951–107959. doi: 10.1039/C6RA24052F

Rahmani, S., Durand, J.-O., Charnay, C., Lichon, L., Férid, M., Garcia, M., et al. (2017). Synthesis of mesoporous silica nanoparticles and nanorods: application to doxorubicin delivery. *Solid State Sci.* 68, 25–31. doi: 10.1016/j.solidstatesciences.2017.04.003

Rasamani, K. D., Foley, J. J, IV., and Sun, Y. (2018). One stone, two birds: silica nanospheres significantly increase photocatalytic activity and colloidal stability of photocatalysts. *Nano Futures* 2:15003. doi: 10.1088/2399-1984/aaa8bd

Rasamani, K. D., Foley, J. J., Beidelman, B., and Sun, Y. (2017). Enhanced optical absorption in semiconductor nanoparticles enabled by nearfield dielectric scattering. *Nano Res.* 10, 1292–1301. doi: 10.1007/s12274-016-1406-1

Son, S., Hwang, S. H., Kim, C., Yun, J. Y., and Jang, J. (2013). Designed synthesis of SiO_2/TiO_2 core/shell structure as light scattering material for highly efficient dye-sensitized solar cells. *ACS Appl. Mater. Interfaces* 5, 4815–4820. doi: 10.1021/am400441v

Ullah, S., Ferreira-Neto, E. P., Pasa, A. A., Alcântara, C. C. J., Acuña, J. J. S., Bilmes, S. A., et al. (2015). Enhanced photocatalytic properties of core@shell SiO_2@TiO_2 nanoparticles. *Appl. Catal. B* 179, 333–343. doi: 10.1016/j.apcatb.2015.05.036

Wei, Q., Wu, S., and Sun, Y. (2018). Quantum-sized metal catalysts for hot-electron-driven chemical transformation. *Adv. Mater.* 30:1802082. doi: 10.1002/adma.201802082

Yin, J., Zang, Y., Yue, C., He, X., Li, J., Wu, Z., et al. (2013). Self-assembled hollow nanosphere arrays used as low *Q* whispering gallery mode resonators on thin film solar cells for light trapping. *Phys. Chem. Chem. Phys.* 15, 16874–16882. doi: 10.1039/c3cp53162g

Zhang, N., Han, C., Xu, Y.-J., Foley, J. J, IV., Zhang, D., Codrington, J., et al. (2016). Near-field dielectric scattering promotes optical absorption by platinum nanoparticles. *Nat. Photo.* 10, 473–482. doi: 10.1038/nphoton.2016.76

Zhu, J., Ozdemir, S. K., Xiao, Y.-F., Li, L., He, L., Chen, D.-R., et al. (2010). On-chip single nanoparticle detection and sizing by mode splitting in an ultrahigh-*Q* microresonator. *Nat. Photon.* 4, 46–49. doi: 10.1038/nphoton.2009.237

Zulfiqar, U., Hussain, S. Z., Awais, M., Khan, M. M. J., Hussain, I., Husain, S.W., et al. (2016). *In-situ* synthesis of bi-modal hydrophobic silica nanoparticles for oil-water separation. *Colloids Surf. A* 508, 301–308. doi: 10.1016/j.colsurfa.2016.08.074

Conflict of Interest Statement: The authors declare that the research was conducted in the absence of any commercial or financial relationships that could be construed as a potential conflict of interest.

REVIEW
published: 09 November 2018
doi: 10.3389/fchem.2018.00550

Encapsulation of Metal Nanoparticle Catalysts Within Mesoporous Zeolites and Their Enhanced Catalytic Performances: A Review

*Dongdong Xu, Hao Lv and Ben Liu**

Jiangsu Key Laboratory of New Power Batteries, Jiangsu Collaborative Innovation Center of Biomedical Functional Materials, School of Chemistry and Materials Science, Nanjing Normal University, Nanjing, China

Metal nanoparticles (NPs) exhibit desired activities in various catalytic reactions. However, the aggregation and sintering of metal NPs usually cause the loss of catalytic performance in practical reaction processes. Encapsulation of catalytically active metal NPs on/within a high-surface-area inorganic support partially resolve such concerns. Microporous zeolites, owing to their rigid frameworks and porous structural features, have been considered as one of ideal inorganic supports. Metal NPs can be easily encapsulated and stabilized within zeolitic frameworks to prevent unwished aggregation during the catalysis. Unfortunately, sole microporous nanochannels (generally <1 nm) in conventional zeolites are not easy to be accessed. The introduction of another set of nanochannel (e.g., mesopore), known as mesoporous zeolites, can greatly improve the mass-transfer efficiency, which is structurally beneficial for most catalytic reactions. The coexistence of micropores and mesopores in inorganic supports provides the synergetic advantages of both fine confinement effect for metal NPs and easy diffusion for organic reactants/intermediates/products. This review focuses on the recent advances in the design and synthesis of mesoporous zeolites-encapsulated metal NP catalysts as well as their desired catalytic performances (activity and stability) in organic reactions. We first discuss the advantages of mesoporous zeolites as the supports and present general strategies for the construction of mesoporous zeolites. Then, the preparation methods on how to encapsulate NP catalysts within both microporous and mesoporous zeolites are clearly demonstrated. Third, some recent important cases on catalytic applications are presented to verify structural advantages of mesoporous zeolite supports. Within the conclusion, the perspectives on future developments in metal NP catalysts encapsulated within mesoporous zeolites are lastly discussed.

Keywords: metal nanoparticle, zeolite, mesoporous, nanoconfinement, mass transfer

Edited by:
Jie He,
University of Connecticut,
United States

Reviewed by:
Gonghu Li,
University of New Hampshire,
United States
Haoquan Zheng,
Shaanxi Normal University, China
Heriberto Pfeiffer,
Universidad Nacional Autónoma de
México, Mexico

***Correspondence:**
Ben Liu
ben.liu@njnu.edu.cn

Specialty section:
This article was submitted to
Nanoscience,
a section of the journal
Frontiers in Chemistry

Received: *31 July 2018*
Accepted: *23 October 2018*
Published: *09 November 2018*

Citation:
Xu D, Lv H and Liu B (2018)
Encapsulation of Metal Nanoparticle
Catalysts Within Mesoporous Zeolites
and Their Enhanced Catalytic
Performances: A Review.
Front. Chem. 6:550.
doi: 10.3389/fchem.2018.00550

INTRODUCTION

Nanocatalysis by metal nanoparticles (NPs) have always attracted sufficient attention from both scientific researches and industrial applications (Astruc et al., 2005; Narayanan and El-Sayed, 2005; Astruc, 2008; Campelo et al., 2009; Cuenya, 2010). Owing to the high surface-to-volume ratio and surface energy, the surface atoms on metal NPs are supposed to be catalytically active for heterogeneous catalytic processes, such as hydrogenation, C-C coupling reaction, carbonylation, oxidation, methanol reforming, fuel cell and so on (Hartwig, 1998; Dyker, 1999; Dupont et al., 2002; Moreno-Manas and Pleixats, 2003; Na et al., 2004; Gilroy et al., 2016). However, precisely because of the high active surface atoms (unstable thermodynamic state), the aggregation and deactivation of the metal NPs by secondary nucleation and recrystallization (or Ostwald ripening) suffer the most serious drawbacks when employed in practical catalytic reactions and hence set great limits on their widely industrial applications (Schmid et al., 1996; Doyle et al., 2003; Challa et al., 2011; Schauermann et al., 2012; Hansen et al., 2013). As a result, the stabilization of metal NPs becomes a challenging research area and can be mainly realized via the combination with soft organic species and hard (or solid) supports (Astruc et al., 2005; Cao et al., 2010). The soft species, also known as capping reagents, are usually classified as polymers (including dendrimers; Corbierre et al., 2001; Crooks et al., 2001), organic or inorganic ligands (Pan et al., 2001), surfactants or micelles (Liz-Marzán and Lado-Touriño, 1996; Kitchens et al., 2003), microemulsions (Capek, 2004), ionic liquids (Dupont et al., 2002; Dupont and Scholten, 2010) and so on. By means of direct chemical binding (generally through heteroatoms) weakly to the surface of metal NPs, these soft protectors will availably block the NP aggregation but also result in the loss of active sites in the meantime due to the subsistent coverage or interfacial interaction (Jin et al., 2017). Additionally, how to resolve the essential question about the recycling potential of these capping metal NPs is always a big challenge. Another significant strategy focuses on the encapsulation of small metal NPs on some hard or solid supports, which will not only prevent NP migration and coalescence but also greatly increase the recycling accessibility (Astruc et al., 2005; Gallon et al., 2007; Campelo et al., 2009; White et al., 2009). Furthermore, the electronic properties of metal NPs on their host support environments can be greatly modified and hence will give rise to various special physical and chemical functions owing to the strong interactions between metal NPs and supports (Ju-Nam and Lead, 2008; Liu et al., 2015, 2017b). Numerous types of nanomaterials can play the role of solid supports, mainly including metal or non-metallic oxides (e.g., TiO_2, ZrO_2, CeO_2, ZnO, Al_2O_3, Fe_3O_4, SiO_2); (Astruc et al., 2005; Campelo et al., 2009), carbon (e.g., carbon sphere, nanotube, graphene, porous carbon); (Joo et al., 2001; Sun and Li, 2004), functionalized polymers (Kralik and Biffis, 2001), and porous framework (MOFs, COFs, zeolites, silica); (Dhakshinamoorthy and Garcia, 2012; Farrusseng and Tuel, 2016; Zhu and Xu, 2016). The oxide supports can classified as inert (e.g., SiO_2) and reactive types based on their chemical reactivity. For example, CeO_2 is a representative kind of reactive oxide support as an enhanced anchoring effect of Ce-O-M born of strong metal-support interaction can efficiently suppress the phase transformation and improve the thermal stability of metal NPs under higher temperature (Alessandro, 2002). When superparamagnetic Fe_3O_4 is utilized as the support, the metal NP/Fe_3O_4 nanomaterials can be easily recovered using a permanent magnet and therefore reused in many runs (Jacinto et al., 2008). Carbon nanostructures, owing to their intrinsic properties, such as high surface area, high electrical conductivity, and unique physical properties and so on, are extremely attractive supports and have been widely employed in the heterogeneous catalysis process (Wildgoose et al., 2006; Kamat, 2009; Liu et al., 2016, 2018). Furthermore, the carbonaceous surface can be easily modified to stabilize the metal NPs. In recent years, the combination between porous frameworks and metal NP technologies has attracted sufficient research and obtained fruitful results (Joo et al., 2001; He et al., 2003; Yang et al., 2003; Mandal et al., 2004; Rioux et al., 2005; White et al., 2009; Aijaz et al., 2012; Lu et al., 2012; Xu et al., 2012). A porous framework generally composed of interconnected network system of pores with distinct diameters, which exist in many natural substances and can be easily created in most of solid chemical nanomaterials. The pores inside the solid structures (usually called interior pore system, while exterior surface can only be accessed in non-porous structures) can nanoconfine the size and shape of metal NPs and inhibit their aggregation and further growth. The throughout pore network renders the mass-transfer more achievable during the catalysis (Satterfield, 1970; Liu et al., 2010, 2017a). Furthermore, the different components of frameworks, dimensions of porous nanochannels, pore sizes and corresponding combinations (hierarchical porosities) endow porous supports with more functional features (Davis, 2002a; Rowsell and Yaghi, 2004). Mesoporous silica with numerous pore sizes, morphologies, and mesochannels have been successfully synthesized by different strategies and also utilized as the support media of metal NPs (Kresge et al., 1992; Zhao et al., 1998; Ciesla and Schüth, 1999; Wan and Zhao, 2007). Additionally, porous carbon materials and MOFs have also been widely prepared to act as the supports for some particular catalytic applications. Each porous support possesses its intrinsic advantages (e.g., carbon receiving greater thermally stabilization) and disadvantages (for example, complex synthesis processes for mesoporous carbon, low framework stabilization of conventional mesoporous silica and MOFs); (Zhao et al., 2006; Arico et al., 2011; Slater and Cooper, 2015).

Compared to abovementioned support media, porous zeolites, due to their inherent structural features, are promised to be an important family of solid supports for the encapsulation of metal NPs. Zeolites, as a kind of highly crystalline inorganic materials having orderly distributed micropores with the diameter <1 nm, have many applications, especially in the field of petrochemical industry (Corma, 1997; Cundy and Cox, 2005; Li and Yu, 2014; Primo and Garcia, 2014; Zaarour et al., 2014). The zeolite framework commonly consists of TO_4 tetrahedra (T denotes Si, Al, and P, etc.) which will build lots of senior structures. Up to 2018, there are totally 239 zeolite framework types (http://www.iza-structure.org/databases/) collected by the International Zeolite Association (IZA) (Guo et al., 2017). Based on different pore windows from TO_4, conventional zeolites can be categorized into small, medium, large, and extra-large pores. The catalytic activities of zeolites largely depend on the structural and compositional features, including pore sizes, channel types and framework compositions. Compared to other catalyst supports, zeolites possess an important and unique feature, known as shape selectivity (e.g., reactants, products and transition-states). When utilized as the solid supports, the regular cavities and nanochannels in zeolites can act as the spaces and sites for the encapsulation of extraneous NPs. When metal NPs form and grow inside the micropores, they would be well-confined at the level of ultrasmall sizes and be not easy to escape from these interconnected cavities. For example, widely studied and applied zeolite ZSM-5 (MFI topology) possesses 10-numbered rings and admits the largest pore accessibility of *ca.* 0.64 nm (Kokotailo et al., 1978), which will greatly confine the crystalline growth of embedded metal NPs. Rigid framework of zeolites offers the important advantages for their applications in harsh catalytic environments; their unique nanochannels also provide the opportunity for shape-selective catalysis (Corma, 1997; Weitkamp, 2000; Davis, 2002a; Moller et al., 2012). So far, many reports on the preparation of zeolite-encapsulated metal NPs show the enhanced catalytic activities. For example, Wang et al. (2016) reported the preparation of ultrasmall Pd NPs encapsulated *in situ* within nanosized silicalite-1 by one-step hydrothermal synthesis. The resultant catalyst showed a highly efficient H_2 generation activity toward the decomposition of formic acid. Liu et al. (2017a) prepared single Pt atoms and Pt NPs with exceptionally high thermal stability within purely siliceous MCM-22 and the catalyst presented good catalytic activity in the dehydrogenation of propane to propylene. Zhang et al. (2017) found that Pd@Beta catalyst exhibited superior selectivity for the hydrogenation of the nitro group when fixing Pd NPs inside Beta zeolite crystals. In addition, there are still many such cases in which metal NPs were well-immobilized inside specific zeolites that exhibited enhanced catalytic performances (Laursen et al., 2010; Moreno et al., 2013; Mielby et al., 2014; Xing et al., 2014; Cheng et al., 2015; Ren et al., 2015; Rubio-Marques et al., 2015; Hosseiniamoli et al., 2018; Tang et al., 2018; Yang et al., 2018).

It is easy to envision that the mass-transfer processes will be greatly restricted as the micropores have been occupied by metal NPs especially involving organic molecules with larger dimensions (Kärger and Ruthven, 1992; Chen et al., 1994; Tao et al., 2006). For purpose of overcoming this shortcoming, massive efforts have been made to construct zeolitic frameworks with larger aperture (Li and Yu, 2014) or create a new set of pore system (known as mesopores) inside the conventional bulk zeolites (Egeblad et al., 2008; Perez-Ramirez et al., 2008; Lopez-Orozco et al., 2011; Möller and Bein, 2013; Parlett et al., 2013; Perego and Millini, 2013; Serrano et al., 2013). Comparatively speaking, the latter is simpler to implement. As shown in **Figure 1A**, purely microporous zeolites (e.g., ZSM-5), ordered mesoporous materials (e.g., MCM-41), and mesoporous zeolites (e.g., meso-ZSM-5) show obviously different Brunauer–Emmett–Teller curves and pore size distributions based N_2 isotherms (Perez-Ramirez et al., 2008). It clearly illustrate that mesoporous zeolites possess both the micropores and mesopores (hierarchical pore systems) inside one crystal, which would be greatly helpful for the mass thransfer of organic molecules. In mesoporous zeolites-encapsulated metal NPs catalysts, metal surfaces (providing the catalytic active sites), the micropores or mesopores (immobilizing and stabilizing the metal NPs) and interconnected mesopores (accelerating the transfer of reactants and products) together built an excellent catalysis system. As schemed in **Figure 1B**, the metal NPs can be immobilized inside both micropores and mesopores. The reactants go through the catalysts along the interconnected mesopores and accelerate the organic reactions. The interior metal NPs also participate in the catalysis, which is not accessible in sole microporous systems.

Considering all of above aspects, this review will highlight the recent progresses on the construction of mesoporous zeolites-encapsulated metal NPs and the investigation of their enhanced activities on various catalytic applications. Conventional zeolites-encapsulated counterparts are not discussed in detail here as some excellent review papers have presented before (Farrusseng and Tuel, 2016; Wang et al., 2018b). In current review, we firstly concern design principles and construction of mesoporous zeolites. Second, we place special focus on how to immobilize or introduce metal NPs into the mesoporous zeolites. Some reported cases will be clearly presented to illustrate the synthetic process of this type of composite catalysts. Third, several typical organic reactions based on mesoporous zeolites-encapsulated metal NPs are recommended to confirm their superior catalytic performances. This review is prospected to provide some important insights on the construction of

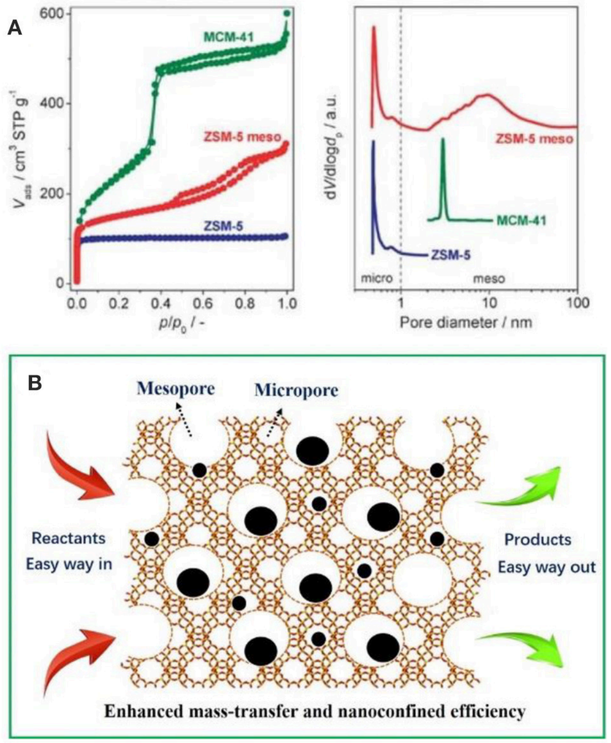

FIGURE 1 | (A) Nitrogen isotherms and corresponded pore size distributions of characteristic porous solids with different diameter. Reprinted with permission from Perez-Ramirez et al. (2008). Copyright 2008 Royal Society of Chemistry. **(B)** Schematic representation of the advantages of mesoporous zeolites-encapsulated metal NP catalysts.

stabilized metal NPs within mesoporous zeolites and how to tune the catalytic performances based on the distinct supports media.

CONSTRUCTION OF MESOPOROUS ZEOLITES

Considering the advantages of hierarchically mesoporous zeolites in various catalytic reactions, many attempts have been made to build the meospores in conventional zeolites. Furthermore, the preparation of mesoporous zeolites is the precondition for the encapsulation of metal NPs. Therefore, the synthetic strategies for mesoporous zeolites are briefly presented here (Lopez-Orozco et al., 2011; Na et al., 2013; Parlett et al., 2013; Serrano et al., 2013; Li et al., 2014a; Shi et al., 2015; Schwieger et al., 2016). The main methods can be generally classified as four aspects: (i) hard-templating, (ii) soft-templating, (iii) post-synthetic treatment, and (iv) stacking or assembly of zeolite crystals. As shown in **Figure 2**, the strategies and the detailed routes are clearly presented schematically.

Most of removable and inert solids with the nanoscale sizes can be employed to act the hard templates for the synthesis of mesoporous zeolites by a hard-templating method, for example, carbon nanostructures (NPs, nanowires, nanotubes, aerogel, ordered porous frameworks), $CaCO_3$ NPs, polystyrene arrays, biological wood and starch (Schwieger et al., 2016). After the removal of these solid species by calcination or acid dissolution, abundant mesopores can be released while the order degree of these mesopores mainly depends on the nanostructures of hard templates. As an instance, three-dimensional ordered mesoporous carbon with large mesopores was developed to construct ordered porous zeolites with distinct framework topologies (e.g., MFI, LTA, FAU, BEA); (Chen et al., 2011). Nevertheless, although the synthesis of mesoporous zeolites using hard-templating methods is greatly high-efficiency, this strategy is often restricted due to the multistep procedures, high costs and health hazards involving during the synthesis.

Soft-templating strategy, referring to the molecular self-assembly of amphiphilic surfactants, is considered as the most possible way to build ordered mesoporous zeolites. The ordered mesopores are greatly favorable for the mass-transfer in the catalytic processes. Choi et al. (2009) and Na et al. (2011) have successfully designed a series of amphiphilic molecules containing quaternary ammoniums, also known as bifunctional surfactants, which were further employed to direct the growth of zeolitic frameworks and ordered mesoscale structures by one-step hydrothermal synthesis. As a consequence, lamellar MFI zeolite nanosheets with a single-unit-cell thickness along *b*-crystallographic axis and a hexagonally-ordered mesoporous aluminosilicate, consisted of truly crystalline zeolitic walls, have successfully obtained. By means of the introduction of aromatic groups into the hydrophobic chain, Xu et al. (2014a,b) prepared single crystalline mesostructured zeolite nanosheets and the ones with 90° rotational boundaries due to the π-π stacking between benzene rings. Additionally, Liu et al. (2012) and Zhu et al. (2014) developed the hydrophilic cationic polymer (e.g., polydiallyldimethylammonium chloride, polystyrene-*co*-4-polyvinylpyridine) to produce single-crystalline mesoporous zeolite Beta and MFI, respectively. The soft-templating method provides the possibility for the better control of both zeolitic framework topologies and mesoporous structures. However, the current synthesis is limited to zeolite MFI or Beta, and therefore how to design the effective organic surfactants for synthesizing other kinds of zeolitic topologies or mesoporous nanostructures is still a big challenge.

The selective removal or extraction of zeolite framework atoms (e.g., Si, Al, or Ti) via post-treatment by acid, alkali, steaming, or other similar methods, can produce some mesopores inside the bulk zeolites. Through the precise control of the desilication or dealumnization from the zeolite frameworks, one could obtain mesoporous zeolites with different Si/Al ratios and desired catalytic sites. This method can effectively result in abundant intracrystalline mesopores but simultaneously decrease the crystallinity of zeolites partially (Groen et al., 2005). The intercrystalline mesopores are a type of mesopores from the stacking of nanocrystals and can be easily found in most of nanomaterials. Through the synthesis of nanosized zeolite crystals, abundant mesopores although in disordered forms but may be destroyed again after the dispersion in the solvents. After the treatment like swelling, intercalation, delamination and pillaring, some layered zeolites can be turned into ultrathin zeolite layers, which further assemble into mesoporous nanostructures. A typical case is the delamination of as-synthesized MCM-22 into two-dimensional ITQ-2, which possess high surface areas and improved catalytic performances (Corma et al., 1998).

Another strategy to construct mesopores in zeolites focuses on the particular crystalline growth model of some particular zeolites. For example, through the intergrowth of MEL/MFI, self-pillared pentasil zeolite with house-of-cards-like morphology was successfully prepared. The hierarchical porosity was created inside the three-dimensional nanosheet assembly by the repetitive branching of the MFI-type zeolitic nanosheets (Zhang et al., 2012). The synthesis process based on this strategy is relatively simple (no need of special templates or tough condition) but only happens in a handful of zeolitic topologies.

Based on the discussion of the strategies to construct mesopores inside zeolites, the different synthetic routes obviously possess their intrinsic advantages and disadvantages. One should consider these processes comprehensively before the choice of a certain route and further combine the corresponded application fields. For instance, when utilized as a porous support, all of routes are suitable for the post-synthetic encapsulation of metal NPs (discussed in next part) but not for the one-step formation of mesoporous zeolite-encapsulated metal NPs composites.

ENCAPSULATION STRATEGIES FOR METAL NPS

The encapsulation of metal NPs inside the porous zeolites can be mainly classified into two types of strategies: post-synthetic process and one-step *in situ* confinement. The post-synthetic

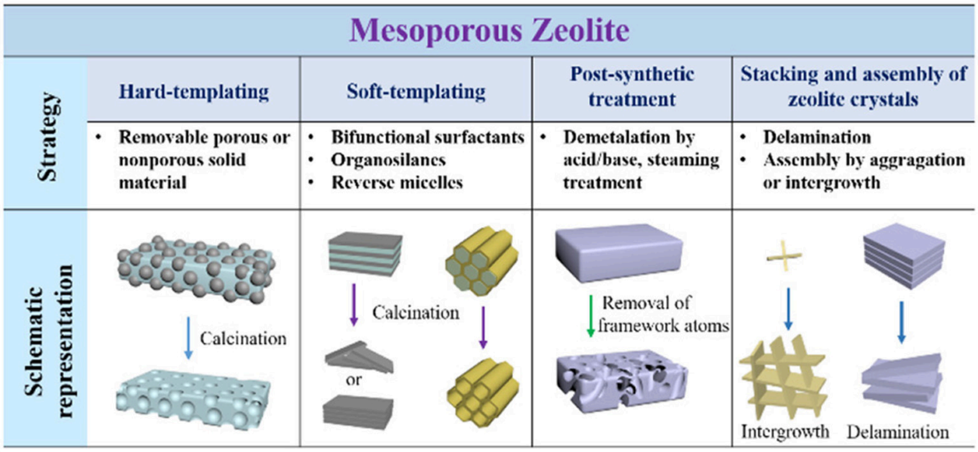

Mesoporous Zeolite

Strategy	Hard-templating	Soft-templating	Post-synthetic treatment	Stacking and assembly of zeolite crystals
	• Removable porous or nonporous solid material	• Bifunctional surfactants • Organosilanes • Reverse micelles	• Demetalation by acid/base, steaming treatment	• Delamination • Assembly by aggragation or intergrowth

FIGURE 2 | Schematic representation of the different strategies for the construction of mesoporous zeolites.

strategy refers to the introduction of metal NPs after the complete construction of zeolitic framework. Contrastively, the one-step confinement method needs the co-crystallization of zeolites and metallic precursors, and follows an *in-situ* reduction to obtain metal NPs.

Post-synthetic Encapsulation Strategy

The post-synthetic strategy is widely utilized to introduce metal NPs into zeolite crystals as it does not limit the framework sorts of zeolites. The process based on this strategy can be reached by means of the soak of zeolite supports in metal colloids (or NPs) or soluble metal precursors. The channels and pores inside zeolites provide the region for the loading of metal NPs. The diffusion of metal NPs or precursors is usually accelerated in a set of relatively large micropores, especially in mesopores. Actually, the diffusion of metal NPs is quite difficult to enter into the interior structures of zeolites where most of them only load at the surface (Wang et al., 2018a). As a representative example, by means of a particular structural transformation of two-dimensional (2D) zeolite into three-dimensional (3D), Liu et al. (2017c) had successfully imbedded single Pt atoms and Pt NPs inside siliceous MCM-22 (Pt@MCM-22). As shown in **Figure 3**, during the swelling process of the lamellar precursor MCM-22 where MWW layers were expanded by the surfactant hexadecyltrimethylammonium, subnanometric Pt species were incorporated into internal channels between individual MWW layers. After the removal of organic species by calcination, lamellar MCM-22 would turn into 3D MCM-22 and simultaneously Pt species were well-confined in external cups (hemi-cages) or encapsulated in the supercages. Subnanometric Pt species were tightly entrapped inside zeolite MCM-22. Due to structural features, Pt@MCM-22 possessed exceptionally high thermal stability even after the treatment in air up to 540°C and showed desired size-selective catalytic activity for the hydrogenation of alkenes.

Most of cases for the preparation of zeolite-encapsulated metal NP catalysts focus on the strategy using soluble metal precursors, also called wetness impregnation method. In this process, metallic species can easily diffuse into the crystal inner and load in the micropores or mesopores after the removal of solvent (e.g., water). Following a conventional reduction step, the metal precursors can be reduced into elementary metal NPs. A synthesis methodology using thiol-based organometallic complexes was presented to encapsulate metal NPs within LTA zeolites, which were successful in encapsulating 1–2 nm monometallic (e.g., Pt, Pd, Ir, Rh, and Ag) or alloyed NPs (e.g., AuPd, AuPt, and PdPt); (Choi et al., 2010; Otto et al., 2016). In pure microporous zeolites, limited by the small diameter of micropores, the size of resultant metals was usually confined in the region of below 2 nm. As for mesoporous zeolite supports, it is more easy to immobilize metal NPs owing to the presence of the larger mesopores. So far, many kinds of metal NPs (Pt, Pd, Ru, Ag, and the corresponded alloys) has been immobilized in mesoporous zeolites with different framework topologies based on this wetness impregnation method (Wang et al., 2015, 2018a; Mendes et al., 2017; Chen et al., 2018; Zhang et al., 2018). Due to the intrinsically structural advantages of mesoporous zeolites and confinement effects for the immobilized metal NPs, all of these reported composite catalysts had exhibited superior catalytic activity in various catalytic reactions (Liu and Corma, 2018).

In situ Confinement Strategy

Metal NPs or precursors can also be introduced into the zeolite crystal inners via the one-pot hydrothermal synthetic process. In this method, as-synthesized metal NPs or soluble metallic precursors were firstly mixed with the synthetic gel for zeolites (e.g., structural-directing agents, silica resources, water, sodium hydroxide, etc.), and then turned into high temperature for the crystallization of zeolites. The as-synthesized composite products were further calcined to remove the organic species and reduced under reduction agents (e.g., H_2, $NaBH_4$) to form metal NPs. Laursen et al. reported the synthesis of zeolite-encapsulated Au NPs for size-selective satalysis (Laursen et al., 2010; Højholt et al., 2011). Ultrasmall Au NPs were uniformly immobilized in silica

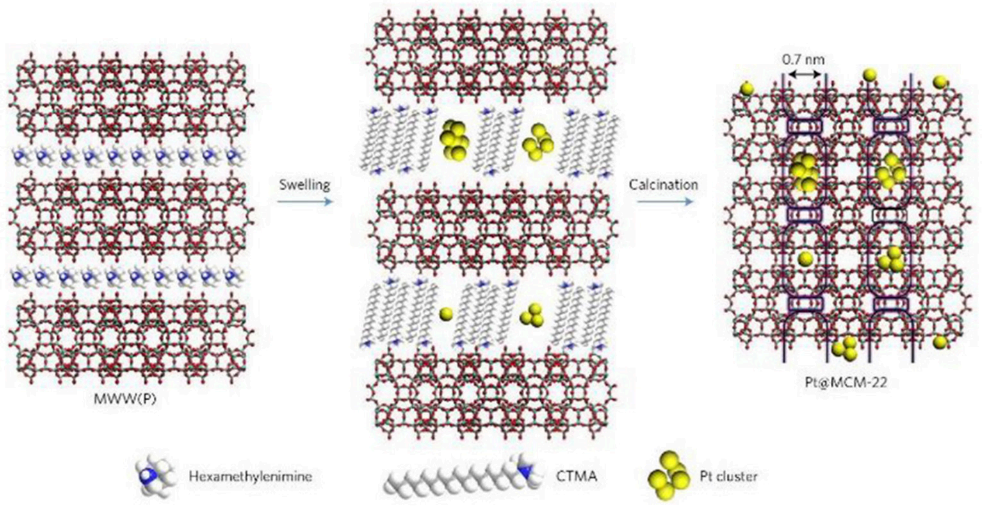

FIGURE 3 | Schematics of the processes for the preparation of Pt@MCM-22. Reprinted with permission from Liu et al. (2017c). Copyright 2016 Macmillan Publishers Ltd: (Nature Materials).

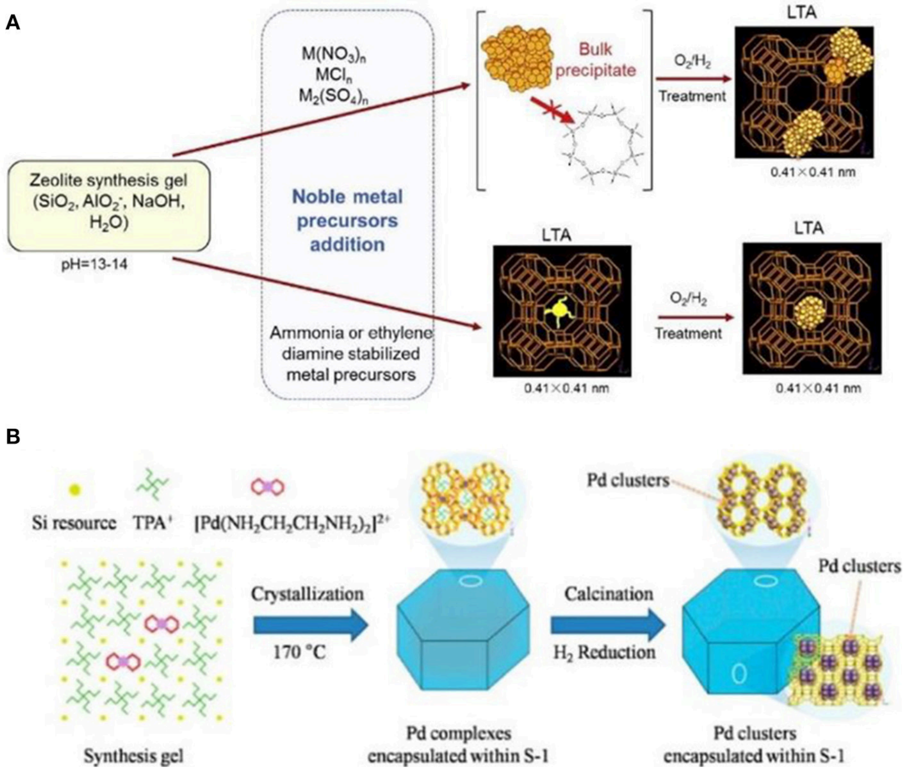

FIGURE 4 | Schematic representation for the formation of zeolite-encapsulated metal NPs via one-pot hydrothermal synthesis process. **(A)** The synthesis process by using metal cations as the precursors (top) and the ligand-stabilized metal precursors (below) to produce LTA-encapsulated metal NPs. Reprinted with permission from Wu et al. (2014). Copyright 2014 Elsevier. **(B)** The MFI-encapsulated Pd NPs synthesized by using [Pd(NH$_2$CH$_2$CH$_2$NH$_2$)$_2$]$^{2+}$ as the Pd precursor. Reprinted with permission from Wang et al. (2016). Copyright 2016 American Chemical Society.

matrix that would be turned into a zeolite phase (silicalite-1). Au NPs embedded inside slicalite-1 mostly possessed a diameter of 1–2 nm; no obvious change in the original size can be seen even under calcination under 500°C. The crystalline zeolite frameworks played the role to confine the growth of Au NPs. However, in this process, a phase separation phenomenon often

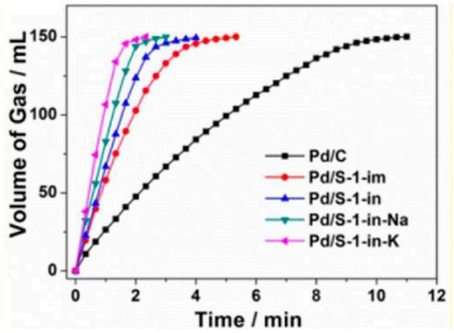

FIGURE 5 | Volume of the generated gas (CO_2 and H_2) vs. time for the dehydrogenation of FA-SF over Pd/C and Pd/S-1. Reprinted with permission from Wang et al. (2016). Copyright 2016 American Chemical Society.

happened due to the harsh crystalline conditions for zeolites, resulting in the formation of larger metal aggregates. Therefore, the usage of metal NPs as the precursors is not widely applied for the construction of zeolite-encapsulated metal catalysts.

Comparatively speaking, metallic precursors are easy to be encapsulated inside the resultant zeolites. Wu et al. (2014) reported the encapsulation of noble metal NPs (Pt, Pd, Rh, Ir, Re, and Ag) in LTA voids (**Figure 4A**). If only metal cations were employed, premature precipitation of these metal hydroxides would be mainly formed. When some ligands (e.g., NH_3, ethylenediamine) were used to stabilize metal cations and protect cationic moieties against precipitation, avoiding premature precipitation resulted in the zeolitic framework units to grow around the ligand-stabilized metal precursors. Finally, a series of metal NPs were successfully encapsulated within the small micropores of LTA zeolite. These composite materials exhibited excellent shape selectivity in both catalytic oxidative dehydrogenation of alkanols and hydrogenation of alkenes. Another important case by using this strategy was reported by Wang et al. (2016). The authors utilized organometallic complex ($[Pd(NH_2CH_2CH_2NH_2)_2]^{2+}$) as the Pd precursor to produce well-dispersed and ultrasmall Pd NPs in nanosized silicalite-1 (MFI). Pd NPs were successfully encapsulated within the intersectional channels of MFI with a diameter of ~1.8 nm (**Figure 4B**), which could be further tuned via the different synthetic conditions (using NaOH or KOH as the base source). They had also reported the preparation of subnanometric bimetallic NPs of $Pd\text{-}M(OH)_2$ (M=Ni, Co) using the similar synthetic methods (Sun et al., 2017). These MFI-encapsulated metal NPs presented superior catalytic performance toward the dehydrogenation of formic acid.

From abovementioned cases, how to balance the crystallization growth of both zeolites and metal NPs is quite important for obtaining the well-dispersed and size-uniform metal NPs inside zeolite crystals. The type of metallic precursors and other synthetic conditions (e.g., alkalinity, silica sources) should be carefully considered. The corresponded catalytic activity may generally depend on how strong the confinement effect is between zeolite frameworks and metal NPs.

CATALYTIC APPLICATIONS

When metal NPs are encapsulated inside conventional zeolites, they are mainly confined in micropores and randomly distributed throughout the zeolite crystals. This type of catalysts proves to be appropriate for organic catalysis involving only small molecules. For example, when Pd cluster-containing zeolite catalysts (Pd/S-1, as shown in **Figure 4B**) was utilized to catalyse the dehydrogenation of formic acid and sodium formate (FA-SF) to produce H_2 (**Figure 5**), Pd/S-1 exhibited complete decomposition of FA in a short time compared to the commercial Pd/C catalyst, also better than the Pd/S-1 catalyst obtained by the impregnation-prepared catalysts (Wang et al., 2016). However, although exhibiting excellent catalytic activity in the dehydrogenation process, this catalyst may miss their ability in organic reactions for the larger molecules, due to the limitation of small microporous channels or accessible void spaces. Additionally, even if the catalytic reactions involving organic molecules with small diameters (less than the micropores) happens in this type of composite catalysts, relatively slow diffusion in the interior zeolites would greatly influence the catalytic processes.

On the other hand, pure zeolite-encapsulated metal NP catalysts will be powerless to catalyse the reactions with big molecular volume (Ju et al., 2015; Dai et al., 2016; Kosinov et al., 2018). The difficulty for mass transfer and bulky molecule catalysis can be significantly improved via producing mesopores inside conventional zeolites as abovementioned. When immobilized on mesoporous zeolites, metal NPs can be not only distributed inside micropores, but also dispersed on the external surface of the mesopores. Those provide more catalytically active sites and easier ways to across the catalysts.

Han et al. (2018) and Kim et al. (2014) successfully prepared mesoporous zeolite nanosponge-encapsulated Co NPs as the efficient catalysts for Fischer-Tropsch (FT) synthesis. In the presence of amphiphilic surfactants containing multiquaternary ammoniums, zeolite nanosponge with ultrathin walls, which could be irregularly interconnected into three-dimensional mesoporous networks, had been synthesized. By means of the incipient wetness impregnation process using $[Co(NO_3)_2{\cdot}6H_2O]$ as the metallic precursor, Co NPs were immobilized into the mesopores. Due to the narrow distribution of mesopore diameters, Co NPs possessed the uniform NP diameters of 4 nm (**Figures 6A,B**). Compared to bulk MFI zeolite or $\gamma\text{-}Al_2O_3$ supports, the cobalt-supporting zeolite nanosponges had higher catalytic performance in FT synthesis (**Figure 6C**). Owing to the strong confinement effect of mesopores, the catalyst exhibited high resistance to sintering, high conversion of CO, and long catalytic lifetime. Meantime, the thin MFI walls contributed to a high selectivity to branched hydrocarbons in the gasoline range (C_5-C_{11}). The authors further increased the loading amount of Co within zeolite Beta or MFI nanosponge, resulting in the construction of Co nanowires or networks along the mesoporous nanochannels (**Figures 6D,E**); (Han et al., 2018). Although the mesopores were blocked by Co nanostructures, the accessibility through microporous windows on the mesopore walls could also ensure a high catalytic activity toward FT

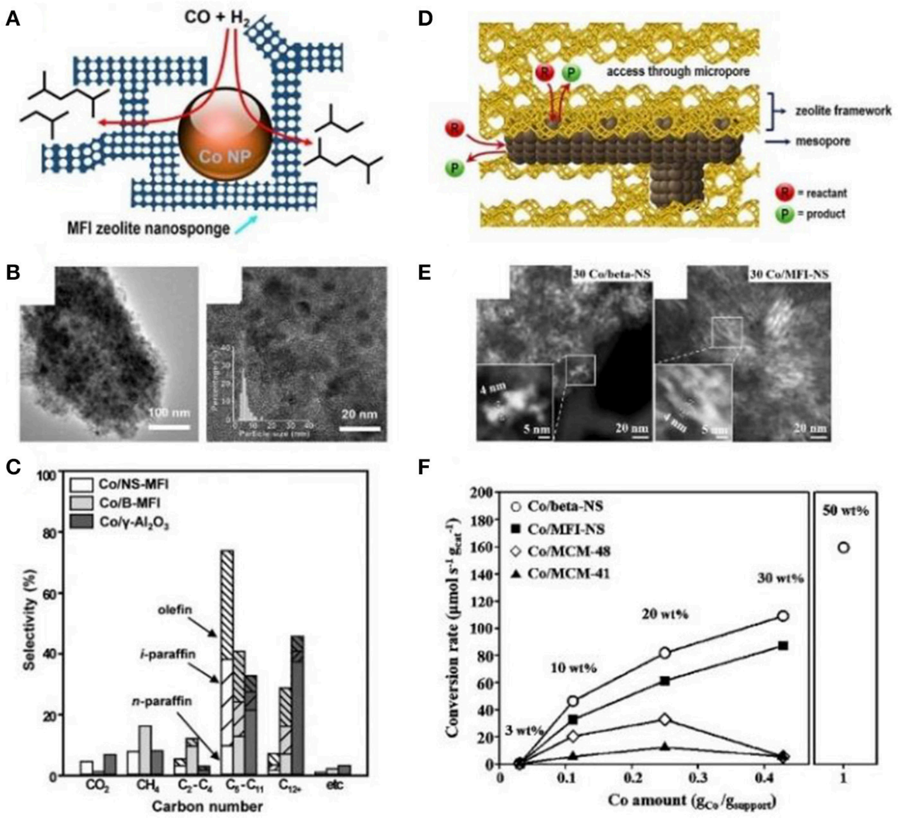

FIGURE 6 | Mesoporous zeolite nanosponge-encapsulated Co NPs for Fischer-Tropsch reaction. **(A)** Schematic representation, **(B)** TEM images, and **(C)** product selectivity of mesoporous MFI nanosheets-encapsulated Co NPs catalysts. Reprinted with permission from Kim et al. (2014). Copyright 2014 American Chemical Society. **(D)** Schematic representation, **(E)** TEM images, and **(F)** CO conversion rates of mesoporous Beta and MFI nanosponge-encapsulated Co NPs with high loading amount, accessible through microporous windows at the encasing mesopore walls. Reprinted with permission from Han et al. (2018). Copyright 2017 American Chemical Society.

synthesis (**Figure 6F**). Furthermore, the zeolite nanosponge-encapsulated Co nanostructures also exhibited high catalytic performance in benzene hydrogenation and furfural-to-γ-valerolactone conversion.

Based on *in situ* confinement strategy, mesoporous silicalite-1 nanocrystals-encapsulated Pd NPs (Pd@mnc-S1) could be well-constructed by Cui et al. (2016) After mixing silica, Pd^{2+}, small amount of polyvinyl pyrrolidone (PVP) and water, silicalite-1 nanocrystals with built-in mesopores were synthesized following the Kirkendall growth process (**Figure 7A**). The presence of PVP could prevent the aggregation of palladium oxide or hydroxide NPs under the high pH value. Metallic Pd NPs were obtained via successive calcination of the as-synthesized products in oxygen and hydrogen atmospheres. Pd NPs with a diameter in the range of 2∼5 nm exhibited a high thermal and chemical stability, indicating the high encapsulation of Pd NPs inside the framework of silicalite-1 nanocrystals. The intrinsic micropores and Pd NPs in Pd@mnc-S1 resulted in good shape selectivity for a series of model reactions, such as hydrogenation, oxidation and C-C coupling reactions (**Figure 7B**). For example, catalytic hydrogenation conversion of nitrobenzene into aniline could be efficiently completed using Pd@mnc-S1 as the catalyst. However, only a negligible amount of 1-nitronaphthalene would be converted into naphthalen-1-amine over Pd@mnc-S1. As well-known, 1-nitronaphthalene possess the molecule size about 7.3 × 6.6 Å, bigger than the micropores of zeolite MFI (5.3 × 5.6 Å), resulting in the inability of Pd@mnc-S1 to catalyse the bulk organic molecules. The same results of shape selectivity had been found in the oxidation and C-C reactions. Additionally, the presence of mesopores inside zeolite supports greatly enhanced the mass-transfer efficiency and thus gave rise to the high catalytic activity. The authors further found that the number of acid sites in mesoporous H-ZSM-5 frameworks could play as "solid ligands" to activate the embedded Pd NPs for organic synthesis (e.g., Suzuki coupling reactions); (Ke et al., 2017).

In order to catalyse the hydrodeoxygenation of the phenolic compounds in bio-oil to alkanes, Wang et al. (2015) immobilized Ru NPs into *b*-axis-aligned mesoporous ZSM-5 (Ru/HZSM-5-OM) as an efficient catalyst. Owing to the open mesopores and rich exposed acid sites, Ru/HZSM-5-OM exhibited better catalytic activity in the hydrodeoxygenation of bulky 2, 6-dimethoxyphenol (as a model reaction) than bulk or mesoporous

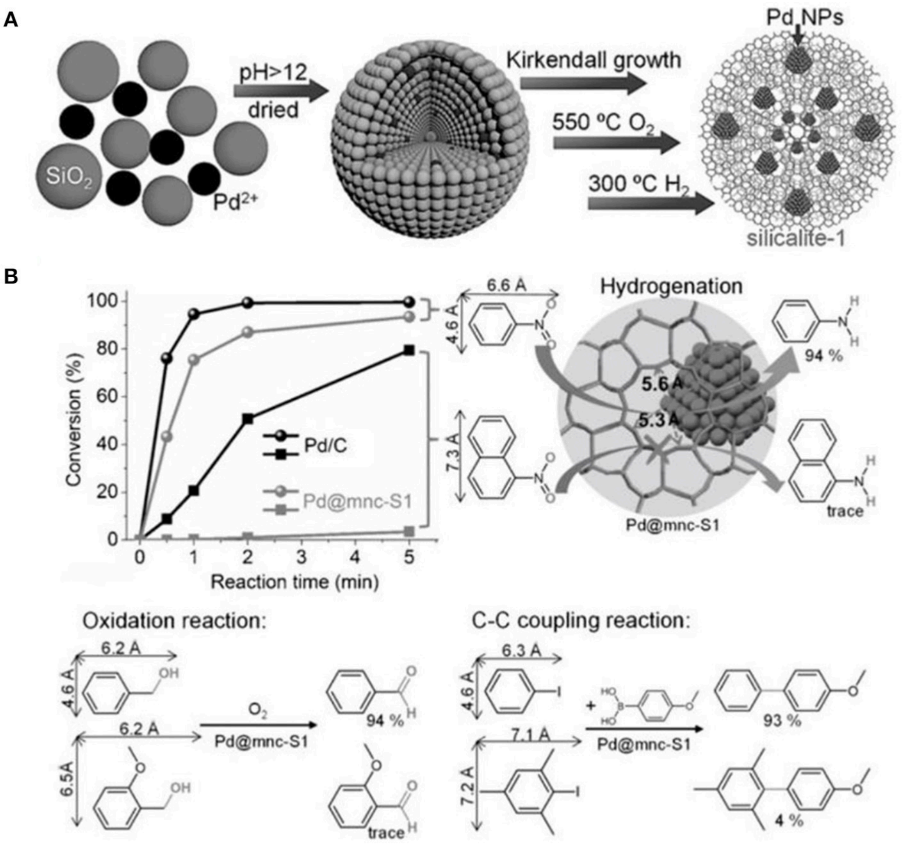

FIGURE 7 | Mesoporous silicalite-1 nanocrystals-encapsulated Pd NPs (Pd@mnc-S1) with enhanced catalytic activity in various organic reactions. **(A)** The synthesis scheme for the preparation of Pd@mnc-S1 via *in situ* confinement process. **(B)** The different organic reactions (hydrogenation, oxidation, and C-C coupling reactions) catalyzed by Pd@mnc-S1. Reprinted with permission from Cui et al. (2016). Copyright 2016 Wiley.

HZSM-5-encapsulated Ru NPs. This is because the bulky reactant molecule could easily transfer through the open mesopores and complete the reaction on the external/mesopore acid sites in HZSM-5-OM. A high conversion rate and cyclohexane selectivity could be reached when using Ru/HZSM-5-OM as the catalyst. Ru/HZSM-5-OM also presented excellent recyclability, keeping the high conversion (95.8%) and cyclohexane selectivity (69.0%) after recycling ten times (**Figure 8**). Due to the fine confinement effect from HZSM-5-OM, Ru NPs could be well-stabilized in zeolitic framework as no Ru species in the liquid had been detected under the reaction conditions or after the recycling test.

Another interesting strategy to build porous zeolite-encapsulated metal NP catalysts is promised to utilize hollow zeolites as the inorganic supports (Dong et al., 2003; Ren et al., 2007; Li et al., 2014b,c; Pagis et al., 2016; Prieto et al., 2016). The structural features endow them into hierarchically macro-microporous or macro-meso-microporous systems, both of which are structurally beneficial for mass transfer of the reactants and products. The active sites of metal NPs on relatively thin shell are easily accessible. For example, Li et al. (2014b) produced Pt NPs inside hollow silicalite-1 crystals as the composite catalysts for size-selective hydrogenation of aromatic compounds (**Figure 9A**). The hydrogenation product of methylcyclohexane from toluene possessed a kinetic diameter less than MFI micropores and thus easily diffused through the zeolitic shell. Contrastively, the product of trimethylcyclohexane from mesitylene could not go across the zeolite shell to reach the reaction sites on Pd NPs, resulting in the poor catalytic activity of

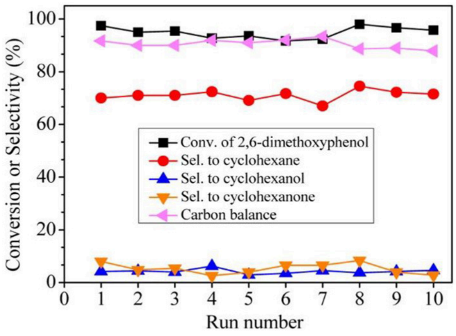

FIGURE 8 | Recycling tests of catalyst Ru/HZSM-5-OM in the hydrodeoxygenation of 2,6-dimethoxyphenol. Reprinted with permission from Wang et al. (2015). Copyright 2015 American Chemical Society.

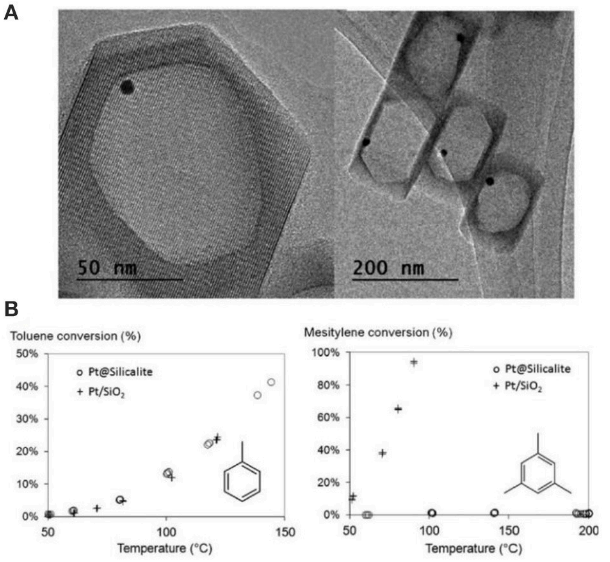

FIGURE 9 | Hollow silicalite-1-encapsulated Pt NPs (Pt@Sil-1) as size selective hydrogenation of aromatic compounds. **(A)** TEM images of Pt@Sil-1. **(B)** Conversion vs. temperature plots for the hydrogenation of toluene and mesitylene from Pt@Sil-1 and Pt/SiO$_2$ catalysts. Reprinted with permission from Li et al. (2014b). Copyright 2014 Royal Society of Chemistry.

Pt@Sil-1 on the hydrogenation of bulky mesitylene (**Figure 9B**). Although the catalyst in this case did not perform the activity toward bulky molecules (only size selectivity), it reminds us that, if some mesopores are created on the zeolite shell (hollow mesoporous zeolites), corresponded catalytic performance will be greatly improved in both shape selectivity and bulky molecular catalysis. Owing to the presence of hierarchically macro-meso-micropores in one zeolite support, the composite catalysts after the encapsulation of metal NPs will be most efficient for various organic reactions.

As for the most cases mentioned above, the mesopores in the final catalysts are not particularly ordered, which may lead to the weak mass transfer efficiency compared to the ordered ones. How to construct a set of ordered mesopores inside the zeolites supports for the encapsulation of metal NPs is always a big challenging subject. The catalytic performances (e.g., conversion, shape selectivity, stability) in these expected catalysts should be greatly improved. The catalysts are theoretically employed in many fields of organic or small inorganic molecule reactions.

SUMMARY AND PERSPECTIVES

Mesoporous zeolite is a type of ideal inorganic supports for the encapsulation of metal NPs to produce composite catalysts for various organic reactions. In this review, the advantages of mesoporous zeolites as the supports are presented in detail with the comparison to other nanomaterials like metal or non-metallic oxides, carbon, polymers, and porous frameworks. The main strategies for the construction of mesoporous zeolites and the encapsulation methods for metal NPs have been summarized as these two aspects are extremely important to combine mesoporous zeolites and metal NPs into composite catalysts. Several representative examples exhibited well-catalytic performances in reactant conversions, shape selectivities, and stabilities in many organic catalytic reactions. There are still a lot of challenges in the preparation of mesoporous zeolite-encapsulated metal NPs, such as the degree of mesoporous order, the dispersity and size distribution of encapsulated metal NPs, and the large-scale synthesis, and so on. Additionally, the structure-performance relationship between catalytic reactions and catalyst structures (different mesopores, micropores, and metals) should be carefully revealed in the future.

As for the construction of ordered mesoporous zeolite-encapsulated metal NP catalysts, some purposed strategies are presented. The appropriate process should be the one-pot synthesis via the mixing of zeolite gel and optimized metallic precursors (Wu et al., 2014) under the presence of some special structural-directing surfactants (Na et al., 2011) or ordered hard templates (Chen et al., 2011). The most metal precursors can be retained after the removal of templates and reduced *in situ* into NPs inside the micropores. In this way, the ordered mesopores can run throughout zeolite crystals and meanwhile metal NPs are tightly immobilized inside microporous frameworks, resulting in the higher mass transfer efficiency and enhanced catalytic activity, especially for the bulky molecular catalysis. We hope this review can provide useful insights on the synthesis of zeolites supported metal NP composite catalysts and the understanding of the relationship between the catalytic performance and nanostructure of composite catalysts.

AUTHOR CONTRIBUTIONS

All authors listed have made a substantial, direct and intellectual contribution to the work, and approved it for publication.

ACKNOWLEDGMENTS

This work is supported by National Natural Science Foundation of China (No. 21501095) and Jiangsu Specially Appointed Professor Plan. The authors also thank the supports from Priority Academic Program Development of Jiangsu Higher Education Institutions, National and Local Joint Engineering Research Center of Biomedical Functional Materials.

REFERENCES

Aijaz, A., Karkamkar, A., Choi, Y. J., Tsumori, N., Rönnebro, E., Autrey, T., et al. (2012). Immobilizing highly catalytically active Pt nanoparticles inside the pores of metal–organic framework: a double solvents approach. *J. Am. Chem. Soc.* 134, 13926–13929. doi: 10.1021/ja3043905

Alessandro, T. (2002). *Catalysis by Ceria and Related Materials*. Singapore: World Scientific.

Arico, A. S., Bruce, P., Scrosati, B., Tarascon, J.-M., and Van Schalkwijk, W. (2011). *Nanostructured Materials for Advanced Energy Conversion and Storage Devices*. Singapore: Nature Publishing Group, World Scientific.

Astruc, D. (2008). *Nanoparticles and Catalysis*. Hoboken, NJ: John Wiley & Sons.

Astruc, D., Lu, F., and Aranzaes, J. R. (2005). Nanoparticles as recyclable catalysts: the frontier between homogeneous and heterogeneous catalysis. *Angew. Chem. Int. Ed.* 44, 7852–7872. doi: 10.1002/anie.200500766

Campelo, J. M., Luna, D., Luque, R., Marinas, J. M., and Romero, A. A. (2009). Sustainable preparation of supported metal nanoparticles and their applications in catalysis. *ChemSusChem* 2, 18–45. doi: 10.1002/cssc.200800227

Cao, A., Lu, R., and Veser, G. (2010). Stabilizing metal nanoparticles for heterogeneous catalysis. *Phys. Chem. Chem. Phys.* 12, 13499–13510. doi: 10.1039/c0cp00729c

Capek, I. (2004). Preparation of metal nanoparticles in water-in-oil (w/o) microemulsions. *Adv. Colloid Interface Sci.* 110, 49–74. doi: 10.1016/j.cis.2004.02.003

Challa, S. R., Delariva, A. T., Hansen, T. W., Helveg, S., Sehested, J., Hansen, P. L., et al. (2011). Relating rates of catalyst sintering to the disappearance of individual nanoparticles during Ostwald ripening. *J. Am. Chem. Soc.* 133, 20672–20675. doi: 10.1021/ja208324n

Chen, H., Wydra, J., Zhang, X., Lee, P. S., Wang, Z., Fan, W., et al. (2011). Hydrothermal synthesis of zeolites with three-dimensionally ordered mesoporous-imprinted structure. *J. Am. Chem. Soc.* 133, 12390–12393. doi: 10.1021/ja2046815

Chen, N., Degnan, T. F., and Smith, C. M. (1994). *Molecular Transport and Reaction in Zeolites*. New York, NY: John Wiley & Sons.

Chen, Z., Chen, C., Zhang, J., Zheng, G., Wang, Y., Dong, L., et al. (2018). Zeolite Y microspheres with perpendicular mesochannels and metal@Y heterostructures for catalytic and SERS applications. *J. Mater. Chem. A* 6, 6273–6281. doi: 10.1039/c7ta10444h

Cheng, K., Zhang, L., Kang, J., Peng, X., Zhang, Q., and Wang, Y. (2015). Selective transformation of syngas into gasoline-range hydrocarbons over mesoporous H-ZSM-5-supported cobalt nanoparticles. *Chem. Eur. J.* 21, 1928–1937. doi: 10.1002/chem.201405277

Choi, M., Na, K., Kim, J., Sakamoto, Y., Terasaki, O., and Ryoo, R. (2009). Stable single-unit-cell nanosheets of zeolite MFI as active and long-lived catalysts. *Nature* 461, 246–249. doi: 10.1038/nature08288

Choi, M., Wu, Z., and Iglesia, E. (2010). Mercaptosilane-assisted synthesis of metal clusters within zeolites and catalytic consequences of encapsulation. *J. Am. Chem. Soc.* 132, 9129–9137. doi: 10.1021/ja102778e

Ciesla, U., and Schüth, F. (1999). Ordered mesoporous materials. *Microporous Mesoporous Mater.* 27, 131–149. doi: 10.1016/S1387-1811(98)00249-2

Corbierre, M. K., Cameron, N. S., Sutton, M., Mochrie, S. G., Lurio, L. B., Rühm, A., et al. (2001). Polymer-stabilized gold nanoparticles and their incorporation into polymer matrices. *J. Am. Chem. Soc.* 123, 10411–10412. doi: 10.1021/ja0166287

Corma, A. (1997). From microporous to mesoporous molecular sieve materials and their use in catalysis. *Chem. Rev.* 97, 2373–2420. doi: 10.1021/cr960406n

Corma, A., Fornes, V., Pergher, S. B., Maesen, T. L. M., and Buglass, J. G. (1998). Delaminated zeolite precursors as selective acidic catalysts. *Nature* 396, 353–356. doi: 10.1038/24592

Crooks, R. M., Zhao, M., Sun, L., Chechik, V., and Yeung, L. K. (2001). Dendrimer-encapsulated metal nanoparticles: synthesis, characterization, and applications to catalysis. *Acc. Chem. Res.* 34, 181–190. doi: 10.1021/ar000110a

Cuenya, B. R. (2010). Synthesis and catalytic properties of metal nanoparticles: size, shape, support, composition, and oxidation state effects. *Thin Solid Films* 518, 3127–3150. doi: 10.1016/j.tsf.2010.01.018

Cui, T. L., Ke, W. Y., Zhang, W. B., Wang, H. H., Li, X. H., and Chen, J. S. (2016). Encapsulating palladium nanoparticles inside mesoporous MFI zeolite nanocrystals for shape-selective catalysis. *Angew. Chem. Int. Ed.* 55, 9178–9182. doi: 10.1002/anie.201602429

Cundy, C. S., and Cox, P. A. (2005). The hydrothermal synthesis of zeolites: Precursors, intermediates and reaction mechanism. *Microporous Mesoporous Mater.* 82, 1–78. doi: 10.1016/j.micromeso.2005.02.016

Dai, C., Zhang, A., Liu, M., Gu, L., Guo, X., and Song, C. (2016). Hollow alveolus-like nanovesicle assembly with metal-encapsulated hollow zeolite nanocrystals. *ACS Nano* 10, 7401–7408. doi: 10.1021/acsnano.6b00888

Davis, M. E. (2002a). Ordered porous materials for emerging applications. *Nature* 417, 813–821. doi: 10.1038/nature00785

Dhakshinamoorthy, A., and Garcia, H. (2012). Catalysis by metal nanoparticles embedded on metal–organic frameworks. *Chem. Soc. Rev.* 41, 5262–5284. doi: 10.1039/C2CS35047E

Dong, A., Ren, N., Yang, W., Wang, Y., Zhang, Y., Wang, D., et al. (2003). Preparation of hollow zeolite spheres and three-dimensionally ordered macroporous zeolite monoliths with functionalized interiors. *Adv. Funct. Mater.* 13, 943–948. doi: 10.1002/adfm.200304405

Doyle, A. M., Shaikhutdinov, S. K., Jackson, S. D., and Freund, H. J. (2003). Hydrogenation on metal surfaces: why are nanoparticles more active than single crystals? *Angew. Chem. Int. Ed.* 42, 5240–5243. doi: 10.1002/anie.200352124

Dupont, J., Fonseca, G. S., Umpierre, A. P., Fichtner, P. F., and Teixeira, S. R. (2002). Transition-metal nanoparticles in imidazolium ionic liquids: recycable catalysts for biphasic hydrogenation reactions. *J. Am. Chem. Soc.* 124, 4228–4229. doi: 10.1021/ja025818u

Dupont, J., and Scholten, J. D. (2010). On the structural and surface properties of transition-metal nanoparticles in ionic liquids. *Chem. Soc. Rev.* 39, 1780–1804. doi: 10.1039/B822551F

Dyker, G. (1999). Transition metal catalyzed coupling reactions under C–H activation. *Angew. Chem. Int. Ed.* 38, 1698–1712.

Egeblad, K., Christensen, C. H., Kustova, M., and Christensen, C. H. (2008). Templating mesoporous zeolites. *Chem. Mater.* 20, 946–960. doi: 10.1021/cm702224p

Farrusseng, D., and Tuel, A. (2016). Perspectives on zeolite-encapsulated metal nanoparticles and their applications in catalysis. *New J. Chem.* 40, 3933–3949. doi: 10.1039/c5nj02608c

Gallon, B. J., Kojima, R. W., Kaner, R. B., and Diaconescu, P. L. (2007). Palladium nanoparticles supported on polyaniline nanofibers as a semi-heterogeneous catalyst in water. *Angew. Chem. Int. Ed.* 46, 7251–7254. doi: 10.1002/anie.200701389

Gilroy, K. D., Ruditskiy, A., Peng, H. C., Qin, D., and Xia, Y. (2016). Bimetallic nanocrystals: syntheses, properties, and applications. *Chem. Rev.* 116, 10414–10472. doi: 10.1021/acs.chemrev.6b00211

Groen, J. C., Peffer, L. A., Moulijn, J. A., and Pérez-Ramírez, J. (2005). Mechanism of hierarchical porosity development in mfi zeolites by desilication: the role of aluminium as a pore-directing agent. *Chem. Eur. J.* 11, 4983–4994. doi: 10.1002/chem.200500045

Guo, P., Yan, N., Wang, L., and Zou, X. (2017). Database mining of zeolite structures. *Cryst. Growth Des.* 17, 6821–6835. doi: 10.1021/acs.cgd.7b01410.

Han, J., Cho, J., Kim, J.-C., and Ryoo, R. (2018). Confinement of supported metal catalysts at high loading in the mesopore network of hierarchical zeolites, with access via the microporous windows. *ACS Catal.* 8, 876–879. doi: 10.1021/acscatal.7b04183

Hansen, T. W., DeLaRiva, A. T., Challa, S. R., and Datye, A. K. (2013). Sintering of catalytic nanoparticles: particle migration or Ostwald ripening? *Acc. Chem. Res.* 46, 1720–1730. doi: 10.1021/ar3002427

Hartwig, J. F. (1998). Transition metal catalyzed synthesis of arylamines and aryl ethers from aryl halides and triflates: scope and mechanism. *Angew. Chem. Int. Ed.* 37, 2046–2067

He, J., Kunitake, T., and Nakao, A. (2003). Facile *in situ* synthesis of noble metal nanoparticles in porous cellulose fibers. *Chem. Mater.* 15, 4401–4406. doi: 10.1021/cm034720r

Højholt, K. T., Laursen, A. B., Kegnæs, S., and Christensen, C. H. (2011). Size-selective oxidation of aldehydes with zeolite encapsulated gold nanoparticles. *Top. Catal.* 54, 1026. doi: 10.1007/s11244-011-9722-x

Hosseiniamoli, H., Bryant, G., Kennedy, E. M., Mathisen, K., Nicholson, D., Sankar, G., et al. (2018). Understanding structure–function relationships in zeolite-supported Pd catalysts for oxidation of ventilation air methane. *ACS Catal.* 5852–5863. doi: 10.1021/acscatal.7b04462

Jacinto, M. J., Kiyohara, P. K., Masunaga, S. H., Jardim, R. F., and Rossi, L. M. (2008). Recoverable rhodium nanoparticles: synthesis, characterization and catalytic performance in hydrogenation reactions. *Appl. Catal. A Gen.* 338, 52–57. doi: 10.1016/j.apcata.2007.12.018

Jin, L., Liu, B., Duay, S. S., and He, J. (2017). Engineering surface ligands of noble metal nanocatalysts in tuning the product selectivity. *Catalysts* 7, 44. doi: 10.3390/catal7020044

Joo, S. H., Choi, S. J., Oh, I., Kwak, J., Liu, Z., Terasaki, O., et al. (2001). Ordered nanoporous arrays of carbon supporting high dispersions of platinum nanoparticles. *Nature* 412, 169–172. doi: 10.1038/35084046

Ju, C., Wang, Y., Huang, Y., and Fang, Y. (2015). Design of mesoporous KA zeolite supported sulfur-tolerant noble metal catalyst for naphthalene hydrogenation. *Fuel* 154, 80–87. doi: 10.1016/j.fuel.2015.03.035

Ju-Nam, Y., and Lead, J. R. (2008). Manufactured nanoparticles: an overview of their chemistry, interactions and potential environmental implications. *Sci. Total Environ.* 400, 396–414. doi: 10.1016/j.scitotenv.2008.06.042

Kamat, P. V. (2009). Graphene-based nanoarchitectures. Anchoring semiconductor and metal nanoparticles on a two-dimensional carbon support. *J. Phys. Chem. Lett*. 1, 520–527. doi: 10.1021/jz900265j

Kärger, J., and Ruthven, D. (1992). *Diffusion in Zeolites*. New York, NY: John Wiley.

Ke, W., Cui, T., Yu, Q., Wang, M., Lv, L., Wang, H., et al. (2017). Mesoporous H-ZSM-5 nanocrystals with programmable number of acid sites as "solid ligands" to activate Pd nanoparticles for C–C coupling reactions. *Nano Res.* 11, 874–881. doi: 10.1007/s12274-017-1698-9

Kim, J.-C., Lee, S., Cho, K., Na, K., Lee, C., and Ryoo, R. (2014). Mesoporous MFI zeolite nanosponge supporting cobalt nanoparticles as a Fischer–Tropsch catalyst with high yield of branched hydrocarbons in the gasoline range. *ACS Catal.* 4, 3919–3927. doi: 10.1021/cs500784v

Kitchens, C. L., and McLeod, M. C., Roberts, C. B. (2003). Solvent effects on the growth and steric stabilization of copper metallic nanoparticles in AOT reverse micelle systems. *J. Phys. Chem. B* 107, 11331–11338. doi: 10.1021/jp0354090

Kokotailo, G., Lawton, S., and Olson, D. (1978). Structure of synthetic zeolite ZSM-5. *Nature* 272, 437–438. doi: 10.1038/272437a0

Kosinov, N., Liu, C., Hensen, E. J. M., and Pidko, E. A. (2018). Engineering of transition metal catalysts confined in zeolites. *Chem. Mater.* 30, 3177–3198. doi: 10.1021/acs.chemmater.8b01311

Kralik, M., and Biffis, A. (2001). Catalysis by metal nanoparticles supported on functional organic polymers. *J. Mol. Catal. A: Chem.* 177, 113–138. doi: 10.1016/S1381-1169(01)00313-2

Kresge, C. T., Leonowicz, M. E., Roth, W. J., Vartuli, J. C., and Beck, J. S. (1992). Ordered mesoporous molecular sieves synthesized by a liquid-crystal template mechanism. *Nature* 359, 710–712. doi: 10.1038/359710a0

Laursen, A. B., Højholt, K. T., Lundegaard, L. F., Simonsen, S. B., Helveg, S., Schüth, F., et al. (2010). Substrate size-selective catalysis with zeolite-encapsulated gold nanoparticles. *Angew. Chem. Int. Ed.* 49, 3504–3507. doi: doi.org/10.1002/anie.200906977

Li, K., Valla, J., and Garcia-Martinez, J. (2014a). Realizing the commercial potential of hierarchical zeolites: new opportunities in catalytic cracking. *ChemCatChem* 6, 46–66. doi: 10.1002/cctc.201300345

Li, S., Boucheron, T., Tuel, A., Farrusseng, D., and Meunier, F. (2014b). Size-selective hydrogenation at the subnanometer scale over platinum nanoparticles encapsulated in silicalite-1 single crystal hollow shells. *Chem. Commun.* 50, 1824–1826. doi: 10.1039/C3CC48648F

Li, S., Tuel, A., Laprune, D., Meunier, F., and Farrusseng, D. (2014c). Transition-metal nanoparticles in hollow zeolite single crystals as bifunctional and size-selective hydrogenation catalysts. *Chem. Mater.* 27, 276–282. doi: 10.1021/cm503921f

Li, Y., and Yu, J. (2014). New Stories of zeolite structures: their descriptions, determinations, predictions, and evaluations. *Chem. Rev.* 114, 7268–7316. doi: 10.1021/cr500010r

Liu, B., Jiang, T., Zheng, H., Dissanayke, S., Song, W., Federico, A., et al. (2017a). Nanoengineering of aggregation-free and thermally-stable gold nanoparticles in mesoporous frameworks. *Nanoscale* 9, 6380–6390. doi: 10.1039/C7NR01988B

Liu, B., Jin, L., Zhong, W., Lopes, A., Suib, S. L., and He, J. (2018). Ultrafine and ligand-free precious metal (Ru, Ag, Au, Rh and Pd) nanoclusters supported on phosphorus-doped carbon. *Chem. Eur. J.* 24, 2565–2569. doi: 10.1002/chem.201705504

Liu, B., Kuo, C. H., Chen, J., Luo, Z., Thanneeru, S., Li, W., et al. (2015). Ligand-assisted co-assembly approach toward mesoporous hybrid catalysts of transition-metal oxides and noble metals: photochemical water splitting. *Angew. Chem. Int. Ed.* 54, 9061–9065. doi: 10.1002/anie.201502892

Liu, B., Wang, P., Lopes, A., Jin, L., Zhong, W., Pei, Y., et al. (2017b). Au–carbon electronic interaction mediated selective oxidation of styrene. *ACS Catal.* 7, 3483–3488. doi: 10.1021/acscatal.7b01048

Liu, B., Yao, H., Song, W., Jin, L., Mosa, I. M., Rusling, J. F., et al. (2016). Ligand-free noble metal nanocluster catalysts on carbon supports via "soft" nitriding. *J. Am. Chem. Soc.* 138, 4718–4721. doi: 10.1021/jacs.6b01702

Liu, F., Willhammar, T., Wang, L., Zhu, L., Sun, Q., Meng, X., et al. (2012). ZSM-5 zeolite single crystals withb-axis-aligned mesoporous channels as an efficient catalyst for conversion of bulky organic molecules. *J. Am. Chem. Soc.* 134, 4557–4560. doi: 10.1021/ja300078q

Liu, J., Qiao, S. Z., Budi, H. S., and Lu, G. Q. (2010). Monodisperse yolk–shell nanoparticles with a hierarchical porous structure for delivery vehicles and nanoreactors. *Angew. Chem.* 122, 5101–5105. doi: 10.1002/anie.201001252

Liu, L., and Corma, A. (2018). Metal catalysts for heterogeneous catalysis: from single atoms to nanoclusters and nanoparticles. *Chem. Rev.* 118, 4981–5079. doi: 10.1021/acs.chemrev.7b00776

Liu, L., Diaz, U., Arenal, R., Agostini, G., Concepcion, P., and Corma, A. (2017c). Generation of subnanometric platinum with high stability during transformation of a 2D zeolite into 3D. *Nat. Mater.* 16, 132–138. doi: 10.1038/nmat4757

Liz-Marzán, L. M., and Lado-Touriño, I. (1996). Reduction and stabilization of silver nanoparticles in ethanol by nonionic surfactants. *Langmuir* 12, 3585–3589. doi: 10.1021/la951501e

Lopez-Orozco, S., Inayat, A., Schwab, A., Selvam, T., and Schwieger, W. (2011). Zeolitic materials with hierarchical porous structures. *Adv. Mater.* 23, 2602–2615. doi: 10.1002/adma.201100462

Lu, G., Li, S., Guo, Z., Farha, O. K., Hauser, B. G., Qi, X., et al. (2012). Imparting functionality to a metal-organic framework material by controlled nanoparticle encapsulation. *Nat. Chem.* 4, 310. doi: 10.1038/nchem.1272

Mandal, S., Roy, D., Chaudhari, R. V., and Sastry, M. (2004). Pt and Pd nanoparticles immobilized on amine-functionalized zeolite: excellent catalysts for hydrogenation and heck reactions. *Chem. Mater.* 16, 3714–3724. doi: 10.1021/cm0352504

Mendes, P. S. F., Taleb, A.-L., Gay, A.-S., Daudin, A., Bouchy, C., Silva, J. M., et al. (2017). Nanoscale insights into Pt-impregnated mixtures of zeolites. *J. Mater. Chem. A* 5, 16822–16833. doi: 10.1039/c7ta02534c

Mielby, J., Abildstrøm, J. O., Wang, F., Kasama, T., Weidenthaler, C., and Kegnæs, S. (2014). Oxidation of bioethanol using zeolite-encapsulated gold nanoparticles. *Angew. Chem.* 126, 12721–12724. doi: 10.1002/ange.201406354

Möller, K., and Bein, T. (2013). Mesoporosity – a new dimension for zeolites. *Chem. Soc. Rev.* 42, 3689–3707. doi: 10.1039/c3cs35488a

Moller, K., Yilmaz, B., Muller, U., and Bein, T. (2012). Nanofusion: mesoporous zeolites made easy. *Chem. Eur. J.* 18, 7671–7674. doi: 10.1002/chem.201200544

Moreno, I., Dummer, N. F., Edwards, J. K., Alhumaimess, M., Sanka, M., Sanz, R., et al. (2013). Selective oxidation of benzyl alcohol using *in situ* generated H 2 O 2 over hierarchical Au–Pd titanium silicalite catalysts. *Catal. Sci. Technol.* 3, 2425–2434. doi: 10.1039/C3CY00493G

Moreno-Manas, M., and Pleixats, R. (2003). Formation of carbon–carbon bonds under catalysis by transition-metal nanoparticles. *Acc. Chem. Res.* 36, 638–643. doi: 10.1021/ar020267y

Na, K., Choi, M., and Ryoo, R. (2013). Recent advances in the synthesis of hierarchically nanoporous zeolites. *Microporous Mesoporous Mater.* 166, 3–19. doi: 10.1016/j.micromeso.2012.03.054

Na, K., Jo, C., Kim, J., Cho, K., Jung, J., Seo, Y., et al. (2011). Directing zeolite structures into hierarchically nanoporous architectures. *Science* 333, 328–332. doi: 10.1126/science.1204452

Na, Y., Park, S., Han, S. B., Han, H., Ko, S., and Chang, S. (2004). Ruthenium-catalyzed heck-type olefination and Suzuki coupling reactions: studies on the nature of catalytic species. *J. Am. Chem. Soc.* 126, 250–258. doi: 10.1021/ja038742q

Narayanan, R., and El-Sayed, M. A. (2005). Catalysis with transition metal nanoparticles in colloidal solution: nanoparticle shape dependence and stability. *J. Phys. Chem. B* 109, 12663–12676. doi: 10.1021/jp051066p

Otto, T., Ramallo-López, J. M., Giovanetti, L. J., Requejo, F. G., Zones, S. I., and Iglesia, E. (2016). Synthesis of stable monodisperse AuPd, AuPt, and PdPt bimetallic clusters encapsulated within LTA-zeolites. *J. Catal.* 342, 125–137. doi: 10.1016/j.jcat.2016.07.017

Pagis, C., Morgado Prates, A. R., Farrusseng, D., Bats, N., and Tuel, A. (2016). Hollow zeolite structures: an overview of synthesis methods. *Chem. Mater.* 28, 5205–5223. doi: 10.1021/acs.chemmater.6b02172

Pan, C., Pelzer, K., Philippot, K., Chaudret, B., Dassenoy, F., Lecante, P., et al. (2001). Ligand-stabilized ruthenium nanoparticles: synthesis, organization, and dynamics. *J. Am. Chem. Soc.* 123, 7584–7593. doi: 10.1021/ja003961m

Parlett, C. M. A., Wilson, K., and Lee, A. F. (2013). Hierarchical porous materials: catalytic applications. *Chem. Soc. Rev.* 42, 3876–3893. doi: 10.1039/c2cs35378d

Perego, C., and Millini, R. (2013). Porous materials in catalysis: challenges for mesoporous materials. *Chem. Soc. Rev.* 42, 3956–3976. doi: 10.1039/c2cs35244c

Perez-Ramirez, J., Christensen, C. H., Egeblad, K., Christensen, C. H., and Groen, J. C. (2008). Hierarchical zeolites: enhanced utilisation of microporous crystals in catalysis by advances in materials design. *Chem. Soc. Rev.* 37, 2530–2542. doi: 10.1039/b809030k

Prieto, G., Tuysuz, H., Duyckaerts, N., Knossalla, J., Wang, G. H., and Schuth, F. (2016). Hollow nano- and microstructures as catalysts. *Chem. Rev.* 116, 14056–14119. doi: 10.1021/acs.chemrev.6b00374

Primo, A., and Garcia, H. (2014). Zeolites as catalysts in oil refining. *Chem. Soc. Rev.* 43, 7548–7561. doi: 10.1039/C3CS60394F

Ren, L., Guo, Q., Kumar, P., Orazov, M., Xu, D., Alhassan, S. M., et al. (2015). Self-pillared, single-unit-cell Sn-MFI zeolite nanosheets and their use for glucose and lactose isomerization. *Angew. Chem. Int. Ed. Engl.* 54, 10848–10851. doi: 10.1002/anie.201505334

Ren, N., Yang, Y., Shen, J., Zhang, Y., Xu, H., Gao, Z., et al. (2007). Novel, efficient hollow zeolitically microcapsulized noble metal catalysts. *J. Catal.* 251, 182–188. doi: 10.1016/j.jcat.2007.07.009

Rioux, R. M., Song, H., Hoefelmeyer, J. D., Yang, P., and Somorjai, G. A. (2005). High-surface-area catalyst design: synthesis, characterization, and reaction studies of platinum nanoparticles in mesoporous SBA-15 silica. *J. Phys. Chem. B* 109, 2192–2202. doi: 10.1021/jp048867x

Rowsell, J. L., and Yaghi, O. M. (2004). Metal-organic frameworks: a new class of porous materials. *Microporous Mesoporous Mater.* 73, 3–14. doi: 10.1016/j.micromeso.2004.03.034

Rubio-Marques, P., Rivero-Crespo, M. A., Leyva-Perez, A., and Corma, A. (2015). Well-defined noble metal single sites in zeolites as an alternative to catalysis by insoluble metal salts. *J. Am. Chem. Soc.* 137, 11832–11837. doi: 10.1021/jacs.5b07304

Satterfield, C. N. (1970). *Mass Transfer in Heterogeneous Catalysis*. Cambridge: The MIT Press.

Schauermann, S., Nilius, N., Shaikhutdinov, S., and Freund, H-J. (2012). Nanoparticles for heterogeneous catalysis: new mechanistic insights. *Acc. Chem. Res.* 46, 1673–1681. doi: 10.1021/ar300225s

Schmid, G., Maihack, V., Lantermann, F., and Peschel, S. (1996). Ligand-stabilized metal clusters and colloids: properties and applications. *J. Chem. Soc., Dalton Trans.* 589–595. doi: 10.1039/DT9960000589

Schwieger, W., Machoke, A. G., Weissenberger, T., Inayat, A., Selvam, T., Klumpp, M., et al. (2016). Hierarchy concepts: classification and preparation strategies for zeolite containing materials with hierarchical porosity. *Chem. Soc. Rev.* 45, 3353–3376. doi: 10.1039/C5CS00599J

Serrano, D. P., Escola, J. M., and Pizarro, P. (2013). Synthesis strategies in the search for hierarchical zeolites. *Chem. Soc. Rev.* 42, 4004–4035. doi: 10.1039/c2cs35330j

Shi, J., Wang, Y., Yang, W., Tang, Y., and Xie, Z. (2015). Recent advances of pore system construction in zeolite-catalyzed chemical industry processes. *Chem. Soc. Rev.* 44, 8877–8903. doi: 10.1039/c5cs00626k

Slater, A. G., and Cooper, A. I. (2015). Function-led design of new porous materials. *Science* 348:aaa8075. doi: 10.1126/science.aaa8075

Sun, Q., Wang, N., Bing, Q., Si, R., Liu, J., Bai, R., et al. (2017). Subnanometric hybrid Pd-M(OH)2, M=Ni, Co, clusters in zeolites as highly efficient nanocatalysts for hydrogen generation. *Chem* 3, 477–493. doi: 10.1016/j.chempr.2017.07.001

Sun, X., and Li, Y. (2004). Colloidal carbon spheres and their core/shell structures with noble-metal nanoparticles. *Angew. Chem. Int. Ed.* 43, 597–601. doi: 10.1002/ange.200352386

Tang, Y., Li, Y., Fung, V., Jiang, D. E., Huang, W., Zhang, S., et al. (2018). Single rhodium atoms anchored in micropores for efficient transformation of methane under mild conditions. *Nat. Commun.* 9, 1231. doi: 10.1038/s41467-018-03235-7

Tao, Y., Kanoh, H., Abrams, L., and Kaneko, K. (2006). Mesopore-modified zeolites: preparation, characterization, and applications. *Chem. Rev.* 106, 896–910. doi: 10.1021/cr040204o

Wan, Y., and Zhao, D. (2007). On the controllable soft-templating approach to mesoporous silicates. *Chem. Rev.* 107, 2821–2860. doi: 10.1021/cr068020s

Wang, G., Xu, S., Wang, L., Liu, Z., Dong, X., Wang, L., et al. (2018a). Fish-in-hole: rationally positioning palladium into traps of zeolite crystals for sinter-resistant catalysts. *Chem. Commun.* 54, 3274–3277. doi: 10.1039/c8cc00513c

Wang, L., Xu, S., He, S., and Xiao, F-S. (2018b). Rational construction of metal nanoparticles fixed in zeolite crystals as highly efficient heterogeneous catalysts. *Nano Today* 20, 74–83. doi: 10.1016/j.nantod.2018.04.004

Wang, L., Zhang, J., Yi, X., Zheng, A., Deng, F., Chen, C., et al. (2015). Mesoporous ZSM-5 zeolite-supported Ru nanoparticles as highly efficient catalysts for upgrading phenolic biomolecules. *ACS Catal.* 5, 2727–2734. doi: 10.1021/acscatal.5b00083

Wang, N., Sun, Q., Bai, R., Li, X., Guo, G., and Yu, J. (2016). *In situ* confinement of ultrasmall Pd clusters within nanosized silicalite-1 zeolite for highly efficient catalysis of hydrogen generation. *J. Am. Chem. Soc.* 138, 7484–7487. doi: 10.1021/jacs.6b03518

Weitkamp, J. (2000). Zeolites and catalysis. *Solid State Ionics* 131, 175–188. doi: 10.1016/S0167-2738(00)00632-9

White, R. J., Luque, R., Budarin, V. L., Clark, J. H., and Macquarrie, D. J. (2009). Supported metal nanoparticles on porous materials. Methods and applications. *Chem. Soc. Rev.* 38, 481–494. doi: 10.1039/B802654H

Wildgoose, G. G., Banks, C. E., and Compton, R. G. (2006). Metal nanoparticles and related materials supported on carbon nanotubes: methods and applications. *Small* 2, 182–193. doi: 10.1002/smll.200500324

Wu, Z., Goel, S., Choi, M., and Iglesia, E. (2014). Hydrothermal synthesis of LTA-encapsulated metal clusters and consequences for catalyst stability, reactivity, and selectivity. *J. Catal.* 311, 458–468. doi: 10.1016/j.jcat.2013.12.021

Xing, C., Shen, W., Yang, G., Yang, R., Lu, P., Sun, J., et al. (2014). Completed encapsulation of cobalt particles in mesoporous H-ZSM-5 zeolite catalyst for direct synthesis of middle isoparaffin from syngas. *Catal. Commun.* 55, 53–56. doi: 10.1016/j.catcom.2014.06.018

Xu, D., Jing, Z., Cao, F., Sun, H., and Che, S. (2014a). Surfactants with aromatic-group tail and single quaternary ammonium head for directing single-crystalline mesostructured zeolite nanosheets. *Chem. Mater.* 26, 4612–4619. doi: 10.1021/cm502027j

Xu, D., Ma, Y., Jing, Z., Han, L., Singh, B., Feng, J., et al. (2014b). π-π interaction of aromatic groups in amphiphilic molecules directing for single-crystalline mesostructured zeolite nanosheets. *Nat. Commun.* 5, 5262. doi: 10.1038/ncomms5262

Xu, X., Li, Y., Gong, Y., Zhang, P., Li, H., and Wang, Y. (2012). Synthesis of palladium nanoparticles supported on mesoporous N-doped carbon and their catalytic ability for biofuel upgrade. *J. Am. Chem. Soc.* 134, 16987–16990. doi: 10.1021/ja308139s

Yang, C. M., Liu, P. H., Ho, Y. F., Chiu, C. Y., and Chao, K. J. (2003). Highly dispersed metal nanoparticles in functionalized SBA-15. *Chem. Mater.* 15, 275–280. doi: 10.1021/cm020822q

Yang, H., Ma, C., Zhang, X., Li, Y., Cheng, J., and Hao, Z. (2018). Understanding the active sites of Ag/zeolites and deactivation mechanism of ethylene catalytic oxidation at room temperature. *ACS Catal.* 8, 1248–1258. doi: 10.1021/acscatal.7b02410

Zaarour, M., Dong, B., Naydenova, I., Retoux, R., and Mintova, S. (2014). Progress in zeolite synthesis promotes advanced applications. *Microporous Mesoporous Mater.* 189, 11–21. doi: 10.1016/j.micromeso.2013.08.014

Zhang, J., Rao, C., Peng, H., Peng, C., Zhang, L., Xu, X., et al. (2018). Enhanced toluene combustion performance over Pt loaded hierarchical porous MOR zeolite. *Chem. Eng. J.* 334, 10–18. doi: 10.1016/j.cej.2017.10.017

Zhang, J., Wang, L., Shao, Y., Wang, Y., Gates, B. C., and Xiao, F. S. (2017). A Pd@Zeolite catalyst for nitroarene hydrogenation with high product selectivity by sterically controlled adsorption in the zeolite micropores. *Angew. Chem. Int. Ed. Engl.* 56, 9747–9751. doi: 10.1002/anie.201703938

Zhang, X., Liu, D., Xu, D., Asahina, S., Cychosz, K. A., Agrawal, K. V., et al. (2012). Synthesis of self-pillared zeolite nanosheets by repetitive branching. *Science* 336, 1684–1687. doi: 10.1126/science.1221111

Zhao, D., Feng, J., Huo, Q., Melosh, N., Fredrickson, G. H., Chmelka, B. F., et al. (1998). Triblock copolymer syntheses of mesoporous silica with periodic 50 to 300 angstrom pores. *Science* 279, 548–552. doi: 10.1126/science.279.5350.548

Zhao, X., Bao, X. Y., Guo, W., and Lee, F. Y. (2006). Immobilizing catalysts on porous materials. *Mater. Today* 9, 32–39. doi: 10.1016/S1369-7021(06)71388-8

Zhu, J., Zhu, Y., Zhu, L., Rigutto, M., van der Made, A., Yang, C., et al. (2014). Highly mesoporous single-crystalline zeolite beta synthesized using a non-surfactant cationic polymer as a dual-function template. *J. Am. Chem. Soc.* 136, 2503–2510. doi: 10.1021/ja411117y

Zhu, Q-L., and Xu, Q. (2016). Encapsulation of ultrafine metal nanoparticles to high-surface-area materials and their catalytic applications. *Chem* 1, 220–245. doi: 10.1016/j.chempr.2016.07.005

Conflict of Interest Statement: The authors declare that the research was conducted in the absence of any commercial or financial relationships that could be construed as a potential conflict of interest.

The handling editor declared a past supervisory role with one of the authors BL.

ORIGINAL RESEARCH
published: 20 November 2018
doi: 10.3389/fchem.2018.00567

Bandgap Engineering of Indium Phosphide-Based Core/Shell Heterostructures Through Shell Composition and Thickness

Reyhaneh Toufanian[1], **Andrei Piryatinski**[2], **Andrew H. Mahler**[3], **Radhika Iyer**[4], **Jennifer A. Hollingsworth**[4] **and Allison M. Dennis**[1,3*]

[1] Division of Materials Science and Engineering, Boston University, Boston, MA, United States, [2] Theoretical Division, Los Alamos National Laboratory, Los Alamos, NM, United States, [3] Department of Biomedical Engineering, Boston University, Boston, MA, United States, [4] Los Alamos National Laboratory, Materials Physics and Applications Division, Center for Integrated Nanotechnologies, Los Alamos, NM, United States

The large bulk bandgap (1.35 eV) and Bohr radius (~10 nm) of InP semiconductor nanocrystals provides bandgap tunability over a wide spectral range, providing superior color tuning compared to that of CdSe quantum dots. In this paper, the dependence of the bandgap, photoluminescence emission, and exciton radiative lifetime of core/shell quantum dot heterostructures has been investigated using colloidal InP core nanocrystals with multiple diameters (1.5, 2.5, and 3.7 nm). The shell thickness and composition dependence of the bandgap for type-I and type-II heterostructures was observed by coating the InP core with ZnS, ZnSe, CdS, or CdSe through one to ten iterations of a successive ion layer adsorption and reaction (SILAR)-based shell deposition. The empirical results are compared to bandgap energy predictions made with effective mass modeling. Photoluminescence emission colors have been successfully tuned throughout the visible and into the near infrared (NIR) wavelength ranges for type-I and type-II heterostructures, respectively. Based on sizing data from transmission electron microscopy (TEM), it is observed that at the same particle diameter, average radiative lifetimes can differ as much as 20-fold across different shell compositions due to the relative positions of valence and conduction bands. In this direct comparison of InP/ZnS, InP/ZnSe, InP/CdS, and InP/CdSe core/shell heterostructures, we clearly delineate the impact of core size, shell composition, and shell thickness on the resulting optical properties. Specifically, Zn-based shells yield type-I structures that are color tuned through core size, while the Cd-based shells yield type-II particles that emit in the NIR regardless of the starting core size if several layers of CdS(e) have been successfully deposited. Particles with thicker CdS(e) shells exhibit longer photoluminescence lifetimes, while little shell-thickness dependence is observed for the Zn-based shells. Taken together, these InP-based heterostructures demonstrate the extent to which we are able to precisely tailor the material properties of core/shell particles using core/shell dimensions and composition as variables.

Keywords: quantum dots, bandgap tunability, optoelectronic properties, photoluminescence, type-I quantum dot, type-II quantum dot, successive ion layer adsorption and reaction (SILAR)

Edited by:
Ou Chen,
Brown University, United States

Reviewed by:
Aiwei Tang,
Beijing Jiaotong University, China
Shuai Chang,
Beijing Institute of Technology, China

***Correspondence:**
Allison M. Dennis
aldennis@bu.edu

Specialty section:
This article was submitted to Nanoscience, a section of the journal Frontiers in Chemistry

Received: *01 September 2018*
Accepted: *31 October 2018*
Published: *20 November 2018*

Citation:
Toufanian R, Piryatinski A, Mahler AH, Iyer R, Hollingsworth JA and Dennis AM (2018) Bandgap Engineering of Indium Phosphide-Based Core/Shell Heterostructures Through Shell Composition and Thickness. Front. Chem. 6:567. doi: 10.3389/fchem.2018.00567

INTRODUCTION

Semiconductor quantum dots (QDs) are used to study the fundamental photophysics of quantum confined systems, as well as, for numerous applications in photovoltaics, solid state lighting, biomedical imaging, and biosensing (Dennis et al., 2012b; Chuang et al., 2014; Lan et al., 2014; Ten Cate et al., 2015; Kagan et al., 2016; Hong et al., 2017; Chandran et al., 2018; Kong L. et al., 2018; McHugh et al., 2018). Quantum confinement is easily observed in simple, single semiconductor nanocrystals (NCs): smaller cores are more quantum confined, resulting in an increase in the energy gap between the conduction and valence bands as observed through higher energy (bluer) photon emission following photoexcitation. Core/shell heterostructures exhibit more complex size and compositional dependencies as the bandgap of the particle depends on both the position and relative offsets of the conduction and valence bands of the separate components (Murray et al., 1993; Alivisatos, 1996; Peng and Peng, 2001; Reiss et al., 2009). This added complexity enables significant tuning of the optoelectronic properties of the NCs well beyond what would be feasible with the individual components in isolation. Thus, the core/shell heterostructure can be designed to exhibit photoluminescent (PL) energies and lifetimes that are not achievable with discrete NCs of either the core or shell material alone. We explore the extent of this heterostructure tunability using indium phosphide cores and four different shell materials, zinc sulfide, zinc selenide, cadmium sulfide, and cadmium selenide.

Indium phosphide QDs have garnered significant interest as a cadmium-free option that is tunable throughout the visible wavelength regime (Micic et al., 1994; Guzelian et al., 1996; Battaglia and Peng, 2002; Xie et al., 2007; Li and Reiss, 2008; Xu et al., 2008; Tamang et al., 2016). As-synthesized InP QDs, however, are non-emissive due to non-radiative relaxation of excitation generated charge carriers facilitated by trapping at surface defects (Dennis et al., 2012a; Omogo et al., 2013; Balan et al., 2017; Reid et al., 2018). Fabrication of emissive cores can be performed through two main synthetic routes: etching the surface of the nanoparticle using a fluoride, or overcoating with a larger bandgap semiconductor to create a core/shell heterostructure (Danek et al., 1996; Dabbousi et al., 1997; Talapin et al., 2002; Adam et al., 2005; Chen et al., 2013; Mordvinova et al., 2014, 2017). The latter approach renders QDs emissive through passivation of surface trap states at the core/shell interface, thus inhibiting non-radiative recombination pathways while protecting the core nanocrystal against photo-oxidation (Battaglia et al., 2003). The bandgap of the shell material, as well as the position of its conduction and valence bands relative to those of the core NC, dictates the bandgap structure of the resulting heterostructure and, thereby, the resulting optoelectronic properties (Li and Wang, 2004; Wang et al., 2018).

In traditional type-I QDs, a low bandgap core material is coated with a second semiconductor with a wider bandgap than the core material with higher energy valence and conduction band offsets (Chandrasekaran et al., 2017; Brodu et al., 2018). Sufficiently large core size allows both the electron and hole to reside within the core, constituting the so-called type-I localization regime. A decrease in the core radius can eventually allow one charge carrier to delocalize into the shell while the other stays localized, especially if the band offset for either the conduction or the valence bands is small. This situation is distinguished as the quasi-type-II localization regime (Kaledin et al., 2018; Kong D. et al., 2018). In the prototypical example of CdSe/CdS, the core/shell conduction band offset is small, such that the core/shell structure exhibits a quasi-type-II localization regime with the electron wavefunction spreading from the core into the shell material, while the wavefunction of the heavy hole is still confined to the core (Kaledin et al., 2018; Kong D. et al., 2018). In cases where either the conduction or valance band of the shell lies within the bandgap of the core, a type-II localization regime is observed, whereby the electron and hole carriers are spatially separated into the core and shell (Dennis et al., 2012a; Acharya et al., 2015). As each carrier relaxes to its lowest energy state prior to radiative recombination, the resulting bandgap of the heterostructure is smaller than the bulk bandgap of either the core or shell material (**Figure 1**). Generally, the size and composition of a core/shell heterostructure dictates different localization regimes and subsequently determines photophysical properties such as the emission energy/wavelength/color and the photoluminescent (PL) lifetime (Reid et al., 2018).

InP QDs are most frequently shelled with ZnS to provide a protective, passivating layer yielding PL (Tessier et al., 2015). The high lattice mismatch between InP and ZnS (7.8%), however, can result in the introduction of interfacial stresses at the core/shell barrier, leading to the formation of defects and non-radiative

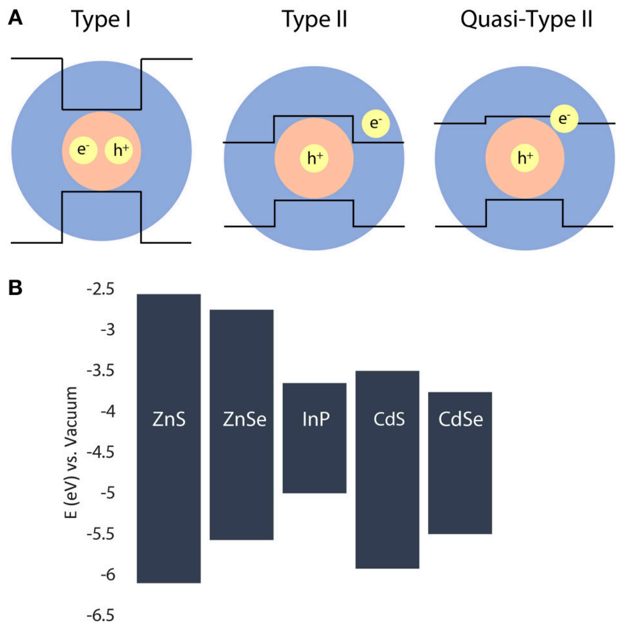

FIGURE 1 | (A) Schematic representation of the relative positions of conduction and valence bands in different core/shell heterostructures. **(B)** Relative positions of the conduction and valance bands of the semiconductors used in this study (Wei and Zunger, 1998; Reiss et al., 2009).

recombination pathways. A shell of ZnSe offers a significantly reduced lattice mismatch and still induces PL, but is itself prone to photo-oxidation, making the final material prone to degradation over time. The current preferred solution is to use a multilayered or alloyed shell of ZnSe then ZnS to satisfy the requirements of low lattice mismatch at the core/shell interface and high stability at the shell/media interface (Ippen et al., 2012; Lim et al., 2013). Shelling with other semiconductor materials changes the band alignment and more dramatically impacts the particle photophysics (Htoon et al., 2010; Vela et al., 2010). For example, we produced type-II InP/CdS QDs (Dennis et al., 2012a) that have been shown by us and others to exhibit shell-thickness-dependent suppressed-blinking behavior in the NIR (Dennis et al., 2012a; Smith et al., 2017).

In this work, we address the role of core size, shell composition, and shell thickness on tuning the PL emission colors and radiative lifetimes of type-I and type-II systems with an InP core. A range of visible and NIR emitters have been produced by synthesizing core/shell QDs using three different sizes of core InP nanocrystals (small, medium, and large), four different shell compositions (ZnS, ZnSe, CdS, and CdSe), and varying the number of shell deposition iterations (1 through 10). A schematic of possible band alignments for each type of heterostructure is shown in **Figure 1**. In addition, we show the relative bulk conduction and valance band positions for each of the semiconductors used in this study. We demonstrate that in our cadmium-free type-I systems, the emission color is tuned throughout the visible wavelength range through variation of the core size alone, where the shell material acts as an optically inactive passivating layer, protecting the core NC. In our charge-separated type-II systems, the core size is less influential, while the shell thickness strongly impacts the emission peak wavelength and radiative lifetimes of the resulting NIR emitters.

MATERIALS AND METHODS

Materials

Oleylamine (OAm, 80–90%), 1-octadecene (ODE, 90%), diphenylphosphine (DPP, 98%), sulfur (S, 99.999%), tris(trimethylsilyl) phosphine (TMS_3P, 98%), cadmium oxide (CdO, 99.95%) and hexanes (99%) were purchased from Fisher Scientific. Indium (III) acetate [$In(Ac)_3$, 99.99%], oleic acid (OA, 90%), n-trioctylphosphine (TOP, 97%), selenium pellets (Se, 99.99%), zinc acetate [$Zn(Ac)_2$, 99.0%], dioctylamine (98%), and ethanol (99.8%) were purchased from Sigma-Aldrich. ODE was heated to 120°C under vacuum for several hours prior to use and stored in an argon glovebox. All other chemicals were used directly without further purification. Quartz glass cuvettes were purchased from Starna Cells Inc. All air-sensitive materials were stored and handled in a glovebox under argon.

Precursors

The metal and chalcogenide precursors were prepared with minor modifications to previously reported protocols. A 0.2 M stock solution of indium oleate with a molar ratio of 1:3 was prepared by mixing 3.2 mmol indium (III) acetate (0.93 g) and 10.61 mmol (3.35 mL) oleic acid and heating the reaction flask to 120°C for 2 h with multiple argon backfill and evacuation cycles to ensure complete removal of acetic acid. After a clear and colorless solution was obtained, 12.58 mL degassed ODE was added to the solution. Once the temperature of the solution reached 120°C, it was cooled to 90°C and vacuumed for another hour. A 0.2 M stock solution of cadmium oleate (Cd:OA 1:4) was prepared by mixing 7 mmol CdO (0.9 g) and 31.15 mmol (9.83 mL) oleic acid. The rust colored solution was degassed at 110°C for 1 h, backfilled with argon, and heated to 280°C until a clear and colorless solution was obtained. This solution was cooled to 100°C and vacuumed for an hour to remove any water produced during the cadmium oleate formation reaction. The flask was backfilled with argon and stored at 80°C for future use. A 0.2 M stock solution of zinc oleate (Zn:OA 1:4) was prepared by mixing 20 mmol zinc acetate (4.39 g) with 88.88 mmol (28.05 mL) oleic acid and degassing under vacuum at room temperature until no vigorous bubbling was observed. The temperature was slowly raised to 120°C and maintained for 2 h, until the solution was clear and no bubbling was observed. At this point, 71.95 mL degassed ODE was added to the solution. The flask was stored at 60°C for further use. Solutions of sulfur in both TOP and ODE were used as sulfur precursors. For the preparation of a 0.2 M stock solution of sulfur in ODE, 3.11 mmol (0.1 g) elemental sulfur and 15.59 mL ODE was mixed and heated to 80°C under vacuum for 2 h. The flask was backfilled with argon and heated at 80°C overnight to ensure complete dissolution of sulfur in ODE, and stored at the same temperature for future use. A similar procedure was followed for the preparation of the 0.2 M stock solutions of sulfur in TOP and selenium in TOP. TOP:S and TOP:Se were stored at room temperature in an argon glovebox for future use.

Diphenylphosphine selenide (DPP:Se) was synthesized as previously described (Evans et al., 2010). In an argon-filled glovebox, 20 mmol (3.48 mL) DPP, 20 mmol (1.58 g) selenium, and 25 mL anhydrous toluene were loaded in a 3-necked round bottom flask attached to a Findenser (Radleys, UK). The flask was heated at 110°C for 16 h. Following the removal of toluene in a rotary evaporator, white crystalline precipitates of DPP:Se were obtained. The collected precipitate was washed with cooled toluene to remove impurities. A 0.2 M stock solution of DPP:Se was prepared by mixing 8 mmol (2.12 g) of this powder and 39.98 mL ODE and heating to 100°C until the crystals completely dissolved in ODE. The solution was kept at 80°C to maintain solubility.

Synthesis of InP Core Nanocrystals

InP core nanocrystals of three different sizes–small, medium, and large (S, M, and L, respectively) were prepared using hot injection synthesis. For the synthesis of the small and medium cores, 2 mL 0.2 M $In(OA)_3$, 1.5 mL OAm, and 2 mL ODE were loaded into a 100 mL round bottom flask. The indium oleate solutions were heated under vacuum to 120°C and backfilled with argon multiple times, while syringes of 0.1 M and 1 M $(TMS)_3P$ in ODE were prepared in the glovebox. An initial 0.2 mL of 1 M $(TMS)_3P$ was rapidly injected into each flask of indium oleate at 191°C with the thermocouple temperature set to 178°C for the growth phase of the reaction. Starting within 45 s of the first injection, 2 mL of 0.1 M $(TMS)_3P$ was added to the flask via dropwise injection. Small cores were reliably produced by quenching this reaction after 3.5 min by removing the heating mantle and adding 12 mL of degassed, room temperature ODE. To generate medium cores, more indium and phosphorus was repeatedly added to the InP cores to provide precursors for growth with a total of 6 mL of warm 0.2 M $In(OA)_3$ and 12 mL of 0.1 M $(TMS)_3P$ added dropwise in 4 separate aliquots each over the span of 20 min. After 32.5 min of total reaction time, the core growth was quenched by removing the heating mantle and adding 24 mL of degassed, room temperature ODE. The large InP cores were produced similarly to the small core protocol described above, except that the OAm was replaced by 0.5 mL dioctylamine and the reaction proceeded at 178°C for 14 h.

For the synthesis of InP/ZnS and InP/ZnSe, core InP QDs were used in their original reaction solution. For the synthesis of InP/CdS and InP/CdSe, core nanocrystals were cleaned by a precipitation and resuspension procedure. To clean the reaction product, aliquots were diluted in hexane and centrifuged to remove any precipitates in an argon glovebox. In a clean centrifuge tube, ethanol was added to the supernatant to precipitate the QDs, and the sample was centrifuged again. At this step, the clear supernatant was discarded and the colored precipitate was resuspended in hexane. A final centrifugation step removed any residual precipitates. The transparent, but colored, supernatant was used for the synthesis of InP/CdS and InP/CdSe. The same procedure was performed for cleaning the core/shell reaction products for further characterization.

Synthesis of Core/Shell Nanocrystals

Four distinct shell compositions comprising CdSe, CdS, ZnSe, and ZnS were deposited on the InP core nanocrystals using a modified SILAR technique, adapted for colloidal synthesis (Li et al., 2003). In this approach, aliquots of cationic and anionic precursors were added to the core solution between long anneals at growth temperatures (150–240°C). The required amounts of anion and cation precursor were calculated based on the number of surface atoms needed to add a monolayer to a certain size of a core/shell nanocrystal. For each reaction, 1 mL OAm and enough ODE to make up a total reaction volume of 10 mL were mixed in a 100 mL round bottom flask on a Schlenk line. The flask was vacuumed at room temperature for 30 min before the solution temperature was raised to 120°C for multiple vacuum/argon cycles. To protect the InP cores from Ostwald ripening caused by sudden exposure to heat, the flask was cooled to 60°C for the addition of 200 nmol of InP cores.

The flasks were kept under dynamic vacuum for an additional 15–20 min before the reaction temperature was raised. In addition, the reaction flask for InP/ZnSe was spiked with 0.21 mL (1.207 mmol) of DPP at this time. For all shell compositions, the cation precursor for the first deposition was injected at 150°C; the first anion injection proceeded 10 min later at the same temperature. Immediately after the anion injection, the temperature was raised to 240°C and the solution was annealed as described in **Table 1**. For InP/CdS and InP/CdSe heterostructures, all subsequent shell precursors were injected dropwise at 240°C (Dennis et al., 2012a). However, for InP/ZnS and InP/ZnSe heterostructures, a temperature cycling procedure was followed as previously described (Xie and Peng, 2009). Specifically, after the anion annealing at 240°C, the temperature of the flask was lowered to 150°C for the subsequent cation and anion injections before the temperature was again increased to 240°C for a longer anneal. To monitor the progress of the reaction, aliquots of the reaction solutions were taken at regular intervals. The reaction was terminated by cooling the solution to room temperature.

TABLE 1 | Summary of shell reaction parameters.

	Shell composition			
	ZnS	**ZnSe**	**CdS**	**CdSe**
Core Preparation [solvent]	Raw [ODE]	Raw [ODE]	PR [hexanes]	PR [hexanes]
Cation Precursor [mol/L]	$Zn(OA)_2$ [0.2]	$Zn(OA)_2$ [0.2]	$Cd(OA)_2$ [0.2]	$Cd(OA)_2$ [0.2]
Anion Precursor [mol/L]	TOP:S [0.2]	DPP:Se [0.2]	S/ODE [0.2]	TOP:Se [0.2]
Cation/Anion Anneal Time [hr]	0.25/1.5	0.25/1.5	1/2.5	1/2.5
Injection/Annealing Temp. [°C]	150/240	150/240	240/240	240/240

QD Characterization

Absorption spectra were obtained using a NanoDrop 2000c spectrophotometer, using the pedestal. Samples were cleaned by precipitation and resuspended in hexane or TCE (to eliminate hexane reabsorption in NIR measurements) for PL measurements and measured in quartz cuvettes. Photoluminescence spectroscopy below 900 nm was measured with a Horiba NanoLog spectrofluorometer (Horiba Jobin Yvon) outfitted with a 450 W Xenon arc lamp, double excitation and double emission monochromators, and silicon CCD detector. NIR emission peaks were measured with a similar instrument outfitted with a liquid nitrogen-cooled InGaAs CCD array. Spectra were taken with 400 nm excitation and a 450 nm, 550 nm, or 800 nm longpass emission filter, depending on the wavelength region being examined. The collected spectra were corrected for lamp power and detector sensitivity using instrument-specific correction files.

Absolute quantum yield values were obtained using the spectrofluorometer described above in conjunction with a Quanta-phi six-inch integrating sphere (HORIBA Jobin Yvon). Cuvettes were loaded with hexanes in order to generate a blank reference following excitation at 400 nm. QD samples were diluted directly into the blanked cuvettes and measured with identical conditions. The absolute quantum yield (i.e., the photons emitted divided by the photons absorbed) was determined using the Horiba software.

Transmission electron microscopy (TEM) images were acquired using a JEOL 2100 LaB6 high-resolution microscope operating at 200 kV. Each sample was precipitated and resuspended in hexane twice and drop-cast on a copper TEM grid, which was washed successively by hexane, ethanol, and

DI water. The grid was then gently heated to evaporate any residual water. TEM images were sized manually using ImageJ. TEM images have been size matched for presentation and the reported sizing information is based on 108–346 QDs, depending on the sample. The shell thickness was calculated by taking the difference between the core/shell radius determined via TEM and the core radius determined using the 1S absorption peak position (Xie et al., 2009).

Photoluminescence lifetime measurements were performed using an Edinburgh Instruments DeltaFlex time-correlated single photon counting (TCSPC) fluorescence lifetime instrument. QD samples were suspended in hexanes and loaded into quartz cuvettes. Samples were excited with a 405 nm EPL picosecond pulsed diode laser using a 1 microsecond pulse period. For each sample, the measurement continued until 10,000 photons were collected in the highest-intensity bin to ensure accurate fits. Photons were collected at the emission peak with a bandwidth window of 15–50 nm, depending on the FWHM of the sample. After collection, data was analyzed with F980 software (Edinburgh Instruments) by fitting the tail to the tri-exponential equation $R(t) = A_1e^{-t/\tau_1} + A_2e^{-t/\tau_2} + A_3e^{-t/\tau_3}$, where A_n is the percent weight of each exponential. The average photoluminescence lifetime, $\overline{\tau}$, was calculated using the following equation (Lakowicz, 2006; Jones and Scholes, 2010):

$$\overline{\tau} = \sum\nolimits_n \frac{A_n\tau_n^2}{\sum_m A_m\tau_m}$$

Effective Mass Model of Core/Shell Heterostructures

The electronic structures of the heterostructures were calculated using a two-band effective mass model applied to each core/shell composition as has been previously described (Efros et al., 2000; Piryatinski et al., 2007; Dennis et al., 2012a). The confinement potential has been parametrized using values for the bulk bandgaps, conduction band energies, electron and hole effective masses, and material dielectric constants listed in **Table S1**. The 1S exciton energy is evaluated as a sum of the electron and hole 1S state energies due to the confinement potential (kinetic energies) plus their Coulomb binding energy (perturbative corrections).

RESULTS AND DISCUSSION

In order to examine the impact of the composition and dimensions of InP-based core/shell heterostructures on their optical properties, we used an effective mass model to generate wavefunctions for the electron and hole carriers as a function of the core and shell compositions and dimensions and, from the overlap integral, predict the bandgap energy of the heterostructure (**Figure 2**). The modeling data predict that InP/ZnS heterostructures with core diameters larger than 2 nm are exclusively type-I emitters with both the electron and hole localized in the core. The vertical bands of equal energy show that the final emission color is primarily dictated by the starting core size and uninfluenced by ZnS shell thickness. The InP/ZnSe data similarly exhibit vertical bands in the bandgap energy plot after a shell ∼1 nm thick is deposited, but a quasi-type-II structure is predicted for core sizes up to 4 nm in diameter—a range that is more relevant for this study than the very small core sizes predicted to exhibit quasi-type-II behavior for the InP/ZnS system. In this context, we would expect the core size to primarily dictate the color of both InP/ZnS and InP/ZnSe heterostructures. The InP/ZnSe particles, however, are predicted to exhibit more red-shifting with the deposition of thin shells than InP/ZnS. After deposition of several atomic monolayers, neither material is expected to show photophysical changes as a function of shell thickness.

In contrast, modeling of the InP/CdS(e) systems predicts a strong influence of both core size and shell thickness on the resulting bandgap. In these systems, larger cores naturally exhibit redder emission, but the bandgap energy also shifts quickly and significantly with CdS(e) shelling. The hole wavefunction is shown to localize in the core in all cases where the core is >1 nm in diameter. The electron wavefunction on the other hand indicates localization of the electron in the shell as soon as the shell is >1 nm (1.5 nm) for InP/CdS(e). Because of these clear localization patterns with such small core sizes and relatively thin shells, nearly all of the InP/CdS(e) parameter space is classified as falling into a type-II localization regime. One of the hallmarks of a type-II system is that it can exhibit radiative recombination at photon energies lower than is possible for either the core or shell material in isolation. Although not all of the bandgaps predicted for the InP/CdS(e) core/shell structures in the type-II regime are lower energy than the bulk bandgap of InP at 1.35 eV, these composition and dimension combinations are still type-II, as they exhibit lower energy bandgaps than would be possible for either InP or CdS(e) of the same size (i.e., with confinement).

It is well established that semiconductor nanocrystals smaller than their exciton Bohr radius are quantum confined and exhibit size-dependent optoelectronic properties (Murray et al., 1993; Battaglia and Peng, 2002). This was seen for the InP core particles generated for this study as well. InP cores were nucleated by injecting the highly reactive phosphorus precursor, tris(trimethyl silyl)phosphine, into an indium oleate solution heated to 191°C. Oleylamine facilitated the fast, uniform growth of the smallest cores; additional indium and phosphorus precursors were added at the growth temperature (178°C) to yield the medium cores. The large cores were synthesized overnight at 178°C in the presence of a secondary amine (di-n-octylamine) without further precursor addition. The resulting cores exhibit exciton 1S peaks (small and medium) or shoulders (large) at 445, 543, and 622 nm, which correlate to particle diameters of 1.5, 2.5, and 3.7 nm, respectively (**Figure S1**) (Xie et al., 2009).

To observe the effect of shell composition and thickness on the optical properties of InP, epitaxial shells of four different semiconductor materials (ZnS, ZnSe, CdS, and CdSe) were grown on each of three sizes of InP cores with shell growth confirmed through TEM imaging (**Figure 3**). Lattice fringes are evident in the images, demonstrating the crystallinity of the nanoparticles. The core sizes determined from the 1S peak position and the average particle diameters obtained from TEM sizing data (**Figure S2**; **Table S2**) were used to determine the average shell

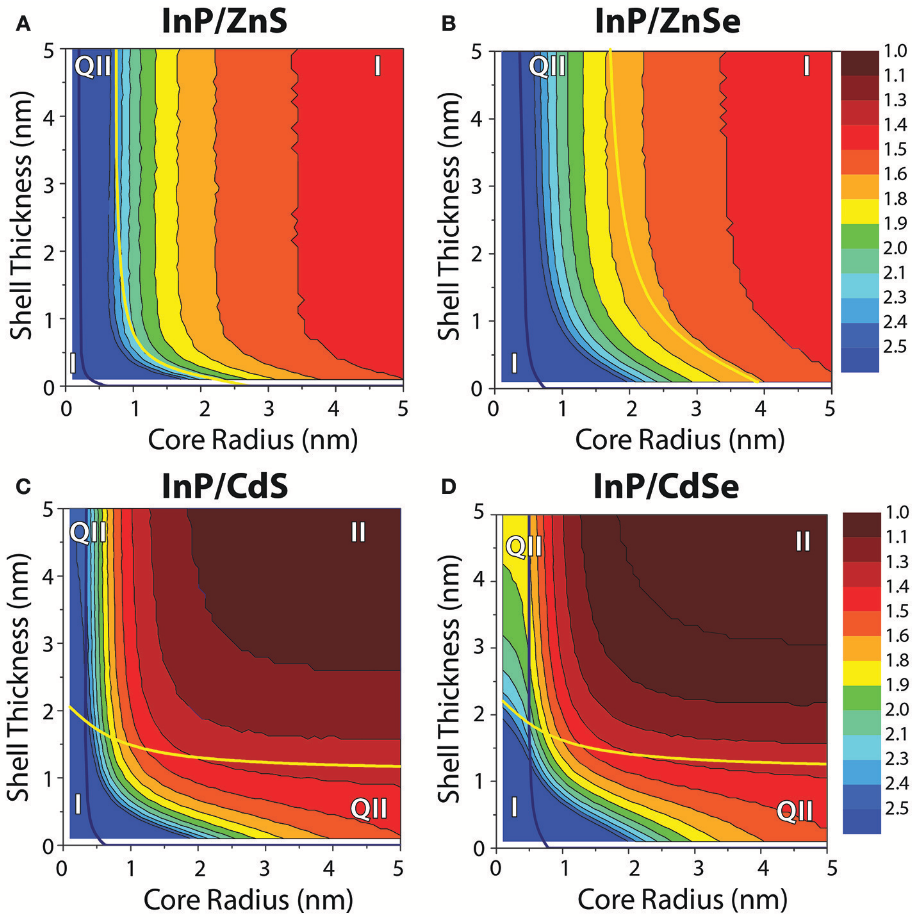

FIGURE 2 | Contour plots depicting the bandgap energies of InP/ZnS, InP/ZnSe, InP/CdS, and InP/CdSe core/shell heterostructures as a function of the core radius and shell thickness, as predicted by effective mass modeling. In each case, the blue line denotes the boundary between regimes for which the hole is either delocalized over the entire heterostructure volume (left of the line) or core-localized (right of the line). For **(A)** InP/ZnS and **(B)** InP/ZnSe, the yellow line separates the regimes where the electron is delocalized over the entire particle volume (left of the line) from the regime where the electron is core localized (right of the line). For **(C)** InP/CdS and **(D)** InP/CdSe, the yellow line again indicates changes in the electron localization, separating the regimes where the electron is delocalized over the entire particle volume (below the line) from the regime where the electron is shell localized (above the line). The plots include notation indicating the regions of core/shell dimensions that correspond to different electron and hole localization regimes, indicating that the charge carriers are co-localized [type-I (I)], spatially separated [type-II (II)], or that one charge carrier is localized while the other is delocalized [quasi-type-II (q-II)]. The same color scale is used for all four plots.

thickness for each sample, assuming spherical core and core/shell particles. The number of shell monolayers (MLs) deposited was determined by dividing the shell thickness in nm by the thickness of one cation/anion layer (i.e., half the lattice constant of the shell material; **Table S1**).

It is apparent from an examination of the sizing data (**Figure S2**; **Table S2**) that the ZnS shell deposition proceeded significantly less efficiently than the deposition of the other shell materials. While the ZnS monolayer is the thinnest of the four materials with a lattice constant of 5.41 Å (**Table S1**), this difference in unit cell size does not account for all of the difference in the final size. The ZnS and ZnSe shells are only 4.1 and 6.5 MLs thick, respectively, after 10 iterative rounds of SILAR deposition. For the cadmium-free systems, the shell growth procedure is not as effective as that of the cadmium-containing systems for which the chemistry is very well developed. This is mainly attributed to the less reactive nature of the zinc precursor compared to the cadmium precursors. The impact of this lower reactivity can be observed in the PL spectra as well, particularly for some InP/1ZnS(e) samples (**Figure 4**; **Figure S3**), which exhibit low energy tails indicative of trap emission. This suggests incomplete formation of the ZnS(e) shell in the early stages of the reaction. This tail disappears and the full width at half maximum (FWHM) of the PL peak decreases with subsequent shelling (**Figure S4**), providing evidence for complete shell formation with successive precursor addition. We suspect that a combination of high lattice strain, due to the large lattice mismatch between InP and ZnS (7.8%), and the lower reactivity of the zinc precursor combines to produce the least efficient shell deposition in the case of ZnS. Several reports describe increasing the reactivity of zinc by means of the addition of phosphorous containing compounds, with the aim of the formation of more reactive

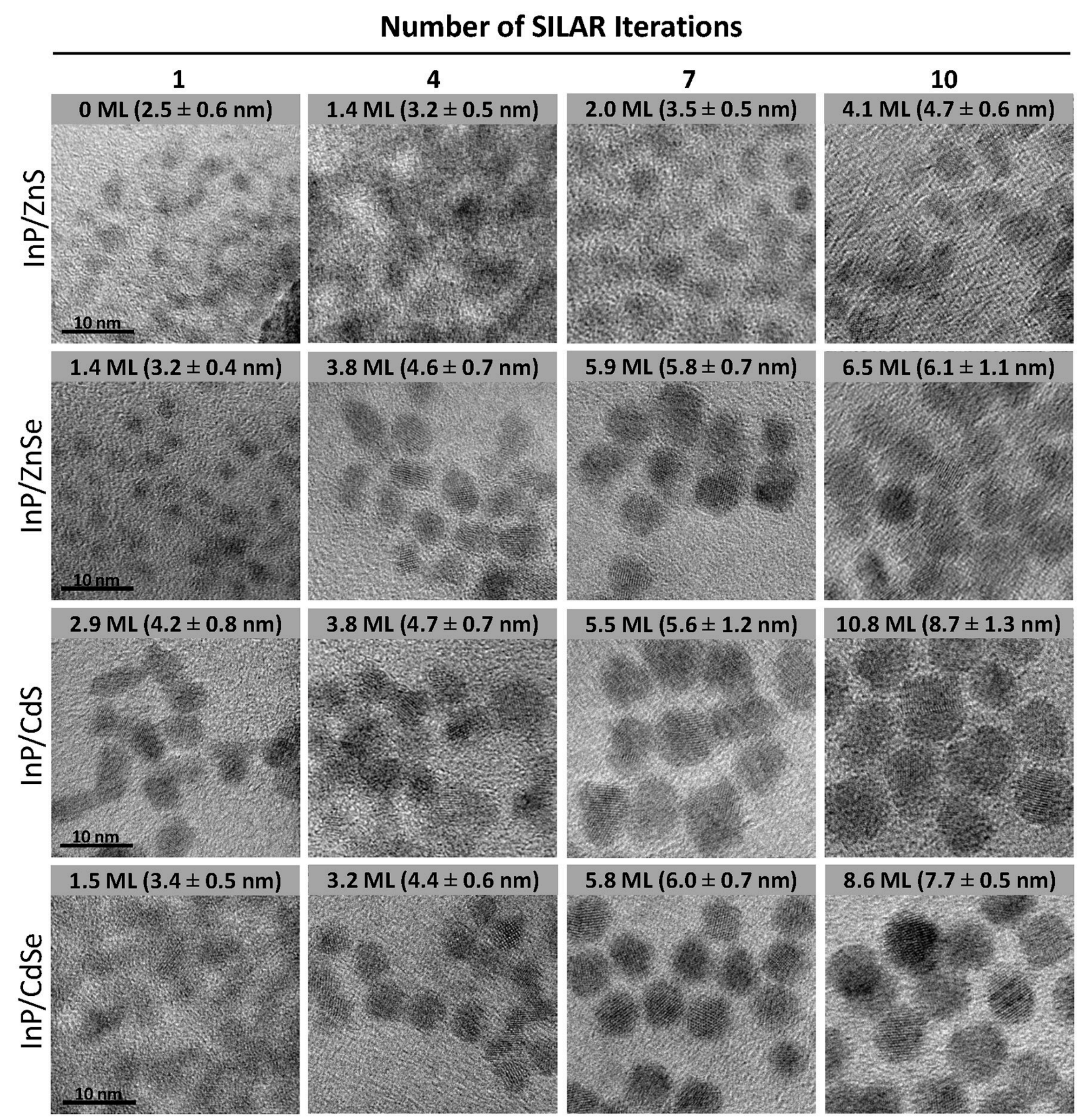

FIGURE 3 | Size-matched TEM images of InP/ZnS, InP/ZnSe, InP/CdS, and InP/CdSe core-shell heterostructures after 1, 4, 7, and 10 successive shell depositions. The scale bar for all images is 10 nm. The average ± standard deviation diameter of the core/shell particles is included in the inset text in the corresponding image. The size statistics are based on *n* = 108–346 particles, depending on the sample.

zinc phosphine complexes, particularly for the synthesis of thick-shelled InP/ZnSe heterostructures (Joo et al., 2009; Evans et al., 2010; Yu et al., 2011).

To improve the efficiency of the ZnS(e) shell depositions, several Se and S precursors were tested for effective shell growth with zinc oleate. Both trioctylphosphine sulfide (TOP:S) and sulfur dissolved in the non-coordinating solvent octadecene (S/ODE) were tested for ZnS deposition. The addition of sulfur caused significant etching of the core nanocrystals at elevated temperatures, especially in the first stages of the synthesis, as seen through the blue-shifting of the 1S exciton peaks (**Figure S5**). Using TOP:S, however, the 1S peak remained stable, indicating that the core nanocrystal remained intact. The selenium precursors tested include trioctylphosphine selenide (TOP:Se) and diphenylphosphine selenide (DPP:Se). When DPP:Se was used, TEM images indicated QDs of a larger average diameter and a more uniform morphology compared to TOP:Se (**Figure S6**). This is likely due to the formation of the more reactive zinc phosphine monomers, resulting in a higher reaction yield and a more effective shell growth with increasing shell thickness (Yu et al., 2011). We found that spiking the reaction flask with 0.21 mL (1.207 mmol) of DPP in addition to using

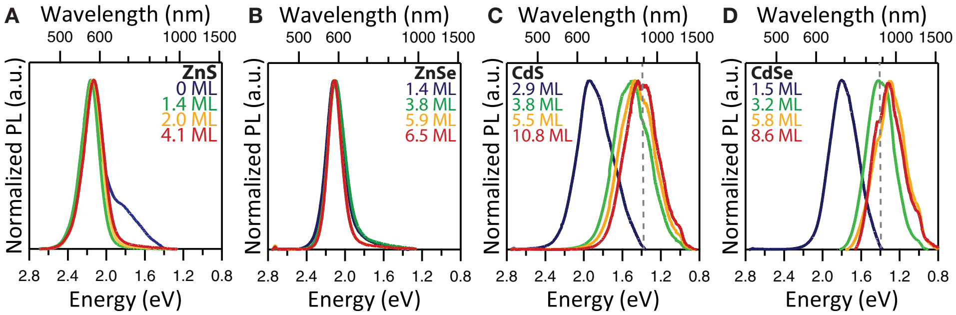

FIGURE 4 | Normalized PL emission spectra of **(A)** InP/ZnS, **(B)** InP/ZnSe, **(C)** InP/CdS, and **(D)** InP/CdSe for medium sized cores after 1, 4, 7, and 10 SILAR iterations. The resulting thickness of the shell in atomic monolayers is indicated in the figure legends. The dotted gray line indicates a detector change at 897 nm.

DPP:Se as the anionic precursor improved the overall quality of the InP/ZnSe QDs (**Figure S6**).

For CdS(e) shell formation, successful shell growth was observed via TEM imaging using S/ODE and TOP:Se as anionic precursors, respectively, with cadmium oleate as the cationic precursor. Little optimization of the SILAR protocol was needed for CdS(e) shell growth, as many of the thick-shell examples in the literature focus on cadmium systems (Zhou et al., 2016, 2017; Niu et al., 2017). The primary struggle in adapting these protocols to the InP-based system hinged on deposition of the first shell layer without excessive etching or dissolution of the InP core. This is successfully achieved by lowering the initial shell growth temperature to 150°C, as we previously reported (Dennis et al., 2012a).

Optical characterization was performed on samples comprising three core sizes and four shell thicknesses for each of the four core/shell heterostructure compositions. This set of forty-eight samples spans a wide range of particle sizes, emission wavelengths, and photoluminescent lifetimes, demonstrating the interplay between the core/shell structure and the photophysical function. By examining the PL peak position, we immediately observe the impact of the different band alignments (**Figures 4**, **5**, **Figure S3**). InP/ZnS and InP/ZnSe heterostructures have shell materials with significantly larger bandgaps than their core material (**Table S1**) and thus exhibit type-I behavior. Both electrons and holes are confined to the core nanocrystal, providing the exciton with protection against oxidation and photobleaching. We can see that the PL peak positions of type-I heterostructures do not red-shift in spite of successful shelling demonstrated by an increase in the average diameter of the samples. The thicker shell deposition is, however, accompanied by a slight decrease in the FWHM of these samples, which demonstrates improved passivation of the core and the absence of electron leakage into the shell. The trap emission evident as a red tail present in some PL spectra indicates incomplete shelling after the deposition of the first ZnS(e) monolayer, but disappears following subsequent shell additions.

Although the modeling results predict stronger confinement for the InP/ZnS system compared to InP/ZnSe, we did not find this to be evident in the PL spectra. During initial experiments, InP/ZnS synthesized using S/ODE exhibited measurably bluer emission than InP/ZnSe synthesized with TOP:Se, but visually observable color shifts during the addition of the sulfur was indicative of core etching (**Figure S5**). Once the sulfur precursor was changed to TOP:S to mitigate etching as discussed above, the difference in the peak PL emission wavelength between the InP/ZnS and InP/ZnSe generated with the same starting cores narrowed. Our modeling predicts that smaller cores will exhibit a more quasi-type-II behavior in the InP/ZnSe system than larger cores, which are predicted to be type-I (**Figure 2**). We would expect this to present as a larger red-shift for InP/ZnSe with smaller core sizes, which we observe in fact for both InP/ZnS and InP/ZnSe systems (**Figure 5**). The red-shift for the small-core InP/ZnS was significantly larger than expected compared to other reactions. This reaction may have been affected by Ostwald ripening, which is more likely with smaller cores than larger ones, prior to successful deposition of the ZnS shell.

Based on the position of the exciton 1S peak of the cores and taking into consideration the average Stokes shift of 60 nm associated with InP, both InP/ZnS and InP/ZnSe largely exhibit type-I behavior (Mićić et al., 1996; Fu and Zunger, 1997). Both the EMA model and our empirical data show that for the type-I systems, the starting core size is the determining parameter in tuning the emission color. The vertical contour plot lines for InP/ZnS(e) in **Figure 2** indicate that quantum confinement and the heterostructure bandgap do not change with additional ZnS(e) shell thickness after the initial deposition of a limited shell. Our graphs of InP/ZnS(e) peak position with respect to SILAR iterations in **Figure 5** confirm this behavior empirically as well. Our results confirm what others have observed—namely that InP/ZnS(e) emission wavelengths are tunable throughout the visible wavelength range by altering core size.

In contrast with the type-I heterostructures, deposition of CdS and CdSe on the InP core is accompanied by a significant red-shifting of the PL peak into the NIR wavelength ranges, which plateaus after the 7th round of SILAR deposition. Using CdSe or CdS as the shell material, the PL was successfully tuned throughout the red and into the near-infrared wavelength ranges. Larger core sizes resulted in emission at even longer wavelengths. In type-II systems, the significant influence of shell thickness on emission tuning is due to the separation of charge

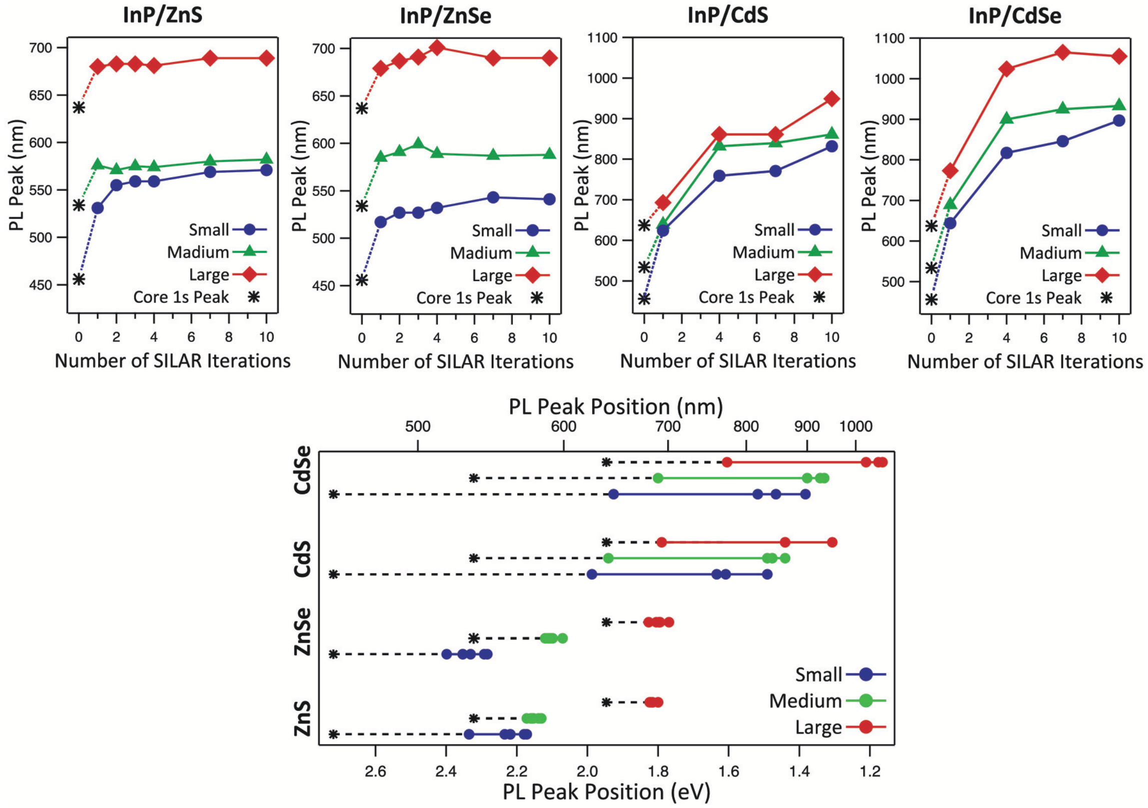

FIGURE 5 | Variation of PL peak position with increasing shell thickness for InP/ZnS, InP/ZnSe, InP/CdS, and InP/CdSe heterostructures with small, medium, and large cores. The asterisk denotes the exciton 1s absorption peak of the InP cores.

carriers: the confinement of holes in the core and electrons in the shell. In both cadmium shell systems, carrier recombination can take place across the core/shell interface at a lower energy than the bandgap of either of the constituent semiconductor materials.

It is important to note that in addition to the expected type-II NIR emission from the InP/CdS(e) structures, thicker shelled (>3 ML) InP/CdSe—but not InP/CdS—also exhibited shell-thickness dependent *visible* emission (**Figure S7**). In an extensive study that is beyond the scope of this paper (Buck et al., in preparation), we demonstrate that both of these photon energies (visible and NIR) are emitted by a single particle, appearing to originate from the type-II recombination described here, as well as, recombination events where both electron and hole carriers are confined in the CdSe shell. It is further notable that this behavior has not been observed in the InP/CdS system. It is likely that the core etching observed upon addition of S/ODE during the InP/ZnS synthesis also occurs when S/ODE is added for CdS deposition. This remodeling of the InP surface could impact surface states, preventing the visible emission originating in the shell. While we have spectroscopic evidence of the InP/ZnS etching (**Figure S5**, discussed above), we can only surmise that the S/ODE behaves similarly during the InP/CdS synthesis because the red-shifting of the optical features is pronounced even at the earliest depositions.

The contrast between the type-I and type-II systems is pronounced in the radiative lifetimes of the heterostructures, as well as, in the PL energy. **Figure 6** illustrates the PL lifetime for the thickest shell of each heterostructure, as well as, the change in lifetime with shell thickness. The lifetime measurements were taken for the emission range comprising one third of the total emission peak width in order to focus on bandgap emission rather than the redder trap state emission visible in the thin-shelled InP/ZnS(e) samples. The InP/ZnS(e) heterostructures exhibit negligible change in PL lifetime with additional shell deposition, as the carriers are both confined in the InP cores; the radiative recombination occurs relatively quickly and the average lifetime does not exceed 100 ns. The InP/CdS(e) structures exhibit dramatically longer lifetimes than the InP/ZnS(e) structures, consistent with type-II behavior. In addition, InP/CdS(e) QDs exhibit a shell thickness-dependent lengthening of the lifetime as the excited electron spreads through a larger shell volume with PL lifetimes approaching 700 ns. Even at particle diameters between 3 and 6 nm, where the particle size across different heterostructures are similar, the radiative lifetimes can be up to an order of magnitude higher for the InP/CdS(e) systems than for InP/ZnS(e).

To see shell-thickness dependent trends in PL intensity, we plotted the absorbance-normalized PL spectra of the medium core samples for four shell thicknesses of each of the four

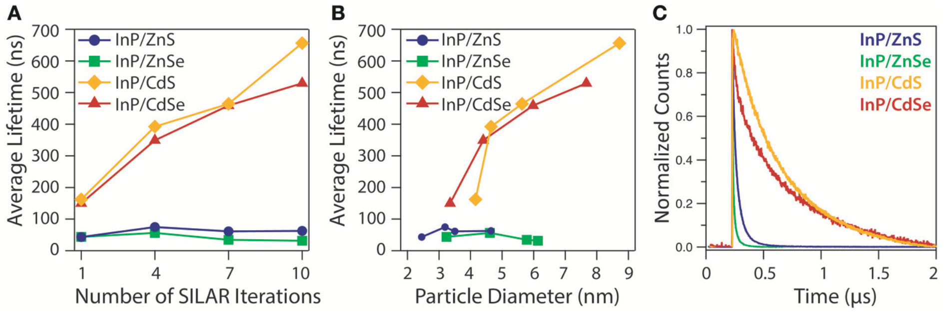

FIGURE 6 | PL lifetime measurements of InP/ZnS, InP/ZnSe, InP/CdS, and InP/CdSe heterostructures synthesized using medium sized cores: average excited state lifetime relative to **(A)** the number of SILAR iterations and **(B)** the particle diameter, as determined by TEM. Lines drawn as a guide to the eye. **(C)** PL decay curves of the largest core/shell heterostructures from each composition.

shell compositions (**Figure S8**). For InP/ZnS and InP/ZnSe, the brightest samples are obtained after the deposition of 1.96 and 3.81 shell MLs, respectively. We observe a clear increase in brightness as the InP surface is completely passivated, but thicker shells result in decreased PL intensity, presumably due to strain effects and defect formation. It's notable that this decline is observable at thinner ZnS shells than ZnSe shells (4.1 vs. 5.9 MLs, respectively); this difference correlates with the higher lattice mismatch for InP/ZnS vs. InP/ZnSe (7.8 vs. 4.9%). For the InP/CdS(e) samples, the first round of shell deposition passivates the InP core, enabling relatively bright emission from the previously non-emissive core. With subsequent shell deposition, however, the effects of spatial charge separation are observed as a significant decrease in the PL intensity. This decrease in PL intensity trends with the increase in PL lifetime as a result of the type-II nature of the heterostructures.

While the trends within each shell composition group are very consistent, we were also interested in the differences in brightness amongst compositions. Here, it is important to note that the absorbance-normalized PL measurements were taken many months after the particles were synthesized. We qualitatively observed that the InP/ZnSe samples significantly dimmed with time through casually monitoring brightness by eye under UV illumination, an option that is not feasible for the NIR-emitting InP/CdSe samples. The thinner-shelled InP/ZnS samples also lost some of their PL intensity with age: months earlier, both the 1.4 and 2.0 ML InP/ZnS exhibited absolute QYs of 43–45%, whereas at the time of the absorbance-normalized PL measurements, the 2.0 ML sample still exhibited a 43% QY, but the relative emission of the 1.4 ML sample had decreased (**Figure S8**). It is challenging to compare the InP/ZnS(e) samples to the InP/CdS(e) samples because of the different detector used for the NIR PL measurements—i.e., the y-axis scaling between the InP/ZnS(e) and InP/CdS(e) plots in **Figure S8** is quite different. We'll note, however, that we were never able to take absolute QY measurements of even the thin-shelled InP/CdS(e) systems on our instrument because the particles were so dim. The high absorptivity of the InP/CdS(e) samples is helpful for brightness, but the QY measurements require very dilute/low absorbing samples, making it more challenging to get a measurement that we were confident in from the very dim samples. In this context, despite the different y-axes of the InP/ZnS(e) and InP/CdS(e) plots, we are quite confident in saying that the type-II heterostructures were considerably dimmer than the type-I QDs.

CONCLUSIONS

We shine light on the optical tunability of InP-based core/shell heterostructures through compositional and dimensional modifications, resulting in a head-to-head comparison of type-I and type-II InP QDs. The emission energy of the InP/ZnS(e) type-I core/shell QDs was tuned by altering the core size, while the emission of the InP/CdS(e) type-II counterparts was primarily shell thickness-dependent. We demonstrate that charge separation in type-II systems caused by the valence and conduction band alignments gives rise to strongly shell thickness-dependent increase in average PL lifetimes compared to either thin-shelled InP/CdS(e) or InP/ZnS(e) of any shell thickness. Our systematic study of these InP core/shell heterostructures provides insight into QD design for a variety of biological and optoelectronic applications.

AUTHOR CONTRIBUTIONS

AD and JH conceived of and designed the project. RT performed the experimental work and data analysis with assistance from AM for sizing of the TEM images. RI performed PL spectroscopy measurements in the NIR wavelength range. AP performed the effective mass modeling of the heterostructures. RT and AD wrote the manuscript.

FUNDING

This publication was supported by the National Center for Advancing Translational Sciences, National Institutes of Health, through BU-CTSI Grant Number 1KL2TR001411. Its contents are solely the responsibility of the authors and do not necessarily represent the official views of the NIH. Funding sources include a Laboratory Directed Research and Development program of Los Alamos National Laboratory (DR20170001). AD was supported in part through a KL2 Fellowship, BU-CTSI Grant Number 1KL2TR001411. RT was funded in part through a Boston University Dean's Catalyst Award. AM was supported in part through Boston University Undergraduate Research Opportunities Program (UROP). AP, RI, and JH were supported by the Laboratory Directed Research and Development program of Los Alamos National Laboratory under DR20170001. This work was performed in part at the Center for Nanoscale Systems (CNS), a member of the National Nanotechnology Coordinated Infrastructure Network (NNCI), which is supported by the National Science Foundation under NSF award no. 1541959. CNS is part of Harvard University. The Dennis Lab is part of the Photonics Center, BUNano, the Precision Diagnostics Center and the Neurophotonics Center at Boston University.

SUPPLEMENTARY MATERIAL

The Supplementary Material for this article can be found online at: https://www.frontiersin.org/articles/10.3389/fchem.2018.00567/full#supplementary-material

REFERENCES

Acharya, K. P., Nguyen, H. M., Paulite, M., Piryatinski, A., Zhang, J., Casson, J. L., et al. (2015). Elucidation of two giants: challenges to thick-shell synthesis in CdSe/ZnSe and ZnSe/CdS Core/shell quantum dots. *J. Am. Chem. Soc.* 137, 3755–3758. doi: 10.1021/jacs.5b00313

Adam, S., Talapin, D. V., Borchert, H., Lobo, A., McGinley, C., de Castro, A. R. B., et al. (2005). The effect of nanocrystal surface structure on the luminescence properties: photoemission study of HF-etched InP nanocrystals. *J. Chem. Phys.* 123:084706. doi: 10.1063/1.2004901

Alivisatos, A. (1996). Semiconductor clusters,nanocrystals, and quantum dots. *Science* 271, 933–937. doi: 10.1126/science.271.5251.933

Balan, A. D., Eshet, H., Olshansky, J. H., Lee, Y. V., Rabani, E., and Alivisatos, A. P. (2017). Effect of thermal fluctuations on the radiative rate in core/shell quantum dots. *Nano Lett.* 17, 1629–1636. doi: 10.1021/acs.nanolett.6b04816

Battaglia, D., Li, J. J., Wang, Y., and Peng, X. (2003). Colloidal two-dimensional systems: CdSe quantum shells and wells. *Angew. Chem. Int. Ed.* 42, 5035–5039. doi: 10.1002/anie.200352120

Battaglia, D., and Peng, X. (2002). Formation of high quality InP and InAs nanocrystals in a noncoordinating solvent. *Nano Lett.* 2, 1027–1030. doi: 10.1021/nl025687v

Brodu, A., Ballottin, M. V., Buhot, J., van Harten, E. J., Dupont, D., La Porta, A., et al. (2018). Exciton fine structure and lattice dynamics in InP/ZnSe Core/Shell quantum dots. *ACS Photonics* 5, 3353–3362. doi: 10.1021/acsphotonics.8b00615

Chandran, H. R., Schiffman, J. D., and Balakrishna, R. G. (2018). Quantum dots as fluorescent probes: synthesis, surface chemistry, energy transfer mechanisms, and applications. *Sens. Actuators B Chem.* 258, 1191–1214.doi: 10.1016/j.snb.2017.11.189

Chandrasekaran, V., Tessier, M., D., Dupont, D., Geiregat, P., Hens, Z., Brainis, E., et al. (2017). Nearly blinking-free, high-purity single-photon emission by colloidal InP/ZnSe quantum dots. *Nano Lett.* 17, 6104–6109. doi: 10.1021/acs.nanolett.7b02634

Chen, O., Zhao, J., Chauhan, V. P., Cui, J., Wong, C., Harris, D. K., et al. (2013). Compact high-quality CdSe-CdS core-shell nanocrystals with narrow emission linewidths and suppressed blinking. *Nat. Mater.* 12, 445–451. doi: 10.1038/nmat3539

Chuang, C. H., Brown, P. R., Bulović, V., and Bawendi, M. G. (2014). Improved performance and stability in quantum dot solar cells through band alignment engineering. *Nat. Mater.* 13, 796–801. doi: 10.1038/nmat3984

Dabbousi, B. O., Rodriguez-Viejo, J., Mikulec, F. V., Heine, J. R., Mattoussi, H., Ober, R., et al. (1997). (CdSe)ZnS core–shell quantum dots: synthesis and characterization of a size series of highly luminescent nanocrystallites. *J. Phys. Chem. B* 101, 9463–9475. doi: 10.1021/jp971091y

Danek, M., Jensen, K. F., Murray, C. B., and Bawendi, M. G. (1996). Synthesis of luminescent thin-film CdSe/ZnSe quantum dot composites using CdSe quantum dots passivated with an overlayer of ZnSe. *Chem. Mater.* 8, 173–180. doi: 10.1021/cm9503137

Dennis, A. M., Mangum, B. D., Piryatinski, A., Park, Y. S., Hannah, D. C., Casson, J. L., et al. (2012a). Suppressed blinking and auger recombination in near-infrared Type-II InP/CdS nanocrystal quantum dots. *Nano Lett.* 12, 5545–5551. doi: 10.1021/nl302453x

Dennis, A. M., Rhee, W. J., Sotto, D., Dublin, S. N., and Bao, G. (2012b). Quantum dot-fluorescent protein fret probes for sensing intracellular pH. *ACS Nano* 6, 2917–2924. doi: 10.1021/nn2038077

Efros, A., L., and Rosen, M. (2000). The electronic structure of semiconductor nanocrystals. *Annu. Rev. Mater. Sci.* 30, 475–521. doi: 10.1146/annurev.matsci.30.1.475

Evans, C. M., Evans, M. E., and Krauss, T. D. (2010). Mysteries of TOPSe revealed: Insights into quantum dot nucleation. *J. Am. Chem. Soc.* 132, 10973–10975. doi: 10.1021/ja103805s

Fu, H., and Zunger, A. (1997). InP quantum dots: electronic structure, surface effects, and the redshifted emission. *Phys. Rev. B* 56, 1496–1508. doi: 10.1103/PhysRevB.56.1496

Guzelian, A. A., Katari, J. E. B., Kadavanich, A. V., Banin, U., Hamad, K., Juban, E., et al. (1996). Synthesis of size-selected, surface-passivated InP nanocrystals. *J. Phys. Chem.* 100, 7212–7219. doi: 10.1021/jp953719f

Hong, G., Antaris, A. L., and Dai, H. (2017). Near-infrared fluorophores for biomedical imaging. *Nat. Biomed. Eng.* 1:0010. doi: 10.1038/s41551-016-0010

Htoon, H., Malko, A. V., Bussian, D., Vela, J., Chen, Y., Hollingsworth, J. A., et al. (2010). Highly emissive multiexcitons in steady-state photoluminescence of individual 'giant' CdSe/CdS Core/Shell Nanocrystals. *Nano Lett.* 10, 2401–2407. doi: 10.1021/nl1004652

Ippen, C., Greco, T., and Wedel, A. (2012). InP/ZnSe/ZnS: a novel multishell system for InP quantum dots for improved luminescence efficiency and its application in a light-emitting device. *J. Inf. Disp.* 13, 91–95. doi: 10.1080/15980316.2012.683537

Jones, M., and Scholes, G. D. (2010). On the use of time-resolved photoluminescence as a probe of nanocrystal photoexcitation dynamics. *J. Mater. Chem.* 20, 3533–3538. doi: 10.1039/c000165a

Joo, J., Pietryga, J. M., McGuire, J. A., Jeon, S. H., Williams, D. J., Wang, H. L., et al. (2009). A reduction pathway in the synthesis of PbSe nanocrystal quantum dots. *J. Am. Chem. Soc.* 131, 10620–10628. doi: 10.1021/ja903445f

Kagan, C. R., Lifshitz, E., Sargent, E. H., and Talapin, D. V. (2016). Building devices from colloidal quantum dots. *Science* 353:aac5523. doi: 10.1126/science.aac5523

Kaledin, A. L., Kong, D., Wu, K., Lian, T., and Musaev, D. G. (2018). Quantum confinement theory of auger-assisted biexciton recombination dynamics in type-I and quasi type-II quantum dots. *J. Phys. Chem. C* 122, 18742–18750. doi: 10.1021/acs.jpcc.8b04874

Kong, D., Jia, Y., Ren, Y., Xie, Z., Wu, K., and Lian, T. (2018). Shell-thickness-dependent biexciton lifetime in type I and quasi-type II CdSe@CdS core/shell quantum dots. *J. Phys. Chem. C* 122, 14091–14098. doi: 10.1021/acs.jpcc.8b01234

Kong, L., Zhang, L., Meng, Z., Xu, C., Lin, N., and Liu, X. Y. (2018). Ultrastable, highly luminescent quantum dot composites based on advanced surface manipulation strategy for flexible lighting-emitting. *Nanotechnology* 29:315203. doi: 10.1088/1361-6528/aac39c

Lakowicz, J. R. (2006). *Principles of Fluorescence Spectroscopy, 3rd edn*. New York, NY: Springer. doi: 10.1007/978-0-387-46312-4

Lan, X., Masala, S., and Sargent, E. H. (2014). Charge-extraction strategies for colloidal quantum dot photovoltaics. *Nat. Mater.* 13, 233–240. doi: 10.1038/nmat3816

Li, J., and Wang, L.-W. (2004). First principle study of core/shell structure quantum dots. *Appl. Phys. Lett.* 84, 3648–3650. doi: 10.1063/1.1737470

Li, J. J., Wang, Y. A., Guo, W., Keay, J. C., Mishima, T., D., Johnson, M, B., et al. (2003). Large-scale synthesis of nearly monodisperse CdSe/CdS core/shell nanocrystals using air-stable reagents via successive ion layer adsorption and reaction. *J. Am. Chem. Soc.* 125, 12567–12575. doi: 10.1021/ja0363563

Li, L., and Reiss, P. (2008). One-pot synthesis of highly luminescent InP / ZnS nanocrystals without precursor injection. *J. Am. Chem. Soc.* 130, 11588–11589. doi: 10.1021/ja803687e

Lim, J., Park, M., Bae, W. K., Lee, D., Lee, S., Lee, C., et al. (2013). Highly efficient cadmium-free quantum dot light-emitting diodes enabled by the direct formation of excitons within InP@ZnSeS quantum dots. *ACS Nano* 7, 9019–9026. doi: 10.1021/nn403594j

McHugh, K. J., Jing, L., Behrens, A. M., Jayawardena, S., Tang, W., Gao, M., et al. (2018). Biocompatible semiconductor quantum dots as cancer imaging agents. *Adv. Mater. Weinheim.* 30, 1–18. doi: 10.1002/adma.201706356

Micic, O. I., Curtis, C. J., Jones, K. M., Sprague, J. R., and Nozik, A. J. (1994). Synthesis and characterization of InP quantum dots. *J. Phys. Chem.* 98, 4966–4969. doi: 10.1021/j100070a004

Mićić, O. I., Sprague, J., Lu, Z., and Nozik, A. J. (1996). Highly efficient band-edge emission from InP quantum dots. *Appl. Phys. Lett.* 68, 3150–3152. doi: 10.1063/1.115807

Mordvinova, N., Vinokurov, A., Dorofeev, S., Kuznetsova, T., and Znamenkov, K. (2014). Phosphine synthetic route features and postsynthetic treatment of InP quantum dots. *J. Alloys Compd.* 582, 43–49. doi: 10.1016/j.jallcom.2013.08.003

Mordvinova, N., Vinokurov, A., Kuznetsova, T., Lebedev, O. I., and Dorofeev, S. (2017). Highly luminescent core-shell InP/ZnX (X = S, Se) quantum dots prepared via a phosphine synthetic route. *Dalt. Trans.* 46, 1297–1303. doi: 10.1039/C6DT03956A

Murray, C. B., Norris, D. J., and Bawendi, M. G. (1993). Synthesis and characterization of nearly monodisperse CdE (E = S, Se, Te) semiconductor nanocrystallites. *J. Am. Chem. Soc.* 115, 8706–8715. doi: 10.1021/ja00072a025

Niu, Y., Pu, C., Lai, R., Meng, R., Lin, W., Qin, H., et al. (2017). One-pot/three-step synthesis of zinc-blende CdSe/CdS core/shell nanocrystals with thick shells. *Nano Res.* 10, 1149–1162. doi: 10.1007/s12274-016-1287-3

Omogo, B., Aldana, J. F., and Heyes, C. D. (2013). Radiative and nonradiative lifetime engineering of quantum dots in multiple solvents by surface atom stoichiometry and ligands. *J. Phys. Chem. C* 117, 2317–2327. doi: 10.1021/jp309368q

Peng, Z. A., and Peng, X. (2001). Formation of high-quality CdTe, CdSe, and CdS nanocrystals using CdO as precursor. *J. Am. Chem. Soc.* 123, 183–184. doi: 10.1021/ja003633m

Piryatinski, A., Ivanov, S. A., Tretiak, S., and Klimov, V. I. (2007). Effect of quantum and dielectric confinement on the exciton-exciton interaction energy in type II core/shell semiconductor nanocrystals. *Nano Lett.* 7, 108–115. doi: 10.1021/nl0622404

Reid, K. R., McBride, J. R., Freymeyer, N. J., Thal, L. B., and Rosenthal, S. J. (2018). Chemical structure, ensemble and single-particle spectroscopy of thick-shell InP-ZnSe quantum dots. *Nano Lett.* 18, 709–716. doi: 10.1021/acs.nanolett.7b03703

Reiss, P., Protière, M., and Li, L. (2009). Core/shell semiconductor nanocrystals. *Small* 5, 154–168. doi: 10.1002/smll.200800841

Smith, C. T., Leontinadou, M. A., Clark, P. C. J., Lydon, C., Savjani, N., Spencer, B. F., et al. (2017). Multiple exciton generation and dynamics in InP/CdS colloidal quantum dots. *J. Phys. Chem. C* 121, 2099–2107. doi: 10.1021/acs.jpcc.6b11744

Talapin, D. V., Gaponik, N., Borchert, H., Rogach, A., L., Haase, M., et al. (2002). Etching of colloidal InP nanocrystals with fluorides: photochemical nature of the process resulting in high photoluminescence efficiency. *J. Phys. Chem. B* 106, 12659–12663. doi: 10.1021/jp026380n

Tamang, S., Lincheneau, C., Hermans, Y., Jeong, S., and Reiss, P. (2016). Chemistry of InP nanocrystal syntheses. *Chem. Mater.* 28, 2491–2506. doi: 10.1021/acs.chemmater.5b05044

Ten Cate, S., Sandeep, C. S., Liu, Y., Law, M., Kinge, S., Houtepen, A. J., et al. (2015). Generating free charges by carrier multiplication in quantum dots for highly efficient photovoltaics. *Acc. Chem. Res.* 48, 174–181. doi: 10.1021/ar500248g

Tessier, M. D., Dupont, D., De Nolf, K., De Roo, J., and Hens, Z. (2015). Economic and size-tunable synthesis of InP/ZnE (E = S, Se) colloidal quantum dots. *Chem. Mater.* 27, 4893–4898. doi: 10.1021/acs.chemmater.5b02138

Vela, J., Htoon, H., Chen, Y., Park, Y. S., Ghosh, Y., Goodwin, P. M., et al. (2010). Effect of shell thickness and composition on blinking suppression and the blinking mechanism in 'giant' CdSe/CdS nanocrystal quantum dots. *J. Biophotonics* 3, 706–717. doi: 10.1002/jbio.201000058

Wang, L., Nonaka, K., Okuhata, T., Katayama, T., and Tamai, N. (2018). Quasi-type II carrier distribution in CdSe/CdS Core/shell quantum dots with type i band alignment. *J. Phys. Chem. C* 122, 12038–12046. doi: 10.1021/acs.jpcc.7b11684

Wei, S. H., and Zunger, A. (1998). Calculated natural band offsets of all II-VI and III-V semiconductors: Chemical trends and the role of cation d orbitals. *Appl. Phys. Lett.* 72, 2011–2013. doi: 10.1063/1.121249

Xie, R., Battaglia, D., and Peng, X. (2007). Colloidal InP nanocrystals as efficient emitters covering blue to near-infrared. *J. Am. Chem. Soc.* 129, 15432–15433. doi: 10.1021/ja076363h

Xie, R., Li, Z., and Peng, X. (2009). Nucleation kinetics vs chemical kinetics in the initial formation of semiconductor nanocrystals. *J. Am. Chem. Soc.* 131, 15457–15466. doi: 10.1021/ja9063102

Xie, R., and Peng, X. (2009). Synthesis of Cu-doped InP nanocrystals (d-dots) with ZnSe diffusion barrier as efficient and color-tunable NIR emitters. *J. Am. Chem. Soc.* 131, 10645–10651. doi: 10.1021/ja903558r

Xu, S., Ziegler, J., and Nann, T. (2008). Rapid synthesis of highly luminescent InP and InP/ZnS nanocrystals. *J. Mater. Chem.* 18, 2653–2656. doi: 10.1039/b803263g

Yu, K., Hrdina, A., Zhang, X., Ouyang, J., Leek, D. M., Wu, X., et al. (2011). Highly-photoluminescent ZnSe nanocrystals via a non-injection-based approach with precursor reactivity elevated by a secondary phosphine. *Chem. Commun.* 47, 8811–8813. doi: 10.1039/c1cc12237a

Zhou, J., Pu, C., Jiao, T., Hou, X., and Peng, X. (2016). A two-step synthetic strategy toward monodisperse colloidal cdSe and CdSe/CdS Core/shell nanocrystals. *J. Am. Chem. Soc.* 138, 6475–6483. doi: 10.1021/jacs.6b00674

Zhou, J., Zhu, M., Meng, R., Qin, H., and Peng, X. (2017). Ideal CdSe/CdS core/shell nanocrystals enabled by entropic ligands and their core size-, shell thickness-, and ligand-dependent photoluminescence properties. *J. Am. Chem. Soc.* 139, 16556–16567. doi: 10.1021/jacs.7b07434

Conflict of Interest Statement: The authors declare that the research was conducted in the absence of any commercial or financial relationships that could be construed as a potential conflict of interest.

frontiers
in Chemistry

ORIGINAL RESEARCH
published: 22 November 2018
doi: 10.3389/fchem.2018.00562

Colloidal Synthesis of Bulk-Bandgap Lead Selenide Nanocrystals

*Thulitha M. Abeywickrama, Asra Hassan and Preston T. Snee**

Department of Chemistry, University of Illinois at Chicago, Chicago, IL, United States

Lead selenide quantum dots (QDs) are low-bandgap IV-VI semiconducting nanomaterials that have been studied for a variety of applications. Their preparation using colloidal methods can create small spherical to larger cubic nanocrystals, with an upper limit of ∼17 nm reported to date. Here we describe methods for preparing cubic PbSe nanocrystals over a 20–40 nm size range using a twostep procedure. Specifically, ∼10 nm PbSe QDs are generated using the rapid injection method, the products from which are overcoated with additional lead and selenium precursors. The use of two lead reagents were studied; lead oleate resulted in a maximum of 20 nm cubes, while more reactive lead hexyldecanoate resulted in much larger nanomaterials with bulk bandgaps. However, PbSe samples prepared with lead hexyldecanoate also contained agglomerates. Special care must be taken when characterizing larger strained nanomaterials with X-ray powder diffraction, for which the Scherrer equation is inadequate. A more rigorous approach using the Williamson–Hall method provides characterizations that are consistent with electron microscopy analysis.

Keywords: lead selenide, quantum dots, semiconductor, nanomaterials, conductivity

Edited by:
Ou Chen,
Brown University, United States

Reviewed by:
Huaibin Shen,
Henan University, China
Liangfeng Sun,
Bowling Green State University,
United States

****Correspondence:***
Preston T. Snee
sneep@uic.edu

Specialty section:
This article was submitted to
Nanoscience,
a section of the journal
Frontiers in Chemistry

Received: *31 August 2018*
Accepted: *30 October 2018*
Published: *22 November 2018*

Citation:
Abeywickrama TM, Hassan A and Snee PT (2018) Colloidal Synthesis of Bulk-Bandgap Lead Selenide Nanocrystals. Front. Chem. 6:562.
doi: 10.3389/fchem.2018.00562

INTRODUCTION

Quantum dots (QDs) are nanoscale particles that have size-tunable optoelectronic properties that may differ substantially from their bulk counterparts. The materials can be prepared using low-cost colloidal methods, which has attracted attention for their use in electronic devices (Talapin and Murray, 2005; Talapin et al., 2010), photovoltaics (Tang et al., 2011; Etgar et al., 2013), sensors (Snee et al., 2006), and in bioimaging (Alivisatos, 2004). Quantum dots are often classified based on the elemental grouping of their composition, which in turn is associated with specific applications. For example, II–VI's such as CdSe are visible emitters often employed in biological sensing applications and have been incorporated into commercially available displays (i.e., television sets). The III–V's such as InP and InAs are of interest for their near-IR emission, and the IV–VI's such as PbS and PbSe are low bandgap materials that have utility in electronics, photodetectors, and solar cells. Lead selenide has been extensively studied due to the high quality of the nanomaterials that can be prepared (Pietryga et al., 2004; Capek et al., 2015) and the ease of tunability of the electronic structure due to the low bulk bandgap (0.27 eV) and large excitonic Bohr radius (46 nm) (Yanover et al., 2012). There are many procedures to synthesize PbSe QDs, although the most robust utilize the rapid injection method since it can produce QDs with narrow, near-atomically precise size distributions (Capek et al., 2015; Shapiro et al., 2016).

Previously reported methods to prepare PbSe QDs often employ high boiling point organic solvents (diphenyl ether or 1-octadecene) containing stabilizers such as oleic acid, into which lead salt and phosphine selenide precursors are injected. For many years the reaction yields were reported to be very low, which was found to result from the near ubiquitous use of trioctylphospine selenide (TOPSe) as the calchogenide precursor (Evans et al., 2010). Specifically, Evans et al.

discovered that purified TOPSe is non-reactive with lead and that previous reports on preparing PbSe QDs using this reagent relied on the fortuitous presence of secondary phosphine impurities (Evans et al., 2010). As such, it is common to incorporate diphenylphosphine with TOPSe in a preparation. At present, there are reports of the colloidal synthesis of small magic-sized clusters to larger PbSe cubes on the order of 15–17 nm, which imparts bandgaps from the higher energy near infrared to shortwave infrared spectral regions (Shapiro et al., 2016).

There is interest in the synthesis of larger nanomaterials using colloidal techniques. For example, Zamkov and co-workers prepared very large (∼25 nm) nanocrystals by ligand-induced digestive ripening of as-prepared CdSe and $CsPbBr_3$ QDs among others (Razgoniaeva et al., 2018). Nanomaterials of this size have minimal interfacial areas, which enhances the conductivity of films made from these systems (Razgoniaeva et al., 2017). We sought to prepare very large monodisperse PbSe nanocrystals for these reasons and to challenge the present ∼15–17 nm size limit (Pietryga et al., 2004; Shapiro et al., 2016). To this end, we explored the use of lead acid precursors of varying reactivity, which resulted in the development of two protocols to produce cubic PbSe QDs over a 20–40 nm in size range. This was achieved by a two-step process whereby ∼10 nm core QDs were overcoated to obtain much larger cubic QDs. The main factors that dictate the sizes and quality of the products are the growth temperature and the identity of the lead precursor. Special care must be taken when characterizing larger strained crystalline nanomaterials using powder X-ray diffraction techniques, for which the Scherrer equation is inadequate. Last, it was found that the larger sized PbSe samples are significantly more conductive than their smaller counterparts.

EXPERIMENTAL

Materials

Acetone (99.5%), diphenyl phosphine (98%), hexane (mixture of isomers, 98.5%), 2-hexyldecanoic acid (96%), lead(II) oxide (PbO, 99%), methanol (99.8%), 1-octadecene (technical grade, 90%), oleic acid (90%), oleylamine (>98% primary amine), 2-propanol (99.5%), tetrabutylammonium iodide (98%), triethylamine (99%), and trifluoroacetic anhydride (99%) were purchased from Sigma-Aldrich. Acetonitrile (HPLC Grade) and trifluoroacetic acid were purchased from Fisher Scientific. Trioctylphosphine (97%) was purchased from Strem. Trioctylphosphine selenide (TOPSe) were prepared by mixing Se metal into trioctylphoshpine and stirring overnight to prepare a 1M solution. Diphenylphosphine selenide was prepared according to the procedure of Evans et al. (2010). Oleic acid was recrystallized according to the procedure of Arudi et al. (1983).

Preparation of $Pb(C_{18}H_{33}O_2)_2$

Lead oleate was synthesized using lead oxide, trifluoroacetic anhydride, and oleic acid as described by Hendricks et al. (2015).

Preparation of $Pb(C_{16}H_{31}O_2)_2$

Lead hexyldecanoate was synthesized using a modification of the method reported by Hendricks et al. (2015). Lead(II) oxide (5.000 g, 22.4 mmol) and 10 mL acetonitrile were added to a 100 mL round bottom flask maintained in an ice bath. After stirring for 10 min, trifluoroacetic acid (0.34 mL, 4.48 mmol) and trifluoroacetic anhydride (3.20 mL, 22.4 mmol) were added. The solution turned clear after 15 min stirring and was then warmed to room temperature. In another 250 mL round bottom flask, 2-hexyldecanoic acid (12.2 mL, 45.0 mmol) and triethylamine (7.13 mL, 50.5 mmol) were mixed in 90 mL of 2-propanol. The lead trifluoroacetate solution was then added to the 2-hexyldecanoic acid solution. The resulting colorless mixture was heated to reflux for 2 h and then cooled to room temperature. The solution was concentrated under vacuum and the precursor was separated as a semisolid by filtration after cooling to the point where solid materials separated. To remove excess triethylamine, the crude product was heated with an attached distillation apparatus with a temperature probe until a condensate appeared at 89°C, which is the boiling point of triethylamine. The product was left at this condition for ∼1 h to assure the removal of the amine and was then characterized with NMR (**Figure S1**) and combustion analysis (**Table S1**). Deviations from the expected results are due to residual triethylamine; these data are provided in the supporting information.

Preparation of "Core" PbSe QDs

PbSe QDs were synthesized using the hot injection method via two protocols that are derivatives of that reported by Shapiro et al. (2016).

Method (1) Stoichiometric Ligand Condition

Into a 50 mL three neck round bottom flask containing 7.5 g 1-octadecene (ODE) solvent, either 0.483 g lead oleate (0.63 mmol) or 0.450 g lead hexyldecanoate (0.63 mmol) was added. The solution was heated under vacuum at 100°C until the pressure stabilized. The selenium precursor in the injection solution was prepared inside a glovebox by mixing 0.4 g of 1.0 M trioctylphosphine selenide (TOPSe, 0.48 mmol) with 0.15 g of diphenylphosphine (DPP, 0.81 mmol) with 1.2 g of trioctylphosphine (TOP), which was then loaded into a 3 mL syringe. The lead precursor/ODE solution was heated to 260°C under nitrogen, at which point the heating mantle was removed. The selenium solution was rapidly injected when the solution cooled to 240°C. This solution was maintained at 230°C for another 10 min before cooling to room temperature.

Method (2) Excess Ligand Condition

Another set of PbSe QDs were prepared following the same procedure above with excess ligand present in the lead precursor/ODE solution. Specifically, 0.551 g of oleic acid (1.95 mmol) was added to the 50 mL three neck round bottom flask when using lead oleate as a precursor. Alternatively, 0.500 g of 2-hexyldecanoic acid (1.95 mmol) was added when using lead hexyldecanoate. The preparation of magic-sized PbSe QDs was attempted using lead hexyldecanoate as above, with the exception that the solution was maintained at room temperature for a 24 h growth period.

An XPS survey spectrum for the processed lead oleate "core" QDs was measured (**Figure S2**). The elemental composition

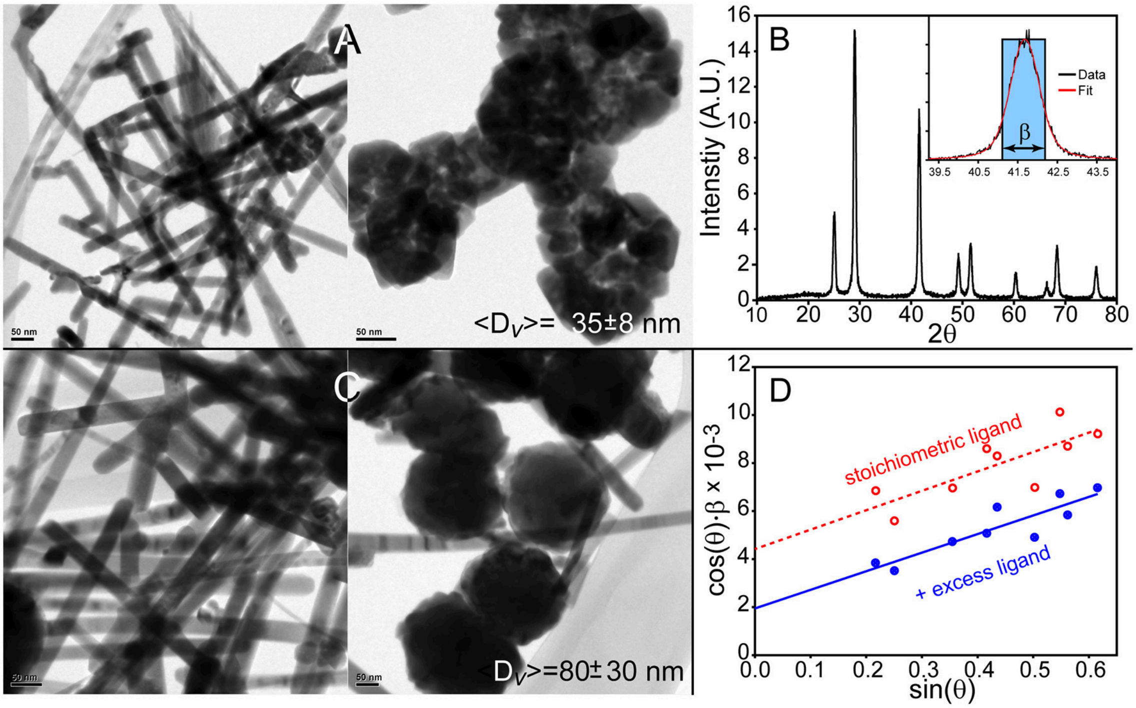

FIGURE 1 | Synthesis of PbSe nanostructures using lead hexyldecanoate results in lead selenide rods and agglomerates of materials. **(A)** Method 1 produces~20 nm thick PbSe rods and agglomerated materials. **(B)** Powder X-ray diffraction pattern of the materials shown in **(A)**. Inset is an example of a resonance's integral breadth. **(C)** Nanostructures prepared with additional hexyldecanoic acid in the solvent results in larger materials although the overall morphology is poorly defined. **(D)** The Williamson–Hall method was applied to the XRD patterns of the materials produced by these methods to determine the volume-weighted average size $\langle D \rangle_V$.

from the XPS analysis is presented in **Table S2**. These data reveal the presence of lead and selenium as well as some oxide. The Pb:Se ratio is 2:1, which is a common observation from PbSe QDs and likely results from the presence of excess Pb precursors that were not removed upon precipitation/washing of the sample before analysis (Jawaid et al., 2011).

Overcoating of PbSe QDs

Due to the low quality of "core" PbSe nanomaterials prepared with lead hexyldecanoate, all subsequent manipulations were performed with PbSe QDs from Method 2 with the lead oleate precursor. This method produced the largest, most homogeneous QDs. When overcoating a sample, a portion (typically ½) of a batch of the as-prepared PbSe QDs were transferred into a 20 mL vial. Addition of hexane and increasing amounts of 2-propanol resulted in precipitation, and the QDs were separated by centrifugation. The precipitate was re-dissolved in a hexane/2-propanol mixture and centrifuged again; this step was repeated twice more.

Method (1) Overcoating With $Pb(C_{18}H_{33}O_2)_2$

Approximately half of a batch of as-prepared "core" QDs were processed as above. The precipitated nanocrystals were added to 20 g ODE containing 0.121 g oleic acid (0.43 mmol) in a 100 mL four neck round bottom flask. The mixture was degassed under the vacuum at 100°C until the pressure stabilized. Then the solution was heated to either 130, 160, or 190°C under a nitrogen atmosphere. Meanwhile, two precursor solutions were prepared for injection. One for lead was prepared by dissolving 0.290 g of lead oleate (0.38 mmol) in 3 mL TOP, and the selenium solution was prepared by dissolving 0.100 g diphenylphosphine selenide (DPPSe, 0.38 mmol) in 3 mL TOP. These manipulations were performed in a glovebox. Once the QD/oleic acid/ODE bath reached the target temperature, the lead and selenium precursor solutions were added using a syringe injector at a 3 mL/h rate while maintaining a constant temperature. After complete addition of the precursors, the mixture was maintained at the overcoating temperature for another 5 m before cooling to ambient. Products were stored as-prepared in a glove box until later analysis.

Two additional protocols were investigated to prepare larger materials. Both methods sought to increase the precursor to QD ratio in the overcoating process. One was realized by doubling the precursors' masses; specifically, 0.580 g of lead oleate was (0.75 mmol) was added to 3 mL TOP and 0.200 g of DPPSe was likewise added to 3 mL TOP, which were subsequently injected into a QD/oleic acid/ODE solution at 160°C. Another method used the original masses of lead and selenium precursors, which were applied to ~¼ of a batch of "core" PbSe QDs.

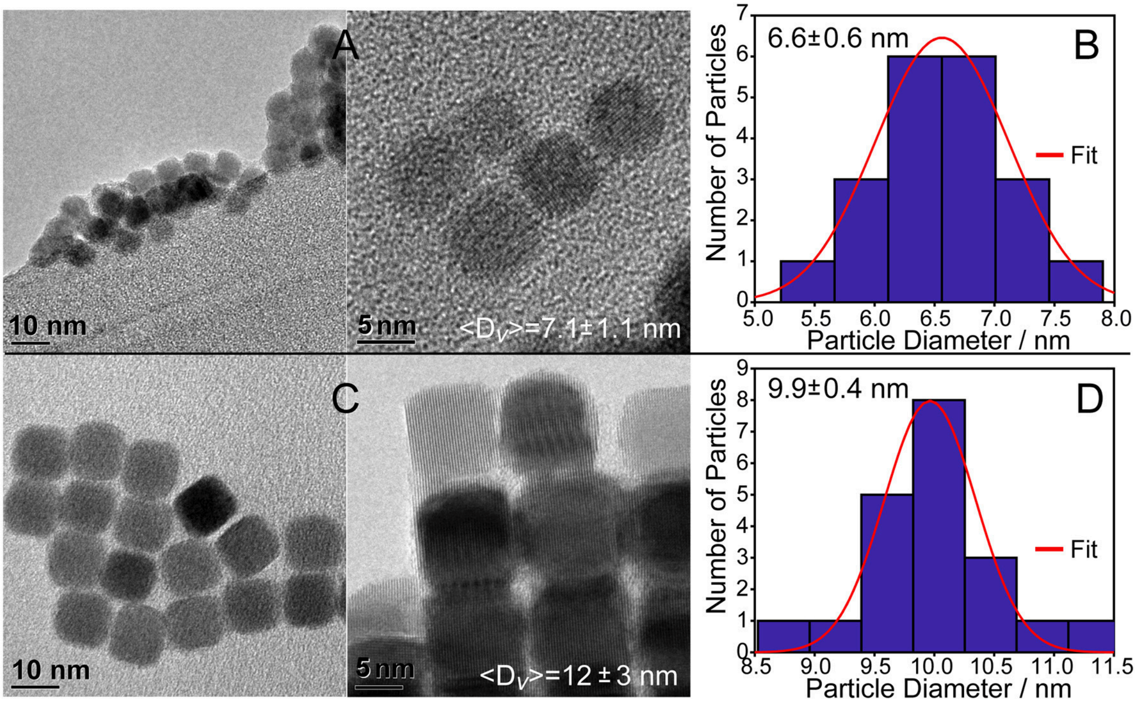

FIGURE 2 | PbSe cubes synthesized using lead(II) oleate. **(A)** Using the reagent without additional oleic acid results in 7.1 ± 1.1 nm cubes as determined using the Williamson–Hall method. **(B)** Histogram of the cube sizes by TEM is consistent with the Williamson–Hall result from XRD analysis. **(C)** Preparing PbSe cubes with additional oleic acid in the solvent results in larger, more homogeneous materials. Additional images are provided in the supporting information, **Figure S3**. **(D)** Histogram of the cube facet sizes of materials shown in C by TEM is consistent with the results from XRD analysis.

Method (2) Overcoating With $Pb(C_{16}H_{31}O_2)_2$

This procedure is similar to Method 1 except where noted. Approximately half of a batch of "core" QDs prepared via Method 2 using lead oleate were processed using hexane/2-propanol as discussed previously. The solvent consisted of a solution of 0.110 g 2-hexyldecanoic acid (0.43 mmol) in 20 g ODE. The injection solutions consisted of 0.540 g lead hexyldecanoate (0.75 mmol) in 3 mL TOP and 0.200 g DPPSe (0.75 mmol) in 3 mL TOP. The overcoatings were performed at either 130 or 160°C. Products were stored as-prepared in a glove box until later analysis.

Characterization

Samples were characterized by removing an appropriately-sized portion from storage in the glovebox, which was centrifuged to separate the PbSe precipitate. The solid was re-dissolved in hexane and centrifuged again; this step was repeated once more. The solid material was re-dispersed in hexane or tetrachloroethylene and was used for further characterizations. Transmission Electron Microscopy (TEM) analyses were performed using JEOL JEM-3010 microscope operating at 300 KeV. TEM grids were prepared by dropcasting a drop of the processed nanoparticle solution onto a 300 mesh carbon-coated Cu grid from Ted Pella. X-ray diffraction measurements were performed using a D8 Advance ECO Bruker XRD diffractometer with Cu Kα (λ = 1.54056 Å) radiation. The instrument was used in both a low and high-resolution modes. The angle-dependent instrument response function of the XRD diffractometer was determined using NIST SRM 640e, a strain-free Si standard composed of ∼4.1 micron sized particles. X-ray photoelectron spectroscopy (XPS) analysis was performed on a Kratos Axis 165 with Al Kα source operate at 12 kV and 10 mA. Fourier-transform infrared spectroscopy analysis was performed using an Thermo Nicolet 6700 FTIR and a Bruker Tensor 27 FTIR. Samples for FTIR analyses were coated onto a KBr pellet. ^{1}H NMR and ^{13}C NMR spectra were recorded using a Bruker Avance DRX 400 NMR spectrometer, and elemental analysis was performed by Midwest Microlab.

Conductivity measurements were performed on "core" ∼12 nm PbSe QDs prepared with method 2 and larger ∼22 nm PbSe overcoated samples. The processing is based on the method of Ning et al. (2014), whereby 1 mL of growth solution was washed with anhydrous hexane and centrifuged 3×. The samples were redispersed into hexane and incubated with 0.6 mL of a 0.6 M solution of tetrabutylammonium iodide in oleylamine for 15 min in a glove box. The samples were washed with excess dry methanol and then hexane, and were redispersed in 2 mL hexane with sonication before spin coating onto a lithographically prepared Si substrate consisting of two Ti electrodes with a 3 μm gap. The samples were dried under vacuum, and then taken out into ambient air and light for measuring current vs. applied voltage using a Kiethley 2450 Sourcemeter, with the voltage swept from −3.00 to +3.00 V in steps of 0.1 V. Five devices were measured and were all found to be qualitatively similar, with differences attributed to lithographic imperfections and the presence of residual photoresist in the device's electrode gap.

RESULTS AND DISCUSSION

Large 20–40 nm cubic-shaped PbSe colloidal nanocrystals were synthesized from "core" PbSe QDs that were overcoated with additional lead and selenium precursors. The first consideration toward the development of protocols was given to precursors. For the chalcogenide, there has been considerable effort to study the chemistry of selenium since the report by Evans et al. whom demonstrated the necessity of a secondary phosphine species in the production of lead selenide QDs (Evans et al., 2010). As a result, many groups have employed TOPSe with additional secondary diphenylphosphine to prepare PbSe QDs. We have used the same system for selenium, and as such we sought to study more effective lead-carboxylate precursors to realize larger nanomaterials. In this regard, recently Peng and co-workers reported the use of "entropic" carboxylate fatty acid ligands for quantum dot core and core/shell synthesis (Yang et al., 2016). In their vocabulary, an entropic ligand includes 2-hexyldecanoic acid, which is a non-viscous liquid at room temperature despite its very high molecular weight. The Peng group reported that this ligand enhances the solubility of large QDs, and that the extra solubility aids in the overcoating of CdSe QDs into larger CdSe/CdS core/shell sizes (Zhou et al., 2017; Lai et al., 2018). As a result, we examined the use of lead oleate as well as "entropic" lead hexyldecanoate as precursors for PbSe QDs synthesis and subsequent overcoating. Several other parameters such as temperature and stoichiometries were also investigated.

Synthesis of "Core" PbSe QDs

The synthesis of PbSe QDs was studied by injecting a solution of TOPSe and DPP in TOP into a hot ODE solvent containing either lead oleate or lead hexyldecanoate. Concerning the latter, our hypothesis is that we could create the largest monodisperse PbSe dots or cubes with hexyldecanoic acid due to enhanced solubility of PbSe particles coated with this "entropic" ligand. However, since we must incorporate the ligand as part of the lead precursor to assure a consistent coating of the QDs, it is necessary to use lead hexyldecanoate as the Pb source. It was found that this precursor is highly reactive as its use resulted in the formation of rod-like structures with ∼20 ± 5 nm diameters and large quantities of bulky, aggregated nanoparticles as seen in **Figure 1A**. Powder X-ray diffraction (XRD) characterization (**Figures 1B,D**) was able to provide a measure of the volume-weighted average size of the ensemble $\langle D\rangle_v$, which is 35 ± 8 nm. Note that the reported error reflects the systematic uncertainty in the measurement and not necessarily the width of the size distribution; more discussion on XRD analysis is provided below. Inclusion of extra ligands in the solvent resulted in thicker rods as seen in **Figure 1C** (37 ± 9 nm, as measured by TEM) and more agglomeration as revealed by the increase in the ensemble average $\langle D\rangle_v = 80 \pm 30$ nm as measured by XRD, see **Figure 1D**. We believe that the high reactivity of lead hexyldecanoate under these conditions leads to a rapid and rather uncontrolled growth of PbSe nanocrystals no matter our attempts to modify the reaction conditions. As such, it was determined that lead hexyldecanoate is not a good reagent for preparing "core" PbSe QDs using the rapid injection method.

Monodisperse PbSe spheres and cubes were realized using lead oleate with and without additional oleic acid in the solvent as seen in **Figures 2A,C**. TEM micrographs of the QDs formed under the stoichiometric ligand condition (Method 1) show spheres and some cube-shaped particles with a size distribution of 6.6 ± 0.6 nm (**Figure 2B**), which is consistent with the XRD measurement of $\langle D\rangle_v = 7.1 \pm 1.1$ nm. QDs formed under extra ligand conditions are cubic-shaped particles with a size distribution of 9.9 ± 0.4 nm (**Figure 2D**), which again correlates with the ensemble average of $\langle D\rangle_v = 12 \pm 3$ nm. Other characterization data such as XPS and elemental analyses as well as additional TEM images (**Figure S3**) are presented in the supporting information.

Overcoating of "Core" PbSe QDs

QDs synthesized with the lead oleate precursor under extra ligand conditions (Method 2) were used as seeds for the addition of a PbSe coating to create larger nanocrystals. In overcoating Method 1, these materials were augmented by the slow addition of lead oleate and highly reactive diphenylphosphine selenide. The overcoating was performed as a function of temperature, with trials at 130, 160, and 190°C. The TEM images of the resulted nanostructures are presented in **Figure 3**. The particles prepared at the lowest temperature of 130°C (**Figure 3A**) did not show any detectable growth as $\langle D\rangle_v = 10 \pm 3$ nm; clearly the temperature was insufficient to activate one or more of the precursors. The best overcoating was realized at 160°C (**Figure 3B**), which formed the most monodisperse, largest cubic QDs with an ensemble average size of $\langle D\rangle_v = 21 \pm 2$ nm. At the highest temperature of 190°C the addition of overcoating precursors resulted in large agglomerated structures formed by the aggregation of smaller particles (**Figure 3C**), which is consistent with the ensemble average of $\langle D\rangle_v = 100 \pm 30$ nm. Additional TEM images of the nanocrystals formed under these conditions are shown in the supporting information (**Figures S4, S5**).

To create even larger materials, the quantity of overcoating precursors was raised 2×. Unfortunately, the average ensemble size was not significantly increased ($\langle D\rangle_v = 22 \pm 4$ nm), and the materials appear unaltered as shown in **Figure 4A**. More TEM images of these structures are shown in the supporting information (**Figure S6**). Another attempt to push the limits of size was pursued by lowering the quantity of core QDs by ½ and repeating the overcoating exactly as before at 160°C. Again, there was no significant increase in size ($\langle D\rangle_v = 22 \pm 1$ nm), although it was noted that there was some alteration of the sample into a more spherical shape as observed in **Figure 4B**.

The use of lead hexyldecanoate was examined in the overcoating process, because although it is too reactive to generate monodisperse "core" PbSe QDs via rapid injection, this same property may engender efficacy when used at lower concentrations and temperatures. The results were successful in part; using this precursor for overcoating at 130°C resulted

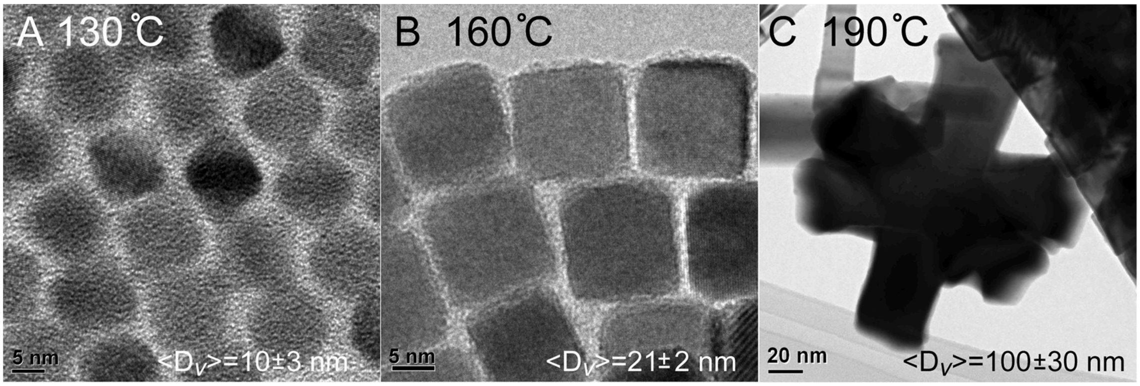

FIGURE 3 | Material size vs. temperature during the overcoating process. **(A)** PbSe cubes do not experience an increase in size when overcoating at 130°C. **(B)** Higher temperatures result in PbSe cubes with~8× more volume than the starting core material. **(C)** Increasing the temperature to 190°C results in uncontrolled growth.

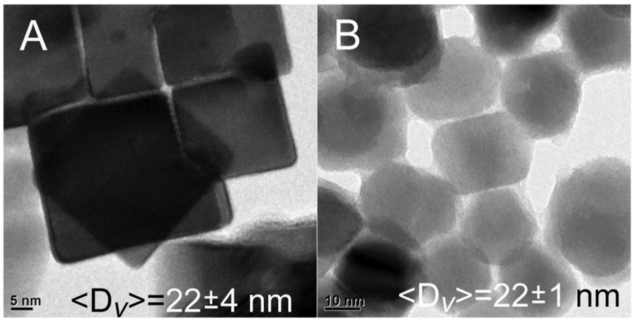

FIGURE 4 | (A) Doubling the amount of Pb and Se precursors in the overcoating process does not change the size of the resulting nanomaterials. **(B)** No significant increase in the sizes of materials is realized by overcoating less~10 nm PbSe cubes, although a loss of the cubic morphology is observed.

in the formation of some stand-alone very large, cubic shaped particles ($\langle D\rangle_v = 39 \pm 5$ nm) along with stacked, rod-like shaped agglomerates as seen in **Figure 5A**. Raising the temperature to 160°C resulted in the formation of bulkier structures ($\langle D\rangle_v = 140 \pm 80$ nm), cubic rods, and a few stand-alone particles as shown in **Figure 5B**. Additional TEM images are provided in **Figures S7**, **S8** of the supporting information. These results present a mixed message; for one, it is possible to prepare colloidal PbSe nanomaterials >20 nm by increasing the reactivity of the precursors. However, lead hexyldecanoate is too reactive to be used for preparing cores using the rapid injection technique or to overcoat materials due to the loss of monodispersity in the products. To find some use of this reagent, we examined the room temperature synthesis of PbSe QDs rather than smaller magic-sized particles (<2 nm) as observed by Evans et al. (2008). In fact, it was found that ~4.8 nm PbSe QDs were produced simply by mixing lead hexyldecanoate with the selenium source in ODE overnight.

An attempt was made to optically characterize quantum confinement effects on these large PbSe nanocrystals using FTIR as shown in **Figure 5D**. These spectra demonstrate bandgaps (~0.15 eV) that are lower than bulk PbSe (0.27 eV). This may be due to doping of the dots by excess lead or ambient oxygen, or defects that create states that tail into the bandgap. Significant difficulty was encountered with characterizing smaller QDs, which may be due to the formation of plasmonic states or simple scattering of light from a QD film on a KBr pellet. These effects are currently being investigated, as well as the development of a robust method for optical characterization.

Powder X-Ray Diffraction Characterization

The application of powder X-ray diffraction analysis to large nanomaterials requires greater attention compared to smaller QDs. This is because the lineshapes of X-ray diffraction resonances are sensitive to size, strain, and instrumental broadening (Balzar, 1999). It is well-known that the Scherrer Equation, $\langle D\rangle_v = \frac{K\cdot\lambda}{\beta(2\theta)\cdot cos(\theta)}$, relates the volume-weighted average size of a particle $\langle D\rangle_v$ to the 2θ full-width-half-maximum $\beta(2\theta)$ of a resonance. The size also depends on the wavelength of the diffractometer λ, the θ angle of the resonance, and a shape factor K that describes the particles under study. The β factor can also be calculated using the transition's integral breadth, which is the width of a rectangle with the same peak intensity and area as the resonance; see the inset of **Figure 1B**. The use of this parameter negates the need for a shape factor and can be incorporated into more rigorous XRD characterization techniques such as the Williamson–Hall analysis discussed below (Williamson and Hall, 1953).

We have spent considerable time studying the samples using XRD and found that the need for enhanced analysis is dependent on the particle size. It was found that, under the conditions that the analyses were conducted, the instrumental broadening of resonances has a minor effect on the calculation of the sizes of small particles. For example, ignoring instrumental lineshape broadening results in a 9% underestimation of the size of ~12 nm particles; see **Figure S9A** of the supporting information. However, greater errors are realized when analyzing larger samples, and the instrument broadening must be characterized. To do so, a NIST standard was measured under the same

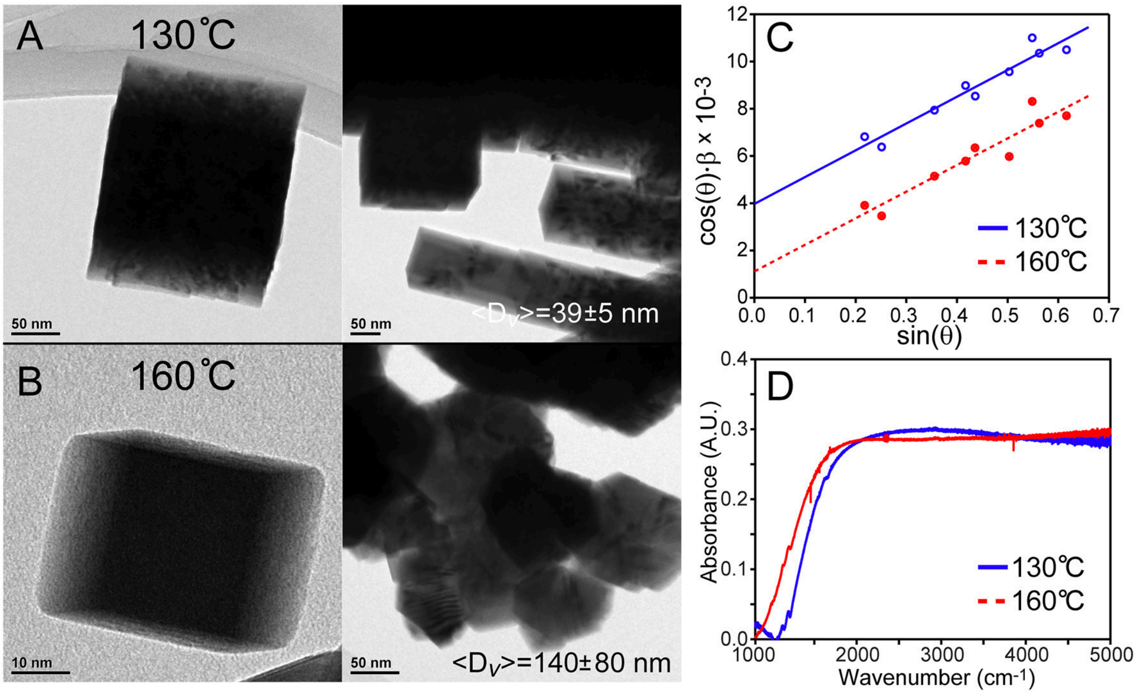

FIGURE 5 | Overcoating PbSe cubes with lead hexyldecanoate. **(A)** Overcoating at 130°C results in singular large cubic materials with $\langle D\rangle_V = 39 \pm 5$ nm as well as agglomeration. **(B)** Overcoating at a higher temperature creates larger materials with more agglomeration. **(C)** Williamson–Hall analyses reveal strain in these large overcoated PbSe nanostructures due to the finite slopes. **(D)** FTIR spectra of the materials demonstrate bulk bandgaps. Surface ligand features are not observed in larger PbSe nanomaterials that have been washed with hexane thoroughly; note that the contribution from atmospheric species have been subtracted for clarity. The structure of the absorption features is not consistent with the expected rise in the density of states of a bulk semiconductor, and may be due to an artifact of unknown origin.

conditions as the sample, the resonances of which were used as the angle-dependent instrument response function. With these data, the effect of instrument broadening can be removed either by Fourier deconvolution, convolution of a fit with the instrument response function, or by simple subtraction of the standard's integral breadth from the same of the sample. All of these approaches have unique strengths and weaknesses, and require adjustment of the instrument response as a function of diffraction angle. To illustrate the need for instrument response deconvolution, ignoring the instrumental broadening in the case of a nominally 80 ± 30 nm sample results in an underestimated size by 44% as shown in **Figure S9B**.

Next, the potential for strain broadening of the XRD lineshapes has to be ascertained. For smaller particles, the Scherrer equation is adequate for characterizing QDs so long as they are ~10 nm or smaller and strain free. This was not found to be the case for larger PbSe particles, and they must be analyzed using the Williamson–Hall equation:

$$\beta\,(2\theta)\cdot cos\,(\theta) = \frac{\lambda}{\langle D\rangle_v} + 4\cdot\epsilon\cdot sin\,(\theta) \qquad (1)$$

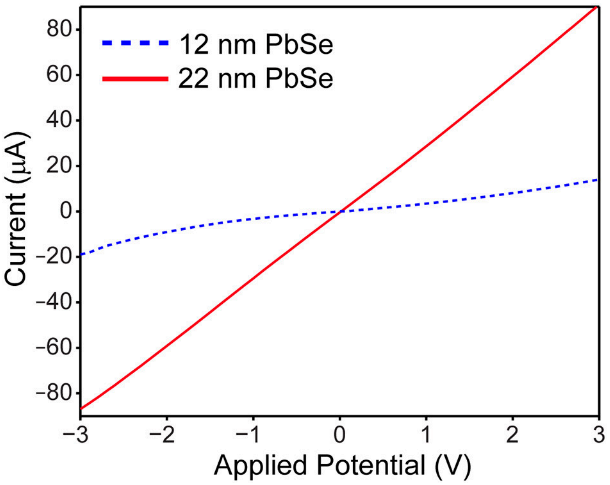

FIGURE 6 | Current vs. voltage plot of ~12 nm PbSe (dotted blue line) vs. ~22 nm PbSe (solid red line) quantum dots reveals that the larger nanomaterials are more linear, symmetric, and ~10× more conductive than their smaller counterparts.

where ϵ is the strain that can be crystallographic direction-dependent. Thus, a plot of the instrument response-corrected integral breadth × cos(θ) vs. sin(θ) yields a straight line with an intercept that provides the volume weighted average size of the particles. It was found that the use of Williamson–Hall equation is necessary for characterizing larger PbSe nanomaterial sizes with XRD data. Several examples can be seen in **Figures 1D**, **5C**, as well as **Figure S9** of the supporting information. All the Williamson–Hall linear fits have positive slopes, which is indicative of strain. The fact that the samples' XRD patterns have strain broadening reveals that use of the Scherrer equation would result in an underestimation of the particle sizes. Furthermore, the analysis allows us to determine that the larger PbSe materials produced during overcoating consistently have more strain than the smaller "core" PbSe QDs. This indicates that the growth of the shell proceeds with some defect formation. In the future we will examine these materials using more sophisticated techniques such as the Warren–Averbach (Warren and Averbach, 1952) or Rietveld analysis (Rietveld, 1969) techniques. While powerful, these methods require very high quality XRD data with superior knowledge of the angle-dependent instrument response function.

Conductivity

To verify the enhanced electrical properties of larger PbSe nanomaterials, the conductivity of small 12 nm vs. larger 22 nm samples were measured across a 3 μm Ti gap under ambient conditions. The quantum dots were washed with n-doping tetrabutylammonium iodine solution prior to measurement, to both enhance the conduction and provide protection from ambient oxygen (Ning et al., 2014). As shown in **Figure 6**, the I-V_{bias} curve is linear, symmetric, and greater in magnitude for the 22 nm PbSe nanomaterials compared to the smaller. These results are consistent with previous studies as electrons and holes must experience less activation energy to make ultimately fewer hops between adjacent ∼22 nm quantum dots (Romero and Drndic, 2005; Mentzel et al., 2008; Liu et al., 2010). The asymmetric and non-linear I–V_{bias} curve observed for the smaller QD sample may result from diode-like behavior from Schottky barriers due to the use of low workfunction Ti electrodes (Weiss et al., 2008; Strasfeld et al., 2012); these issues will be the subject of further investigation.

CONCLUSION

Presented here is a core/shell growth protocol for producing 20–40 nm PbSe cubic nanomaterials. These large sizes are achieved using a core/shell growth technique, although XRD analysis indicates that the larger sized particles have some strain which likely originates from crystal defects. The size augmentation can be enhanced using more reactive precursors, here lead hexyldecanoate, but there is some agglomeration due to the reagent's high reactivity.

Our survey of the literature returned few examples of using enhanced X-ray diffraction analyses techniques for characterizing semiconductor quantum dots. While the small sizes of most QD systems obliviates the need to do so, we demonstrate here that great care must be taken when characterizing larger particles (>10 nm). To summarize, we hope that colloidal techniques may be studied and refined further to prepare larger nanomaterials, which may have enhanced efficacy for electronic applications which will pave the way for future research opportunities.

AUTHOR CONTRIBUTIONS

TA synthesized and analyzed samples and prepared the manuscript. AH assisted with characterizations of samples. PS assisted with data analysis and manuscript preparation.

FUNDING

The authors thank the University of Illinois at Chicago for funding of this work.

ACKNOWLEDGMENTS

We thank Prof. Richard Schaller of Northwestern University and Argonne National Labs with assistance on the optical properties of PbSe nanocrystals. Also Dr. Seyoung An of UIC for assistance with conductivity measurements. Use of the Center for Nanoscale Materials, an Office of Science user facility, was supported by the U.S. Department of Energy, Office of Science, Office of Basic Energy Sciences, under Contract No. DE-AC02-06CH11357.

SUPPLEMENTARY MATERIAL

The Supplementary Material for this article can be found online at: https://www.frontiersin.org/articles/10.3389/fchem.2018.00562/full#supplementary-material

REFERENCES

Alivisatos, P. (2004). The use of nanocrystals in biological detection. *Nat. Biotechnol.* 22, 47–52. doi: 10.1038/nbt927

Arudi, R. L., Sutherland, M. W., and Bielski, B. H. (1983). Purification of oleic acid and linoleic acid. *J. Lipid Res.* 24, 485–488.

Balzar, D. (1999). Voigt-function model in diffraction line-broadening analysis. *Int.Union Crystallogr. Monogr. Crystallogr.* 10, 94–126.

Capek, R. K., Yanover, D., and Lifshitz, E. (2015). Size control by rate control in colloidal PbSe 393 quantum dot synthesis. *Nanoscale* 7, 5299–5310. doi: 10.1039/C5NR00028A

Etgar, L., Yanover, D., Karel Capek, R., Vaxenburg, R., Xue, Z., Liu, B., et al. (2013). Core/shell PbSe/PbS QDs TiO_2 heterojunction solar cell. *Adv. Funct. Mater.* 23, 2736–2741. doi: 10.1002/adfm.201202322

Evans, C. M., Evans, M. E., and Krauss, T. D. (2010). Mysteries of TOPSe revealed: insights into quantum dot nucleation. *J. Am. Chem. Soc.* 132, 10973–10975. doi: 10.1021/ja103805s

Evans, C. M., Guo, L., Peterson, J. J., Maccagnano-Zacher, S., and Krauss, T. D. (2008). Ultrabright PbSe magic-sized clusters. *Nano Lett.* 8, 2896–2899. doi: 10.1021/nl801685a

Hendricks, M. P., Campos, M. P., Cleveland, G. T., Plante, I. J.-L., and Owen, J. S. (2015). A tunable library of substituted thiourea precursors to metal sulfide nanocrystals. *Science* 348, 1226–1230. doi: 10.1126/science.aaa2951

Jawaid, A. M., Asunskis, D. J., and Snee, P. T. (2011). Shape-controlled colloidal synthesis of rock-salt lead selenide nanocrystals. *ACS Nano* 5, 6465–6471. doi: 10.1021/nn2016716

Lai, R., Pu, C., and Peng, X. (2018). On-surface reactions in the growth of high-quality CdSe nanocrystals in nonpolar solutions. *J. Am. Chem. Soc.* 140, 9174–9183. doi: 10.1021/jacs.8b04743

Liu, Y., Gibbs, M., Puthussery, J., Gaik, S., Ihly, R., Hillhouse, H. W., et al. (2010). Dependence of carrier mobility on nanocrystal size and ligand length in PbSe nanocrystal solids. *Nano Lett.* 10, 1960–1969. doi: 10.1021/nl101284k

Mentzel, T. S., Porter, V. J., Geyer, S., Maclean, K., Bawendi, M. G., and Kastner, M. A. (2008). Charge transport in PbSe nanocrystal arrays. *Phys. Rev. B* 77:075316. doi: 10.1103/PhysRevB.77.075316

Ning, Z. J., Voznyy, O., Pan, J., Hoogland, S., Adinolfi, V., Xu, J. X., et al. (2014). Air-stable n-type colloidal quantum dot solids. *Nat. Mater.* 13, 822–828. doi: 10.1038/NMAT4007

Pietryga, J. M., Schaller, R. D., Werder, D., Stewart, M. H., Klimov, V. I., and Hollingsworth, J. A. (2004). Pushing the band gap envelope: mid-infrared emitting colloidal PbSe quantum dots. *J. Am. Chem. Soc.* 126, 11752–11753. doi: 10.1021/ja047659f

Razgoniaeva, N., Moroz, P., Yang, M., Budkina, D. S., Eckard, H., Augspurger, M., et al. (2017). One-dimensional carrier confinement in "Giant" CdS/CdSe excitonic nanoshells. *J. Am. Chem. Soc.* 139, 7815–7822. doi: 10.1021/jacs.7b02054

Razgoniaeva, N., Yang, M., Garrett, P., Kholmicheva, N., Moroz, P., Eckard, H., et al. (2018). Just add ligands: self-sustained size focusing of colloidal semiconductor nanocrystals. *Chem. Mater.* 30, 1391–1398. doi: 10.1021/acs.chemmater.7b05165

Rietveld, H. M. (1969). A profile refinement method for nuclear and magnetic structures. *J. Appl. Crystallogr.* 2, 65–71. doi: 10.1107/S0021889869006558

Romero, H. E., and Drndic, M. (2005). Coulomb blockade and hopping conduction in PbSe quantum dots. *Phys. Rev. Lett.* 95:156801. doi: 10.1103/PhysRevLett.95.156801

Shapiro, A., Jang, Y., Rubin-Brusilovski, A., Budniak, A. K., Horani, F., Sashchiuk, A., et al. (2016). Tuning optical activity of IV–VI colloidal quantum dots in the short-wave infrared (SWIR) spectral regime. *Chem. Mater.* 28, 6409–6416. doi: 10.1021/acs.chemmater.6b02917

Snee, P. T., Somers, R. C., Nair, G., Zimmer, J. P., Bawendi, M. G., and Nocera, D. G. (2006). A ratiometric CdSe/ZnS nanocrystal pH sensor. *J. Am. Chem. Soc.* 128, 13320–13321. doi: 10.1021/ja0618999

Strasfeld, D. B., Dorn, A., Wanger, D. D., and Bawendi, M. G. (2012). Imaging Schottky barriers and ohmic contacts in PbS quantum dot devices. *Nano Lett.* 12, 569–575. doi: 10.1021/nl204116b

Talapin, D. V., Lee, J.-S., Kovalenko, M. V., and Shevchenko, E. V. (2010). Prospects of colloidal nanocrystals for electronic and optoelectronic applications. *Chem. Rev.* 110, 389–458. doi: 10.1021/cr900137k

Talapin, D. V., and Murray, C. B. (2005). PbSe nanocrystal solids for n- and p-channel thin film field-effect transistors. *Science* 310, 86–89. doi: 10.1126/science.1116703

Tang, J., Kemp, K. W., Hoogland, S., Jeong, K. S., Liu, H., Levina, L., et al. (2011). Colloidal-quantum-dot photovoltaics using atomic-ligand passivation. *Nat. Mater.* 10, 765–771. doi: 10.1038/nmat3118

Warren, B. E., and Averbach, B. L. (1952). The separation of cold-work distortion and particle size broadening in X-ray patterns. *J. Appl. Phys.* 23, 497–497. doi: 10.1063/1.1702234

Weiss, E. A., Chiechi, R. C., Geyer, S. M., Porter, V. J., Bell, D. C., Bawendi, M. G., et al. (2008). Size-dependent charge collection in junctions containing single-size and multi-size arrays of colloidal CdSe quantum dots. *J. Am. Chem. Soc.* 130, 74–82. doi: 10.1021/ja076438h

Williamson, G. K., and Hall, W. H. (1953). X-ray line broadening from filed aluminium and wolfram. *Acta Metal.* 1, 22–31. doi: 10.1016/0001-6160(53)90006-6

Yang, Y., Qin, H., Jiang, M., Lin, L., Fu, T., Dai, X., et al. (2016). Entropic ligands for nanocrystals: from unexpected solution properties to outstanding processability. *Nano Lett.* 16, 2133–2138. doi: 10.1021/acs.nanolett.6b00730

Yanover, D., Capek, R. K., Rubin-Brusilovski, A., Vaxenburg, R., Grumbach, N., Maikov, G. I., et al. (2012). Small-sized PbSe/PbS Core/Shell colloidal quantum dots. *Chem. Mater.* 24, 4417–4423. doi: 10.1021/cm302793k

Zhou, J., Zhu, M., Meng, R., Qin, H., and Peng, X. (2017). Ideal CdSe/CdS core/shell nanocrystals enabled by entropic ligands and their core size-, shell thickness-, and ligand-dependent photoluminescence properties. *J. Am. Chem. Soc.* 139, 16556–16567. doi: 10.1021/jacs.7b07434

Conflict of Interest Statement: The authors declare that the research was conducted in the absence of any commercial or financial relationships that could be construed as a potential conflict of interest.

frontiers
in Chemistry

ORIGINAL RESEARCH
published: 14 February 2019
doi: 10.3389/fchem.2019.00027

Surface Plasmon Resonance, Formation Mechanism, and Surface Enhanced Raman Spectroscopy of Ag^+-Stained Gold Nanoparticles

Sumudu Athukorale [1], Xue Leng [2], Joanna Xiuzhu Xu [1], Y. Randika Perera [1], Nicholas C. Fitzkee [1] and Dongmao Zhang [1,3]*

[1] Department of Chemistry, Mississippi State University, Starkville, MS, United States, [2] Department of Chemistry, Chengdu University of Technology, Chengdu, China, [3] Department of Chemistry, Xihua University, Chengdu, China

A series of recent works have demonstrated the spontaneous Ag^+ adsorption onto gold surfaces. However, a mechanistic understanding of the Ag^+ interactions with gold has been controversial. Reported herein is a systematic study of the Ag^+ binding to AuNPs using several *in-situ* and *ex-situ* measurement techniques. The time-resolved UV-vis measurements of the AuNP surface plasmonic resonance revealed that the silver adsorption proceeds through two parallel pseudo-first order processes with a time constant of 16(±2) and 1,000(±35) s, respectively. About 95% of the Ag^+ adsorption proceeds through the fast adsorption process. The *in-situ* zeta potential data indicated that this fast Ag^+ adsorption is driven primarily by the long-range electrostatic forces that lead to AuNP charge neutralization, while the time-dependent pH data shows that the slow Ag^+ binding process involves proton-releasing reactions that must be driven by near-range interactions. These experimental data, together with the *ex-situ* XPS measurement indicates that adsorbed silver remains cationic, but not as a charged-neutral silver atom proposed by the anti-galvanic reaction mechanism. The surface-enhanced Raman activities of the Ag^+-stained AuNPs are slightly higher than that for AuNPs, but significantly lower than that for the silver nanoparticles (AgNPs). The SERS feature of the ligands on the Ag^+-stained AuNPs can differ from that on both AuNPs and AgNPs. Besides the new insights to formation mechanism, properties, and applications of the Ag^+-stained AuNPs, the experimental methodology presented in this work can also be important for studying nanoparticle interfacial interactions.

Keywords: anti-galvanic reaction (AGR), gold nanoparticles, silver, zeta potential, Raman

Edited by:
Jing Zhao,
University of Connecticut,
United States

Reviewed by:
Laura Sagle,
University of Cincinnati, United States
Julia Bingham Wiester,
Saint Xavier University, United States

***Correspondence:**
Dongmao Zhang
Dongmao@chemistry.msstate.edu

Specialty section:
This article was submitted to
Nanoscience,
a section of the journal
Frontiers in Chemistry

Received: 30 September 2018
Accepted: 11 January 2019
Published: 14 February 2019

Citation:
Athukorale S, Leng X, Xu JX,
Perera YR, Fitzkee NC and Zhang D
(2019) Surface Plasmon Resonance,
Formation Mechanism, and Surface
Enhanced Raman Spectroscopy of
Ag^+-Stained Gold Nanoparticles.
Front. Chem. 7:27.
doi: 10.3389/fchem.2019.00027

INTRODUCTION

Gold nanoparticles (AuNPs) are among the most studied nanomaterial owing to their unique photochemical properties and their applications in biosensing, catalysis, biomedicine, electronics, and surface-enhanced Raman spectroscopy (SERS) (El-Sayed et al., 2006; Anker et al., 2008; Ghosh et al., 2008; Brown et al., 2010; Homberger and Simon, 2010; Zhou et al., 2010; Ansar et al., 2011; Athukorale et al., 2018). Current methods for preparing AuNPs with different structural characteristics and functionalities can be categorized into two classes of approaches. The first class is by synthetically controlling AuNP sizes, shapes, and chemical compositions (Jana et al., 2001a,b; Bastús et al., 2011) and the second is to tune the AuNP structural parameters and functionality through post-modification of AuNP surface (Daniel and Astruc, 2004; Eustis and El-Sayed, 2006; Dykman and Khlebtsov, 2012; Siriwardana et al., 2014). Indeed, AuNP surface chemistries, including ligand interfacial interactions of plasmonic AuNPs, have evolved as one of the most active research areas due to their importance in essentially every aspect of AuNP applications (Perera et al., 2016a,b; Athukorale et al., 2018). The most common ligands used for AuNP surface functionalization are proteins (Vangala et al., 2012; Siriwardana et al., 2013; Wang et al., 2016; Woods et al., 2016), organothiols (Ansar et al., 2011, 2013b, 2014), and thiolated chemicals such as poly(ethylene glycol) (Siriwardana et al., 2014).

Silver binding to gold has been the focus of several recent publications (Wu, 2012; Wang et al., 2014; Kang et al., 2015; Athukorale et al., 2017a; Liu and Astruc, 2017; Nguyen et al., 2018). However, most of the gold substrates are aggregated AuNPs or planar gold films including gold electrodes. The mechanism of binding has been ambiguous, too. Primarily on the basis of x-ray photon spectroscopy (XPS) analysis, Wu et al. proposed that Ag^+ binding to AuNP proceeds through an anti-galvanic reduction in which the Ag^+ is reduced into Ag^0 by the chemically inert Au surface atom (Wu, 2012; Wang et al., 2014). However, the reliability of the XPS for identification of the Ag charge state is highly questionable. Indeed, a survey of the National Institute of Standards and Technology (NIST) X-ray photoelectron spectroscopy database shows that the binding energy of 3d(Wu, 2012)$_{3/2}$ electron for the zero valence silver varies from 373.40 to 374.27 eV, while that for Ag^+ $3d_{3/2}$ is 373.90 eV (Naumkin et al., 2012). The binding energy of the $3d_{5/2}$ electron for the zero valence silver is from 367.90 to 368.40 eV, while that for the Ag^+ is from 367.40 to 369.00 eV (Naumkin et al., 2012). The fact that Ag^0 and Ag^+ overlap tremendously in both their $3d_{3/2}$ and $3d_{5/2}$ electron binding energy indicates the difficulty of unambiguously assigning silver charge state using XPS data.

Care should be exercised on XPS data interpretation. Literature XPS analyses were performed almost exclusively with dried samples (Wu, 2012; Wang et al., 2014; Perera et al., 2018). However, the sample drying process can change the ligand surface composition through multiple mechanisms. As an example, as-synthesized AuNPs are usually negatively charged, but the dried AuNPs are charge-neutral. Such charge neutralization can occur either by reducing the number of the anionic species on the AuNPs and/or by enhancing adsorption of the cationic species that are initially confined within the electrical double layer or in the bulk solution. Furthermore, solvent drying also introduces the adsorption of impurities onto AuNP surfaces, further compromising the reliability of the measurement results (Perera et al., 2018). Exposing the XPS samples to ambient air also introduces impurities. Indeed, even a brief exposure of X-ray cleaned gold film into air or Nanopure water can introduce significant surface contamination. Such surface contamination can be readily concluded by the appearance of carbon and oxygen species in the XPS spectrum obtained with gold film (Perera et al., 2018). Unfortunately, Wu et al. have shown the XPS features for silver and gold alone, with no information given for other elements in their publications, making it impossible to assess the complexity of contaminating surface adsorbates on their AuNPs (Wu, 2012; Wang et al., 2014).

Indeed, electrolyte binding to AuNPs should be studied with measurement strategies capable of differentiating ionic species directly absorbed on the surface and those confined within the electrolyte double layer or diffuse in the bulk solution. We recently reported the spontaneous adsorption of Ag^+ onto all explored gold substrates, including pure gold foil, sputter-coated gold film, and washed AuNP aggregates synthesized with both citrate- and borohydride reaction methods (Athukorale et al., 2017a). The adsorbed silver most likely remains cationic as a component of the insoluble salts attached onto the AuNP surfaces. The key supporting evidence is: (1) There are carbon and oxygen features in these samples whenever silver XPS peaks are observed, (2) A drastic reduction of solution pH reduction accompanies spontaneous Ag^+ adsorption, a phenomenon that can't be explained by the proposed anti-galvanic mechanism, (3) Ag^+ induces desorption of the soluble organothiols that are initially anchored onto the AuNPs.

Herein we provide further supporting evidence that Ag^+ adsorbed onto gold surface remains as a cation and not as a charge-neutral silver atom. In this study, we use the dialysis-purified and citrate-reduced AuNPs, instead of the AuNP aggregates or planar gold film as the model gold substrate. The dialyzed AuNPs maintain their dispersion stability in solution, as does the monolayer Ag^+-functionalized AuNPs. This enabled us to investigate the effect of Ag^+-staining on the AuNP charge states through zeta-potential titration and time-dependent zeta potential measurement. Further, by taking advantage of the fact the Ag^+ adsorption introduces significant spectral change in the AuNP surface plasmonic resonance, we probed the kinetics of the Ag^+ adsorption using the time-resolved UV-vis spectroscopic analysis. The structure and properties of the Ag^+-treated AuNPs were also studied with surface enhanced Raman spectroscopy (SERS) by using butanethiol (BuT), a monothiol, and 1,4-benzenedimethanethiol (BDMT), a dithiol as the model probes, which provides rich information regarding the mobility of the surface silver and the SERS activity of the Ag^+-stained AuNPs.

MATERIALS AND METHODS

Materials and Equipments

All the chemicals were purchased from Sigma-Aldrich and used as received. Nanopure water (18 MΩ-cm) (Thermo Scientific) is used throughout all experiments. UV-vis spectra were acquired with an Olis HP 8452 diode array spectrophotometer. Polarized resonance synchronous spectra (PRS2) were acquired using the Fluoromax-4 spectrofluorometer equipped with an excitation and detection polarizer. PerkinElmer ELAN DRC II inductively coupled plasma-mass spectrometer (ICP-MS) was used for the silver quantification. Litesizer 500 (Anton-Paar) instrument was used for the zeta potential measurements. A Thermo Scientific K-Alpha X-ray photoelectron spectrometer system was used for the XPS measurements. A LabRam HR800 confocal Raman microscope was used for Raman and SERS acquisitions with 632 nm laser excitation. Reflective sample substrate (RSS) slides from Raminescent, LLC were used for all SERS acquisitions. These RSS slides are highly reflective with negligible fluorescence and Raman background (Athukorale et al., 2017a).

AuNP and AgNP Synthesis

Aqueous ∼13 nm (diameter) AuNP were synthesized in-house using the citrate reduction method (Frens, 1973). The ∼30 and ∼50 nm AuNPs were synthesized according to the reported kinetically controlled citrate-reduced method described by Bastús et al. (2011). The size and concentration of the as-synthesized AuNPs were estimated on the basis of the AuNP UV-vis extinction spectra (Hurst et al., 2006; Zhao et al., 2008). AgNPs were synthesized in-house using the Lee-Meisel method (Lee and Meisel, 1982). Briefly, 0.027 g of $AgNO_3$ was dissolved in 150 mL of Nanopure water, and the solution was heated. Then 3 mL of 1% trisodium citrate dehydrate was added when the solution starts to boil, and the mixture was kept boiling for ∼60 min with stirring.

AuNP Silver-Staining

All the as-synthesized AuNPs were dialyzed four times with Nanopure water using standard regenerated-cellulose membrane (MWCO is 12–14 kD) purchased from Spectrum Labs. The as-received dialysis membranes were washed thoroughly before use. The silver staining was conducted by adding known amount of $AgNO_3$ to the dialyzed AuNPs and mixed using a vortex mixer. The mixture was left to sit overnight at ambient conditions before further usage. The kinetics of the Ag^+ binding to AuNP was conducted with the time-resolved UV-measurements for the sample prepared by mixing the dialysis-purified 13 nm AuNPs.

PRS2 Acquisition and Analysis

PRS2 is a new spectroscopic method that enables quantitative decomposition of the sample UV-vis extinction spectrum into its absorption extinction and scattering extinction spectrum. The theoretical background, spectral acquisition, and data analysis procedure are available in recent publications (Athukorale et al., 2017b; Siriwardana et al., 2017; Xu et al., 2018a,b). Briefly, the excitation polarization of the spectrofluorometer is set vertical (V) and the detection polarization is kept either vertical or horizontal (H) to acquire PRS2 VV or VH spectra, respectively. The depolarization is, by definition, the ratio of VH and VV intensity corrected by the polarization bias G factor. The as-acquired PRS2 solution spectra were inner-filter-effect (IFE) corrected and solvent background removed to get the analyte specific PRS2 spectra for further data analysis. The slit width of the excitation and detection monochromator is set as 2 nm with wavelength increment of 1 nm. The integration time for each wavelength variable is 0.3 s. The G-factor spectrum for correcting the instrument polarization bias, the effective pathlength for correction the sample inner filter effect, and cuvette and solvent PRS2 spectra for background subtraction were obtained using the method described previously (Siriwardana et al., 2017).

Zeta-Potential Measurements

Dialyzed AuNPs were mixed with $AgNO_3$ of predefined concentrations and incubated overnight before performing Ag^+-concentration-dependent zeta potential measurements. The time-resolved AuNP zeta potentials were acquired as a function of the Ag^+ treatment time for a freshly prepared AuNP/$AgNO_3$ mixture. All zeta potentials were measured at 25°C in a reusable 350 μL Omega Cuvette Z (Anton-Paar). Each zeta potential is an average of 500 scans. The sample solution was equilibrated in the cuvette for 2 min prior to each acquisition.

SERS Spectral Acquisitions

All the SERS spectra were acquired using Olympus 10 × objective (NA = 0.25). The He/Ne laser with an excitation wavelength of 632 nm was used and the laser power before the objective was 1.3 mW for the SERS acquisition. The spectrograph grating was 600 grooves/mm. The acquisition times for SERS spectra were varied between 10 and 200 s. The Raman shift was calibrated with a neon lamp.

ICP-MS Quantification for the Adsorption of Silver on to AuNPs

The amount of Ag^+ adsorbed was quantified using similar procedure described previously (Athukorale et al., 2017a). The AuNPs/$AgNO_3$ mixture was incubated overnight and centrifuged at 9,000 rcf for 1 h so that the AuNP-containing pallet and supernatant were separated. In order to quantify the adsorbed Ag^+, AuNP-containing pallet was centrifuged and washed several times to remove the free Ag^+ ions and a known volume of freshly prepared aqua regia was added to digest the sample (Note that aqua regia is very corrosive and must be handled with extreme caution). A known volume of the supernatant was digested with aqua-regia to quantify the free Ag^+ ions in the solution. All the digested samples were diluted with 18 MΩ-cm Nanopure water.

RESULTS AND DISCUSSION

Effect of Silver-Staining on AuNP Surface Plasmon Resonance

As-synthesized AuNPs are purified by dialysis prior to the silver-staining, in order to remove the excess chloride, citrate, and other by-products in the AuNP synthesis solution. This is because Ag^+ can react with the excess reagents, complicating the study of the Ag^+ binding to AuNPs. While the dialysis is effective in removal of the free small molecules in solutions (**Figure S1**), it is inadequate to eliminate the surface-bound citrate and the adsorbed impurities as we demonstrated earlier with AuNPs synthesized with deuterated citrate (Perera et al., 2018). Further evidence indicating the presence of surface adsorbates on the dialyzed AuNPs comes from zeta potential measurements (see below).

Ag^+ treatment of the dialyzed AuNPs induces significant change in the AuNP surface plasmonic resonance. The UV-vis peak intensity increased by 30 ± 3, 12 ± 1, and 8 ± 1% after the Ag^+ treatment for the AuNPs with particle size of 13, 30, and 50 nm, respectively (**Figure 1**). The fact that the relative change

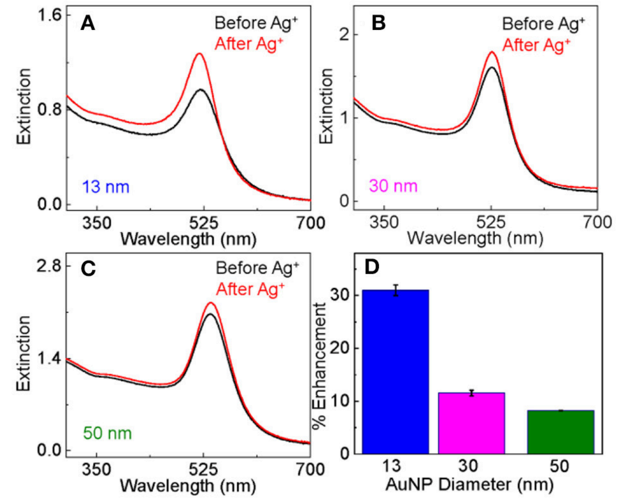

FIGURE 1 | Comparison of the UV-vis extinction spectra of as-prepared dialyzed AuNPs before and after the Ag^+-staining for AuNPs with particle size of **(A)** 13 nm, **(B)** 30 nm, and **(C)** 50 nm. **(D)** Bar plot showing the percentage increase in the AuNP peak UV-vis intensity induced by Ag^+-staining as a function of AuNPs size.

in the AuNP surface plasmon resonance intensity decreases with increasing AuNP particle sizes is expected because the Ag^+ adsorption perturbs the structure of the immediate AuNP surface layer. This is because the surface to volume ratio decreases with increasing particle sizes.

UV-vis evaluates the sample total photon extinction, the sum of the photon absorption extinction and scattering extinction. With sample UV-vis (**Figure 2A**) and PRS2 spectra (**Figures 2B,C**), we decomposed the AuNP UV-vis extinction cross-section spectra (**Figure 2D**) into their absorption and scattering component spectra (**Figures 2E,F**), and quantified the AuNP light scattering depolarization spectrum (**Figure 2G**) as well as the scattering to extinction ratio spectrum. This enables us to reveal insights that have not been accessible before. We have recently demonstrated that light scattering depolarization is very sensitive to the deformation of the spherical AuNPs (Xu et al., 2018a). The silver-staining has no significant effect on the AuNPs light scattering depolarization spectrum, indicating that the AuNPs remain spherical after the silver-staining. The fact that Ag^+ adsorption increases both the absorption and scattering extinction intensity (**Figures 2D,E**), but not the scattering to extinction ratio (S/E) spectrum intensity (**Figure 2H**) indicates that silver-staining enhanced the photon absorption and scattering by approximately the same degree.

Kinetics and Adsorption Capacity on Ag^+ Adsorption

The fact that the Ag^+ adsorption induced a significant change to the AuNP surface plasmon resonance spectrum allows us to study the adsorption kinetics using time-resolved UV-vis measurements (**Figure 3A**). The working hypothesis is that the change in the AuNP surface plasmon is proportional to the amount of adsorbed Ag^+ (**Figure 3B**). Over 50% of the silver adsorption occurs within the measurement's 10 s dead time in the time-resolved UV-vis study (**Figure 3B**). This is extraordinarily fast considering the ultralow AuNP concentration (low nM) and its small mobility in solution as a nanoparticle. Fitting the time-resolved UV-vis data with one first order equations produces large errors (**Figure S3**), but near perfect fitting is achieved with two pseudo-first-order reaction equations that yield reaction time constants of $\tau_1 = 16 \pm 2$ s and $\tau_2 = 1{,}000 \pm 35$ s, respectively. Therefore, the Ag^+ adsorption process can be approximated empirically by two parallel first-order reactions differing drastically in the reaction time scale. The Γ_1 and Γ_2 values associated with the two time constants are 0.4 and 0.079, respectively, indicating that over 94% of the Ag^+ adsorption occurs through the fast process that has the time constant of 16(±2) s.

$$M = \Gamma_1 \left(1 - exp\left(-t/\tau_1\right)\right) + \Gamma_2 \left(1 - exp\left(-t/\tau_2\right)\right) \tag{1}$$

Empirically, the Ag^+ adsorption onto dialyzed AuNPs follows a Langmuir adsorption isotherm with the binding constant and saturation packing density of $K \sim 4 \times 10^6$ M^{-1} and $\Gamma_{max} \sim 4.7$ nmol/cm^2, respectively (**Figures 3C,D**). The saturation packing density of Ag^+ on AuNPs was calculated similarly as before (Athukorale et al., 2017a) by assuming the AuNPs are perfectly spherical with identical sizes. The binding constant and packing density of the Ag^+ on the dialyzed AuNP are higher than their respective counterparts on the extensively washed citrate-reduced AuNPs that are pre-aggregated with KNO_3. The binding constant and packing density for the Ag^+ adsorption onto pre-aggregated AuNPs are 4.3×10^3 M^{-1} and ~2.8 nmol/cm^2 respectively (Athukorale et al., 2017a). The small difference in the Ag^+ packing density between the dialyzed AuNPs and the pre-aggregated AuNPs can be readily understood by the fact that the pre-aggregated AuNPs must have a smaller fraction of surface area accessible for Ag^+ adsorption.

The large difference in the Ag^+ binding constant between the dialyzed and pre-aggregated AuNPs is due most likely to the difference in the surface charge states as well as the chemical compositions on the AuNPs that are caused by the post-synthesis process. Zeta-potential measurement reveals that the dialyzed AuNPs remain highly negatively charged (**Figure 4**), but the charge density on the aggregated AuNPs should be likely negligibly small. Therefore, due to the electrostatic attraction, the Ag^+ adsorption onto the dialyzed AuNPs is energetically more favorable than that onto the pre-aggregated AuNPs.

Evidence supporting that the electrostatic interaction comes from both the concentration-dependent and time-resolved zeta potential measurements (**Figure 4**). Ag^+ adsorption neutralizes the surface charge of the dialyzed AuNPs. The AuNP zeta potential monotonically increases (becomes less negative) with increasing Ag^+ concentration before it reaches a plateau value of 3 mV when the nominal Ag^+ concentration is 150 µM (**Figure 4A**). This is consistent with the data obtained with UV-vis measurements that showed ~150 µM Ag^+ induces a maximum AuNP UV-vis intensity change (**Figure 1**). Moreover, the Ag^+-induced charge neutralization of the AuNPs is a very

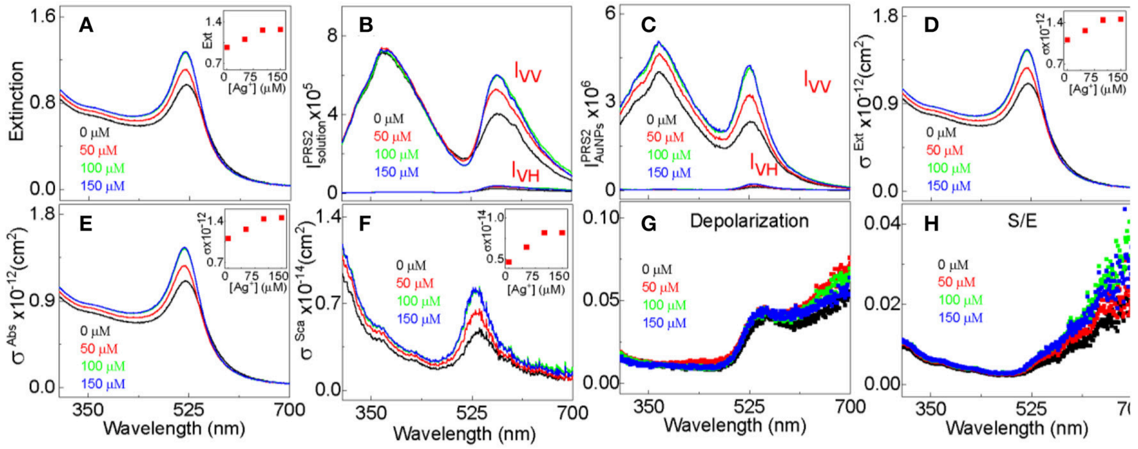

FIGURE 2 | PRS2 quantification of the extinction, absorption, and scattering cross-section, depolarization, and S/E for 13 nm- AuNPs stained with 50, 100, and 150 μM $AgNO_3$. An example data analysis of PRS2 spectra are showed in the **Figure S2**. **(A)** UV-vis extinction spectra, **(B)** as-acquired PRS2 spectra, **(C)** sample inner-filter-effect- and solvent-background-corrected PRS2 spectra, **(D–F)** extinction, absorption, and scattering cross-section spectra, respectively. **(G,H)** The AuNP depolarization spectra and S/E spectra, respectively. The Ag^+ concentration for the spectrum in black, red, green, and blue are 0, 50, 100, and 150 μM, respectively. Insets in **(A,D–F)** showing the spectral peak intensity as a function of the Ag^+ concentration.

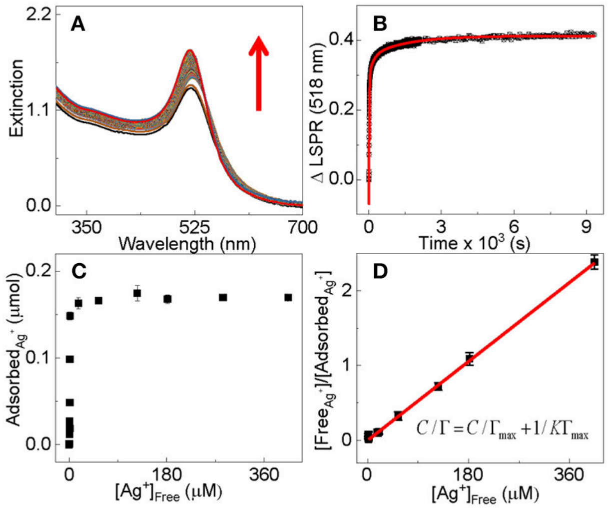

FIGURE 3 | (A) Time-resolved UV-vis extinction spectra for the adsorption of Ag^+ onto dialyzed AuNPs of 13 nm in diameter, **(B)** time-course for the AuNP UV-vis intensity change at 518 nm in the spectra shown in **(A)**. Black dots are experimental data and the red solid curve is the fitted curve with the two pseudo-first-order reaction equation (Equation 1). The nominal concentration of Ag^+ is 100 μM for the time-resolved UV-vis data. **(C)** ICP-MS quantification of the Ag^+ adsorption onto dialyzed AuNPs as a function of the concentration of the excess Ag^+. The samples are prepared by mixing 1 mL of the dialyzed 13 nm AuNPs with equal volume of $AgNO_3$.The nominal Ag^+ concentrations in the mixtures are 1, 6, 12, 20, 50, 100, 150, 180, 200, 220, 300, and 575 μM, respectively. **(D)** Empirical Langmuir fitting of the adsorption data in **(C)**.

rapid process, completed within the 8 min dead time of the zeta potential measurement (**Figure 4B**).

Like what has been observed in the Ag^+ binding to other gold substrates, including the high-purity gold foil, planar gold

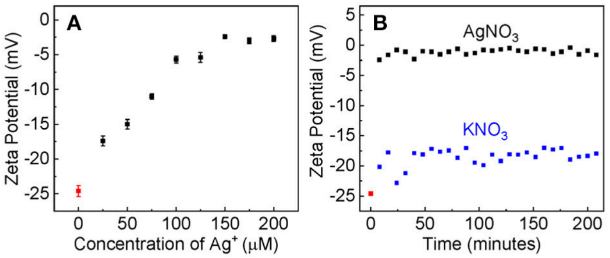

FIGURE 4 | (A) The AuNP zeta potential as the function of the nominal Ag^+ concentration. The AuNP/$AgNO_3$ mixtures were incubated overnight before measurements. **(B)** The time-dependent zeta potential of AuNPs treated with $AgNO_3$ or KNO_3 with the same nominal concentration of 100 μM.

film, and aggregated AuNPs (Athukorale et al., 2017a), Ag^+ adsorption on the dialyzed AuNPs also induces significant pH change in the $AgNO_3$/AuNP solution (**Figure 5**). Kinetically, however, the rate of this proton generation reaction is drastically slower than the Ag^+-adsorption-induced zeta potential change that occurs instantaneously upon $AgNO_3$ addition. It takes more than 2 h for the solution pH or proton concentration to reach a constant value. Beside the intrinsic proton generating reaction as it will be further discussed, slow mass-transfer in the pH measurement samples can also contribute to the slow proton releasing induced by the $AgNO_3$ addition (**Figure 5C**). The AuNP used in these samples were centrifugation precipitated before the AgNO3 addition (**Figure 5**) to prevent contamination of the pH probe by AuNPs. In contrast, the AuNPs were dispersed in solution in the UV-vis and zeta potential studies. Nonetheless, the fact $AgNO_3$ are significantly more effective than KNO_3 in causing pH reduction in AuNP-containing solution (**Figure 5**),

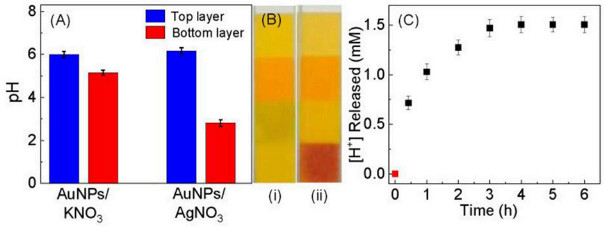

FIGURE 5 | (A) Bar plot showing the pH change occurring in solution after the addition of KNO_3 and $AgNO_3$. 30 mL of dialyzed AuNPs was centrifugation precipitated and split into two equal volume portions. Those two are AuNP-free top layer and AuNP-containing bottom layer. pH measurements were conducted 1 h after incubating top and bottom layer with 10 mM KNO_3 and $AgNO_3$. **(B)** Photograph of the pH papers used to check the pH of the Ag^+ treated (i) top and (ii) bottom layers, respectively. **(C)** Time-dependent proton concentration as a function of the ($AgNO_3$/AuNP) incubation time. The sample was prepared by mixing 10 mM of $AgNO_3$ with 30 mL of dialyzed AuNPs that were centrifugation precipitated before $AgNO_3$ addition.

confirms that the proton-release is predominantly due to the Ag^+ adsorption.

Collectively, the time-dependent zeta potential and the pH measurement offer an excellent explanation for the empirical two-first-order-reaction model proposed on the basis of the time-resolved UV-vis study of the Ag^+ binding to AuNPs (**Figure 3**). Mechanistically, the Ag^+ binding most likely proceeds through a fast charge neutralization reaction in combination with a relatively slow proton-generating displacement reaction. This charge neutralization is driven by the long-range electrostatic force, therefore can be completed within a few minutes of the sample incubation period. This hypothesis is supported by the zeta-potential measurement. In contrast, the proton-generation reaction is most likely a displacement reaction that occurs only through interactions with proximal molecules, i.e., Ag^+ and the ionisable-hydrogen-bearing adsorbates must be in direct contact with an appropriate orientation in order for the reaction to occur. Consequently, this displacement reaction must be slower than the Ag^+ adsorption driven by the electrostatic interactions.

The mostly likely reason why Ag^+ are drastically more effective than K^+ in neutralizing the AuNP surface charge is that Ag^+ can form insoluble particles with the surface adsorbates remaining on the dialyzed AuNPs. Earlier reports with deuterated citrate showed that citrate remains adsorbed onto AuNP surface even with extensive solvent washing (Perera et al., 2018). Chlorides in the AuNP synthesis solution can also remain on the dialyzed AuNP surfaces. The solubility of silver citrate is 5.5×10^{-4} mol/L (Seidell, 1928), while the solubility of AgCl is 1.2×10^{-5} mol/L (Seidell, 1928). In contrast, both potassium citrate and potassium chloride are highly water-soluble. Their solubility values are 5.9 mol/L and 4.8 mol/L, respectively (Seidell, 1928). Indeed, silver can readily react with citrate, forming an insoluble Ag-citrate salt (**Figure S4**).

The protons generated by the Ag^+ binding are due likely to the Ag^+ reaction with citrate or its reaction by-product that contain intact carboxylic groups. The as-synthesized AuNPs are weakly acidic with a pH value of around 5 (Gadogbe et al., 2013; Karunanayake et al., 2015). The surface bound citrates most likely bear substantial amount of the ionizable protons. The pK_a values of the three carboxylic groups of citrate acid in water are 3.2, 4.8, and 6.4 (Ji et al., 2007; Ojea-Jiménez and Campanera, 2012). However, it is unlikely all carboxylic acid groups on the surface-adsorbed citrate have been ionized under the experimental condition performed under neutral condition. First, the average pK_a values of those carboxylic groups for the citrate acid on AuNPs are likely higher, due to coulombic repulsion among confined likely-charged species (Perera et al., 2016a, p. 6392; Perera et al., 2015, p. 6245), than their respective counterpart in water. Positive pKa shifts of acids assembled onto solid substrate has been extensively reported (Sugihara et al., 2000, p. 6720; Masheter et al., 2007, p. 6721). Second, the pKa for the third carboxylic acid in citrate in water is 6.4, indicating third carboxylic group must have a substantial faction remaining intact even for citrate acid in pH ~7 solutions. The fraction of intact carboxylic acid groups in citrate adsorbed on AuNPs likely significantly higher than that dispersed in solution. While it is unreliable to experimentally measure pH due to the poor solution conductivity, pH of the dialyzed AuNPs is likely around 7.

The fact that silver has a higher saturation binding capacity on the "naked" dialyzed AuNPs (**Figure 3**) than that reported earlier for the organothiol- and dithiol-functionalized AuNPs also supports the proposed charge neutralization and the proton-displacing reaction pathways. The predominant surface adsorbates on the dialyzed AuNPs are likely citrate, but that on the organothiol-functionalized AuNPs are mono- or di-thiols. Early work showed that thiols can readily displace citrate on AuNP surfaces (Perera et al., 2018). Each citrate can react with three Ag^+ through combination of the charge-neutralization and proton-displacement reactions, but mono- and di-thiol can only react with one or two Ag^+. What further contributes to the larger Ag^+ adsorption onto the dialyzed AuNPs than the thiol-functionalized AuNP aggregates is that all citrates in the dialyzed AuNPs are accessible for reacting with Ag^+, but the steric hindrance in the thiol-functionalized AuNPs limits the AuNP surface accessibility. The thiol-functionalized AuNPs are all aggregated prior to the $AgNO_3$ treatment (Perera et al., 2018).

SERS of the Ag^+-Stained AuNPs

Studying SERS of the Ag^+-stained AuNPs is important not only for their potential applications as SERS substrates but also for probing the structure and properties of the Ag^+-containing AuNPs. Taking the advantage of the excellent dispersion stability of the Ag^+-stained AuNPs in water, we compared the SERS spectra obtained with dialyzed AuNPs, Ag^+-stained AuNPs, and the AgNPs for both BuT and BMDT. The SERS intensity of the ligands on the Ag^+-stained AuNPs is marginally higher than that on the as-prepared dialyzed AuNPs, but significantly lower than that on the AgNPs (**Figure 6**).

The structure and conformation of alkanethiols on AuNPs are deduced from its skeletal C-S and C-C stretching frequencies. The C-S stretching peaks for the *trans* $\upsilon(\text{C-S})_T$, and *gauche* $\upsilon(\text{C-S})_G$ conformers are at ~680 and ~610 cm^{-1}, respectively and C-C stretching peaks for *trans* $\upsilon(\text{C-C})_T$, and *gauche* $\upsilon(\text{C-C})_G$

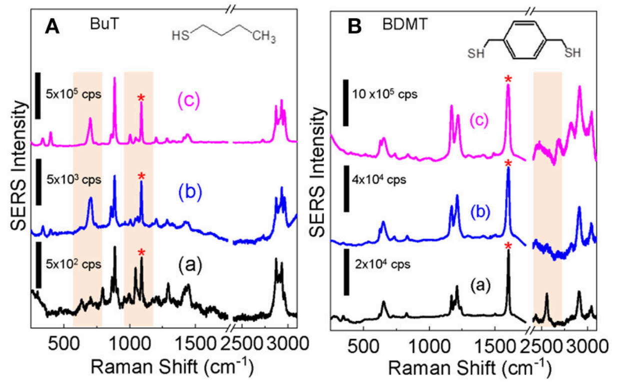

FIGURE 6 | Comparison of the SERS spectra obtained for **(A)** BuT and **(B)** BDMT with dialyzed AuNPs **(a)** before and **(b)** after the Ag^+ staining, **(c)** is the SERS spectra obtained with AgNPs. The structure of BuT and BMDT are also shown. The SERS spectra are normalized to the peak denoted by "*".

are ∼1,070 and ∼1,020 cm^{-1}, respectively (Rycenga et al., 2009; Bantz et al., 2012). C-S and C-C stretching features (b) indicate that the BuT on AgNPs and Ag^+-stained AuNPs are mostly in highly ordered *trans* conformers, but totally disordered on the AuNPs without Ag^+ staining.

Earlier research showed that BuT is in a highly ordered *trans* conformer on the AgNPs, but totally disordered on the AuNPs (Ansar et al., 2014). This is due to the surface atoms on AgNPs are mobile, therefore the intermolecular van der Waals force among the BuT-Ag complexes drives the ordering by overcoming the constrain of the AgNP surface curvatures (Ansar et al., 2013a, 2014; Athukorale et al., 2017a). In contrast, the surface gold atoms are immobile. The BuT on the AuNPs are totally disordered due to their nanoparticle surface curvature (Ansar et al., 2014). The similarity between the BuT SERS spectra obtained with the AgNPs and Ag^+-stained AuNP indicates that the Ag-BuT complex formed on the Ag^+-stained AuNPs are also mobile.

Further evidence of the mobility of the surface adsorbed Ag^+ on the Ag^+-stained AuNPs comes from the SERS spectra obtained with dithiol BDMT. There is a relatively strong S-H peak in the 2,600 cm^{-1} region in the SERS spectrum obtained with the BDMT on AuNPs, indicating there are significant intact thiols on the BDMT on AuNPs. Earlier study has shown that the intact S-H appears only when BDMT is at upright positions when BDMT approaches full monolayer adsorption on the AuNP surfaces (Gadogbe et al., 2015). The absence of detectable S-H stretching feature in the BDMT SERS spectra obtained with the Ag^+-stained AuNPs indicates that the adsorbed Ag^+ on the dialyzed AuNP can reach the distal thiol that otherwise unreactive to the AuNPs.

CONCLUSIONS

In conclusion, we have conducted a systematic study of the Ag^+ binding to AuNPs using a series of *in-situ* techniques including the AuNP surface plasmonic resonance, zeta-potential titration, pH measurements, and SERS acquisitions. All the experimental data indicate that the Ag^+ adsorbs onto AuNPs as cationic silver species, but not as the zero-charged silver atoms. Mechanistically, the Ag^+ adsorption is mediated by the surface adsorbates remaining on the surface of the dialyzed AuNPs, and it proceeds through a fast charge neutralization reaction in combination with a relatively slow proton generation reaction. This work is important not only for its new insights into the Ag^+ binding to AuNPs, but also for the experimental strategies that should be useful for probing a wide range of nanoparticle interfacial interactions.

AUTHOR CONTRIBUTIONS

SA, XL, and JX all helped with experiment design, performed experiments, analyzed data, plotted graphs, and prepared manuscript. YP conducted Zeta potential measurement. NF supervised the Zeta potential measurement and responsible for part of the writing. DZ designed and supervised the experiments and was responsible for writing the manuscript.

FUNDING

This work was supported by National Science Foundation (CHE 1151057, EPS-0903787, BIO 1818090) and the National Institutes of Allergies and Infectious Disease of the National Institutes of Health (R01AI139479). The content is solely the responsibility of the authors and does not necessarily represent the official views of the NSF or NIH.

SUPPLEMENTARY MATERIAL

The Supplementary Material for this article can be found online at: https://www.frontiersin.org/articles/10.3389/fchem.2019.00027/full#supplementary-material

REFERENCES

Anker, J. N., Hall, W. P., Lyandres, O., Shah, N. C., Zhao, J., and Van Duyne, R. P. (2008). Biosensing with plasmonic nanosensors. *Nat. Mater*. 7, 442–453. doi: 10.1142/9789814287005_0032

Ansar, S. M., Gadogbe, M., Siriwardana, K., Howe, J. Y., Dogel, S., Hosseinkhannazer, H., et al. (2014). Dispersion stability, ligand structure and conformation, and SERS activities of 1-alkanethiol functionalized gold and silver nanoparticles. *J. Phys. Chem. C* 118, 24925–24934. doi: 10.1021/jp507142v

Ansar, S. M., Haputhanthri, R., Edmonds, B., Liu, D., Yu, L., Sygula, A., et al. (2011). Determination of the binding affinity, packing, and conformation of thiolate and thione ligands on gold nanoparticles. *J. Phys. Chem. C* 115, 653–660. doi: 10.1021/jp110240y

Ansar, S. M., Perera, G. S., Gomez, P., Salomon, G., Vasquez, E. S., Chu, I. W., et al. (2013a). Mechanistic study of continuous reactive aromatic organothiol adsorption onto silver nanoparticles. *J. Phys. Chem. C* 117, 27146–27154. doi: 10.1021/jp4090102

Ansar, S. M., Perera, G. S., Jiang, D., Holler, R. A., and Zhang, D. (2013b). Organothiols self-assembled onto gold: evidence for deprotonation of the sulfur-bound hydrogen and charge transfer from thiolate. *J. Phys. Chem. C* 117, 8793–8798. doi: 10.1021/jp312836q

Athukorale, S., De Silva, M., LaCour, A., Perera, G. S., Pittman, C. U., and Zhang, D. (2018). NaHS induces complete nondestructive ligand displacement from aggregated gold nanoparticles. *J. Phys. Chem. C* 122, 2137–2144. doi: 10.1021/acs.jpcc.7b10069

Athukorale, S., Perera, G. S., Gadogbe, M., Perez, F., and Zhang, D. (2017b). Reactive Ag^+ adsorption onto gold. *J. Phys. Chem. C* 121, 22487–22495. doi: 10.1021/acs.jpcc.7b07077

Athukorale, S. A., Zhou, Y., Zou, S., and Zhang, D. (2017a). Determining the liquid light scattering cross section and depolarization spectra using polarized resonance synchronous spectroscopy. *Anal. Chem.* 89, 12705–12712. doi: 10.1021/acs.analchem.7b02721

Bantz, K. C., Nelson, H. D., and Haynes, C. L. (2012). Plasmon-enabled study of self-assembled alkanethiol ordering on roughened Ag substrates. *J. Phys. Chem. C* 116, 3585–3593. doi: 10.1021/jp2098334

Bastús, N. G., Comenge, J., and Puntes, V. (2011). Kinetically controlled seeded growth synthesis of citrate-stabilized gold nanoparticles of up to 200 nm: size focusing versus ostwald ripening. *Langmuir* 27, 11098–11105. doi: 10.1021/la201938u

Brown, S. D., Nativo, P., Smith, J.-A., Stirling, D., Edwards, P. R., Venugopal, B., et al. (2010). Gold nanoparticles for the improved anticancer drug delivery of the active component of oxaliplatin. *J. Am. Chem. Soc.* 132, 4678–4684. doi: 10.1021/ja908117a

Daniel, M.-C., and Astruc, D. (2004). Gold nanoparticles: assembly, supramolecular chemistry, quantum-size-related properties, and applications toward biology, catalysis, and nanotechnology. *Chem. Rev.* 104, 293–346. doi: 10.1021/cr030698+

Dykman, L., and Khlebtsov, N. (2012). Gold nanoparticles in biomedical applications: recent advances and perspectives. *Chem. Soc. Rev.* 41, 2256–2282. doi: 10.1039/c1cs15166e

El-Sayed, I. H., Huang, X., and El-Sayed, M. A. (2006). Selective laser photo-thermal therapy of epithelial carcinoma using anti-Egfr antibody conjugated gold nanoparticles. *Cancer Lett.* 239, 129–135. doi: 10.1016/j.canlet.2005.07.035

Eustis, S., and El-Sayed, M. A. (2006). Why gold nanoparticles are more precious than pretty gold: noble metal surface plasmon resonance and its enhancement of the radiative and nonradiative properties of nanocrystals of different shapes. *Chem. Soc. Rev.* 35, 209–217. doi: 10.1039/b514191e

Frens, G. (1973). Controlled nucleation for the regulation of the particle size in monodisperse gold suspensions. *Nature* 241, 20–22. doi: 10.1038/physci241020a0

Gadogbe, M., Ansar, S. M., He, G., Collier, W. E., Rodriguez, J., Liu, D., et al. (2013). Determination of colloidal gold nanoparticle surface areas, concentrations, and sizes through quantitative ligand adsorption. *Anal. Bioanal. Chem.* 405, 413–422. doi: 10.1007/s00216-012-6489-2

Gadogbe, M., Chen, M., Zhao, X., Saebo, S., Beard, D. J., and Zhang, D. (2015). Can para-aryl-dithiols cross-link two plasmonic noble nanoparticles as monolayer dithiolate spacers? *J. Phys. Chem. C* 119, 6626–6633. doi: 10.1021/acs.jpcc.5b00293

Ghosh, P. S., Kim, C.-K., Han, G., Forbes, N. S., and Rotello, V. M. (2008). Efficient gene delivery vectors by tuning the surface charge density of amino acid-functionalized gold nanoparticles. *ACS Nano* 2, 2213–2218. doi: 10.1021/nn800507t

Homberger, M., and Simon, U. (2010). On the application potential of gold nanoparticles in nanoelectronics and biomedicine. *Phil. Trans. R. Soc. A* 368, 1405–1453. doi: 10.1098/rsta.2009.0275

Hurst, S. J., Lytton-Jean, A. K. R., and Mirkin, C. A. (2006). Maximizing DNA loading on a range of gold nanoparticle sizes. *Anal. Chem.* 78, 8313–8318. doi: 10.1021/ac0613582

Jana, N. R., Gearheart, L., and Murphy, C. J. (2001a). Seed-mediated growth approach for shape-controlled synthesis of spheroidal and rod-like gold nanoparticles using a surfactant template. *Adv. Mater.* 13, 1389–1393. doi: 10.1002/1521-4095(200109)13:18<1389::AID-ADMA1389>3.0.CO;2-F

Jana, N. R., Gearheart, L., and Murphy, C. J. (2001b). Seeding growth for size control of 5–40 nm diameter gold nanoparticles. *Langmuir* 17, 6782–6786. doi: 10.1021/la0104323

Ji, X., Song, X., Li, J., Bai, Y., Yang, W., and Peng, X. (2007). Size control of gold nanocrystals in citrate reduction: the third role of citrate. *JACS* 129, 13939–13948. doi: 10.1021/ja074447k

Kang, H., Kim, B.-G., Na, H. B., and Hwang, S. (2015). Anti-galvanic reduction of silver ion on gold and its role in anisotropic growth of gold nanomaterials. *J. Phys. Chem. C* 119, 25974–25982. doi: 10.1021/acs.jpcc.5b08216

Karunanayake, A. G., Gunatilake, S. R., Ameer, F. S., Gadogbe, M., Smith, L., Mlsna, D., et al. (2015). Undergraduate laboratory experiment modules for probing gold nanoparticle interfacial phenomena. *J. Chem. Educ.* 92, 1924–1927. doi: 10.1021/acs.jchemed.5b00535

Lee, P. C., and Meisel, D. (1982). Adsorption and surface-enhanced raman of dyes on silver and gold sols. *J. Phys. Chem.* 86, 3391–3395. doi: 10.1021/j100214a025

Liu, X., and Astruc, D. (2017). From galvanic to anti-galvanic synthesis of bimetallic nanoparticles and applications in catalysis, sensing, and materials science. *Adv. Mater.* 29:1605305-n/a. doi: 10.1002/adma.201605305

Masheter, A. T., Abiman, P., Wildgoose, G. G., Wong, E., Xiao, L., Rees, N. V., et al. (2007). Investigating the reactive sites and the anomalously large changes in surface pKa values of chemically modified carbon nanotubes of different morphologies. *J. Mater. Chem.* 17, 2616–2626. doi: 10.1039/B702492D

Naumkin, A. V., Kraut-Vass, A., Gaarenstroom, S. W., and Powell, C. J. (2012). *NIST Standard Reference Database 20, Version 4.1 (Web Version)* [Online]. Available online at: https://srdata.nist.gov/xps/ (Accessed September 9, 2018).

Nguyen, H. M., Park, K., and Hwang, S. (2018). The effect of an antigalvanic reduction of silver on gold for the stability of a self-assembled alkanethiol monolayer and chemical lift-off lithography. *J. Phys. Chem. C* 122, 16070–16078. doi: 10.1021/acs.jpcc.8b03435

Ojea-Jiménez, I., and Campanera, J. M. (2012). Molecular modeling of the reduction mechanism in the citrate-mediated synthesis of gold nanoparticles. *J. Phys. Chem. C* 116, 23682–23691. doi: 10.1021/jp305830p

Perera, G. S., Athukorale, S. A., Perez, F., Pittman, C. U., and Zhang, D. (2018). Facile displacement of citrate residues from gold nanoparticle surfaces. *J. Colloid Interface Sci.* 511, 335–343. doi: 10.1016/j.jcis.2017.10.014

Perera, G. S., Gadogbe, M., Alahakoon, S. H., Zhou, Y., Zou, S., Perez, F., et al. (2016a). Ion pairing as the main pathway for reducing electrostatic repulsion among organothiolate self-assembled on gold nanoparticles in water. *J. Phys. Chem. C* 120, 19878–19884. doi: 10.1021/acs.jpcc.6b07466

Perera, G. S., Nettles, C. B., Zhou, Y., Zou, S., Hollis, T. K., and Zhang, D. (2015). Direct observation of ion pairing at the liquid/solid interfaces by surface enhanced raman spectroscopy. *Langmuir* 31, 8998–9005. doi: 10.1021/acs.langmuir.5b01903

Perera, G. S., Yang, G., Nettles, C. B., Perez, F., Hollis, T. K., and Zhang, D. (2016b). Counterion effects on electrolyte interactions with gold nanoparticles. *J. Phys. Chem. C* 120, 23604–23612. doi: 10.1021/acs.jpcc.6b07885

Rycenga, M., McLellan, J. M., and Xia, Y. (2009). A SERS study of the molecular structure of alkanethiol monolayers on Ag nanocubes in the presence of aqueous glucose. *Chem. Phys. Lett.* 463, 166–171. doi: 10.1016/j.cplett.2008.08.062

Seidell, A. (1928). Solubilities of inorganic and organic compounds. A compilation of quantitative solubility data from the periodical literature, Washington. Supplement to the second edition containing data published during the years 1917–1926 inclusive. D. van Nostrand Company, Inc., New York/Gauthier-Villars et Cie., Paris, 1928. 569 Seiten. *Archiv der Pharm.* 266, 544c−544. doi: 10.1002/ardp.192800154

Siriwardana, K., Gadogbe, M., Ansar, S. M., Vasquez, E. S., Collier, W. E., Zou, S., et al. (2014). Ligand adsorption and exchange on pegylated gold nanoparticles. *J. Phys. Chem. C* 118, 11111–11119. doi: 10.1021/jp501391x

Siriwardana, K., Vithanage, B. C. N., Zou, S., and Zhang, D. (2017). Quantification of the depolarization and anisotropy of fluorophore stokes-shifted fluorescence, on-resonance fluorescence, and rayleigh scattering. *Anal. Chem.* 89, 6686–6694. doi: 10.1021/acs.analchem.7b00907

Siriwardana, K., Wang, A., Vangala, K., Fitzkee, N., and Zhang, D. (2013). Probing the effects of cysteine residues on protein adsorption onto gold nanoparticles using wild-type and mutated GB3 proteins. *Langmuir* 29, 10990–10996. doi: 10.1021/la402239h

Sugihara, K., Shimazu, K., and Uosaki, K. (2000). Electrode potential effect on the surface pka of a self-assembled 15-mercaptohexadecanoic acid monolayer on a gold/quartz crystal microbalance electrode. *Langmuir* 16, 7101–7105. doi: 10.1021/la991301t

Vangala, K., Ameer, F., Salomon, G., Le, V., Lewis, E., Yu, L., et al. (2012). Studying protein and gold nanoparticle interaction using organothiols as molecular probes. *J. Phys. Chem. C* 116, 3645–3652. doi: 10.1021/jp2107318

Wang, A., Perera, Y. R., Davidson, M. B., and Fitzkee, N. C. (2016). Electrostatic interactions and protein competition reveal a dynamic surface in gold nanoparticle–protein adsorption. *J. Phys. Chem. C* 120, 24231–24239. doi: 10.1021/acs.jpcc.6b08469

Wang, M., Wu, Z., Chu, Z., Yang, J., and Yao, C. (2014). Chemico-physical synthesis of surfactant- and ligand-free gold nanoparticles and their anti-galvanic reduction property. *Chem. Asian J.* 9, 1006–1010. doi: 10.1002/asia.201301562

Woods, K. E., Perera, Y. R., Davidson, M. B., Wilks, C. A., Yadav, D. K., and Fitzkee, N. C. (2016). Understanding protein structure deformation on the surface of gold nanoparticles of varying size. *J. Phys. Chem. C* 120, 27944–27953. doi: 10.1021/acs.jpcc.6b08089

Wu, Z. (2012). Anti-galvanic reduction of thiolate-protected gold and silver nanoparticles. *Angew. Chem. Int. Ed.* 51, 2934–2938. doi: 10.1002/anie.201107822

Xu, J. X., Siriwardana, K., Zhou, Y., Zou, S., and Zhang, D. (2018a). Quantification of gold nanoparticle ultraviolet–visible extinction, absorption, and scattering cross-section spectra and scattering depolarization spectra: the effects of nanoparticle geometry, solvent composition, ligand functionalization, and nanoparticle aggregation. *Anal. Chem.* 90, 785–793. doi: 10.1021/acs.analchem.7b03227

Xu, J. X., Vithanage, B. C. N., Athukorale, S. A., and Zhang, D. (2018b). Scattering and absorption differ drastically in their inner filter effects on fluorescence, resonance synchronous, and polarized resonance synchronous spectroscopic measurements. *Analyst* 143, 3382–3389. doi: 10.1039/C8AN00790J

Zhao, W., Chiuman, W., Lam, J. C. F., McManus, S. A., Chen, W., Cui, Y., et al. (2008). DNA aptamer folding on gold nanoparticles: from colloid chemistry to biosensors. *J. Am. Chem. Soc.* 130, 3610–3618. doi: 10.1021/ja710241b

Zhou, X., Xu, W., Liu, G., Panda, D., and Chen, P. (2010). Size-dependent catalytic activity and dynamics of gold nanoparticles at the single-molecule level. *J. Am. Chem. Soc.* 132, 138–146. doi: 10.1021/ja904307n

Conflict of Interest Statement: The authors declare that the research was conducted in the absence of any commercial or financial relationships that could be construed as a potential conflict of interest.

Advantages of publishing in Frontiers

OPEN ACCESS
Articles are free to read
for greatest visibility
and readership

FAST PUBLICATION
Around 90 days
from submission
to decision

HIGH QUALITY PEER-REVIEW
Rigorous, collaborative,
and constructive
peer-review

TRANSPARENT PEER-REVIEW
Editors and reviewers
acknowledged by name
on published articles

Frontiers
Avenue du Tribunal-Fédéral 34
1005 Lausanne | Switzerland

Visit us: www.frontiersin.org
Contact us: info@frontiersin.org | +41 21 510 17 00

REPRODUCIBILITY OF RESEARCH
Support open data
and methods to enhance
research reproducibility

DIGITAL PUBLISHING
Articles designed
for optimal readership
across devices

FOLLOW US
@frontiersin

IMPACT METRICS
Advanced article metrics
track visibility across
digital media

EXTENSIVE PROMOTION
Marketing
and promotion
of impactful research

LOOP RESEARCH NETWORK
Our network
increases your
article's readership